40 CFR Part 191
Subparts B and C
Compliance Recertification Application 2026
for the
Waste Isolation Pilot Plant

Appendix PA-2026
Performance Assessment

United States Department of Energy
Waste Isolation Pilot Plant

Carlsbad Field Office
Carlsbad, New Mexico

Compliance Recertification Application 2026
Appendix PA

TABLE OF CONTENTS

PA-1.0 INTRODUCTION 1
PA-1.1 Definition of Performance Assessment 1
PA-1.2 Organization of this Appendix 2
PA-1.3 Changes since the CRA-2019 PA 4
PA-1.3.1 Repository Design 8
PA-1.3.2 Grid for Flow and Transport in the Salado 10
PA-1.3.3 Repository Area and Volume Parameters 10
PA-1.3.4 Waste Area Pressure at the Time of Closure 11
PA-1.3.5 Porosity of Waste Areas with Creep Closure 11
PA-1.3.6 Capillary Pressure Model for Anhydrite Marker Beds 11
PA-1.3.7 Porosity-Permeability Distribution for Panel Closures 11
PA-1.3.8 Castile Brine Reservoir 11
PA-1.3.9 Iron Surface Area 12
PA-1.3.10 MgO Hydration 12
PA-1.3.11 Borehole Long-Term Permeability 12
PA-1.3.12 Waste Inventory 12
PA-1.3.13 Baseline Actinide Solubilities and Uncertainties 13
PA-1.3.14 Oxidation State Model 13
PA-1.3.15 Colloid Enhancement Parameters 14
PA-1.3.16 Minimum Brine Volume Associated with DBR 14
PA-1.3.17 Grid for DBR 14
PA-1.3.18 Mass Release Locations in the Culebra 14
PA-1.3.19 Culebra Transmissivity 14
PA-1.3.20 Panel Adjacency and Neighboring Assignments 15
PA-1.3.21 Drilling Frequency and Plugging Pattern Probabilities 15
PA-1.3.22 Probability of a Castile Intrusion 16
PA-1.3.23 Sample of Uncertain Parameters 16
PA-1.3.24 Computational Platform and Code Updates 16

PA-2.0 OVERVIEW OF THE PA 17
PA-2.1 Regulatory Requirements 17
PA-2.2 PA Methodology 20
PA-2.2.1 Identification and Screening of FEPs 21
PA-2.2.2 Scenario Development and Selection 21
PA-2.2.3 Calculation of Scenario Consequences 31
PA-2.3 Conceptual Description of the Undisturbed Repository System 32
PA-2.4 Conceptual Description of the Disturbed Repository System 34
PA-2.4.1 Cuttings and Cavings 35
PA-2.4.2 Spallings 35
PA-2.4.3 Direct Brine Releases 36
PA-2.4.4 Long-Term Brine Releases 36
PA-2.5 Structure of the PA 40

PA-2.5.1 Probabilistic Characterization of Different Futures 40
PA-2.5.2 Estimation of Releases 41
PA-2.5.3 Probabilistic Characterization of Parameter Uncertainty 44
PA-2.6 Compliance Demonstration Method 45

PA-3.0 PROBABILISTIC CHARACTERIZATION OF FUTURES 47
PA-3.1 Institutional Controls 47
PA-3.2 Drilling Intrusion 47
PA-3.2.1 Penetration of Excavated/Nonexcavated Area 48
PA-3.2.2 Drilling Location 49
PA-3.2.3 Penetration of Pressurized Brine 49
PA-3.2.4 Plugging Pattern 49
PA-3.2.5 Waste Activity Level 50
PA-3.3 Mining Time 51
PA-3.4 Scenarios and Scenario Probabilities 51

PA-4.0 ESTIMATION OF RELEASES 53
PA-4.1 Results for Specific Futures 53
PA-4.2 Two-Phase Flow in the Salado: BRAGFLO 55
PA-4.2.1 Mathematical Description 55
PA-4.2.2 Material Properties 62
PA-4.2.3 Initial Conditions 82
PA-4.2.4 Creep Closure of Repository 84
PA-4.2.5 Fracturing of MBs and DRZ 85
PA-4.2.6 Gas Generation and Brine Production 86
PA-4.2.7 Capillary Action in the Waste 86
PA-4.2.8 Shafts 87
PA-4.2.9 Panel Closures 88
PA-4.2.10 Borehole Model 90
PA-4.2.11 Castile Brine Reservoir 91
PA-4.2.12 Numerical Solution 92
PA-4.2.13 Gas and Brine Flow across Specified Boundaries 96
PA-4.2.14 Additional Information 96
PA-4.3 Radionuclide Source Term 97
PA-4.3.1 Determination of Oxidation State 97
PA-4.3.2 Mobile Concentration Limits 97
PA-4.3.3 Radionuclides for Transport in the Salado 99
PA-4.3.4 Radionuclides for Direct Solid Releases 100
PA-4.3.5 Radionuclides for Direct Releases in Brine 100
PA-4.4 Radionuclide Transport in the Salado: NUTS 100
PA-4.4.1 Mathematical Description 101
PA-4.4.2 Numerical Solution 103
PA-4.4.3 Additional Information 107
PA-4.5 Radionuclide Transport in the Salado: PANEL 107

PA-4.5.1 Mathematical Description 107
PA-4.5.2 Numerical Solution 108
PA-4.5.3 Additional Information 109
PA-4.6 Cuttings and Cavings to Surface: CUTTINGS_S 109
PA-4.6.1 Cuttings 109
PA-4.6.2 Cavings 110
PA-4.6.3 Additional Information 118
PA-4.7 Spallings to Surface: DRSPALL and CUTTINGS_S 118
PA-4.7.1 Summary of Assumptions 118
PA-4.7.2 Mathematical Description 119
PA-4.7.3 Numerical Model 132
PA-4.7.4 Implementation in the PA 140
PA-4.7.5 Additional Information 141
PA-4.8 DBR to Surface: BRAGFLO 141
PA-4.8.1 Material Properties for DBR 144
PA-4.8.2 Initial Conditions for DBR 145
PA-4.8.3 Representation of the Flow Rate *rDBR*(*t*) 146
PA-4.8.4 Determination of the Productivity Index J_p 146
PA-4.8.5 Determination of the Waste Panel Pressure $p_w(t)$ and DBR 148
PA-4.8.6 Boundary Value Pressure p_{wf} 150
PA-4.8.7 Boundary Value Pressure p_{wE1} 158
PA-4.8.8 End of DBR 162
PA-4.8.9 Numerical Solution 163
PA-4.8.10 Additional Information 165
PA-4.9 Groundwater Flow in the Culebra Dolomite 165
PA-4.9.1 Mathematical Description 165
PA-4.9.2 Computational Grid and Boundary Conditions 166
PA-4.9.3 Generation of T-fields 168
PA-4.9.4 Mining Area and Modification 169
PA-4.9.5 Flow in the Culebra 172
PA-4.9.6 Numerical Solution 172
PA-4.9.7 Additional Information 173
PA-4.10 Radionuclide Transport in the Culebra Dolomite 174
PA-4.10.1 Mathematical Description 174
PA-4.10.2 Numerical Solution 179
PA-4.10.3 Additional Information 183

PA-5.0 PROBABILISTIC CHARACTERIZATION OF SUBJECTIVE UNCERTAINTY 184
PA-5.1 Probability Space 184
PA-5.2 Variables Included for Subjective Uncertainty 184

PA-6.0 COMPUTATIONAL PROCEDURES 190
PA-6.1 Sampling for Epistemic Uncertainty 190
PA-6.1.1 Generation of Latin Hypercube Samples 191

PA-6.1.2 Statistical Confidence on Mean CCDF 192
PA-6.2 Sampling for Aleatory Uncertainty 192
PA-6.3 Mechanistic Calculations 194
PA-6.3.1 BRAGFLO Calculations 194
PA-6.3.2 NUTS Calculations 195
PA-6.3.3 PANEL Calculations 196
PA-6.3.4 DRSPALL Calculations 197
PA-6.3.5 CUTTINGS_S Calculations 197
PA-6.3.6 BRAGFLO Calculations of DBR Volumes 198
PA-6.3.7 MODFLOW6 Calculations 198
PA-6.3.8 SECOTP2D Calculations 199
PA-6.4 Computation of Releases 200
PA-6.4.1 Releases from the Undisturbed Repository 200
PA-6.4.2 Releases from the Disturbed Repository 200
PA-6.4.3 Radionuclide Transport Through the Culebra 205
PA-6.5 Construction of CCDFs 206
PA-6.6 Sensitivity Analysis 207
PA-6.6.1 Scatterplots 208
PA-6.6.2 Stepwise Regression Analysis 208

PA-7.0 RESULTS FOR THE UNDISTURBED REPOSITORY 210
PA-7.1 Flow in the Salado 210
PA-7.2 Radionuclide Transport 217

PA-8.0 RESULTS FOR A DISTURBED REPOSITORY 218
PA-8.1 Fluid Flow 218
PA-8.1.1 Salado Flow Results for E1 Intrusion Scenarios 219
PA-8.1.2 Salado Flow Results for E2 Intrusion Scenarios 224
PA-8.1.3 Salado Flow Summarized Results 229
PA-8.1.4 Culebra Flow 232
PA-8.2 Radionuclide Transport 233
PA-8.2.1 Radionuclide Mobilized Concentrations 234
PA-8.2.2 Transport through MBs and Shaft 235
PA-8.2.3 Transport to the Culebra 235
PA-8.2.4 Transport through the Culebra 237
PA-8.3 Direct Releases 239
PA-8.3.1 Cuttings and Cavings 239
PA-8.3.2 Spallings 240
PA-8.3.3 Direct Brine Releases 244

PA-9.0 NORMALIZED RELEASES 248
PA-9.1 Cuttings and Cavings 248
PA-9.2 Spallings 249
PA-9.3 Direct Brine 250

PA-9.4 Groundwater Transport 252
PA-9.5 Total Normalized Releases 253
PA-9.6 Parameter Sensitivity Analysis 257
PA-9.7 Summary of Comparison with the RPPCR PA 258

PA-10.0 REFERENCES 259

LIST OF FIGURES

Figure PA-1. Interim State Repository Layout 9
Figure PA-2. Logic Diagram for Scenario Analysis 22
Figure PA-3. Conceptual Release Pathways for the UP Scenario 24
Figure PA-4. Conceptual Release Pathways for the Disturbed Repository Deep Drilling E2 Scenario. 27
Figure PA-5. Conceptual Release Pathways for the Disturbed Repository Deep Drilling E1 Scenario. 28
Figure PA-6. Conceptual Release Pathways for the Disturbed Repository Deep Drilling E1E2 Scenario. .. 29
Figure PA-7. Conceptual Release Pathways for the Disturbed Repository M Scenario 30
Figure PA-8. Computational Models Used in PA 42
Figure PA-9. Construction of the CCDF Specified in 40 CFR Part 191 Subpart B 43
Figure PA-10. Distribution of CCDFs Resulting from Possible Values for the Sampled Parameters. 45
Figure PA-11. CDF for Time Between Drilling Intrusions 48
Figure PA-12. Generic CRA-2026 PA BRAGFLO grid with modeled area descriptions (Δx, Δy, and Δz dimensions in meters) 60
Figure PA-13. BRAGFLO Grid Indices and Cell Numbers 61
Figure PA-14. CRA-2026 PA BRAGFLO Grid and Material Map; Years −5 to 0 (all scenarios) (Δx, Δy, and Δz Dimensions in Meters) 66
Figure PA-15. CRA-2026 PA BRAGFLO Grid and Material Map; Years 0 to 100 (all scenarios) (Δx, Δy, and Δz Dimensions in Meters) 67
Figure PA-16. CRA-2026 PA BRAGFLO Grid and Material Map; Years 100 to 200 (all scenarios) (Δx, Δy, and Δz Dimensions in Meters). 68
Figure PA-17. CRA-2026 PA BRAGFLO Grid and Material Map; Years 200 to 10,000 (E0 scenario), Years 200 to First Intrusion Time (E1, E2, and E1E2 scenario) (Δx, Δy, and Δz Dimensions in Meters). 69
Figure PA-18. CRA-2026 PA BRAGFLO Grid and Material Map; From E2 Intrusion to 200 Years After Intrusion (E2 and E1E2 scenario) (Δx, Δy, and Δz Dimensions in Meters). 70
Figure PA-19. CRA-2026 PA BRAGFLO Grid and Material Map; From 200 Years After E2 Intrusion to 10,000 Years (E2 scenario), From 200 Years After E2 Intrusion to E1 Intrusion (E1E2 scenario) (Δx, Δy, and Δz Dimensions in Meters). 71
Figure PA-20. CRA-2026 PA BRAGFLO Grid and Material Map; From E1 Intrusion to 200 Years After E1 Intrusion (E1 scenario) (Δx, Δy, and Δz Dimensions in Meters). 72
Figure PA-21. CRA-2026 PA BRAGFLO Grid and Material Map; From E1 Intrusion to 200 Years After E1 Intrusion (E1E2 scenario) (Δx, Δy, and Δz Dimensions in Meters). 73
Figure PA-22. CRA-2026 PA BRAGFLO Grid and Material Map; From 200 Years After E1 Intrusion to 1,200 Years After E1 Intrusion (E1 and E1E2 scenario) (Δx, Δy, and Δz Dimensions in Meters). 74
Figure PA-23. CRA-2026 PA BRAGFLO Grid and Material Map; From 1,200 Years After E1 Intrusion to 10,000 Years (E1 and E1E2 scenario) (Δx, Δy, and Δz Dimensions in Meters). 75
Figure PA-24. Schematic View of the Simplified Shaft Model (numbers on right indicate length in meters) 88
Figure PA-25. Schematic Diagram of the ROMPCS (adapted from U.S. DOE 2011) 89
Figure PA-26. Detail of Rotary Drill String Adjacent to Drill Bit 112
Figure PA-27. Schematic Diagram of the Flow Geometry Prior to Repository Penetration (from U.S. DOE 2004) 120
Figure PA-28. Schematic Diagram of the Flow Geometry After Repository Penetration (from U.S. DOE 2004) 120
Figure PA-29. Effective Wellbore Flow Geometry Before Bit Penetration (adapted from U.S. DOE 2004) 121

Figure PA-30. Effective Wellbore Flow Geometry After Bit Penetration (adapted from U.S. DOE 2004) 121
Figure PA-31. Finite-Difference Zoning for Wellbore 133
Figure PA-32. Finite Difference Molecules for the Implicit Scheme using Constant Zone Sizes 140
Figure PA-33. CRA-2026 grid for DBR (Δx, Δy, and Δz dimensions in meters) 143
Figure PA-34. Regions Used to Transfer Initial Pressure and Saturation from the BRAGFLO Salado Grid to the DBR Grid. 144
Figure PA-35. Borehole Representation Used for Poettmann-Carpenter Correlation (adapted from U.S. DOE 2004). 152
Figure PA-36. Modeling Domains for Groundwater Flow (MODFLOW6) and Radionuclide Transport (SECOTP2D) in the Culebra. 167
Figure PA-37. Extent of Mineable Potash within Model Domain 170
Figure PA-38. Illustration of Model Cells Affected by Mining-Related Subsidence 171
Figure PA-39. Mining Impacted Areas for Full and Partial Mining Scenarios 171
Figure PA-40. Finite-Difference Grid Showing Cell Index Numbering Convention Used by MODFLOW6.173
Figure PA-41. Parallel-Plate, Dual-Porosity Conceptualization 174
Figure PA-42. Schematic of Finite-Volume Staggered Mesh Showing Internal and Ghost Cells 180
Figure PA-43. Illustration of Stretched Grid Used for Matrix Domain Discretization 182
Figure PA-44. Logic Diagram for Determining the Intrusion Type 201
Figure PA-45. Minimum, Maximum, and Mean of WP Pressure, Scenario S1-BF 212
Figure PA-46. Minimum, Maximum, and Mean of SROR Pressure, Scenario S1-BF 212
Figure PA-47. Minimum, Maximum, and Mean of NROR Pressure, Scenario S1-BF 213
Figure PA-48. Minimum, Maximum, and Mean of WROR Pressure, Scenario S1-BF 213
Figure PA-49. Minimum, Maximum, and Mean of WP Brine Saturation, Scenario S1-BF 214
Figure PA-50. Minimum, Maximum, and Mean of SROR Brine Saturation, Scenario S1-BF 214
Figure PA-51. Minimum, Maximum, and Mean of NROR Brine Saturation, Scenario S1-BF 215
Figure PA-52. Minimum, Maximum, and Mean of WROR Brine Saturation, Scenario S1-BF 215
Figure PA-53. Minimum, Maximum, and Mean of Brine Flow up the Shaft, Scenario S1-BF 216
Figure PA-54. Minimum, Maximum, and Mean Brine Flow in Anhydrite Layers Across LWB, Scenario S1-BF. 216
Figure PA-55. Minimum, Maximum, and Mean of WP Pressure, Scenario S2-BF 220
Figure PA-56. Minimum, Maximum, and Mean of SROR Pressure, Scenario S2-BF 220
Figure PA-57. Minimum, Maximum, and Mean of NROR Pressure, Scenario S2-BF 221
Figure PA-58. Minimum, Maximum, and Mean of WROR Pressure, Scenario S2-BF 221
Figure PA-59. Minimum, Maximum, and Mean of WP Brine Saturation, Scenario S2-BF 222
Figure PA-60. Minimum, Maximum, and Mean of SROR Brine Saturation, Scenario S2-BF 222
Figure PA-61. Minimum, Maximum, and Mean of NROR Brine Saturation, Scenario S2-BF 223
Figure PA-62. Minimum, Maximum, and Mean of WROR Brine Saturation, Scenario S2-BF 223
Figure PA-63. Minimum, Maximum, and Mean of Cumulative Brine Flow up the Borehole, Scenario S2-BF 224
Figure PA-64. Minimum, Maximum, and Mean of WP Pressure, Scenario S4-BF 225
Figure PA-65. Minimum, Maximum, and Mean of SROR Pressure, Scenario S4-BF 225
Figure PA-66. Minimum, Maximum, and Mean of NROR Pressure, Scenario S4-BF 226
Figure PA-67. Minimum, Maximum, and Mean of WROR Pressure, Scenario S4-BF 226
Figure PA-68. Minimum, Maximum, and Mean of WP Brine Saturation, Scenario S4-BF 227
Figure PA-69. Minimum, Maximum, and Mean of SROR Brine Saturation, Scenario S4-BF 227
Figure PA-70. Minimum, Maximum, and Mean of NROR Brine Saturation, Scenario S4-BF 228
Figure PA-71. Minimum, Maximum, and Mean of WROR Brine Saturation, Scenario S4-BF 228

Figure PA-72. Minimum, Maximum, and Mean of Cumulative Brine Flow up the Borehole, Scenario S4-BF 229
Figure PA-73. Ensemble mean flow for a) no mining, b) partial mining, and c) full mining. Arrows show ensemble mean flow direction as unit vectors 233
Figure PA-74. Mean Mobilized Radionuclide Concentrations vs. Time, Castile (ERDA-6) Brine 234
Figure PA-75. Cumulative Radionuclide Discharge to Culebra at 10,000 Years 236
Figure PA-76. Cumulative Brine Discharge Up Borehole at 10,000 Years[4] 237
Figure PA-77. Mass Breakthrough by Release Point at 10,000-yr: Full Mining Scenario 238
Figure PA-78. Mass Breakthrough by Release Point at 10,000-yr: Partial Mining Scenario 239
Figure PA-79. Scatterplot of Waste Permeability Versus Spallings Volume for Replicate 1 241
Figure PA-80. Scatterplot of Waste Particle Diameter Versus Spallings Volume for Replicate 1 242
Figure PA-81. Release Volume Frequency, All Intrusions 246
Figure PA-82. Release Volume Boxplots, All Nonzero Events[5] 246
Figure PA-83. S2-DBR Release Volumes, All Intrusions 247
Figure PA-84. Overall Mean CCDFs for Cuttings and Cavings Releases with Confidence Limits 249
Figure PA-85. Overall Mean CCDFs for Spallings Releases with Confidence Limits 250
Figure PA-86. Overall Mean CCDFs for DBRs with Confidence Limits 252
Figure PA-87. Mean CCDFs for Releases from the Culebra with Confidence Limits 253
Figure PA-88. Total Normalized Releases, Replicate 1 254
Figure PA-89. Total Normalized Releases, Replicate 2 254
Figure PA-90. Total Normalized Releases, Replicate 3 255
Figure PA-91. Comparison of CRA-2026 Overall Means for Release Components 256
Figure PA-92. Overall Mean CCDFs for Total Normalized Releases with Confidence Limits 257

LIST OF TABLES

Table PA-1. Changes Since the CRA-2019 PA Incorporated in the CRA-2026 PA 4
Table PA-2. Changed Repository Parameters 10
Table PA-3. Drilling Frequency and Plugging Pattern Parameters 16
Table PA-4. Release Limits for Containment Requirements (40 CFR 191, Appendix A, Table 1) 19
Table PA-5. Parameter Values Used in Representation of Two-Phase Flow 76
Table PA-6. Models for Relative Permeability and Capillary Pressure in Two-Phase Flow 81
Table PA-7. Initial Conditions in the Rustler 82
Table PA-8. Permeabilities for Drilling Intrusions Through the Repository 91
Table PA-9. Boundary Value Conditions for P_g and P_b 93
Table PA-10. Auxiliary Dirichlet Conditions for S_g and P_b 93
Table PA-11. Radionuclides Considered in Releases 97
Table PA-12. Initial and Boundary Conditions for $C_{bl}(x, y, t)$ and $C_{sl}(x, y, t)$ 104
Table PA-13. Uncertain Parameters in DRSPALL Calculations 141
Table PA-14. Boundary Conditions for p_b and S_g in DBR Calculations 150
Table PA-15. Diffusion Coefficients by Oxidation State 176
Table PA-16. Sampled Parameters with Updated Distributions Since the CRA-2019 PA 185
Table PA-17. Variables Representing Epistemic Uncertainty in the CRA-2026 PA 185
Table PA-18. Algorithm to Generate a Single Future 193
Table PA-19. BRAGFLO Scenarios in the CRA-2026 PA 194
Table PA-20. NUTS Release Calculations in the CRA-2026 PA 195
Table PA-21. Scenarios for spallings and DBRs in the CRA-2026 PA 197
Table PA-22. MODFLOW6 Scenarios in the CRA-2026 PA 199
Table PA-23. SECOTP2D Scenarios in the CRA-2026 PA 199
Table PA-24. Pressure (MPa) Statistics on Replicate 1 Means 230
Table PA-25. Brine Saturation Statistics on Replicate 1 Means 231
Table PA-26. Brine Flow (m^3) Statistics for Replicate 1 232
Table PA-27. CRA-2026 PA Cavings Area Statistics 240
Table PA-28. Spallings Volume Statistics for Replicate 1 243
Table PA-29. RPPCR and CRA-2026 PA DBR Volume Statistics 245
Table PA-30. RPPCR and CRA-2006 Statistics on the Overall Mean for Total Normalized Releases in EPA Units at Probabilities of 0.1 and 0.001 257

ACRONYMS AND ABBREVIATIONS

%	percent
AIC	active institutional control
APCS	Abandonment of Panel Closures in South End of Repository
APPA	Additional Panels Performance Assessment
C	Celsius
CCA	Compliance Certification Application
CCDF	complementary cumulative distribution function
CDF	cumulative distribution function
CFR	Code of Federal Regulations
CH	contact-handled
Ci	curies
CL	confidence limit
CPR	cellulosic, plastic, and rubber
CRP	Culebra Release Point
CRA	Compliance Recertification Application
CRA26_FS	CRA-2026 performance assessment for the final state (FS) repository
CRA26_IS	CRA-2026 performance assessment for the interim state (IS) repository
DBMAR	Delaware Basin Monitoring Annual Report
DBR	direct brine release
DDZ	drilling damaged zone
DOE	U.S. Department of Energy
DP	disturbed repository performance
DRZ	disturbed rock zone
E	deep drilling scenario
EPA	U.S. Environmental Protection Agency
ERDA	U.S. Energy Research and Development Administration
eV	electron volt
EXP	experimental area
FEP	feature, event, and process
FS	final state

FVW	fraction of excavated repository volume occupied by waste
ft	feet
gal	gallon
GWB	Generic Weep Brine
in	inch
IS	interim state
J	Joule
K	Kelvin
K_d	distribution coefficient
kg	kilogram
km	kilometer
km^2	square kilometers
L	liter
L_i	release limit for radionuclide *i*
LANL-ACRSP	Los Alamos National Laboratory Actinide Chemistry and Repository Science Program
LHS	Latin hypercube sampling
LWA	Land Withdrawal Act
LWB	Land Withdrawal Boundary
M	mining scenario
m	meter
m^2	square meters
m^3	cubic meters
MB	marker bed
ME	mining and drilling scenario
MeV	million electron volt
mol	mole
MPa	megapascal
MTHM	metric tons of heavy metal
MWd	megawatt-days
N	Newton

NROR	North Rest-of-Repository
OPS	operations area
Pa	Pascal
PA	performance assessment
PABC	performance assessment baseline calculation
PAIR	Performance Assessment Inventory Report
PAPDB	Performance Assessment Parameter Database
PAVT	Performance Assessment Verification Test
PCC	partial correlation coefficient
PCN	Planned Change Notice
PCS	panel closure system area
PDE	partial differential equation
PDF	probability distribution function
pH	negative logarithm of H^+ activity
PIC	passive institutional control
ppm	parts per million
PR	productivity ratio
PRESS	predicted error sum of squares
psia	pounds per square inch absolute
RH	remote-handled
RKS	Redlich-Kwong-Soave
ROM	run-of-mine
ROMPCS	run-of-mine salt panel closure system
RoR	rest of repository
RPPCR	Replacement Panels Planned Change Request
s	second
s^2	seconds squared
SCF/d	standard cubic feet per day
SMC	Salado Mass Concrete
SNL	Sandia National Laboratories
SOP	South Operations Area

SPR	Software Problem Report
SRC	standardized regression coefficient
SROR	South Rest-of-Repository
T-field	transmissivity field
TDEM	time-domain electromagnetic
TRU	transuranic
TSD	Technical Support Document
TVD	Total Variation Diminishing
UP	undisturbed repository performance
WIPP	Waste Isolation Pilot Plant
WOP	West Operations Area
WP	waste panel
WROR	West Rest-of-Repository
yr	year

ELEMENTS AND CHEMICAL COMPOUNDS

Al	aluminum
Am	americium
C	carbon
$C_6H_{10}O_5$	generic formula for CPR
Cf	californium
Cm	curium
CO_2	carbon dioxide
EDTA	ethylenediaminetetraacetic acid
Fe	iron
$FeOH_2$	ferrous iron hydroxide
H_2	hydrogen gas
H_2O	water
H_2S	hydrogen sulfide
Mg	magnesium
MgO	magnesium oxide, or periclase

$Mg(OH)_2$	brucite
Np	neptunium
O_2	oxygen
Pa	protactinium
Pb	lead
Pm	promethium
Pu	plutonium
Sm	samarium
Th	thorium
U	uranium

PA-1.0 Introduction

This appendix presents the methods and mathematical models used to evaluate performance of the Waste Isolation Pilot Plant (WIPP) disposal system and the results of these models for the 2026 Compliance Recertification Application (CRA-2026) Performance Assessment (PA).

All previous WIPP certifications have been based on a repository consisting of 10 panels. In March 2024, the U.S. Department of Energy (DOE) submitted the Replacement Panels Planned Change Request (RPPCR) to seek approval from the U.S. Environmental Protection Agency (EPA) for waste emplacement in two new panels, referred to as replacement panels, located to the west of the existing operations area (Bollinger 2024). The RPPCR received EPA approval in July of 2025 (U.S. EPA 2025).

The addition of the two replacement panels is not expected to provide sufficient space for the disposal of the allowable waste volume designated for WIPP under the Land Withdrawal Act (LWA) (U.S. Congress 1992; U.S. Congress 1996). The 12-panel configuration is thus regarded as an interim state (IS) of the repository. The DOE may seek approval to dispose of waste in up to seven additional panels to accommodate the full allowable waste volume. This 19-panel configuration is considered the anticipated final state (FS) of the repository.

This appendix documents the methods and models used to represent the IS repository and presents results from the performance assessment for the IS repository, hereafter referred to as the CRA-2026 PA. This calculation corresponds to the internal model run identified as CRA26_IS.

An additional analysis was performed for the FS repository configuration (CRA26_FS) and is summarized in Attachment A: Final State Analysis.

PA-1.1 Definition of Performance Assessment

The term PA means an analysis that (1) identifies the processes and events that might affect the disposal system; (2) examines the effects of these processes and events on the performance of the disposal system; and (3) estimates the cumulative releases of radionuclides, considering the associated uncertainties, caused by all significant processes and events (40 CFR 191.12 (U.S. EPA 1993)). The PA is designed to address three primary questions about the WIPP:

Q1: What processes and events that might affect the disposal system could occur at the WIPP site over the next 10,000 years?

Q2: How likely are the various processes and events that might affect the disposal system to occur at the WIPP site over the next 10,000 years?

Q3: What are the consequences of the occurrence of various processes and events that might affect the disposal system at the WIPP site over the next 10,000 years?

In addition, uncertainty in the parameters of the PA models leads to a further question:

Q4: How much confidence should be placed in answers to the first three questions?

These questions give rise to a methodology for quantifying the probability distribution of possible radionuclide releases from the WIPP repository over the next 10,000 years, and for characterizing the uncertainty in that distribution due to imperfect knowledge of the parameters used to predict releases. The containment requirements of 40 CFR 191.13 require the use of this probabilistic methodology.

PA-1.2 Organization of this Appendix

This appendix is organized as follows: Section PA-1.3 summarizes changes made to the WIPP PA since the CRA-2019 PA (U.S. DOE 2019).

Section PA-2.0 provides an overview of the CRA-2026 PA. The PA is designed to address the requirements of 40 CFR 191.13 and thus computes a mean complementary cumulative distribution function (CCDF) of potential releases from the disposal system. This computation involves three mathematical entities: (1) models for both the physical processes that take place at the WIPP site and the estimation of potential radionuclide releases that may be associated with these processes; (2) a probabilistic characterization of the uncertainty in the models and parameters that underlay the WIPP PA (to account for epistemic uncertainty); and (3) a probabilistic characterization of events that could occur at the WIPP site over the next 10,000 years (to account for aleatory uncertainty)[1]. Section PA-2.0 is supplemented by Appendix SCR-2026, which documents the results of the screening process for features, events, and processes (FEPs) that are retained in the conceptual models of repository performance.

Section PA-3.0 describes the probabilistic characterization of different futures and summarizes the stochastic variables that represent future drilling and mining events in the PA. This characterization plays an important role in the construction of the CCDF specified in 40 CFR 191.13. Based on regulatory guidance, FEP screening, extensive review of the WIPP site, and years of performance assessment experience, exploratory drilling for natural resources and potash mining have been identified as the only disruptions with the potential to affect radionuclide releases to the accessible environment.

Section PA-4.0 presents the mathematical models for the physical processes that occur at the WIPP site and for the estimation of potential radionuclide releases. The mathematical models

[1] Aleatory uncertainty is the uncertainty associated with randomness in future states of the WIPP system and is implemented in WIPP PA via the probabilistic treatment of future events (see Section PA-2.5.1). In contrast, epistemic uncertainty represents a lack of knowledge about parameters or models and is implemented in WIPP PA via the probabilistic treatment of parameters (see Section PA-2.5.3).

implement the conceptual models as prescribed in 40 CFR 194.23 and permit the construction of the CCDF specified in 40 CFR 191 Appendix C. Models presented in Section PA-4.0 include two-phase (i.e., gas and brine) flow in the vicinity of the repository; radionuclide transport in the Salado formation (hereafter referred to as the Salado); releases to the surface at the time of a drilling intrusion due to cuttings, cavings, spallings, and direct brine releases (DBRs); brine flow in the Culebra Dolomite member of the Rustler formation (hereafter referred to as the Culebra); and radionuclide transport in the Culebra. Section PA-4.0 is supplemented by Appendices GEOCHEM-2026, MASS-2026, PORSURF-2026, SOTERM-2026, and TFIELD-2026. Appendix GEOCHEM-2026 sets forth the chemical conditions and processes in the repository. Appendix MASS-2026 discusses the modeling assumptions used in the WIPP PA. Appendix PORSURF-2026 presents results from modeling the effects of excavated region closure, waste consolidation, and gas generation in the repository. Appendix SOTERM-2026 describes the actinide source term for the WIPP performance calculations, including the mobile concentrations of actinides that may be released from the repository in brine. Appendix TFIELD-2026 discusses the generation of the transmissivity fields (T-fields) used to model groundwater flow in the Culebra.

Section PA-5.0 discusses the probabilistic characterization of parameter uncertainty, including the uncertain variables incorporated into the CRA-2026 PA, the distributions assigned to these variables, and the correlations between them. Section PA-5.0 is supplemented by Feng and Kicker (2025a) and King and Zeitler (2025).

Section PA-6.0 summarizes the computational procedures used in the CRA-2026 PA, including sampling techniques for epistemic uncertainty, generation of random futures, calculations performed with the models discussed in Section PA-4.0, construction of releases for each future, construction of CCDFs, and the sensitivity analysis techniques in use.

Section PA-7.0 presents results for the undisturbed repository. Releases from the undisturbed repository are determined by radionuclide transport in brine flowing from the repository to the LWA-defined Land Withdrawal Boundary (LWB) through the marker beds (MBs) or shafts. Releases in the undisturbed scenario are used to demonstrate compliance with the individual and groundwater protection requirements in 40 CFR 194.51 and 194.52.

Section PA-8.0 presents intermediate results for a disturbed repository. Intermediate results show releases conditional on specific future events. As discussed in Section PA-2.2, the future events and processes considered in the analysis of disturbed repository performance are those associated with mining and deep drilling. Release mechanisms include direct releases at the time of the intrusion via cuttings, cavings, spallings, and DBRs, and long-term releases via radionuclide transport up abandoned boreholes to the Culebra and thence to the LWB.

Section PA-9.0 presents the CCDFs of normalized releases. The CCDFs of normalized releases account for uncertainty in future events and model parameters. Section PA-9.0 also presents results of a sensitivity analysis to determine which subjectively uncertain parameters are most influential in the uncertainty of PA results.

The results of the PA for CRA-2026, as documented in Section PA-7.0, Section PA-8.0, and Section PA-9.0, confirm that direct releases from drilling intrusions are the major contributors to radionuclide release to the accessible environment. The CRA-2026 PA results demonstrate that the WIPP continues to comply with the quantitative containment requirements in 40 CFR 191.13(a).

The overall structure of Appendix PA-2026 is essentially unchanged from that of the Appendix PA-2019 (U.S. DOE 2019). Some content previously included in Appendix MASS has been moved to Appendix PA-2026 for consistency in separating modeling assumptions from methodology and results. This appendix follows the approach used by Helton et al. (1998) to document the mathematical models used in the Compliance Certification Application (CCA) PA and the results of that analysis. Much of the content of this appendix derives from Helton et al. (1998); these authors' contributions are gratefully acknowledged.

PA-1.3 Changes since the CRA-2019 PA

The CRA-2019 submitted by the DOE included results from the CRA-2019 PA (U.S. DOE 2019). The WIPP was recertified in 2022 based on the EPA review of the CRA-2019 (U.S. EPA 2022). The CRA-2019 PA used the same PA methodology as the CCA PA (Helton et al. 1998, Section 2), as changes since EPA's first certification in 1998 do not affect the methodology. The CRA-2026 PA retains this methodology, which is summarized in Section PA-2.2.

Compared to the CRA-2019 PA, the CRA-2026 PA incorporates changes to the repository design and new information available since the CRA-2019 PA. Changes included in the CRA-2026 PA relative to the CRA-2019 PA are summarized in Table PA-1. Because the RPPCR PA falls between the CRA-2019 PA and the CRA-2026 PA, Table PA-1 also indicates where the CRA-2026 PA differs from the RPPCR PA. The remainder of this section provides additional details on each change.

Table PA-1. Changes Since the CRA-2019 PA Incorporated in the CRA-2026 PA

WIPP PA Element	Summary of Change and Cross-Reference
Repository Design	Incorporation of 2 replacement panels and associated operations and access drifts to the northwest of the 10 original panels (see Section PA-1.3.1). CRA-2026 PA differs from the RPPCR PA
Grid for Flow and Transport in the Salado	Modifications of computational grids to accommodate 12-panel interim state repository design, as-built repository excavation dimensions, plans for future excavations, and planned change for alternative panel closure locations for Panels 1 and 2 (see Section PA-1.3.2). CRA-2026 PA differs from the RPPCR PA

WIPP PA Element	Summary of Change and Cross-Reference
Repository Area and Volume Parameters	Revision to parameters describing modified repository dimensions (see Section PA-1.3.3). CRA-2026 PA differs from the RPPCR PA
Waste Area Pressure at the Time of Closure	Implementation of methodology to calculate the initial repository pressure at the time of closure to account for the high initial rate of microbial degradation gas generation (see Section PA-1.3.4). CRA-2026 uses the same method as the RPPCR PA
Porosity of Waste Areas with Creep Closure	Implementation of a revised porosity surface based on a refined geomechanics model to model creep closure (see Section PA-1.3.5). CRA-2026 uses the same method as the RPPCR PA
Capillary Pressure Model for Anhydrite Marker Beds	Implementation of a capillary pressure model modification to facilitate limiting the lower bound on capillary pressure for the modified van Genucthen-Parker model in the anhydrite layers (see Section PA-1.3.6). Introduced in the CRA-2026 PA
Porosity-Permeability Distribution for Panel Closures	Modification of sampled run-of-mine salt panel closure system (ROMPCS) parameter (PCS_T2:POR2PERM) from truncated normal to cumulative distribution (see Section PA-1.3.7). Introduced in the CRA-2026 PA
Castile Brine Reservoir	Update to the pore volume of the possible Castile brine reservoir based on reevaluation of data for implementation in the Salado flow grid (see Section PA-1.3.8). CRA-2026 uses the same method as the RPPCR PA
Iron Surface Area	Modification of the calculation of iron surface area in the waste based on the mass of iron in the waste rather than the surface area of waste disposal drums (see Section PA-1.3.9). CRA-2026 uses the same method as the RPPCR PA
MgO Hydration	Incorporation of new parameter distributions for the rate of Magnesium Oxide (MgO) to form brucite for Castile and Salado brine inundated conditions (see Section PA-1.3.10). Introduced in the CRA-2026 PA

WIPP PA Element	Summary of Change and Cross-Reference
Borehole Long-Term Permeability	Revision of the borehole permeability after plug failure distribution (see Section PA-1.3.11). CRA-2026 uses the same method as the RPPCR PA
Waste Inventory	Revision of the inventory data associated with the interim state repository (see Section PA-1.3.12). CRA-2026 PA differs from the RPPCR PA
Baseline Actinide Solubilities and Uncertainties	Revision of baseline actinide solubility and uncertainty parameters based on inventory, minimum DBR brine volume, and thermodynamic database changes (see Section PA-1.3.13). CRA-2026 PA differs from the RPPCR PA
Oxidation State Model	Incorporation of new parameters to control the oxidation state distribution for Np, Pu, and U (see Section PA-1.3.14). CRA-2026 PA differs from the RPPCR PA
Colloid Enhancement Parameters	Revision to proportionality constant parameters for humic colloids and movement to an element-oxidation state basis for microbial colloid enhancement parameters (see Section PA-1.3.15). CRA-2026 PA differs from the RPPCR PA
Minimum Brine Volume Associated with DBR	Revision to the parameter for the minimum brine volume associated with a direct brine release (see Section PA-1.3.16). CRA-2026 PA differs from the RPPCR PA
Grid for DBR	Modification of the direct brine release computational grid to account for the replacement waste panels (see Section PA-1.3.17). CRA-2026 PA differs from the RPPCR PA
Mass Release Locations in the Culebra	Transition from a single release point above the centroid of a 10-panel repository to include an additional release point at the centroid of the two replacement panels in a 12-panel repository (see Section PA-1.3.18). CRA-2026 PA differs from the RPPCR PA
Culebra Transmissivity	Incorporation of revised T-fields into the Culebra flow model (see Section PA-1.3.19). CRA-2026 PA differs from the RPPCR PA

WIPP PA Element	Summary of Change and Cross-Reference
Panel Adjacency and Neighboring Assignments	Update to panel adjacency and neighboring assignments to accommodate a 12-panel repository (see Section PA-1.3.20). CRA-2026 PA differs from the RPPCR PA
Drilling Frequency and Plugging Pattern Probabilities	Revision to drilling frequency and plugging pattern probabilities based on updated Delaware basin reported drilling activity and revised area of reporting for plugging pattern data (see Section PA-1.3.21). CRA-2026 PA differs from the RPPCR PA
Probability of a Castile Intrusion	Minor update to add a data point at probability 0 to the parameter distribution defining the probability of encountering pressurized brine in the Castile to remedy a PRELHS code error (see Section PA-1.3.22). CRA-2026 PA differs from the RPPCR PA
Sample of Uncertain Parameters	Acknowledgment of observed minor differences in sampled values for certain sampled parameters due to an error correction in the PRELHS code (see Section PA-1.3.23). CRA-2026 PA differs from the RPPCR PA
Computational Platform and Code Updates	Modified computational platform and modified codes for the CRA-2026 PA (see Section PA-1.3.24). CRA-2026 uses the same method as the RPPCR PA

Each of the changes summarized in Table PA-1 is documented in one or more CRA-2026 PA analysis reports. A summary of the overall CRA-2026 PA results is provided in Brunell et al. (2025), and the individual reports listed below provide detailed descriptions of the data, methods, and analysis supporting the updated PA:

- Interim State Performance Assessment Inventory Report – 2024 (ISPAIR-2024) (Van Soest 2025)
- Los Alamos National Laboratory Actinide Chemistry and Repository Science Program (LANL-ACRSP) Parameter Recommendations for CRA-2026 Performance Assessment (Kaplan et al. 2025)
- Inventory Screening Analysis (Kicker 2025)
- Inventory EPA Unit Calculation (Kim and Kicker 2025)
- Parameter Sampling (King and Zeitler 2025)
- Salado Flow (Day and King 2025)

- DBR Volumes (Zeitler 2025)
- Cuttings, Cavings, and Spallings (Brunell and Kicker 2025)
- Actinide Mobilization and Salado Transport (Docherty and Kim 2025)
- Culebra Flow and Transport (Wilgus and Bethune 2025)
- CCDF Normalized Releases (King et al. 2025)
- Run Control (Long 2025)

PA-1.3.1 Repository Design

The CRA-2026 PA represents the 12-panel IS repository, consisting of the 10 original panels and 2 replacement panels. Figure PA-1 depicts the layout of the IS repository. In contrast, the CRA-2019 PA (U.S. DOE 2019) represented only the 10 original panels, while the RPPCR PA (Brunell et al. 2024) represented the anticipated final state repository, including a total of 19 waste panels and the full allowable inventory volume.

The inclusion of the replacement panels required modifications to the implementation of three conceptual models (Hansen 2021):

- Disposal System Geometry
- Repository Fluid Flow
- Direct Brine Release.

The Additional Panels Performance Assessment (APPA) Changed Conceptual Models Peer Review examined changes to the implementation of these three conceptual models and concluded that, with these changes, the models provided an adequate and reasonable representation of the repository system (Falta et al. 2021).

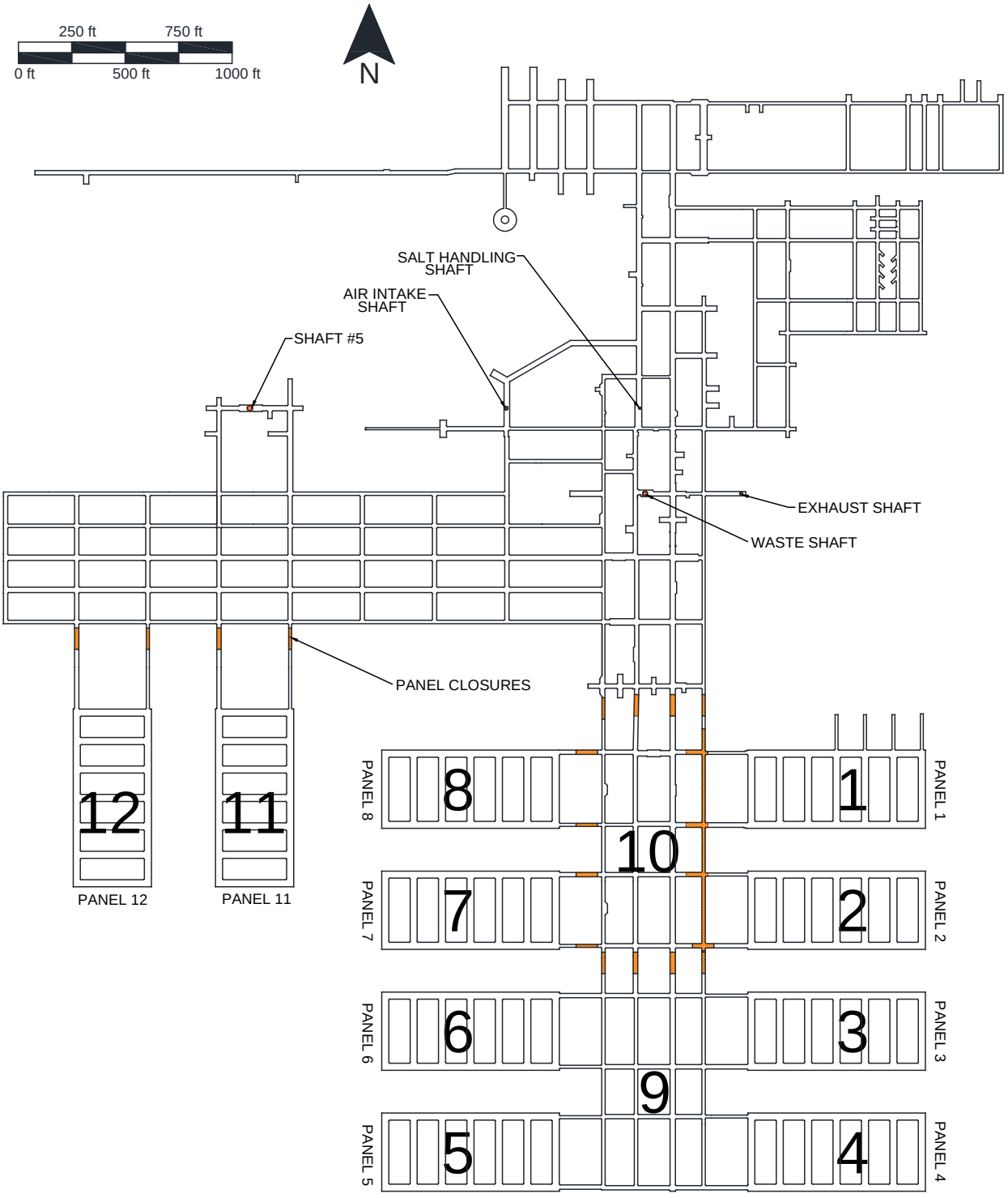


Figure PA-1. Interim State Repository Layout

PA-1.3.2 Grid for Flow and Transport in the Salado

The addition of two replacement waste panels to the west of the originally planned 10-panel repository requires modification of the computational grids for flow and transport in the Salado. Figure PA-12 shows the computational grid for flow and transport in the Salado, where the two replacement panels are represented by the "West Rest-of-Repository (RoR)" region.

Compared with the computational grid used in the CRA-2019, the grid in Figure PA-12 differs primarily by:

- Addition of the West RoR region that represents the replacement waste panels.
- Addition of the West Operations and West Drifts regions that represent non-waste-filled repository areas to the west of the current operations area.
- Addition of panel closure materials between the West Drifts and West RoR.

Details of the computational grid, such as flaring to represent volumes and assignment of material properties to regions, are presented in Day and King (2025), Section 3.0. The representation of the Castile reservoir differs from the CRA-2019, as discussed in Section PA-1.3.8.

The APPA Changed Conceptual Models Peer Review examined the changes to the repository representation in the computational grid and concluded that the grid provides an adequate and reasonable representation of the repository system (Falta et al. 2021).

PA-1.3.3 Repository Area and Volume Parameters

Parameters describing repository dimensions are changed to account for the addition of the replacement panels. Table PA-2 compares these parameter values for the CRA-2026 PA and CRA-2019 PA; supporting information is found in Brunell (2025) and King (2025a).

Table PA-2. Changed Repository Parameters

Material	Property	Description	CRA-2019 Value	CRA-2026 Value	Units
REFCON	VREPOS	Excavated storage volume of repository	438,406.08	560,722.29	m^3
REFCON	ABERM	Area of Berm Placed Over Waste Panel	628,500	750,000	m^2
REFCON	AREA_CH	Area For CH Waste Disposal	111,500	141,511	m^2
REFCON	FVW	Fraction of Repository Volume Occupied By CH-Waste	0.385	0.279	-
REFCON	AREA_RH	Area For RH Waste Disposal	15,760	3,528	m^2

PA-1.3.4 Waste Area Pressure at the Time of Closure

Microbial biodegradation of cellulose, plastic, and rubber (CPR) produces gas. Degradation occurs at a high initial rate followed by a lower long-term rate (Nemer et al. 2005). The long-term rate is modeled in the PA (see Section PA-4.2.6 for a summary). Gas produced at the initial high rate is accounted for by setting the initial pressure at repository closure above atmospheric pressure. A methodology for calculating initial pressure is outlined in Nemer et al. (2005). The increase in pressure above atmospheric is part of the ALGEBRACDB1 step of the Salado flow calculation (Figure 15 of Day and King (2025)). The CRA-2026 calculation of the initial gas pressure includes a new parameter named WAS_AREA:EGRATMIC that represents the moles of gas generated per kilogram of CPR from early-time biodegradation (King 2021a). For the CRA-2026, the initial waste area pressure is 1.24×10^5 Pa, compared to 1.28×10^5 Pa in the CRA-2019.

PA-1.3.5 Porosity of Waste Areas with Creep Closure

The creep closure of the salt around the waste is simulated in detail with a geomechanical model (Appendix PORSURF-2026). This detailed model produces a response surface for waste area porosity as a function of time and pressure. This response surface is used in the Salado flow calculation to model the effects of creep closure in the waste area on fluid flow in and around the repository (Section PA-4.2.4). For the CRA-2026, the response surface is based on the new disposal room porosity model by Vignes et al. (2023). The response surface is compared with the surface used in the CRA-2019 in Brunell et al. (2024), Section 2.7.

PA-1.3.6 Capillary Pressure Model for Anhydrite Marker Beds

To improve the numerical stability of the Salado flow model the modified van Genuchten-Parker capillary pressure function incorporates a lower bound on capillary pressure of 101,325 Pa (Equation PA.36) when applied to the anhydrite marker beds (Day and King 2025, Section 2.9).

PA-1.3.7 Porosity-Permeability Distribution for Panel Closures

The probability distribution for the parameter representing the relationship between porosity and permeability in a run-of-mine salt panel closure system (PCS_T2:POR2PERM in Feng and Kicker (2025a), Table 3) was changed from a truncated normal to a cumulative distribution. The change has minimal effect on the sample values of the parameter (King 2025b).

PA-1.3.8 Castile Brine Reservoir

The pore volume of the possible brine reservoir in the Castile in the CRA-2019 was assigned a range of 4×10^6 m^3 to 2×10^7 m^3 (Docherty 2023a; U.S. EPA 1998b, Section 4.5). For the CRA-2026, the pore volume was assigned a range of 1.18×10^6 m^3 to 5.9×10^6 m^3 based on a re-evaluation of data from the WIPP-12 well (Gross and Gjerapic 2022). Additionally, for the CRA-2026, the reservoir is represented in the grid for flow in the Salado ("Castile Brine Reservoir"

region in Figure PA-12) with an extended range of cells to better represent reservoir porosity (Docherty 2023a).

PA-1.3.9 Iron Surface Area

In the CRA-2019, the iron surface area in the waste was based on the surface area of waste from a representative disposal drum and optimal loading of the repository. For the CRA-2026, this calculation is based on the mass of iron in the waste (King 2021b).

PA-1.3.10 MgO Hydration

Nemer (2025) and King (2025b) specify new parameter distributions for the rate of hydration of MgO to form brucite, $Mg(OH)_2$, for the Castile and Salado brine-inundated conditions.

PA-1.3.11 Borehole Long-Term Permeability

In the CRA-2019, the base 10 logarithm of the permeability of a borehole after plug failure and degradation of borehole materials (material BH_SAND, properties PRMX_LOG, PRMY_LOG, PRMZ_LOG) was specified as a uniform distribution between −16.3 and −11 log(m^2). For the CRA-2026 PA, the range of the uniform distribution is reduced to between −16.3 and −14 log(m^2) (i.e. approximately 5×10^{-17} to 10^{-14} m^2) (Gjerapic et al. 2023).

PA-1.3.12 Waste Inventory

The Interim State Performance Assessment Inventory Report – 2024 (ISPAIR-2024) (Van Soest 2025) contains updated estimates of radionuclide content and waste material parameters, based on inventory information collected through December 31, 2023. The LWA establishes a statutory limit on the volume of waste that can be disposed of in the WIPP repository, set at 175,564 m^3 (6,200,000 ft^3). Current assessments indicate that the IS repository will accommodate less waste than the LWA volume. Ward (2025) provided an assessment of the projected waste storage capacity of 157,831.92 m^3, including 156,247.12 m^3 of contact-handled (CH) waste and 1,584.80 m^3 of remote-handled (RH) waste. The ISPAIR offers an inventory estimate scaled to the waste volume specified by Ward (2025).

Kicker (2025) conducted a screening analysis of the inventory estimates for the ISPAIR-2024 to define the inventory-related input parameters for the CRA-2026 PA calculation. Inventory parameters for the CRA-2026 PA are listed in Appendix D of Kicker (2025).

The ISPAIR-2024 also includes information on the volume and radionuclide content for each waste stream. This information was used to determine the probability of encountering a waste stream and to generate the time-dependent normalized release of cuttings and cavings for each waste stream. Waste stream information is stored in the input files for the WIPP PA code EPAUNI. These input files are updated in the CRA-2026 PA to reflect the most current waste stream information.

PA-1.3.13 Baseline Actinide Solubilities and Uncertainties

The solubility of actinides is influenced by their concentrations and the chemical components of the waste, including complexing ligands, iron, lead, and CPR. The ISPAIR-2024 (Van Soest 2025) updates information on the amount of various chemical components in the waste.

Thermodynamic calculations are used to compute the baseline solubilities for actinides in the +III, +IV, and +V oxidation states in Generic Weep Brine (GWB) and U.S. Energy Research and Development Administration Well 6 (ERDA-6) brines for five multiples of the minimum brine volume for a DBR event (Appendix GEOCHEM-2026, Section 1.1.1).[2] These baseline solubility calculations account for inventory components and thus are updated to be consistent with inventory estimates. Details of the development of radionuclide solubilities and their associated uncertainty are contained in AP-153 (Brush et al. 2012). Domski (2025a) reports baseline solubilities based on the CRA-2026 inventory.

Additionally, uncertainty ranges and probability distributions for actinide solubilities are recalculated using an updated thermodynamic database and updated literature screening criteria (Domski 2023; Domski 2025b). The updated solubility parameters for the CRA-2026 PA are listed in Domski (2025b, 2025c).

The LANL-ACRSP recommended a solubility of 3×10^{-6} mol/L for actinides in the +VI oxidation state in both Salado and Castile brines (Kaplan et al 2025).

PA-1.3.14 Oxidation State Model

The CRA-2026 PA uses the oxidation state model introduced in the RPPCR PA (Brunell et al. 2024). The model captures the behavior of the different multi-valence actinides across a range of oxidation-reduction (redox) potentials. New parameters (property OXCUTOFF for materials NP, PU, and U) were implemented in the RPPCR based on the recommended values from Lucchini and Swanson (2023).

As in the RPPCR PA, the PU:OXCUTOFF parameter is set to 0.25, meaning 25% of realizations assume the +III state-controlled Pu solubility and 75% of realizations assume the +IV state-controlled Pu solubility.

[2] Given the concentrations of organic ligands (e.g., ethylenediaminetetraacetic acid (EDTA)) that may influence radionuclide solubility are inventory limited, concentrations of radionuclides may vary as a function of brine volume. As such, radionuclide solubility is modeled as a function of brine volume.

PA-1.3.15 Colloid Enhancement Parameters

Based on updates to the thermodynamic model and baseline solubilities, Mariner (2025) reevaluated the proportionality constant for humic colloids. Values are updated for radionuclides in the +III oxidation state for both Castile and Salado brines (PHUMOX3:PHUMCIM and PHUMOX3:PHUMSIM). Values for radionuclides in the +IV oxidation state are updated for only the Salado brines (PHUMOX4:PHUMSIM).

In previous PAs, microbial colloid enhancement parameters (PROPMIC and CAPMIC) have been specified for each element (parameter materials AM, NP, PU, TH, and U). For the CRA-2026 PA, the microbial enhancement parameters are specified for each element-oxidation state (i.e., AM+3, NP+4, NP+5, PU+3, PU+4, U+4, and U+6), to more closely align with the experimental data used to derive the parameter values (Kaplan et al. 2025). Intrinsic colloid enhancement parameters (CONCINT) for elements Am and Th were also updated (Lucchini and Swanson 2023).

PA-1.3.16 Minimum Brine Volume Associated with DBR

The parameter representing the minimum brine volume associated with a DBR, material GLOBAL, property DBRMINBV, is revised (Brunell 2025) to a value of 6,314 m^3 for consistency with geomechanical modeling that predicts repository porosity (Section PA-1.3.5) and with the repository geometry described in Section PA-1.3.1.

PA-1.3.17 Grid for DBR

The computational grid for DBRs (Figure PA-33) is modified to account for the replacement waste panels. Compared to the grid used for the CRA-2019, the CRA-2026 grid adds a fourth intrusion location (“other”) that represents DBRs from intrusions into the replacement waste panels. In addition, it relocates the “upper” intrusion location which represents intrusions into Panels 1, 2, 7, 8 and 10. The CRA-2026 grid is conceptually the same as the grid approved by the APPA Changed Conceptual Models Peer Review (Falta et al. 2021); however, some grid dimensions have been modified.

PA-1.3.18 Mass Release Locations in the Culebra

The CRA-2019 PA modeled all radionuclides transported through a borehole to the Culebra as entering the Culebra at a common point above the centroid of the 10-panel repository. The CRA-2026 PA models radionuclide entry at two locations: the CRA-2019 location for intrusions into the original 10 waste panels, and a location over the centroid of the two replacement waste panels (Wilgus and Brunell 2025).

PA-1.3.19 Culebra Transmissivity

The Culebra Hydrogeology model incorporates spatially variable, calibrated fields of transmissivity, storativity, anisotropy, and recharge (collectively referred to as T-fields). For the

CRA-2026, new T-fields are calibrated with updated steady-state and transient targets and model boundary conditions as described in Appendix TFIELD-2026.

PA-1.3.20 Panel Adjacency and Neighboring Assignments

Panel adjacency (Section PA-6.4.2.3) is extended in the CRA-2026 by adding the "other" category to account for replacement panels. For CRA-2026, panel neighbor groups are extended to "same", "connected", "adjacent", and "non-adjacent" for the 12 repository panels in a manner consistent with the RPPCR PA (Brunell et al. 2024, Section 3.9.1).

PA-1.3.21 Drilling Frequency and Plugging Pattern Probabilities

Regulations governing WIPP (40 CFR 194.33) require that current drilling practices be assumed for future inadvertent intrusions. The DOE continues to survey drilling activity in the Delaware Basin in accordance with the criteria established in 40 CFR 194.33. Local well operators are surveyed annually to provide the WIPP project with information on drilling practices, Castile brine encounters, and related topics. Survey results through August 2024 are documented in the 2024 Delaware Basin Monitoring Annual Report (DBMAR) (U.S. DOE 2025).

Drilling parameters for the CRA-2026 PA are updated based on the 2024 DBMAR (U.S. DOE 2025). The DBMAR indicates a drilling frequency of 0.01534 boreholes per km² per year based on a 100-year reference period, which is used as the value for WIPP PA parameter GLOBAL:LAMBDAD for the CRA-2026 PA. This represents a notable increase compared to the value of 9.90×10^{-3} specified for this parameter in the CRA-2019 PA and reflects updated drilling activity data collected in the Delaware Basin.

Borehole plugging pattern parameters are also updated based on data contained in the 2024 DBMAR. The DBMAR reports six types of plugging patterns (summarized in Table 9 of the DBMAR), which have historically been translated into three unique plugging patterns for PA purposes. This same translation scheme (i.e., type VI is the same as a full plug, types II and IV are the same as a three-plug, and types I, III, and V are the same as a two-plug configuration) is used for the parameterization of the GLOBAL:ONEPLG, GLOBAL:TWOPLG, and GLOBAL:THREEPLG parameters for the CRA-2026 PA (see WIPP Performance Assessment (2022a) for a description of the use of the plugging pattern parameters in WIPP PA).

Although the plugging pattern translation scheme remains the same as for the CRA-2019 PA, the physical area over which plugging pattern data were collected was changed for CRA-2026. Prior to the CRA-2019 PA, plugging data were gathered from plugged and abandoned wells in the New Mexico portion of the Delaware Basin. For the CRA-2019 PA, plugging data were gathered from a reduced area known as the Known Potash Leasing Area (U.S. DOE 2018). The RPPCR and the CRA-2026 used plugging data gathered from the nine townships surrounding WIPP, truncated to the north by the boundary of the Delaware Basin (U.S. DOE 2025). As a result, the plugging pattern dataset differs somewhat from previous versions. Table PA-3 compares drilling frequency and plugging pattern probabilities for the CRA-2019 and CRA-2026.

Table PA-3. Drilling Frequency and Plugging Pattern Parameters

Material	Property	Description	Units	CRA-2019 Value	CRA-2026 Value
GLOBAL	LAMBDAD	Drilling rate per unit area	$km^{-2}\ yr^{-1}$	9.90×10^{-3}	1.534×10^{-2}
GLOBAL	ONEPLG	Probability of having Plug Pattern 1 (full plug)	(-)	4.03×10^{-1}	3.59×10^{-1}
GLOBAL	TWOPLG	Probability of having Plug Pattern 2 (two plugs)	(-)	3.31×10^{-1}	4.64×10^{-1}
GLOBAL	THREEPLG	Probability of having Plug Pattern 3 (three plugs)	(-)	2.66×10^{-1}	1.77×10^{-1}

PA-1.3.22 Probability of a Castile Intrusion

Time Domain Electromagnetic (TDEM) sounding data (The Earth Technology Corporation 1987) were used to derive the probability of encountering pressurized brine in the Castile Formation (hereafter referred to as the Castile) under the WIPP repository (WIPP PA parameter GLOBAL:PBRINE). Zeitler (2023) overlaid the electrical conductivity contours, and found that the data adequately covers most of panels 11 and 12. Zeitler then calculated the probability of a brine encounter for those panels and found it to be lower than the EPA-prescribed value; the higher value was therefore retained as conservative. Thus, no change is made to the GLOBAL:PBRINE distribution for the CRA-2026 PA for the IS repository. The cumulative distribution for the parameter has been modified to add a point at probability 0 to ensure LHS algorithm correctly captures the full range of the distribution (Docherty 2023b).

PA-1.3.23 Sample of Uncertain Parameters

Although the random number seeds used in the CRA-2026 PA are the same as in the CRA-2019 PA, correction of an error in the PRELHS code causes negligible differences in the samples for a few parameters (Docherty 2023b).

PA-1.3.24 Computational Platform and Code Updates

Calculations for the CRA-2019 PA were performed on the WIPP PA Solaris Cluster, which consists of Intel hardware running the Solaris operating system (Long 2019). The CRA-2026 PA was executed on the WIPP PA HPC/Linux Cluster, which consists of Dell PowerEdge C6420 hardware running CentOS 7 (Long and King 2022). Software used for the CRA-2026 PA is described in Long (2025).

PA-2.0 Overview of the PA

The containment requirements in Part 191 require a PA to demonstrate a reasonable expectation that cumulative releases of radionuclides to the accessible environment over 10,000 years after disposal are less than specified limits (40 CFR 191.13). The PA is to determine the effects of all significant processes and events that may affect the disposal system, consider the associated uncertainties of these processes and events, and estimate the probable cumulative radionuclide releases.

The foundations of PA are a thorough understanding of the disposal system and the possible future interactions of the repository, waste, and surrounding geology. Confidence in the results of PA is based in part on the strength of the original research conducted during site characterization, experimental results used to develop and confirm parameters and models, and the robustness of the facility design.

As required by regulation, results of the PA are displayed as CCDFs showing the probability of exceeding various levels of cumulative radionuclide release from the disposal system. The CCDFs are calculated using peer-reviewed models based on the scientifically accepted understanding of the disposal system's behavior. The parameters used in these models are derived from experimental data, field observations, expert opinion, regulatory mandates, and relevant technical literature. Parameters used in the CRA-2026 PA are cataloged in Feng and Kicker (2025a).

The WIPP PA is described below, organized as follows:

Section PA-2.1 – Regulatory requirements.

Section PA-2.2 – Summary of the PA methodology.

Section PA-2.3 – Conceptual description of the undisturbed repository system.

Section PA-2.4 – Conceptual description of the disturbed repository system.

Section PA-2.5 – Conceptual structure of the PA used to evaluate compliance with the containment requirements.

Section PA-2.6 – Compliance demonstration method.

PA-2.1 Regulatory Requirements

The methodology employed in PA derives from the EPA's standard for the geologic disposal of radioactive waste, Environmental Radiation Protection Standards for the Management and Disposal of Spent Nuclear Fuel, High-Level and Transuranic Radioactive Wastes (Part 191) (U.S. EPA 1993), which is divided into three subparts. Subpart A applies to a disposal facility prior to decommissioning and establishes standards for annual radiation doses to the public from waste

management and storage operations. Subpart B applies after decommissioning and sets probabilistic limits on cumulative releases of radionuclides to the accessible environment for 10,000 years (40 CFR 191.13) and assurance requirements to provide confidence that 40 CFR 191.13 will be met (40 CFR 191.14). Subpart B also sets limits on radiation doses to members of the public in the accessible environment for 10,000 years of undisturbed repository performance (40 CFR 191.15). Subpart C limits radioactive contamination of groundwater for 10,000 years after disposal (40 CFR 191.24). The DOE must demonstrate a reasonable expectation that the WIPP will continue to comply with the requirements of Part 191 Subparts B and C as a necessary condition for WIPP recertification.

The following is the central requirement in Part 191 Subpart B, and the primary determinant of the PA methodology:

> § 191.13 Containment Requirements:
>
> (a) Disposal systems for spent nuclear fuel or high-level or transuranic radioactive wastes shall be designed to provide a reasonable expectation, based upon performance assessments, that cumulative releases of radionuclides to the accessible environment for 10,000 years after disposal from all significant processes and events that may affect the disposal system shall:
>
> (1) Have a likelihood of less than one chance in 10 of exceeding the quantities calculated according to Table 1 (Appendix A); and
>
> (2) Have a likelihood of less than one chance in 1,000 of exceeding ten times the quantities calculated according to Table 1 (Appendix A).
>
> (b) Performance assessments need not provide complete assurance that the requirements of 191.13(a) will be met. Because of the long time period involved and the nature of the events and processes of interest, there will inevitably be substantial uncertainties in projecting disposal system performance. Proof of the future performance of a disposal system is not to be had in the ordinary sense of the word in situations that deal with much shorter time frames. Instead, what is required is a reasonable expectation, on the basis of the record before the implementing agency, that compliance with 191.13(a) will be achieved.

Title 40 CFR 191.13 (a) refers to "quantities calculated according to Table 1 (Appendix A)," which means a normalized radionuclide release to the accessible environment based on the type of waste being disposed of, the initial waste inventory, and the size of release that may occur (40 CFR 191, Appendix A). Table 1 of Appendix A specifies allowable releases (i.e., release limits) for individual radionuclides and is reproduced as Table PA-4. The WIPP is a repository for transuranic (TRU) waste, which is defined as "waste containing more than 100 nanocuries of alpha-emitting TRU isotopes, with half-lives greater than twenty years, per gram of waste" (40 CFR 191.02). The normalized release R for TRU waste is defined by:

$$R = \sum_i \left(\frac{Q_i}{L_i} \right) \left(\frac{1 \times 10^6 \text{ Ci}}{C} \right) \quad \text{(PA.1)}$$

where Q_i is the cumulative release of radionuclide *i* (curies (Ci)) to the accessible environment during the 10,000 years following closure, L_i is the release limit for radionuclide *I* (CI per unit of

waste) given in Table PA-4, and *C* is the activity of TRU waste (Ci) emplaced in the repository. In the CRA-2026 PA, $C = 7.37 \times 10^6$ Ci (Kicker 2025, Table 4). As defined by 40 CFR 191.12, "accessible environment" means (1) the atmosphere, (2) land surfaces, (3) surface waters, (4) oceans, and (5) all of the lithosphere beyond the controlled area. Also, "Controlled area" means (1) a surface location, to be identified by passive institutional controls (PICs), that encompasses no more than 100 square kilometers (km^2) and extends horizontally no more than 5 kilometers (km) in any direction from the outer boundary of the original radioactive waste's location in a disposal system, and (2) the subsurface underlying such a location (40 CFR 191.12). For WIPP, DOE demonstrates compliance with the containment requirements by evaluating releases of regulated radionuclides to the surface or across the LWB established under the WIPP Land Withdrawal Act (U.S. Congress 1992). The LWB lies within the controlled area defined by 40 CFR 191.12 and extends downward from the surface through the subsurface.

Table PA-4. Release Limits for Containment Requirements (40 CFR 191, Appendix A, Table 1)

Radionuclide	Release Limit L_i per 1,000 MTHMa or Other Unit of Wasteb
Americium-241 or -243	100
Carbon-14	100
Cesium-135 or -137	1,000
Iodine-129	100
Neptunium-237	100
Pu-238, -239, -240, or -242	100
Radium-226	100
Strontium-90	1,000
Technetium-99	10,000
Thorium (Th) -230 or -232	10
Tin-126	1,000
Uranium (U) -233, -234, -235, -236, or -238	100
Any other alpha-emitting radionuclide with a half-life greater than 20 years	100
Any other radionuclide with a half-life greater than 20 years that does not emit alpha particles	1,000

a Metric tons of heavy metal (MTHM) exposed to a burnup between 25,000 megawatt-days (MWd) per metric ton of heavy metal (MWd/MTHM) and 40,000 MWd/MTHM.

b An amount of TRU waste containing one million Ci of alpha-emitting TRU radionuclides with half-lives greater than 20 years.

PAs are the basis for addressing the containment requirements. The EPA defines PA at 40 CFR 191.12:

> Performance assessment means an analysis that:
>
> (1) Identifies the processes and events that might affect the disposal system;
>
> (2) Examines the effects of these processes and events on the performance of the disposal system; and
>
> (3) Estimates the cumulative releases of radionuclides, considering the associated uncertainties, caused by all significant processes and events. These estimates shall be incorporated into an overall probability distribution of cumulative release to the extent practicable.

To help clarify the intent of Part 191, the EPA promulgated 40 CFR Part 194, Criteria for the Certification and Recertification of the Waste Isolation Pilot Plant's Compliance with the Part 191 Disposal Regulations. There, an elaboration on the intent of 40 CFR 191.13 is prescribed.

> § 194.34 Results of performance assessments.
>
> (a) The results of performance assessments shall be assembled into "complementary, cumulative distribution functions" (CCDFs) that represent the probability of exceeding various levels of cumulative release caused by all significant processes and events.
>
> (b) Probability distributions for uncertain disposal system parameter values used in performance assessments shall be developed and documented in any compliance application.
>
> (c) Computational techniques, which draw random samples from across the entire range of the probability distributions developed pursuant to paragraph (b) of this section, shall be used in generating CCDFs and shall be documented in any compliance application.
>
> (d) The number of CCDFs generated shall be large enough such that, at cumulative releases of 1 and 10, the maximum CCDF generated exceeds the 99th percentile of the population of CCDFs with at least a 0.95 probability.
>
> (e) Any compliance application shall display the full range of CCDFs generated.
>
> (f) Any compliance application shall provide information which demonstrates that there is at least a 95% level of statistical confidence that the mean of the population of CCDFs meets the containment requirements of § 191.13 of this chapter.

PA-2.2 PA Methodology

The PA methodology uses information about the disposal system and waste to evaluate performance over the 10,000-year regulatory period. To accomplish this task, the FEPs with potential to affect the future of the WIPP are first identified (Section PA-2.2.1). Next, scenarios that describe potential future conditions in the WIPP are formed from logical groupings of retained FEPs (Section PA-2.2.2). Conceptual models of the disposal system and of processes that could lead to releases are developed from retained FEPs (Sections PA-2.3 and PA-2.4). A probability space is defined to characterize different futures that could occur at the WIPP

(Section PA-2.5.1). Computational models are developed to estimate the radionuclide releases from the repository (Section PA-2.5.2). Finally, uncertainty in model parameters is characterized using probability distributions (Section PA-2.5.3).

PA-2.2.1 Identification and Screening of FEPs

The EPA has provided criteria concerning the scope of PAs in 40 CFR 194.32. Criteria relating to the identification of potential processes and events that may affect disposal system performance are provided in 40 CFR 194.32(e), which states:

> Any compliance application(s) shall include information which:
>
> (1) Identifies all potential processes, events or sequences and combinations of processes and events that may occur during the regulatory time frame and may affect the disposal system;
>
> (2) Identifies the processes, events or sequences and combinations of processes and events included in performance assessments; and
>
> (3) Documents why any processes, events or sequences and combinations of processes and events identified pursuant to paragraph (e)(1) of this section were not included in performance assessment results provided in any compliance application.

Appendix SCR of this application fulfills these criteria by documenting the DOE's identification, screening, and screening results of all potential processes and events consistent with the criteria specified in 40 CFR 194.32(e). The first two steps in scenario development involve identifying and screening FEPs that are potentially relevant to the performance of the disposal system. The FEPs screening arguments used for the CRA-2026 PA are described in Appendix SCR-2026, Sections SCR-4.0, SCR-5.0, and SCR-6.0.

PA-2.2.2 Scenario Development and Selection

Logic diagrams illustrate the formation of scenarios for consequence analysis from combinations of events that remain after FEP screening (Cranwell et al. 1990) (Figure PA-2). Each scenario shown in Figure PA-2 is defined by a combination of occurrence and nonoccurrence for all potentially disruptive events. Disruptive events are defined as those that create new pathways or significantly alter existing pathways for fluid flow and, potentially, radionuclide transport within the disposal system.

As shown in Figure PA-2, scenarios fall into two broad classes: undisturbed repository performance (UP) and disturbed repository performance (DP). The UP scenario is used for compliance assessments (40 CFR 194.54 and 40 CFR 194.55). The DP scenario class comprises combinations of the deep-drilling (E) scenario and the mining (M) scenario. The mining scenario (M) involves future mining within the controlled area. The deep-drilling scenario (E) involves at least one deep-drilling event that intersects the waste-disposal region. The M and the E scenarios may both occur in the same future. In PA, a future in which both events occur is known as the mining and drilling scenario (ME). More detailed descriptions are found in Section

PA-2.2.2.2. Both the UP and DP scenario classes are used for consequence analysis to determine compliance with the containment requirements in 40 CFR 191.13.

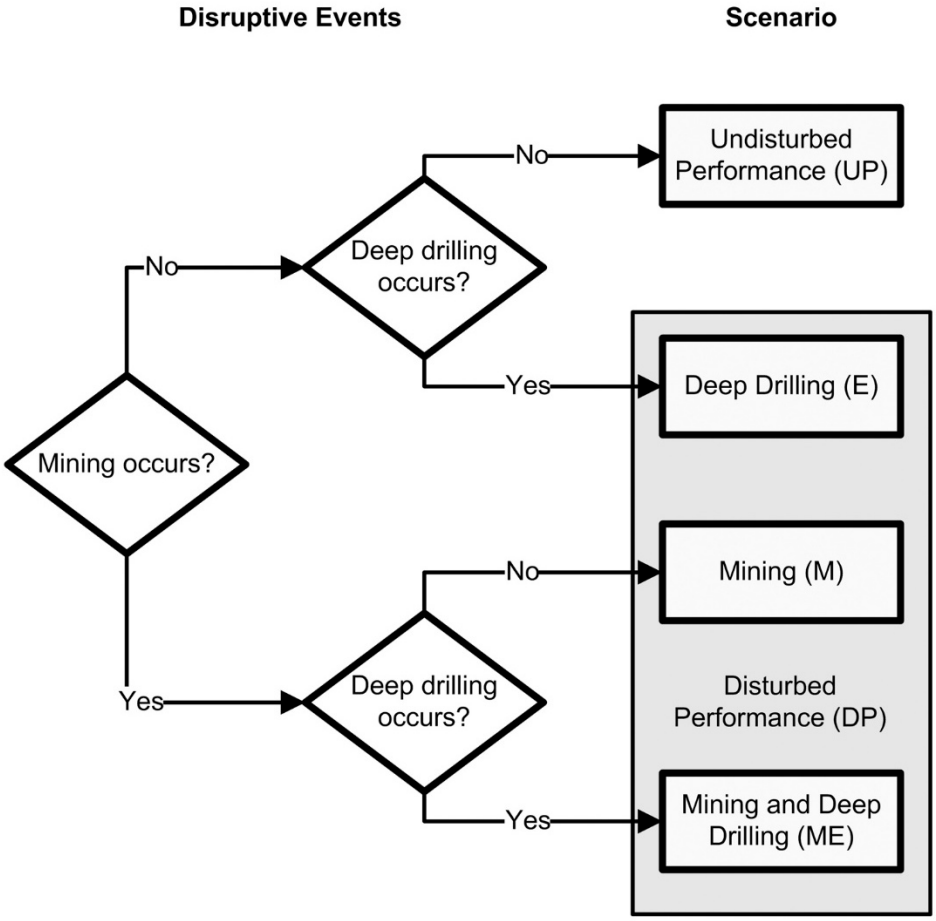


Figure PA-2. Logic Diagram for Scenario Analysis

PA-2.2.2.1 Scenario for Undisturbed Repository Performance

The UP scenario is defined in 40 CFR 191.12 to mean "the predicted behavior of a disposal system, including consideration of the uncertainties in predicted behavior, if the disposal system is not disrupted by human intrusion or the occurrence of unlikely natural events." For compliance assessments of the Individual and Groundwater Protection Requirements, only the UP scenario must be considered (Appendix IGP-2026). The UP scenario is also considered with the DP scenario for compliance with the containment requirements (40 CFR 191.13).

No natural events and processes that are likely to occur during the regulatory time frame are potentially disruptive. All naturally occurring events and processes retained for scenario

construction are nondisruptive and are considered part of the UP scenario. For the UP scenario, mining outside the LWB is assumed at the end of active institutional control (AIC). The potential effects of future deep drilling and/or mining within the controlled area are the only FEPs retained after screening that are excluded from the UP scenario.

The UP scenario is controlled by several important features, events, and processes. The most significant of these include:

- Excavation Induced Fracturing – Excavation and the resulting changes in the surrounding stress field produce a disturbed rock zone (DRZ) with mechanical and hydrological properties that differ from those of the intact host rock.

- Gas generation – Organic material may degrade through microbial activity, radionuclide decay and radiolysis, brine will corrode metals in the waste and containers. These processes generate gases that may produce pressures high enough to influence fractures and fluid flow around the disposal region.

- Salt creep – Salt creep will progressively heal fractures and reduce the permeability of the DRZ, the crushed salt in shaft seals, and the run-of-mine salt in panel closures, bringing permeabilities close to those of intact rock salt.

- Engineered barrier – MgO in disposal rooms will react with carbon dioxide CO_2 and maintain mildly alkaline conditions, while metal corrosion will maintain reducing conditions. Together, these effects keep radionuclide solubilities low.

Radionuclides may become mobile through waste dissolution and colloid generation following brine flow into the disposal rooms. These colloids can be derived from waste materials (humics, mineral fragments, microbes, and intrinsic actinide colloids) or from other repository sources (humics, mineral fragments, and microbes).

Conceptually, there are several pathways for radionuclide transport within the undisturbed disposal system that may result in releases to the accessible environment (Figure PA-3). Contaminated brine may migrate away from the waste disposal panels if pressure within the panels is elevated by gas generated from corrosion, microbial degradation of CPR, or brine radiolysis. Radionuclide transport may occur laterally, through the anhydrite interbeds toward the subsurface boundary of the accessible environment in the Salado, or through access drifts or anhydrite interbeds to the base of the shafts. In the latter case, if the pressure gradient between the panels and overlying strata is sufficient, contaminated brine may migrate up the shafts. As a result, radionuclides may be transported directly to the ground surface or laterally away from the shafts through permeable strata such as the Culebra toward the subsurface boundary of the accessible environment. These conceptual pathways are shown in Figure PA-3. The modeling system described in Section PA-4.0 includes potential radionuclide transport along other pathways, such as migration through Salado halite. However, the natural properties of the undisturbed system make radionuclide transport to the accessible environment via these

other pathways insignificant. For evaluating the undisturbed repository performance, the DOE has defined the E0 scenario.

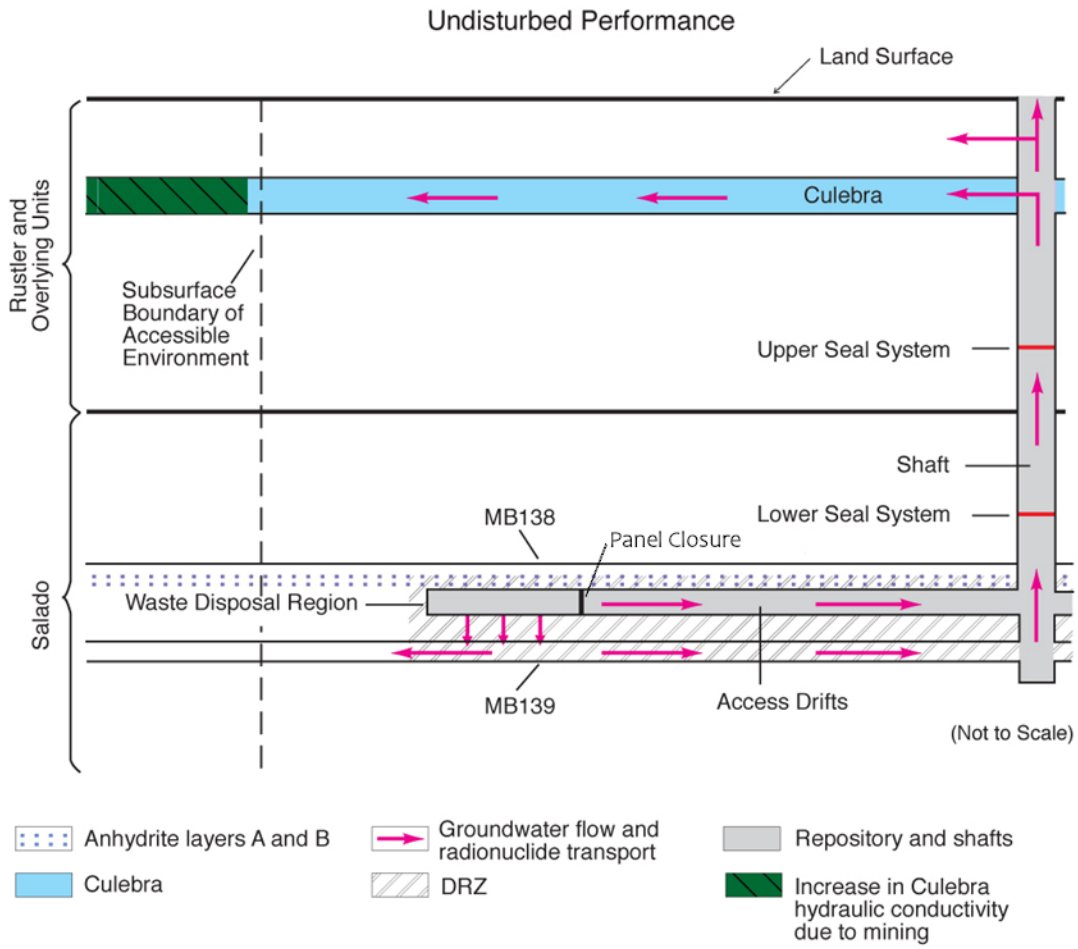


Figure PA-3. Conceptual Release Pathways for the UP Scenario

PA-2.2.2.2 Scenarios for Disturbed Repository Performance

Assessments for compliance with 40 CFR 191.13 need to consider the potential effects of future disruptive natural and human-initiated events and processes on the performance of the disposal system. No potentially disruptive natural events and processes are considered sufficiently likely to require inclusion in analyses of either the UP or DP scenario. The only future human-initiated events and processes retained after FEP screening are those associated with mining and deep drilling (but not the subsequent use of a borehole) within the controlled area or LWB when institutional controls cannot be assumed to eliminate the possibility of such activities (Section PA-3.1 and the CRA-2004, Chapter 6.0, Section 6.4.12.1). In total, 21 disturbed repository FEPs associated with future mining and deep drilling have been identified. These FEPs are assigned a screening designator of the DP scenario.

To evaluate the consequences of disturbance on repository performance, PA considers the E, M, and ME scenarios. These scenarios are described in the following sections.

PA-2.2.2.2.1 Disturbed Repository E Scenario

The disturbed repository E scenario involves at least one deep drilling event that intersects the waste disposal region. The EPA provides criteria for analyzing the consequences of future drilling events in PA in 40 CFR 194.33(c).

> Performance assessments shall document that in analyzing the consequences of drilling events, the Department assumed that:
>
> (1) Future drilling practices and technology will remain consistent with practices in the Delaware Basin at the time a compliance application is prepared. Such future drilling practices shall include, but shall not be limited to: the types and amounts of drilling fluids; borehole depths, diameters, and seals; and the fraction of such boreholes that are sealed by humans; and
>
> (2) Natural processes will degrade or otherwise affect the capability of boreholes to transmit fluids over the regulatory time frame.

Consistent with these criteria, there are several pathways for radionuclides to reach the accessible environment in the E scenario. Before any deep drilling intersects the waste, potential release pathways are identical to those in the undisturbed repository scenario.

If a borehole intersects the waste in the disposal rooms, direct releases to the accessible environment may occur as material entrained in the circulating drilling fluid is brought to the surface. Particulate waste brought to the surface may include cuttings, cavings, and spallings. During drilling, contaminated brine may flow up the borehole and reach the surface, depending on fluid pressure within the waste disposal panels.

When abandoned, the borehole is assumed to be plugged in a manner consistent with current practices in the Delaware Basin as prescribed in 40 CFR 194.33(c)(1). An abandoned intrusion borehole may provide a pathway for fluid flow and contaminant transport from the intersected waste panel to overlying units, such as the Culebra, if the fluid pressure within the panel is sufficiently greater than the hydrostatic pressure. Brine flows through the borehole may carry dissolved and colloidal actinides upward to the Culebra. Groundwater flow within the Culebra can then transport these contaminates laterally to the accessible environment.

The units intersected by an intrusion borehole may also serve as sources of brine flow to a waste panel. For example, in the northern Delaware Basin, the Castile, which underlies the Salado, contains isolated brine reservoirs at fluid pressures greater than hydrostatic (McCormick et al. 2024; U.S. DOE 2004, Chapter 2.0, Section 2.2.1.2.2). The WIPP-12 borehole penetrated one of these pressurized brine reservoirs within the controlled area. The location and properties of brine reservoirs cannot be reliably predicted; thus, the possibility of a deep borehole penetrating both a waste panel and a brine reservoir is accounted for in the PA (Section PA-4.2.11). Such a borehole could provide a conduit for brine flow from the Castile to the waste panel, thereby affecting fluid pressure and brine volume in the waste panel.

A borehole drilled through a disposal room pillar, that does not intersect waste, could also penetrate the brine reservoir underlying the waste disposal region. Such an event would partially depressurize the brine reservoir and thus would affect the consequences of any subsequent reservoir intersections. The PA does not take credit for possible brine reservoir depressurization.

Two types of deep drilling events are distinguished by whether the borehole connects to a Castile brine reservoir. A borehole that intersects a waste panel but does not connect the repository with a Castile brine reservoir is designated an E2 event. A borehole that intersects a waste disposal panel and connects the repository with a Castile brine reservoir is designated an E1 event. The consequences of deep drilling intrusions depend not only on the type of drilling event, but on the type of earlier drilling events. The consequences of each type of event are represented in a corresponding scenario described in the following sections.

PA-2.2.2.2.1.1 The E2 Scenario

In the E2 scenario, a waste disposal panel is penetrated by a drill bit, but the borehole does not connect the repository with brine in the Castile. Cuttings, cavings, spallings, and brine flow releases may occur, and brine flow may occur in the borehole after it is abandoned (see Section PA-2.4). Sources for brine that may contribute to long-term flow up the abandoned borehole are the Salado or, under certain conditions, the units above the Salado. Features and release pathways of the E2 scenario are illustrated in Figure PA-4.

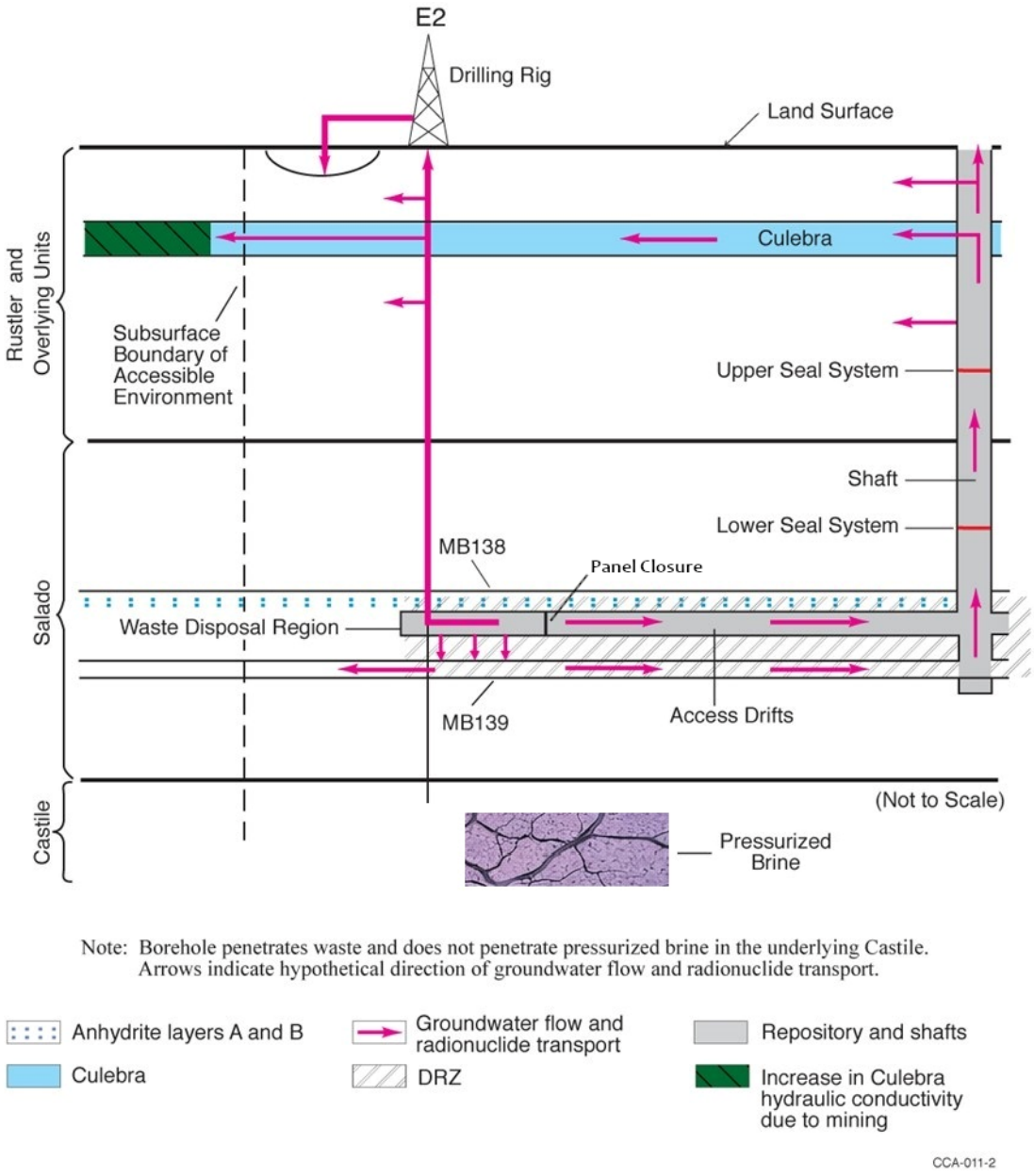


Figure PA-4. Conceptual Release Pathways for the Disturbed Repository Deep Drilling E2 Scenario.

PA-2.2.2.2.1.2 The E1 Scenario

A drilling intrusion that connects the repository with a Castile brine reservoir is called E1. The features and release pathways of this scenario are illustrated in Figure PA-5. As in the E2 scenario, cuttings, cavings, spallings, and brine flow releases may occur, and brine flow may occur in the borehole after it is abandoned (see Section PA-2.4). Sources of brine in the E1 scenario are the Castile brine reservoir, the Salado, and, under certain conditions, the units above the Salado.

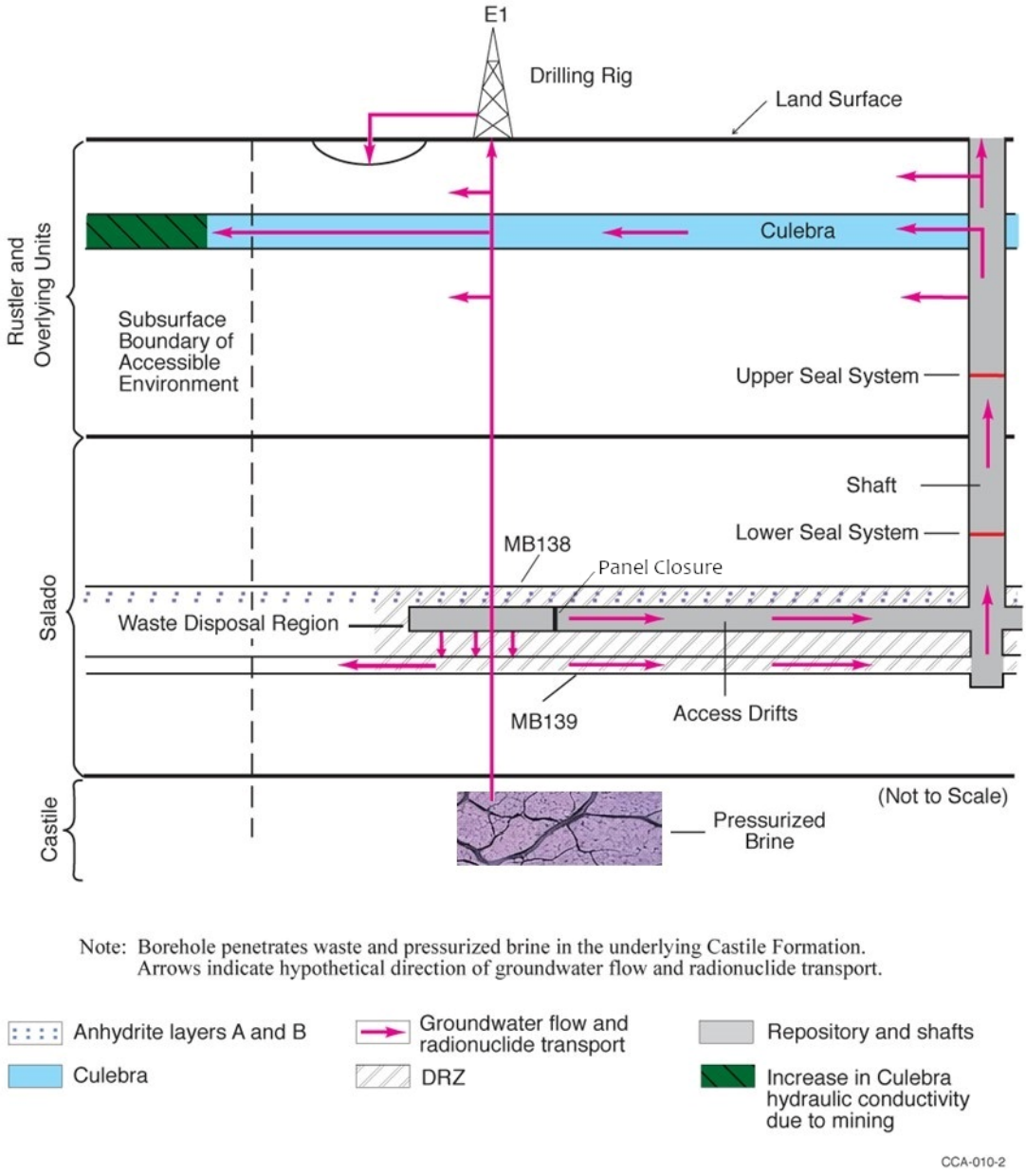


Figure PA-5. Conceptual Release Pathways for the Disturbed Repository Deep Drilling E1 Scenario.

PA-2.2.2.2.1.3 The E1E2 Scenario

The E1E2 scenario is defined by two sequential penetrations of a common waste panel, one of which is an E1 intrusion. One example of this scenario, with a single E1 event and a single E2 event penetrating the same panel, is illustrated in Figure PA-6. The sources of brine in this scenario are the same as those listed for the E1 scenario. The E1E2 scenario includes a potential flow path not present in the E1 or E2 scenarios: flow from an E1 borehole through the waste panel to another borehole. This flow path has the potential to (1) bring quantities of brine in direct contact with waste and (2) provide a less restrictive path for this brine to flow to the

units above the Salado (via multiple boreholes) compared to either the individual E1 or E2 scenarios. It is both the presence of a brine reservoir and the potential for flow through the waste to other boreholes that make this scenario different from combinations of E2 boreholes in terms of potential consequences.

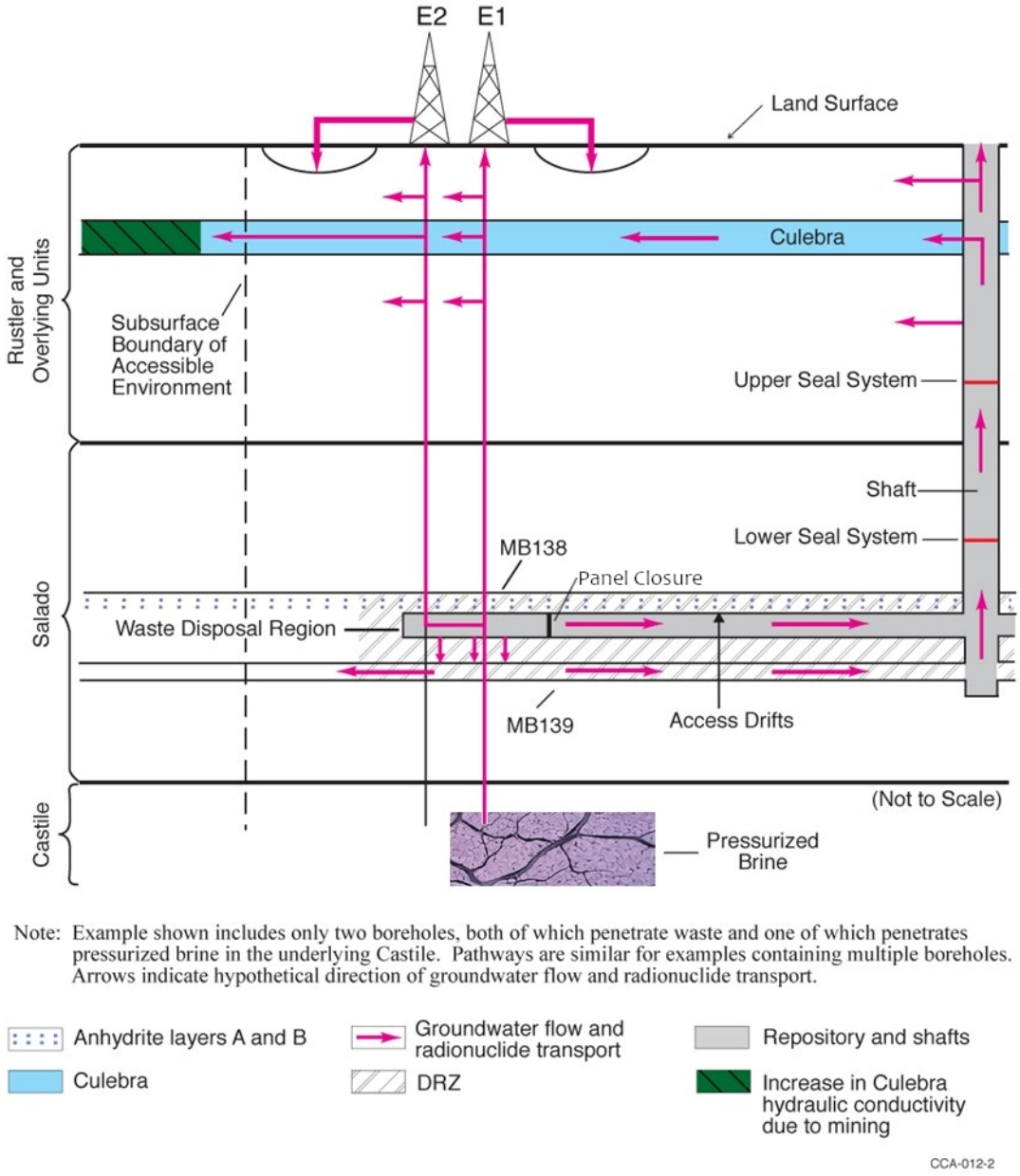


Figure PA-6. Conceptual Release Pathways for the Disturbed Repository Deep Drilling E1E2 Scenario.

PA-2.2.2.2.2 Disturbed Repository M Scenario

The M scenario involves future mining within the controlled area. Consistent with the criteria stated by the EPA in 40 CFR 194.32(b) for PA calculations, the effects of potential future mining

within the controlled area are limited to changes in hydraulic conductivity of the Culebra that result from subsidence (as described in Section PA-3.3). Features of the M scenario are illustrated in Figure PA-7.

The modeling system used for the M scenario is similar to that developed for the UP scenario, but with a modified Culebra T-field in the controlled area to account for the mining effects. Radionuclide transport may be affected in the M scenario if pressure causes brine contaminated with radionuclides to move from the waste disposal panels to the base of the shafts and up to the Culebra. The changes in the Culebra T-field may affect the rate and direction of radionuclide transport within the Culebra.

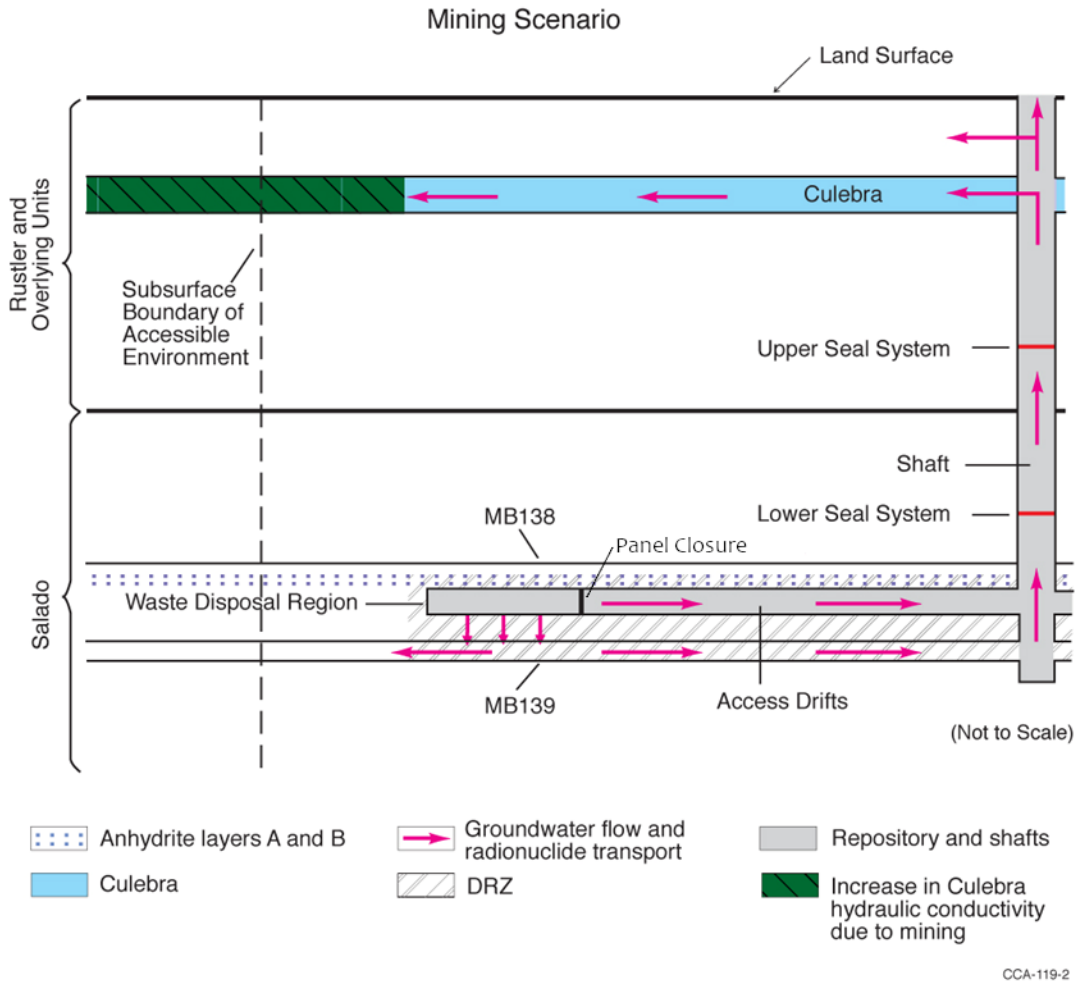


Figure PA-7. Conceptual Release Pathways for the Disturbed Repository M Scenario

PA-2.2.2.2.3 Disturbed Repository ME Scenario

The occurrence of the M scenario (mining without deep drilling) and the E scenario (deep drilling without mining) are considered as independent events. A future in which both mining

and deep drilling occur is referred to as the ME scenario. The occurrence of both mining and deep drilling does not introduce processes beyond those already described separately for the M and E scenarios. For example, mining does not alter the interactions between deep boreholes and the repository or brine reservoirs, nor does deep drilling change the effects of mining on Culebra hydrogeology.

In the ME scenario, the deep drilling events correspond to the same E1, E2, and E2E1 intrusion sequences defined for the E scenario, but they occur in a repository system that has also undergone mining.

PA-2.2.3 Calculation of Scenario Consequences

Calculating scenario consequences requires quantitative modeling. Development of the quantitative models proceeds from FEPs by defining a sequence of models and their associated parameters. These models progress through a structured hierarchy that moves from qualitative statements to computational simulations, as outlined below:

1. **Conceptual models** are sets of qualitative assumptions that describe a system or subsystem for a given purpose. At a minimum, these assumptions concern the geometry and dimensionality of the system, initial and boundary conditions, time dependence, and the nature of the relevant physical and chemical processes. The assumptions should be consistent with one another and with existing information within the context of the given purpose (U.S. DOE 1996, Section 6.4.1). Conceptual models are derived from the FEPs that are deemed important to repository performance. The disposal system is represented by 24 peer-reviewed conceptual models (McCormick et al. 2024).

2. **Mathematical models** represent the processes at the site. The conceptual models provide the context within which these mathematical models must operate and define the processes they must characterize. The mathematical models are predictive in the sense that, given appropriate properties of the system and possible perturbations, they predict the system's response. The processes represented by these mathematical models include fluid flow, mechanical deformation, radionuclide transport in groundwater, and removal of waste through intruding boreholes.

3. **Numerical models** are developed to approximate solutions to mathematical models.

4. **Computational models** generally refer to the implementation of numerical models in computer code with specific initial and boundary conditions and parameter values. The complexity of the system requires computer codes to solve the numerical models.

Parameters are values necessary in mathematical, numerical, or computational models. Data are descriptors of the physical system being considered, normally obtained by experiment or observation. The distinction between data and parameters can be subtle. Parameters are distinct from data, however, for three reasons: (1) data may be evaluated, statistically or otherwise, to generate model parameters that account for uncertainty in data; (2) some

parameters have no relation to the physical system, such as the parameters in a numerical model to determine when an iterative solution scheme has converged; and (3) many model parameters are applied at a different scale than one directly observed or measured in the physical system. The distinction between data and parameter values is described further in Tierney (1990), where derivations of distributions for specific parameters are given.

PA-2.3 Conceptual Description of the Undisturbed Repository System

Evaluations of past and present natural geologic processes in the region indicate that none has the potential to breach the repository within 10,000 years. Disposal system behavior is dominated by the coupled processes of rock deformation surrounding the excavation, fluid flow, and waste degradation. Each of these processes can be described independently, but the extent to which they occur is affected by the others.

Rock deformation immediately around the repository begins as soon as an excavation disturbs the stress field. Stress relief results in some degree of brittle fracturing and the formation of a DRZ, which surrounds excavations in all deep mines, including the WIPP repository. For the WIPP, the DRZ is characterized by increased permeability and porosity, and it may ultimately extend several meters (m) beyond the excavated region. Salt will also deform by creep processes driven by deviatoric stress, causing it to move inward and fill voids. Salt creep will continue until deviatoric stress is dissipated and the system is once again at stress equilibrium (McCormick et al. 2024; U.S. DOE 2004, Chapter 6.0, Section 6.4.3.1).

The ability of salt to creep, thereby healing fractures and filling porosity, is one of its fundamental advantages as a medium for geologic disposal of radioactive waste, and one reason it was recommended by the National Academy of Sciences (U.S. DOE 1996, Chapter 1.0, Section 1.3). Salt creep provides the mechanism for crushed salt compaction in the shaft seal system, yielding properties approaching those of intact salt within 200 years (U.S. DOE 1996, Appendix SEAL, Appendix D, Section D5.2). Salt creep will also cause the DRZ surrounding the shaft to heal rapidly around the concrete components of the seal system. In the absence of elevated gas pressure in the repository, salt creep would also substantially compact the waste and heal the DRZ around the disposal region. Fluid pressures generated by gas production from waste degradation can become large enough to reverse creep closure, with the pressurized fluid supporting the overburden load and maintaining elevated porosity throughout portions of the performance period (U.S. DOE 2004, Chapter 6.0, Section 6.4.3; Appendix PORSURF-2026).

Characterization of the Salado indicates that fluid flow from the far field does not occur on time scales of interest in the absence of an artificially imposed hydraulic gradient (see U.S. DOE 2004, Chapter 2.0, Section 2.1.3.4 for a description of Salado investigations). This lack of fluid flow is the second fundamental reason for choosing salt as a medium for geologic disposal of radioactive waste. Lack of fluid flow results from the extremely low permeability of the evaporite rocks that make up the Salado. Excavating the repository has disturbed the natural hydraulic gradient and rock properties, resulting in some fluid flow. Small quantities of interstitial brine present in the Salado move toward regions of low hydraulic potential, and

brine seeps are observed in the underground repository. The slow flow of brine from halite into more permeable anhydrite MBs, and then through the DRZ into the repository, is expected to continue as long as the hydraulic potential within the repository is below that of the far field. The repository environment will also include gas, so the fluid flow must be modeled as a two-phase process. Initially, the gaseous phase will consist primarily of air trapped at the time of closure, although other gases may form from waste degradation. In the PA, the gas-phase pressure will rise due to creep closure, gas generation, and brine inflow, potentially leading to flow from the excavated region (U.S. DOE 2004, Chapter 6.0, Section 6.4.3).

Waste degradation can generate significant gas by three processes (Appendix GEOCHEM-2026, Section GEOCHEM-2.0):

1. Anoxic corrosion of steel, other iron-based alloys, aluminum, and aluminum-based alloys, which may produce hydrogen (H_2);

2. Anaerobic microbial consumption of waste containing CPR materials, which may produce CO_2 and H_2S; and

3. Brine radiolysis by alpha particles, generated by radioactive decay, which may produce H_2.

Coupling these gas-generation reactions to fluid-flow and salt-creep processes is complex. Gas generation will increase fluid pressure in the repository, thereby decreasing the hydraulic gradient between the far field and the excavated region and inhibiting brine inflow. Gas generation also reduces deviatoric stress, and therefore, reduces the salt creep. Anoxic corrosion will also consume water (H_2O) as it breaks down H_2O to oxidize steel and other Fe-based alloys and release H_2 (lead corrosion is not assumed to contribute to gas generation in the repository (Appendix SCR-2026, Section SCR-6.5.1.5). Thus, corrosion is a self-limiting process, in that when it consumes all water in contact with steel and other Fe-based alloys, it will cease. Microbial reactions also require water, either in brine or the gaseous phase. Brine radiolysis is also assumed to consume water in generating H_2 gas. The consumption or generation of water from reactions other than those described above is also considered (see Appendix GEOCHEM-2026, Section GEOCHEM-2.2).

The total volume of gas generated by anoxic corrosion, microbial respiration, and brine radiolysis may be sufficient to achieve repository pressures approaching lithostatic pressure. Sustained pressures above lithostatic are not physically reasonable within the disposal system because the more brittle anhydrite layers are expected to fracture if sufficient gas is present. The conceptual model implemented in the PA assumes anhydrite MB permeability and porosity will increase rapidly as pore pressure approaches and exceeds lithostatic pressure. This conceptual model for pressure-dependent fracturing assumes pressure-induced fracturing allows gas and brine to move more freely within the MBs at higher pressures (U.S. DOE 2004, Chapter 6.0, Section 6.4.5.2).

Overall, the undisturbed disposal system provides extremely effective isolation of transuranic waste. The concrete, clay, and asphalt components of the shaft seal system provide an immediate and effective barrier to fluid flow through the shafts, isolating the repository until salt creep consolidates the compacted crushed salt components and permanently seals the shafts. Around the shafts, the DRZ in halite layers will heal rapidly because the presence of the solid material within the shafts will provide rigid resistance to creep. The DRZ around the shaft, therefore, will not provide a continuous pathway for fluid flow (U.S. DOE 2004, Chapter 6.0, Section 6.4.4). Similarly, the ROM salt in each emplaced panel closure will reconsolidate and resist creep, leading to a build-up of compressive stress that, in turn, will cause local healing of the DRZ. In PA, it is conservatively assumed that the DRZ does not heal around the disposal region, open panel closure areas, or the operations (OPS) and experimental (EXP) regions, and pathways for fluid flow may exist indefinitely to the overlying and underlying anhydrite layers (e.g., MB 139 and Anhydrites A and B). Some quantity of brine will be present in the repository under most conditions and may contain actinides mobilized as both dissolved and colloidal species. Gas generation from corrosion, microbial degradation, and brine radiolysis is expected, and will result in elevated pressures within the repository. Fracturing due to high gas pressures may enhance gas and brine migration from the repository, but gas transport will not contribute to the release of actinides from the disposal system. Brine flowing out of the waste disposal region through anhydrite layers may transport actinides as dissolved and colloidal species. However, during undisturbed repository performance, quantities of actinides reaching the LWB through the interbeds are expected to be insignificant and have no effect on the compliance determination. In addition, no migration of radionuclides is expected to occur vertically through the Salado.

PA-2.4 Conceptual Description of the Disturbed Repository System

The E scenarios represent the effects on the disposal system of intrusions caused by inadvertent, intermittent drilling for resources. Future drilling practices are assumed to be the same as current practice, consistent with regulatory criteria (40 CFR 194.33). These practices include the type and rate of drilling, emplacement of casing in boreholes, and the procedures implemented when boreholes are plugged and abandoned.

Human intrusion by drilling may cause releases from the disposal system through five mechanisms:

1. Cuttings, which include material intersected by the rotary drilling bit.
2. Cavings, which include material eroded from the borehole wall during drilling.
3. Spallings, which include solid material carried into the borehole during rapid depressurization of the waste disposal region.
4. DBRs, which include contaminated brine that may flow to the surface during drilling.

5. Long-term brine releases, which include the contaminated brine that may flow through a borehole after it is abandoned.

The first four mechanisms immediately follow an intrusion event and are collectively referred to as direct releases. The accessible environment boundary for these releases is the ground surface. The fifth mechanism, actinide transport by long-term groundwater flow, begins when concrete plugs are assumed to degrade in an abandoned borehole and may continue throughout the regulatory period. The accessible environment boundary for these releases is the lateral subsurface limit of the LWB (CRA-2004, Chapter 6.0, Section 6.0.2.3).

Repository conditions prior to intrusion correspond to those of the undisturbed repository. An intrusion provides a pathway for radionuclides to reach the ground surface and to enter the geological units above the Salado. The Culebra is the most transmissive unit above the repository and thus is a potential pathway for lateral migration of contaminated brine (U.S. DOE 2004, Chapter 6.0, Section 6.4.6.2).

Each mechanism is described in the following sections.

PA-2.4.1 Cuttings and Cavings

In a rotary drilling operation, the volume of material brought to the surface as cuttings is equal to the cylinder defined by the thickness of the unit and the diameter of the drill bit. The quantity of radionuclides released as cuttings is therefore a function of the activity of the intersected waste and the diameter of the intruding drill bit. The PA uses a constant value of 0.31115 m (12.25 inches (in)), consistent with bits currently used at the WIPP depth in the Delaware Basin (U.S. DOE 2025). The intersected waste activity may vary depending on the type of intersected waste. For cuttings and cavings releases, PA considers random penetrations into the 105 remote-handled transuranic (RH-TRU) and 485 contact-handled transuranic (CH-TRU) waste streams (Kicker 2025, Table 1).

Cavings are the particulate material eroded from the borehole wall by the drilling fluids and brought to the surface. Cavings volume may be affected by the drill bit diameter, effective shear resistance of the intruded material, speed of the drill bit, viscosity of the drilling fluid, and the rate at which it is circulated in the borehole, among other properties related to the drilling process. In a drilling intrusion the drilling mud flows up the borehole in a predominantly vertical direction. Drilling mud flowing up the borehole will apply a hydrodynamic shear stress on the borehole wall. Erosion of the wall material can occur if this stress is high enough, resulting in radionuclides being carried up the borehole with the drilling mud. The quantity of radionuclides released as cavings depends on the volume of eroded material and its activity, which is treated in the same manner as the activity of cuttings (see also Section PA-4.6 and Section PA-6.4.2.4).

PA-2.4.2 Spallings

Spallings are waste solids introduced into a borehole by the movement of gas towards the lower-pressure borehole. Spalling releases can occur if pressure in the waste-disposal region is

sufficiently high (e.g., greater than about 10 megapascals (MPa)). At these high pressures, gas flow toward the borehole may be sufficiently rapid to cause additional solid material to enter the borehole. If spalling occurs, the volume of spalled material depends on the physical properties of the waste, such as tensile strength and particle size. The quantity of radionuclides released with spalled material depends on the volume of spalled waste and its activity. Spalled waste is assumed to have the volume-averaged activity of CH-TRU waste, rather than the sampled activities of individual waste streams (see also Section PA-4.7 and Section PA-6.4.2.5 for further description of the spallings model).

PA-2.4.3 Direct Brine Releases

Radionuclides may be released to the ground surface if contaminated brine from the waste flows into the borehole during drilling. The quantity of radionuclides released by direct brine flow depends on the volume of brine reaching the ground surface and the concentration of radionuclides contained in the brine. DBRs will not occur if repository pressure is below the hydrostatic pressure in the borehole, assumed to be 8 MPa in the WIPP PA, or if waste area saturation does not exceed residual brine saturation. If the volume of brine flowing from the repository into the borehole is small, it will not affect the drilling operation, and flow may continue until the driller reaches the base of the evaporite section and installs casing in the borehole (see also Section PA-4.8 and Section PA-6.4.2.6). DBR events are of a relatively short duration (a few days) (see Section PA-4.8.8).

PA-2.4.4 Long-Term Brine Releases

After concrete plugs in an abandoned borehole degrade, contaminated brine in the repository may flow up the borehole to overlying units and then migrate laterally to the LWB. The brine volume in the repository can be affected by boreholes that intersect pressurized brine in the Castile unit below the repository.

PA-2.4.4.1 Castile Brine Reservoirs

Deep-drilling scenarios consider two types of boreholes: those that penetrate a region of pressurized brine in the underlying Castile, and those that do not. The presence of pressurized brine reservoir under the repository is speculative but, based on current information cannot be ruled out. Pressurized brine was encountered at the WIPP-12 borehole within the LWB to the north of the disposal region. Other encounters of pressurized brine associated with regions of deformation in the Castile have occurred elsewhere in the Delaware Basin (U.S. DOE 2004, Chapter 2.0, Section 2.2.1.2.2). The probability of a pressurized brine encounter is uncertain (see parameter GLOBAL:PBRINE in Feng and Kicker (2025a), Table 3).

The primary consequence of penetrating a pressurized brine source is the supply of an additional source of brine beyond that which might flow into the repository from the Salado. Direct releases at the ground surface resulting from the first repository intrusion would be unaffected by additional Castile brine, even if it flowed to the surface, because brine moving straight up a borehole will not significantly mix with waste. However, the presence of Castile

brine could significantly increase radionuclide releases from later intrusions in two ways. First, the volume of contaminated brine that could flow to the surface may be greater for a subsequent intrusion into a repository that has already been connected to a Castile brine source by a previous borehole. Second, the volume of contaminated brine that may flow up an abandoned borehole after plug degradation may be greater for combinations of two or more boreholes that intrude the same panel if one of the boreholes penetrates a source of pressurized brine. Both processes are modeled in PA.

PA-2.4.4.2 Mobilization of Actinides in Repository Brine

Actinides may be mobilized in repository brine as dissolved species and as colloidal species. The solubilities of actinides depend on their oxidation states. Conditions within the repository will be strongly reducing because of large quantities of metallic iron (Fe) in the steel containers and the waste. Consequently, in the case of plutonium (Pu), only the lower-solubility oxidation states (Pu(III) and Pu(IV)) will persist (see Appendix SOTERM-2026, Section SOTERM-6.3). Microbial activity is also assumed to help create reducing conditions.

Solubilities also vary with pH. MgO is emplaced in the waste-disposal region to ensure conditions that reduce uncertainty and establish low actinide solubilities. MgO consumes CO_2 and buffers pH, lowering actinide solubilities in the WIPP brines (see Appendix GEOCHEM-2026, Section GEOCHEM-3.1.1). Solubilities in the PA are based on the chemistry of brines that might be present in the waste-disposal region, reactions of these brines with the MgO engineered barrier, and strongly reducing conditions produced by anoxic corrosion of steel and other Fe-based alloys (Section PA-4.3).

The waste contains organic ligands that could increase actinide solubility by forming complexes with dissolved actinide species. However, these organic ligands may also form complexes with other dissolved metals that will be present in repository brines due to corrosion of steel and other Fe-based alloys, dissolution of the waste itself, and from the MgO backfill (see Appendix GEOCHEM-2026, Section GEOCHEM-4.1.6).

Four types of colloids have been identified to represent the possible behavior at the WIPP (Appendix GEOCHEM-2026, Section GEOCHEM-5.0). These include microbial colloids, humic substances, actinide intrinsic colloids, and mineral fragments. Concentrations of actinides mobilized as these colloidal forms are included in the estimates of total actinide concentrations (see Section PA-4.3; Appendix SOTERM-2026, Section SOTERM-3.5).

PA-2.4.4.3 Long-Term Brine Flow up an Intrusion Borehole

Long-term releases to the ground surface or groundwater in the Rustler Formation (hereafter referred to as the Rustler) or overlying units may occur after a borehole has been plugged and abandoned. In keeping with regulatory criteria (40 CFR 194.33), borehole plugs are assumed to have properties consistent with current practice in the basin, i.e., concrete plugs are emplaced at various locations. Initially, concrete plugs effectively limit fluid flow in the borehole. However, under most circumstances, these plugs cannot be expected to remain fully effective

indefinitely. For PA, discontinuous borehole plugs above the repository are assumed to degrade 200 years after emplacement. From then on, the borehole is assumed to fill with a silty-sand-like material containing degraded concrete, corrosion products from the degraded casing, and material sloughing from the walls. Of six possible plugged borehole configurations in the Delaware Basin (U.S DOE 2025), three are considered either likely or adequately representative of other possible configurations (see Section PA-3.2.4); one configuration (a two-plug configuration) is explicitly modeled in the flow and transport model (see Section PA-4.2.2.3).

If sufficient brine is available in the repository, and the pressure in the repository is higher than that in the overlying units, brine may flow up the borehole following plug degradation. In principle, this brine could flow into any permeable unit or to the ground surface if the repository pressure were high enough. Lower-permeability anhydrite and mudstone layers in the Rustler are treated as impermeable to simplify the analysis while maximizing the amount of flow into units where it could contribute to disposal system releases. Model results indicate that essentially all flow occurs into the Culebra, which has been recognized since the early stages of site characterization as the most transmissive unit above the repository and the most likely pathway for subsurface transport (U.S. DOE 2004, Chapter 2.0, Section 2.2.1.4.1.2).

PA-2.4.4.4 Groundwater Flow in the Culebra

Identification of the Culebra as one of the most likely subsurface transport pathways in the units above the Salado has motivated continued Culebra-focused characterization activities (Hart et al. 2009; Bowman et al. 2023). These activities have shown that the direction of groundwater flow in the Culebra varies somewhat regionally, but in the area that overlies the repository, flow is generally southward. Regional variation in the Culebra's groundwater flow direction is influenced by the lateral (facies) changes in the lithology of the Culebra in the groundwater basin where the WIPP is located. Features in the Culebra such as fractures, fracture fillings, and vuggy pores, can affect transmissivity which in turn impact groundwater flow (U.S. DOE 2004, Chapter 2.0, Section 2.1.3.5).

For PA calculations the Culebra is conceptualized as a two-dimensional confined aquifer (McCormick et al. 2024). Uncertainty in the flow field is incorporated by using 100 realizations of T-fields. Each T-field is calibrated with available head and transmissivity data and with updated information on geologic factors potentially affecting transmissivity in the Culebra (see Appendix TFIELD-2026).

Although the calibrated T-fields characterize the natural distribution of transmissivity in the Culebra, anthropogenic activities may further influence groundwater flow behavior. Potash mining in the McNutt Potash Zone of the Salado, which occurs now in the Delaware Basin outside the LWB and may continue in the future, could affect flow in the Culebra if subsidence over mined areas causes fracturing or other changes in rock properties (U.S. DOE 2004, Chapter 6.0, Section 6.3.2.3).(U.S. DOE 2004, Chapter 6.0, Section 6.3.2.3).

Under the regulatory criteria of 40 CFR 194.32, mining outside the LWB is assumed to occur in the near future, and mining within the LWB is assumed to occur with a probability of 1 in 100

per century (adjusted for the effectiveness of AICs during the first 100 years after closure). In accordance with EPA guidance, the effects of mine subsidence are incorporated in PA by increasing the transmissivity of the Culebra over the areas identified as mineable by a factor sampled from a uniform distribution between 1 and 1,000 (U.S. EPA 1996a, p. 5229). The T-fields used in PA are therefore adjusted and steady-state flow fields recalculated for two scenarios. One scenario considers mining that occurs only outside the LWB, and the other considers mining that occurs both inside and outside the LWB (Section PA-4.9).

In addition to potential mining related disturbances, climatic changes during the next 10,000 years may affect groundwater flow by altering recharge to the Culebra. The extent to which the climate will change during the next 10,000 years and how such changes will affect groundwater flow in the Culebra are uncertain. The uncertainty in recharge due to climate change is incorporated into PA by scaling the calculated steady-state specific discharge in the Culebra using a sampled parameter, GLOBAL:CLIMTIDX, which ranges from 1 to 2.25 based on regional three-dimensional groundwater flow modeling of reasonably possible future climates (see parameter GLOBAL:CLIMTIDX in Table 3 of Feng and Kicker (2025a); U.S. DOE 1996, Appendix CLI).U.S. DOE 1996, Appendix CLI).

PA-2.4.4.5 Actinide Transport in the Culebra

Field tests have shown that the Culebra is best characterized as a double-porosity medium for estimating contaminant transport in groundwater (U.S. DOE 2004, Chapter 2.0, Section 2.2.1.4.1.2). Groundwater flow and advective transport of dissolved and colloidal species occur primarily in a small fraction of the rock's total porosity which corresponds to the porosity associated with open and interconnected fractures and vugs (Holt 1997). Diffusion and slower advective transport occur in the remaining porosity associated with the low-permeability dolomite matrix. Transported actinides, will diffuse in and out of this porosity.

Diffusion from the fracture porosity into the dolomite matrix will retard actinide transport through two mechanisms. Physical retardation occurs simply because actinides that diffuse into the matrix are no longer transported with the flowing groundwater. The mass of solute transported by advection decreases until the actinides diffuse back into the fracture porosity. In situ tracer tests have demonstrated this phenomenon (Meigs et al. 2000). Chemical retardation also occurs within the matrix as actinides are sorbed onto dolomite grains. The relationship between sorbed and liquid concentrations is assumed to be linear and reversible. The distribution coefficients (K_ds) that characterize the extent to which actinides will sorb on dolomite are based on experimental data (U.S. DOE 2004, Chapter 6.0, Section 6.4.6.2).

Experimental work has demonstrated that transport of colloidal actinides is not a significant mechanism in the Culebra (Papenguth 1996). Conceptually, colloidal humic materials transport identically to dissolved phases, microbial and mineral fragment colloids are effectively attenuated, and intrinsic colloids are considered insignificant (McCormick et al. 2024).

PA-2.5 Structure of the PA

This section outlines the structure of the WIPP PA with an emphasis on how its development is guided by regulatory requirements. The conceptual structure of the CRA-2026 PA is identical to that of the CRA-2019 PA. In broad terms, the PA combines representations of uncertainty in future disruptive events and in system parameters with computational models that calculate repository releases. This framework provides a consistent basis for evaluating the combined effects of stochastic events and parameter uncertainty on projected releases.

The formal structure of the WIPP PA involves three mathematical entities:

1. A probability space $(S_{st}, \mathbb{S}_{st}, p_{st})$ that characterizes aleatory uncertainty in the occurrence and properties of future events (Section PA-2.5.1).
2. A deterministic function $f(\mathbf{x}_{st}|\mathbf{v}_{su})$ that computes releases from the repository given an element $\mathbf{x}_{st}$ of S_{st} and an element $\mathbf{v}_{su}$ of S_{su} (Section PA-2.5.2).
3. A probability space $(S_{su}, \mathbb{S}_{su}, p_{su})$ that characterizes epistemic uncertainty in the parameters and models that describe the WIPP repository system (Section PA-2.5.3).

PA-2.5.1 Probabilistic Characterization of Different Futures

The projection of releases over the 10,000 years following closure of the repository is modeled for scenarios defined by the nature and timing of intrusion and mining events.

The collection of all possible futures $\mathbf{x}_{st}$ forms the basis for a probability space $(S_{st}, \mathbb{S}_{st}, p_{st})$ that characterizes aleatory uncertainty, where S_{st} = {$\mathbf{x}_{st}$: $\mathbf{x}_{st}$ is a possible future of the repository}, $\mathbb{S}_{st}$ is a suitably restricted collection of sets of futures and p_{st} is a probability measure for the elements of $\mathbb{S}_{st}$. The elements $\mathbf{x}_{st}$ of S_{st} are vectors of the form:

$$\mathbf{x}_{st} = [(t_1, e_1, l_1, b_1, p_1, \mathbf{a}_1), \ldots, (t_n, e_n, l_n, b_n, p_n, \mathbf{a}_n), t_{min}] \quad \text{(PA.2)}$$

where

n is the number of drilling intrusions,

t_j is the time (year) of the j^{th} intrusion,

e_j designates the penetration of an excavated or nonexcavated area by the j^{th} intrusion,

l_j designates the panel (location) of the j^{th} intrusion,

b_j designates whether the j^{th} intrusion penetrates pressurized brine in the Castile,

p_j designates the plugging procedure used with the j^{th} intrusion (i.e., continuous plug, two discrete plugs, three discrete plugs),

$\mathbf{a}_j$ designates the type of waste penetrated by the j^{th} intrusion (i.e., no waste, CH-TRU waste, RH-TRU waste and, for CH-TRU or RH-TRU waste, the waste stream(s) encountered),

t_{min} is the time at which potash mining occurs within the LWB.

The subscript *st* indicates that aleatory (i.e., stochastic) uncertainty is being considered.

The probabilistic characterization of n, t_j, l_j, and e_j is based on the assumption that drilling intrusions will occur randomly in time and space at a constant average rate (i.e., follow a Poisson process); the probabilistic characterization of b_j derives from assessed properties of brine reservoirs; the probabilistic characterization of p_j derives from current drilling practices in the sedimentary basin (i.e., the Delaware Basin) in which the WIPP is located; and the probabilistic characterization of $\mathbf{a}_j$ derives from the volumes of waste streams emplaced in the WIPP in relation to the volume of the repository. A vector notation is used for $\mathbf{a}_j$ because it is possible for a given drilling intrusion to miss the waste or to penetrate different waste types (CH-TRU or RH-TRU), as well as to encounter different waste streams in the CH-TRU wastes. Further, the probabilistic characterization for t_{min} follows from the criteria in Part 194 that the occurrence of potash mining within the LWB should be assumed to occur randomly in time (i.e., follow a Poisson process with a rate constant of $\lambda_m = 10^{-4}$ yr^{-1}), with all commercially viable potash reserves within the LWB extracted at time t_{min}. In practice, the probability measure p_{st} is defined by specifying probability distributions for each component of $\boldsymbol{x}_{st}$, as discussed further in Section PA-3.0.

PA-2.5.2 Estimation of Releases

Based on the retained FEPs (Section PA-2.2.1), release mechanisms include direct transport of material to the surface at the time of a drilling intrusion (i.e., cuttings, cavings, spallings, and DBRs) and releases subsequent to a drilling intrusion due to brine flow up a borehole with degraded plugs (i.e., groundwater transport). Computational models for estimating releases are summarized in Figure PA-8. These computational models implement the conceptual models representing the repository system (Sections PA-2.3 and PA-2.4) and the mathematical models for physical processes (presented in Section PA-4.0). Most of the computational models involve the numerical solution of partial differential equations (PDEs) used to represent processes such as material deformation, fluid flow, and radionuclide transport.

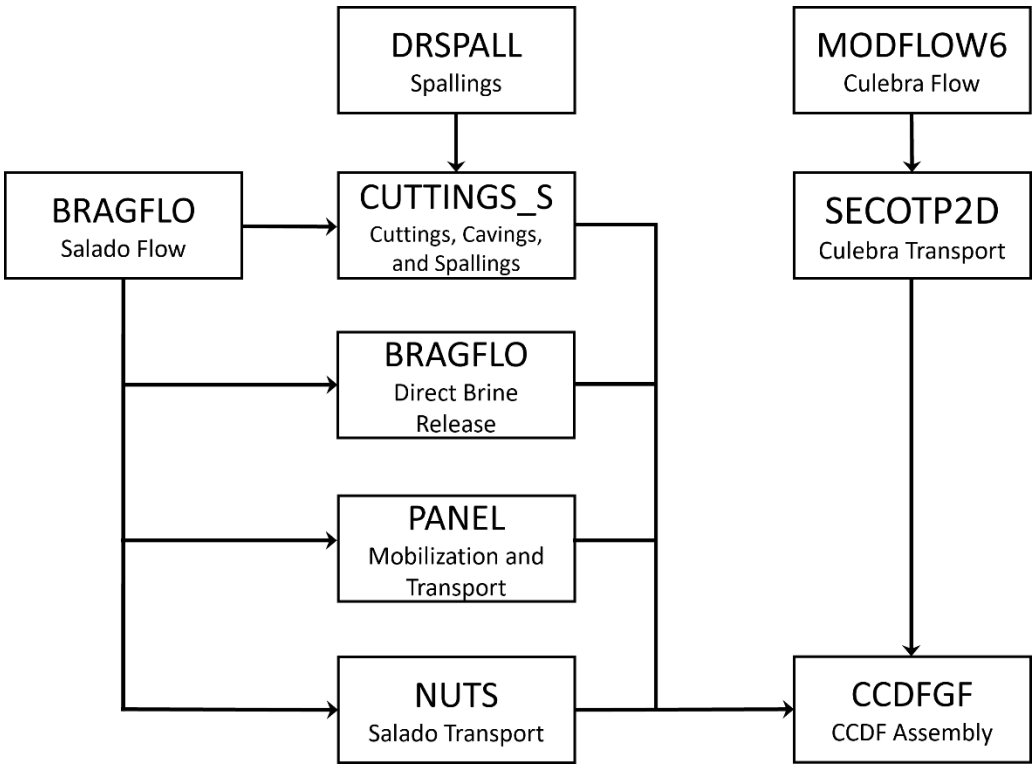


Figure PA-8. Computational Models Used in PA

The collection of computational models can be represented abstractly as a function $f(\mathbf{x}_{st}|\mathbf{v}_{su})$, which quantifies the release that could result from the occurrence of a specific future $\mathbf{x}_{st}$ and a specific value for model parameters $\mathbf{v}_{su}$. The probability space $(S_{st}, \mathbb{S}_{st}, p_{st})$, together with the function $f(\mathbf{x}_{st}|\mathbf{v}_{su})$, give rise to the CCDF specified in 40 CFR 191.13 (a), as illustrated in Figure PA-9. The CCDF is the probability that a release from the repository greater than *R* will be observed, where *R* is a point on the abscissa (x-axis) of the graph.

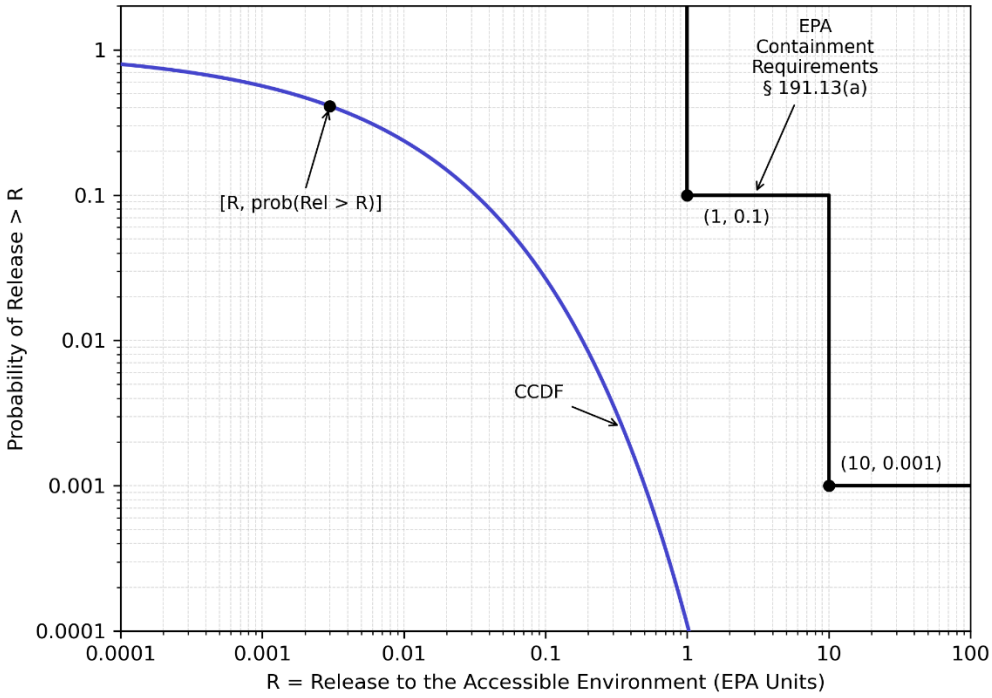


Figure PA-9. Construction of the CCDF Specified in 40 CFR Part 191 Subpart B

Formally, the CCDF depicted in Figure PA-9 results from an integration over the probability space $(S_{st}, \mathbb{S}_{st}, p_{st})$:

$$prob\left(rel > R \middle| \mathbf{v}_{su}\right) = \int_{st} \delta_r\left(f\left(\mathbf{x}_{st} \middle| \mathbf{v}_{su}\right)\right) d_{st}\left(\mathbf{x}_{st} \middle| \mathbf{v}_{su}\right) dV_{st} \quad \text{(PA.3)}$$

where $\delta_R\left(f(\mathbf{x}_{st}|\mathbf{v}_{su})\right) = 1$ if $f(\mathbf{x}_{st}|\mathbf{v}_{su}) > R$, $\delta_R\left(f(\mathbf{x}_{st}|\mathbf{v}_{su})\right) = 0$ if $f(\mathbf{x}_{st}|\mathbf{v}_{su}) \leq R$, and $d_{st}(\mathbf{x}_{st}|\mathbf{v}_{su})$ is the probability density function associated with the probability space $(S_{st}, \mathbb{S}_{st}, p_{st})$ (δ_R is a delta function that selects releases exceeding R). The models in Figure PA-8 are too complex to permit a closed-form evaluation of the integral in Equation (PA.3). In practice, the integral in Equation (PA.3) is evaluated by a Monte Carlo technique, where a random sample $\mathbf{x}_{st,i}$, i = 1, nS is generated from S_{st} consistent with the probability distribution p_{st}. Using this random sample, Equation (PA.3) is numerically evaluated as:

$$prob\left(rel > R \middle| \mathbf{v}_{su}\right) \cong \sum_{i=1}^{nS} \delta_R\left(f\left(\mathbf{x}_{st,i} \middle| \mathbf{v}_{su}\right)\right) \Big/ nS \quad \text{(PA.4)}$$

The number of samples nS used to construct a CCDF is 10,000. However, the models in Figure PA-8 are too computationally intensive to permit their evaluation for each of these 10,000 futures. Due to this constraint, the models in Figure PA-8 are evaluated for a relatively small number of representative scenarios, and the results of these evaluations are used to construct the value of $f(\mathbf{x}_{st.i}|\mathbf{v}_{su})$ for each future $\mathbf{x}_{st.i}$. The representative scenarios are labeled E0, E1,

E2, and E1E2, and are described in Sections PA-2.2.2 and PA-3.4; the procedure for constructing a future's release from these scenarios is described in Section PA-6.5.

PA-2.5.3 Probabilistic Characterization of Parameter Uncertainty

If the parameters used in the computational models of Figure PA-8 were known with certainty, the actual value for $\mathbf{v}_{su}$ would be known, the deterministic function $f(\mathbf{x}_{st.i}|\mathbf{v}_{su})$ would vary only with the scenario $\mathbf{x}_{st.i}$, and one CCDF would result from evaluation of Equation (PA.4). Because the parameters are not precisely known, it is necessary to consider uncertainty in parameters and the effect of this uncertainty on the CCDF being constructed. The uncertainty associated with the parameters is termed epistemic, or subjective, uncertainty.

The probabilistic characterization of the uncertainty in the model parameters is the outcome of the data development effort for the WIPP. Formally, uncertainty in the parameters that underlie the WIPP PA can be characterized by a second probability space $(S_{su}, \mathbb{S}_{su}, p_{su})$, where the sample space S_{su} is defined by:

$$S_{su} = \{\mathbf{v}_{su}: \mathbf{v}_{su} \text{ is a vector of possible parameter values}\} \quad \text{(PA.5)}$$

The subscript *su* indicates that epistemic (i.e., subjective) uncertainty is being considered. An element $\mathbf{v}_{su} \in S_{su}$ is a vector ($\mathbf{v}_{su} = [v_{su,1}, v_{su,2}, \ldots, v_{su,N}]$) of length N, where each element $v_{su,k}$ is an uncertain parameter used in the models to estimate releases. In practice, the probability measure p_{su} is defined by specifying probability distributions for each element of $\mathbf{v}_{su}$, discussed further in Section PA-5.0.

Uncertainty in $\mathbf{v}_{su}$ as characterized by $(S_{su}, \mathbb{S}_{su}, p_{su})$ leads to a distribution of CCDFs (Figure PA-10), with a different CCDF resulting from each of the possible values of $\mathbf{v}_{su}$. The WIPP PA uses a stratified sampling design called Latin hypercube sampling (LHS) (McKay et al. 1979) to generate a sample $\mathbf{v}_{su,i}, i = 1, \ldots, nLHS$, from S_{su} consistent with the probability distribution represented by p_{su} (see Section PA-6.1). LHS is an efficient scheme for sampling the range of a distribution using a relatively small sample.

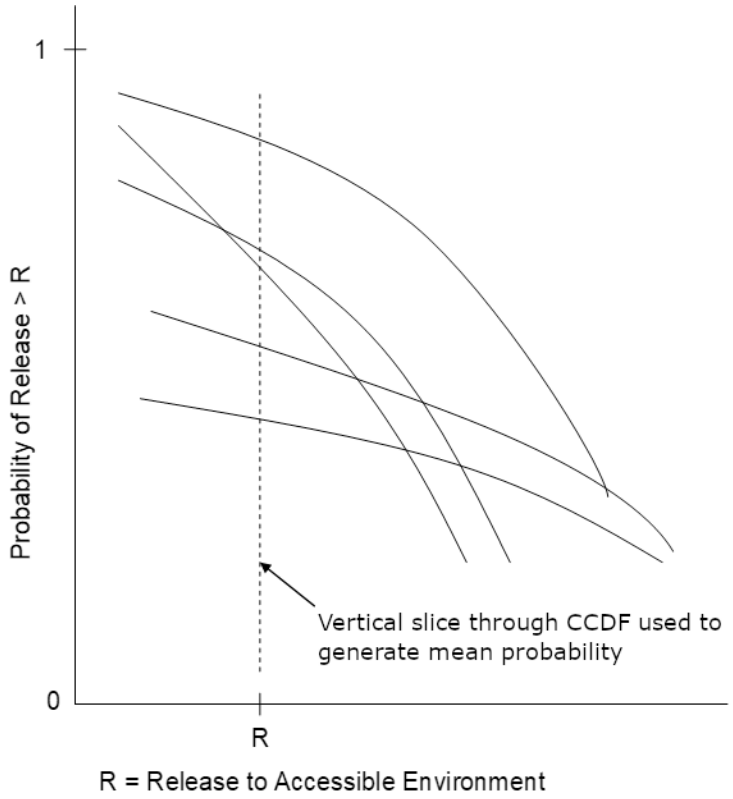


Figure PA-10. Distribution of CCDFs Resulting from Possible Values for the Sampled Parameters.

PA-2.6 Compliance Demonstration Method

The containment requirements of 40 CFR 191.13(a) are answered using the mean of the distribution of CCDFs of releases. The mean CCDF is created by averaging the CCDFs across vertical slices (Figure PA-10). A formal definition of this construction is provided in Helton et al. (1998). Statistical confidence in the mean CCDF is computed as described in Section PA-6.1.2. The proximity of these curves to the boundary line in Figure PA-9 indicates the confidence with which the containment requirements will be met. Confidence is also established by examining the distribution of the CCDFs in relation to the release limits.

Criteria specified in 40 CFR 194.34 require the sample size to be sufficient to represent the 99th percentile of the distribution of CCDFs at specified release levels, and to demonstrate confidence in the sample mean. Per the EPA: “The LHS sample sizes should be demonstrated operationally to improve (reduce the size of) the confidence interval for the estimated mean. The underlying principle is to show convergence of the mean” (U.S. EPA 1996b, p. 8-41). To address the associated criteria of Part 194, convergence of the mean is demonstrated using an operational approach of multiple replication, as proposed by Iman (1982). The complete set of PA calculations is repeated three times, with, all aspects of the analysis identical except for the

random seeds used to initiate the LHS procedure and the stochastic sampling of future events. Thus, PA results are available for 3 replicates, each based on an independent sample of size nLHS=100 drawn from identical distributions for imprecisely known parameters and propagated through an identical modeling system. Multiple replication allows the adequacy of the sample size to be evaluated and provides a suitable measure of confidence in the mean CCDF as required by 40 CFR 194.34(f) (see Section PA-6.1.2).

PA-3.0 Probabilistic Characterization of Futures

This section describes the individual components $t_j, e_j, l_j, b_j, p_j, \mathbf{a}_j$, and t_{min}, and their associated probability distributions, of an element $\mathbf{x}_{st}$ of S_{st} (Equation PA.2). The effect of institutional controls on future events is summarized in Section PA-3.1. Components of $\mathbf{x}_{st}$ that describe a drilling intrusion are detailed in Section PA-3.2, and the time of mining in Section PA-3.3. The concept of a scenario as a subset of the sample space of $\mathbf{x}_{st}$ is discussed in Section PA-3.4. The procedure used to sample the individual elements $\mathbf{x}_{st}$ is described in Section PA-6.2.

PA-3.1 Institutional Controls

This section describes the representation in PA of the effects of AICs and PICs. The AICs and PICs will be implemented at the WIPP site to deter human activity that could be detrimental to repository performance. The AICs and PICs are described in Sections 41 and 43 of this CRA, with full detail provided in Chapter 7.0 of CRA-2004 and the appendices referenced therein. Permanent markers will be installed to inform future populations of the location of the WIPP. Part of the marker system will include a berm that defines the active areas of the repository.

The AICs will be implemented at the WIPP after final facility closure to control site access and prevent activities detrimental to disposal system performance within the controlled area. The AICs will preclude human intrusion in the disposal system. A 100-year limit on the effectiveness of AICs in PA is established in 40 CFR 191.14 (a). Because of regulatory restrictions and the nature of the AICs to be implemented, PA assumes there are no inadvertent human intrusions or mining in the controlled area for 100 years following repository closure.

The PICs are designed to deter inadvertent human intrusion into the disposal system. Only minimal assumptions were made about the nature of future society when designing the PICs to comply with the assurance requirements. The preamble to Part 194 limits any credit for PICs in deterring human intrusion to 700 years after disposal (U.S. EPA 1996a, p. 5231). The PA does not credit PICs with reducing intrusions into the disposal system. Excluding PICs is a conservative implementation, as no credit is taken for a beneficial component of the disposal system.

PA-3.2 Drilling Intrusion

Drilling intrusions considered in the PA are described in Section PA-2.2.2.2. Drilling intrusions in PA are assumed to occur randomly in time and space. AICs are assumed to prevent any drilling intrusions for the first 100 years after the decommissioning of the WIPP (Section PA-3.1). For the CRA-2026, the drilling frequency considered within the area marked by a berm as part of the system for PICs is 1.534×10^{-2} intrusions per square kilometer per year ($km^{-2}\ yr^{-1}$) (parameter GLOBAL:LAMBDAD in Feng and Kicker (2025a), Table 35). In the computational implementation of PA, it is convenient to represent the Poisson process for drilling intrusions by its corresponding rate term $\lambda_d(t)$ for intrusions into the area marked by the berm. Specifically:

$$\lambda_d(t) = \begin{cases} 0 & 0 \le t < 100 \text{ yr} \\ 1.1505 \times 10^{-2} \text{ yr}^{-1} & 100 \le t \le 10{,}000 \text{ yr} \end{cases} \quad \text{(PA.6)}$$

where $1.1505 \times 10^{-2}\ \text{yr}^{-1} = (0.75\ \text{km}^2) \times (0.01534\ \text{km}^{-2}\ \text{yr}^{-1})$, 0.75 km^2 is the area enclosed by the berm (parameter REFCON:ABERM in Feng and Kicker (2025a), Table 35) and *t* is the elapsed time (in years) since decommissioning the WIPP.

The function $\lambda_d(t)$ defines the parameter of the exponential distribution that governs the times of intrusions, t_j in Equation (PA.2). In the computational implementation of the analysis, the exponential distribution is randomly sampled to define the times between successive drilling intrusions (Figure PA-11 and Section PA-6.2). Due to the 10,000-year regulatory period specified in 40 CFR 191.13, t_j is assumed to be bounded above by 10,000 years in the definition of $\mathbf{x}_{st}$. Further, t_j is bounded below by 100 years as defined in Equation (PA.6).

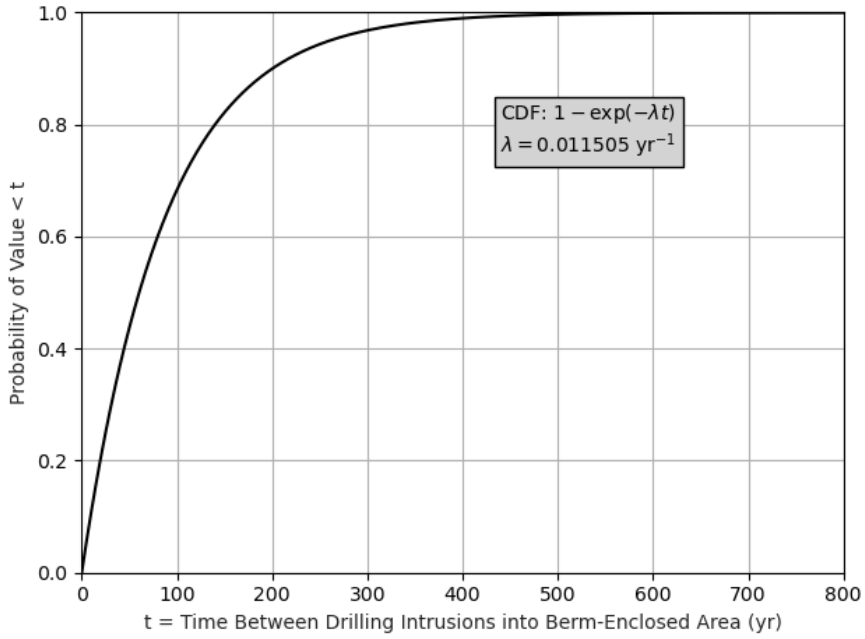


Figure PA-11. CDF for Time Between Drilling Intrusions

PA-3.2.1 Penetration of Excavated/Nonexcavated Area

The variable e_j indicates whether the j^{th} drilling intrusion penetrates an excavated, waste-filled area of the repository: e_j = 0 indicates penetration of a nonexcavated area, and e_j = 1 indicates penetration of an excavated, waste-filled area. The corresponding probabilities $P[e_j = 0]$ and $P[e_j = 1]$ for e_j = 0 (nonexcavated) and e_j = 1 (excavated) are:

$$pEx_1 = P[e_j = 1] = \frac{(0.1415\,\text{km}^2 + 0.003528\,\text{km}^2)}{0.75\,\text{km}^2} = 0.1934 \quad \text{(PA.7)}$$

$$pEx_0 = P[e_j = 0] = 1 - pEx_1 = 0.8066 \quad \text{(PA.8)}$$

where 0.1415 km^2 is the excavated area of the repository with CH waste (REFCON:AREA_CH), 0.003528 km^2 is the excavated area of the repository with RH waste (REFCON:AREA_RH), and 0.75 km^2 is the area of the berm (REFCON:ABERM) (see parameters in Feng and Kicker 2025a, Table 35).

PA-3.2.2 Drilling Location

Each intrusion into an excavated, waste-filled area is randomly located in one of the waste panels. The probability pL_k that a drilling intrusion will occur at a given panel *k* is calculated as the ratio of panel area to the total area of all panels. For example, pL_k = 0.083412 for Panel 5 (Day 2025).

PA-3.2.3 Penetration of Pressurized Brine

The conceptual models for the Castile include the possibility that pressurized brine reservoirs underlie the repository (Section PA-4.2.11). The variable b_j is a designator for whether the j^{th} drilling intrusion penetrates pressurized brine, where b_j = 0 signifies nonpenetration and b_j = 1 signifies penetration of pressurized brine. In the CRA-2026 PA, the probability of encountering pressurized brine during a drilling intrusion is the same as in the CRA-2019, although there has been a slight change in sampling of the probability's uncertainty distribution due to a code correction (Section PA-1.3.23). Specifically, the probability $pB_1 = P[b_j = 1]$ in the CRA-2026 PA is sampled from a cumulative distribution ranging from 0.04 to 0.57 (see parameter GLOBAL:PBRINE in Feng and Kicker (2025a), Table 3).

PA-3.2.4 Plugging Pattern

Three borehole plugging patterns are considered in PA: (1) p_1, a full concrete plug through the Salado to the Bell Canyon Formation (hereafter referred to as Bell Canyon), (2) p_2, a two-plug configuration with concrete plugs at the Rustler/Salado interface and the Castile/Bell Canyon interface, and (3) p_3, a three-plug configuration with concrete plugs at the Rustler/ Salado, Salado/Castile, and Castile/Bell Canyon interfaces.

In accordance with the criteria established in 40 CFR 194.33, drilling activity in the Delaware Basin continues to be surveyed (U.S. DOE 2025). Plugging pattern parameters for the CRA-2026 are calculated by King (2025c). The probability that a given drilling intrusion will be sealed with plugging pattern p_k, *k*= 1, 2, 3, is given by pPL_k, where $pPL_1 = P[k = 1]$ = 0.359 (GLOBAL:ONEPLG), $pPL_2 = P[k = 2]$ = 0.464 (GLOBAL:TWOPLG), $pPL_3 = P[k = 3]$ = 0.177 (GLOBAL:THREEPLG) (Feng and Kicker 2025a, Table 36).

PA-3.2.5 Waste Activity Level

The waste intended for disposal at the WIPP comprises 590 distinct waste streams, of which 485 are designated as CH-TRU waste and 105 as RH-TRU waste (Kicker 2025). The activity levels in EPA units per cubic meter for the waste streams at WIPP closure are given in Kim and Kicker (2025), Table 8.4.

Each waste container emplaced in the repository contains waste from a single waste stream. Waste packaged in 55-gallon (gal) drums is stacked three drums high within the repository. Although waste in other packages (e.g., standard waste boxes, 10-drum overpacks, etc.) may not be stacked three high, PA assumes that a drilling intrusion into CH-TRU waste intersects three waste streams chosen at random with a probability based on waste stream volume (it is possible to select the same waste stream multiple times for a single CH-TRU waste intrusion). An intrusion into RH-TRU intersects a single randomly chosen RH-TRU waste stream.

The vector $\mathbf{a}_j$ characterizes the waste penetrated by the j^{th} drilling intrusion in a potential future. Specifically:

$$\mathbf{a}_j = 0 \text{ if } e_j = 0 \tag{PA.9}$$

(i.e., if the j^{th} drilling intrusion does not penetrate an excavated area of the repository)

$$\mathbf{a}_j = [CH_{j1}, CH_{j2}, CH_{j3}] \text{ if } e_j = 1 \text{ and CH-TRU waste is penetrated} \tag{PA.10}$$

$$\mathbf{a}_j = [RH_{j1}] \text{ if } e_j = 1 \text{ and RH-TRU waste is penetrated} \tag{PA.11}$$

where CH_{j1}, CH_{j2}, CH_{j3}, and RH_{j1} are integer indices for waste streams intersected by the j^{th} drilling intrusion. The individual waste stream volumes in Kim and Kicker (2025), Table 8.1, are used to determine the specific waste streams (CH_{j1}, CH_{j2}, and CH_{j3}, or RH_{j1}) encountered, given a penetration of CH-TRU or RH-TRU waste.

Given the penetration of an excavated area, the type of waste penetrated is determined by the probabilities *pCH* and *pRH*. The excavated area used for disposal of CH-TRU waste, *aCH*, is 141,511 m^2 (parameter REFCON:AREA_CH), and the area used for disposal of RH-TRU waste, *aRH*, is 3,528 m^2 (parameter REFCON:AREA_RH) for a total disposal area of *aEX* = *aCH* + *aRH* = 145,039 m^2 (Feng and Kicker (2025a), Table 35). Given an intrusion that penetrates an excavated area, the probabilities *pCH* and *pRH* of penetrating CH-TRU and RH-TRU waste are given by:

$$pCH = \frac{aCH}{aCH + aRH} = 0.9757 \tag{PA.12}$$

$$pRH = \frac{aRH}{aCH + aRH} = 0.0243 \tag{PA.13}$$

Given that CH-TRU waste is penetrated, the probability of encountering a particular CH-TRU waste stream is computed as the ratio of the volume of that waste stream to the total volume of CH-TRU waste. Likewise, given that RH-TRU waste is penetrated, the probability of encountering a particular RH-TRU waste stream is computed as the ratio of the volume of that waste stream to the volume of RH-TRU waste.

PA-3.3 Mining Time

Full mining of known potash reserves within the LWB is assumed to occur at time t_{min}. AICs are assumed to result in no possibility of mining for the first 100 years after decommissioning of the WIPP. In PA, PICs do not affect the mining rate. After 100 years, the occurrence of mining within the LWB in 10,000 years is specified as following a Poisson process with a rate of $\lambda_m(t) = 1 \times 10^{-4}$ yr^{-1} (parameter GLOBAL:MINERT in Feng and Kicker (2025a), Table 36). Thus, the mining rate $\lambda_m(t)$ is:

$$\lambda_m(t) = \begin{cases} 0 \text{ yr}^{-1} & 0 \le t < 100 \text{ yr} \\ 10^{-4} \text{ yr}^{-1} & 100 \le t \le 10{,}000 \text{ yr} \end{cases} \quad \text{(PA.14)}$$

where t is the elapsed time since decommissioning of the WIPP.

In the computational implementation of the analysis, $\lambda_m(t)$ is used to define the distribution of time to mining. Only one mining event is assumed to occur (i.e., $\mathbf{x}_{st,i}$ contains only one value for t_{min}) to be consistent with guidance given in Part 194 that mining within the LWB should be assumed to remove all economically viable potash reserves. Due to the 10,000-year regulatory period specified in 40 CFR 191.13, t_{min} is assumed to be bounded above by 10,000 years in the definition of $\mathbf{x}_{st,i}$.

PA-3.4 Scenarios and Scenario Probabilities

Formally, a scenario is a subset of the sample space for aleatory uncertainty. Given the complexity of the futures $\mathbf{x}_{st}$ (see Equation (PA.2)), many different scenarios can be defined. The computational complexity of the function $f(\mathbf{x}_{st}|\mathbf{v}_{su})$ in Section PA-2.5.2 limits evaluation to only a few scenarios. As presented in Section PA-2.2.2, PA considers four fundamental intrusion scenarios:

E0 = no drilling intrusion through an excavated area of the repository.

E1 = a single drilling intrusion through an excavated area of the repository that connects the repository with pressurized brine in the Castile.

E2 = a single drilling intrusion through an excavated area of the repository that does not connect the repository with pressurized brine in the Castile.

E1E2 = two intrusions in the same waste panel, one of which is an E1 intrusion.

These intrusion scenarios capture the most important effects of drilling intrusions on the state of the repository: whether the repository is connected to a brine reservoir via a borehole and whether the borehole creates a possible upward release route.

The probability that no drilling event penetrates the excavated area during the 10,000-year interval can be computed from the frequency of drilling events that do penetrate. The rate of drilling events that penetrate the excavated area is $\lambda_d \times pEx_1$ where λ_d is the mean drilling frequency per year in the area enclosed by the berm (1.1505×10^{-2} yr^{-1}; Section PA-3.2), and pEx_1 is the fraction of area of the berm that is underlain by the excavated area (0.1934; Section PA-3.2.1). The probability of there being *n* drilling events in the 10,000-year history that penetrate the excavated area is:

$$\frac{1}{n!}e^{-\lambda_d \times pEx_1 \times 9900}(\lambda_d \times pEx_1 \times 9900)^n \text{ for } n = 0, 1, 2, 3, \ldots \quad \text{(PA.15)}$$

where 9,900 is the number of years in which drilling can occur after the institutional control period of 100 years. The probability of no drilling intrusions into an excavated area is given by evaluating Equation (PA.15) at *n* = 0:

$$\exp[-(1.1505\times10^{-2}) \times (0.1934) \times (9900)] = 2.71\times10^{-10} \quad \text{(PA.16)}$$

This probability is a lower bound on the probability that the repository is in an E0 state, as it does not account for the plugging pattern.

PA-4.0 Estimation of Releases

This section describes the mechanistic models used to estimate releases to the accessible environment for a specific future in the PA.

PA-4.1 Results for Specific Futures

The function $f\left(\mathbf{x}_{st,i}\middle|\mathbf{v}_{su,j}\right)$ estimates the radionuclide releases to the accessible environment associated with the possible future $\mathbf{x}_{st,i}$ and a vector $\mathbf{v}_{su,j}$ of possible parameter values. In practice, $f\left(\mathbf{x}_{st,i}\middle|\mathbf{v}_{su,j}\right)$ is quite complex and is constructed by the models implemented in computer programs used to simulate important processes and releases at the WIPP. For brevity, the notation indicating dependence on $\mathbf{v}_{su,j}$ is omitted in this section. The total release estimate is obtained by summing the contributions from each distinct release pathway, as defined in the following equation.

In the context of these models, $f\left(\mathbf{x}_{st,i}\right)$ has the form:

$$\begin{aligned} f\left(\mathbf{x}_{st,i}\right) = {} & f_C\left(\mathbf{x}_{st,i}\right) + f_{SP}\left[\mathbf{x}_{st,i},\, f_B\left(\mathbf{x}_{st,i}\right)\right] + f_{DBR}\left[\mathbf{x}_{st,i},\, f_B\left(\mathbf{x}_{st,i}\right)\right] \\ & + f_{MB}\left[\mathbf{x}_{st,i},\, f_B\left(\mathbf{x}_{st,i}\right)\right] + f_{DL}\left[\mathbf{x}_{st,i},\, f_B\left(\mathbf{x}_{st,i}\right)\right] + f_S\left[\mathbf{x}_{st,i},\, f_B\left(\mathbf{x}_{st,i}\right)\right] \\ & + f_{ST}\left[\, f_{MF}\left(\mathbf{x}_{st,0}\right),\, f_{NP}\left[\mathbf{x}_{st,i},\, f_B\left(\mathbf{x}_{st,i}\right)\right]\right] \end{aligned} \qquad \text{(PA.17)}$$

where

$\mathbf{x}_{st,i}$ ~ particular future under consideration

$\mathbf{x}_{st,0}$ ~ future involving no drilling intrusions but a mining event at the same time t_{min} as in $\boldsymbol{x}_{st,i}$

$f_C(\mathbf{x}_{st,i})$ ~ cuttings and cavings release to accessible environment for $\mathbf{x}_{st,i}$ calculated with CUTTINGS_S

$f_B(\mathbf{x}_{st,i})$ ~ two-phase flow in and around the repository calculated for $\mathbf{x}_{st,i}$ with BRAGFLO; in practice, $f_B(\mathbf{x}_{st,i})$ is a vector containing a large amount of information, including pressure and brine saturation in various geologic members

$f_{SP}\left[\mathbf{x}_{st,i},\, f_B\left(\mathbf{x}_{st,i}\right)\right]$ ~ spallings release to accessible environment for $\mathbf{x}_{st,i}$ calculated with the spallings model contained in DRSPALL and CUTTINGS_S; this calculation requires repository conditions calculated by $f_B(\mathbf{x}_{st,i})$ as input

$f_{DBR}\left[\mathbf{x}_{st,i}, f_B\left(\mathbf{x}_{st,i}\right)\right]$ ~ DBR to accessible environment for $\mathbf{x}_{st,i}$ also calculated with BRAGFLO; this calculation requires repository conditions calculated by $f_B(\mathbf{x}_{st,i})$ as input

$f_{MB}\left[\mathbf{x}_{st,i}, f_B\left(\mathbf{x}_{st,i}\right)\right]$ ~ release through anhydrite MBs to accessible environment for $\mathbf{x}_{st,i}$ calculated with NUTS; this calculation requires flows in and around the repository calculated by $f_B(\mathbf{x}_{st,i})$ as input

$f_{DL}\left[\mathbf{x}_{st,i}, f_B\left(\mathbf{x}_{st,i}\right)\right]$ ~ release through Dewey Lake to accessible environment for $\mathbf{x}_{st,i}$ calculated with NUTS; this calculation requires flows in and around the repository calculated by $f_B(\mathbf{x}_{st,i})$ as input

$f_S\left[\mathbf{x}_{st,i}, f_B\left(\mathbf{x}_{st,i}\right)\right]$ ~ release to land surface due to brine flow up a plugged borehole for $\mathbf{x}_{st,i}$ calculated with NUTS; this calculation requires flows in and around the repository calculated by $f_B(\mathbf{x}_{st,i})$ as input

$f_{MF}\left(\mathbf{x}_{st,0}\right)$ ~ flow field in the Culebra calculated for $\mathbf{x}_{st,0}$ with MODFLOW6; $\mathbf{x}_{st,0}$ is used as an argument to f_{MF} because drilling intrusions are assumed to cause no perturbations to the flow field in the Culebra

$f_{NP}\left[\mathbf{x}_{st,i}, f_B\left(\mathbf{x}_{st,i}\right)\right]$ ~ release to Culebra for $\mathbf{x}_{st,i}$ calculated with NUTS or PANEL as appropriate; this calculation requires flows in and around the repository calculated by $f_B(\mathbf{x}_{st,i})$ as input

$f_{ST}\left[f_{MF}\left(\mathbf{x}_{st,0}\right), f_{NP}\left[\mathbf{x}_{st,i}, f_B\left(\mathbf{x}_{st,i}\right)\right]\right]$ ~ groundwater transport release through Culebra to accessible environment calculated with SECOTP2D. This calculation requires MODFLOW6 results (i.e., $f_{MF}(\mathbf{x}_{st,0})$) and NUTS or PANEL results (i.e., $f_{NP}\left[\mathbf{x}_{st,i}, f_B\left(\mathbf{x}_{st,i}\right)\right]$) as input

The remainder of this section describes the mathematical structure of the mechanistic models that underlie the component functions of $f(\mathbf{x}_{st,i})$ in Equation (PA.17).

A two-step procedure is used to evaluate $f(\mathbf{x}_{st})$ for an arbitrary future $\mathbf{x}_{st}$. First, the component functions of f (described in this section) are evaluated for a set of preselected futures $\mathbf{x}_{st,k}$, as described in Section PA-6.3. The preselected futures implement the fundamental scenarios described in Section PA-2.2.2. Second, values of $f(\mathbf{x}_{st,k})$ for the preselected futures $\mathbf{x}_{st,k}$ are used to construct, by interpolation, a value of $f(\mathbf{x}_{st})$ for the arbitrary future $\mathbf{x}_{st}$. These constructions are described in Section PA-6.4.

For notational simplicity, the functions on the right-hand side of Equation (PA.17) are written with only $\mathbf{x}_{st}$ as an argument (e.g., $f_{SP}(\mathbf{x}_{st})$ is used instead of $f_{SP}[\mathbf{x}_{st}, f_B(\mathbf{x}_{st})]$). However, the underlying dependency on the other arguments is still present.

This chapter describes:

- two-phase flow in the vicinity of the repository as modeled by BRAGFLO (i.e., f_B) (Section PA-4.2);
- radionuclide mobilization in the repository as modeled by PANEL (Section PA-4.3);
- radionuclide transport in the vicinity of the repository as modeled by NUTS (i.e., f_{MB}, f_{DL}, f_S, f_{NP}) (Section PA-4.4);
- radionuclide transport in the vicinity of the repository as modeled by PANEL (i.e., f_{NP}) (Section PA-4.5);
- cuttings and cavings releases to the surface as modeled by CUTTINGS_S (i.e., f_C) (Section PA-4.6);
- spallings releases to the surface as modeled by DRSPALL and CUTTINGS_S (i.e., f_{SP}) (Section PA-4.7);
- DBRs to the surface as modeled by BRAGFLO (i.e., f_{DBR}) (Section PA-4.8);
- brine flow in the Culebra as modeled by MODFLOW6 (i.e., f_{MF}) (Section PA-4.9); and
- radionuclide transport in the Culebra as modeled by SECOTP2D (i.e., f_{ST}) (Section PA-4.10).

PA-4.2 Two-Phase Flow in the Salado: BRAGFLO

Quantifying the effects of gas and brine flow on radionuclide transport from the repository requires a two-phase (brine and gas) flow code. The two-phase flow code BRAGFLO is used to simulate gas and brine flow in and around the repository (WIPP Performance Assessment 2025). Additionally, the BRAGFLO code incorporates the effects of disposal room consolidation and closure, gas generation, and rock fracturing in response to gas pressure. This section describes the mathematical models on which BRAGFLO is based, the representation of the repository in the model, and the numerical techniques employed in the solution.

PA-4.2.1 Mathematical Description

Two-phase flow in the vicinity of the repository is represented by the following system of two conservation equations, two constraint equations, and three equations of state:

Gas Conservation

$$\nabla \cdot \left[\frac{\alpha \rho_g K_g k_{rg}}{\mu_g} \left(\nabla P_g + \rho_g g \nabla \mathrm{h} \right) \right] + \alpha q_g + \alpha q_{rg} = \alpha \frac{\partial \left(\phi \rho_g S_g \right)}{\partial t} \qquad \text{(PA.18)}$$

Brine Conservation

$$\nabla \cdot \left[\frac{\alpha \rho_b K k_{rb}}{\mu_b} \left(\nabla P_b + \rho_b g \nabla \mathrm{h} \right) \right] + \alpha q_b + \alpha q_{rb} = \alpha \frac{\partial \left(\phi \rho_b S_b \right)}{\partial t} \quad \text{(PA.19)}$$

Saturation Constraint

$$S_g + S_b = 1 \quad \text{(PA.20)}$$

Capillary Pressure Constraint

$$P_c = P_g - P_b = P_c(S_b) \quad \text{(PA.21)}$$

Gas Density

ρ_g (determined by Redlich-Kwong-Soave (RKS) equation of state; see Equation (PA.27)) (PA.22)

Brine Density

$$\rho_b = \rho_{b0} \exp[c_b(P_b - P_{b0})] \quad \text{(PA.23)}$$

Formation Porosity

$$\phi = \phi_0 \exp\left[c_\phi (P_b - P_{b0})\right] \quad \text{(PA.24)}$$

where

g = acceleration due to gravity (meters per second squared (m/s^2))

h = vertical distance from a reference location (m)

k_{rl} = relative permeability (dimensionless) to fluid *l*, *l* = *b* (brine), *g* (gas); see Section PA-4.2.2.1

P_c = capillary pressure in Pascals (Pa); see Section PA-4.2.2.1

P_l = pressure of fluid *l* (Pa)

q_{rl} = rate of production (or consumption, if negative) of fluid *l* due to chemical reaction (kilograms per cubic meter per second ($kg/m^3/s$))

q_l = rate of injection (or removal, if negative) of fluid *l* ($kg/m^3/s$)

S_l = saturation of fluid *l* (dimensionless)

t = time (s)

α = geometry factor (m)

ρ_l = density of fluid *l* (kg/m^3)

μ_l = viscosity of fluid *l* (Pa s)

ϕ = porosity (dimensionless)

ϕ_0 = reference (i.e., initial) porosity (dimensionless); see Section PA-4.2.2.2

P_{b0} = reference (i.e., initial) brine pressure (Pa), constant in Equation (PA.23) and spatially variable in Equation (PA.24)

ρ_0 = reference (i.e., initial) brine density (kg/m^3)

c_ϕ = pore compressibility (Pa^{-1}); see Section PA-4.2.2.2

c_b = brine compressibility (Pa^{-1})

K = permeability of the material (m^2), isotropic for PA (Howarth and Christian-Frear 1997); see Section PA-4.2.2.1

The conservation equations are valid in one (i.e., $\nabla = [\partial/\partial x]$), two (i.e., $\nabla = [\partial/\partial x, \partial/\partial y]$), and three (i.e., $\nabla = [\partial/\partial x, \partial/\partial y, \partial/\partial z]$) dimensions. In PA, the preceding system of equations is used to model two-phase fluid flow within the two-dimensional region shown in Figure PA-12.

The α term in Equation (PA.18) and Equation (PA.19) is a dimension-dependent geometry factor and is specified by:

α = area normal to flow direction in one-dimensional flow (i.e., $\Delta y \Delta z$; units = m^2)

= thickness normal to flow plane in two-dimensional flow (i.e., Δz; units = m)

= 1 in three-dimensional flow (dimensionless) (PA.25)

Figure PA-12 shows the generic CRA-2026 PA BRAGFLO grid, which is two-dimensional with 71 cells in the *x*-direction (horizontal) and 33 cells in the *y*-direction (vertical), for a total of 2,343 grid cells. Figure PA-13 shows the corresponding BRAGFLO grid indices. The grid is initially defined with 14 regions; that are subdivided and redefined as the repository evolves over time. Cell dimensions (Δx, Δy) vary across the grid to provide finer resolution in areas of interest, such as the waste panel and surrounding Salado, and coarser resolution in more distant regions. The *z*-dimension represents the out-of-plane thickness. Materials are assigned to grid cells from a set of defined material properties, with the assignment varying as repository conditions evolve over time.

In the two-dimensional geometry used by PA, α is the thickness of the modeled region normal to the flow plane, i.e., Δz in Figure PA-12. Thus, α is spatially dependent and increases with distance from the repository edge in both directions to account for the increasing pore volume through which fluid flows. This flaring (Day 2025, Figure 5) ensures that the total volume surrounding the repository is represented in the numerical grid. The methods used to determine α for BRAGFLO grids used in the WIPP PA were developed by Stein (2002).

The *h* term in Equation (PA.18) and Equation (PA.19) defines vertical distance from a reference point. In PA, this reference point is taken to be the center of MB 139 at the location of the shaft, which is the center of cell 1206 in Figure PA-13. Specifically, *h* is defined by:

$$h(x,y) = (x - x_{ref})\sin\theta + (y - y_{ref})\cos\theta \qquad \text{(PA.26)}$$

where θ is the inclination of the formation in which the point (*x*, *y*) is located. In PA, the Salado is modeled as having an inclination of 1 degree from north to south, and all other formations are modeled as being horizontal. Thus, θ = 1 degree for points within the Salado, and θ = 0 degrees otherwise. Treating the Salado as an inclined formation and treating the Castile, Castile brine reservoir, Rustler, and overlying units as horizontal creates discontinuities in the grid at the lower and upper boundaries of the Salado. However, this treatment does not create a computational problem, since the Salado is isolated from vertical flow; its upper boundary adjoins the impermeable Los Medaños Member (formerly referred to as the Unnamed Member) at the base of the Rustler, and its lower boundary adjoins the impermeable Castile.

Gas density is computed using the RKS equation of state, assuming the gas is pure H_2. For a pure gas, the RKS equation of state has the form (Walas 1985, pp. 43–54):

$$P_g = \frac{RT}{V-b} - \frac{a\alpha}{V(V+b)} \qquad \text{(PA.27)}$$

where

R = gas constant = 8.31451 Joules (J) mole (mol)$^{-1}$ K^{-1}

T = temperature (K) = 300.15 K (= 30 °C; 81 °F)

V = molar volume (m^3 mol^{-1})

a = $0.42747\, R^2 T^2_{crit}/P_{crit}$

b = $0.08664\, RT_{crit}/P_{crit}$

α = $[1 + (0.48508 + 1.55171\omega - 0.15613\omega^2)(1 - T_r^{0.5})]^2$

≈ $1.202\exp(-0.30288T_r)$ for H_2 (Graboski and Daubert 1979)

T_{crit} = critical temperature (K)

P_{crit} = critical pressure (Pa)

T_r = T / T_{crit} = reduced temperature

ω = acentric factor

= 0 for H_2 (Graboski and Daubert 1979)

In order to account for quantum effects in H_2, effective critical temperature and pressure values of T_{crit} = 43.6 K and P_{crit} = 2.047 × 10^6 Pa are used instead of the true values for these properties (Prausnitz 1969). Equation (PA.27) is solved for molar volume V. The gas density ρ_g then is given by:

$$\rho_g = \frac{M_{w,H_2}}{V} \quad \text{(PA.28)}$$

where M_{w,H_2} is the molecular weight of H_2 (i.e., 2.01588 × 10^{-3} kg/mol; see Weast 1969, p. B-26).

Brine density ρ_b is defined by Equation (PA.23), with ρ_{b0} = 1,220.0 kg/m^3 at a pressure of P_{b0} = 1.0132 × 10^5 Pa and c_b = 3.1 × 10^{-10} Pa^{-1} (Roberts 1996, Roberts 1996a). Porosity, ϕ, is used as defined by Equation (PA.24) with two exceptions: in the repository (see Section PA-4.2.4) and in the DRZ and MBs subsequent to fracturing (see Section PA-4.2.5). The values of ϕ_0 and c_ϕ used in conjunction with Equation (PA.24) are listed in Table PA-5. The reference pressure P_{b0} in Equation (PA.24) is spatially variable and corresponds to the initial pressures $P_b(x, y, -5)$ (here, −5 means at time equal to −5 years; see Section PA-4.2.3). The gas and brine viscosities μ_g and μ_b in Equation (PA.18) and Equation (PA.19) are assumed to have values of μ_g = 8.93 × 10^{-6} Pa s (H2:VISCO; see Vargaftik 1975) and μ_b = 2.1 × 10^{-3} Pa s (BRINESAL:VISCO; see McTigue 1993).

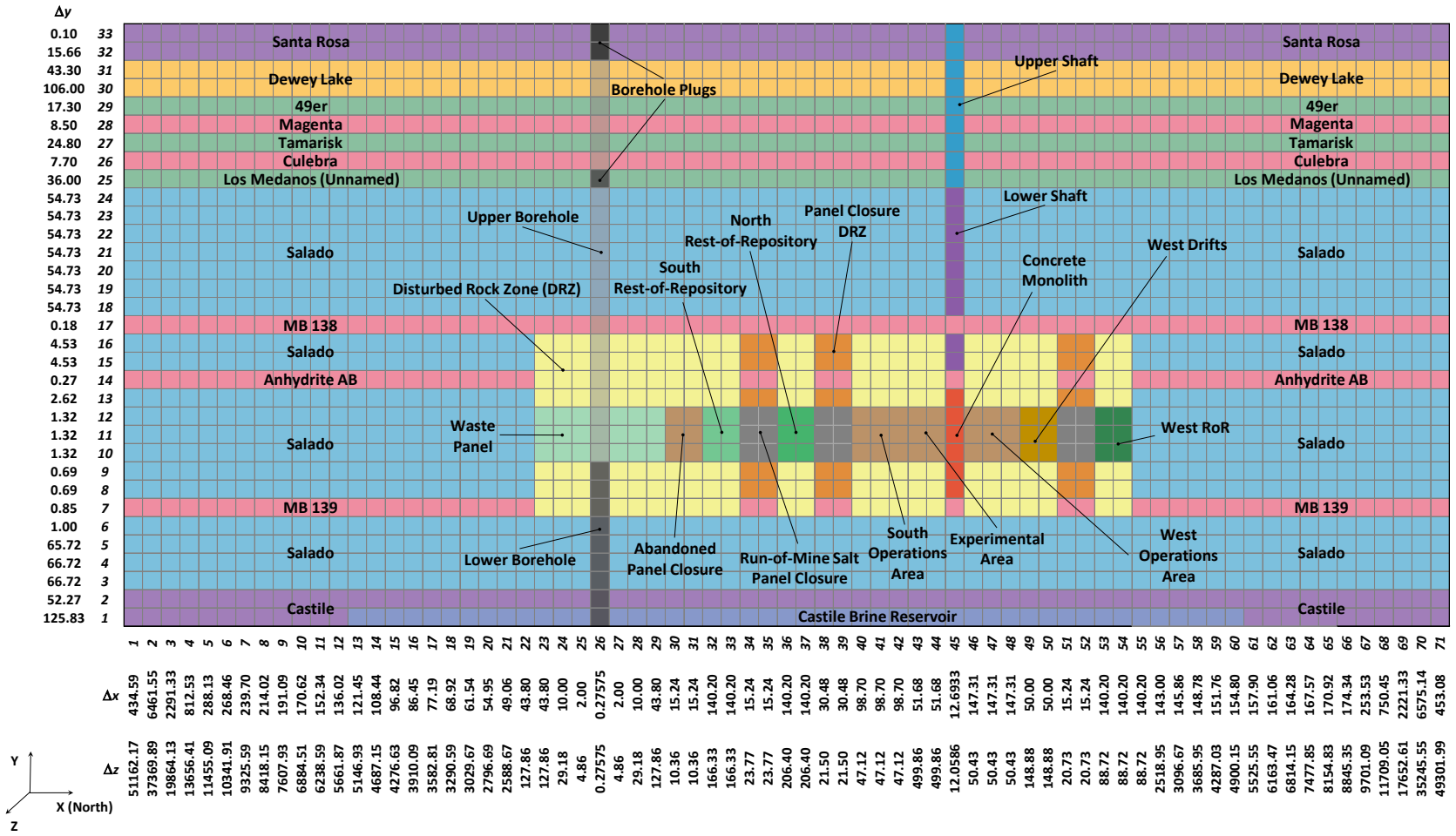


Figure PA-12. Generic CRA-2026 PA BRAGFLO grid with modeled area descriptions (Δx, Δy, and Δz dimensions in meters)

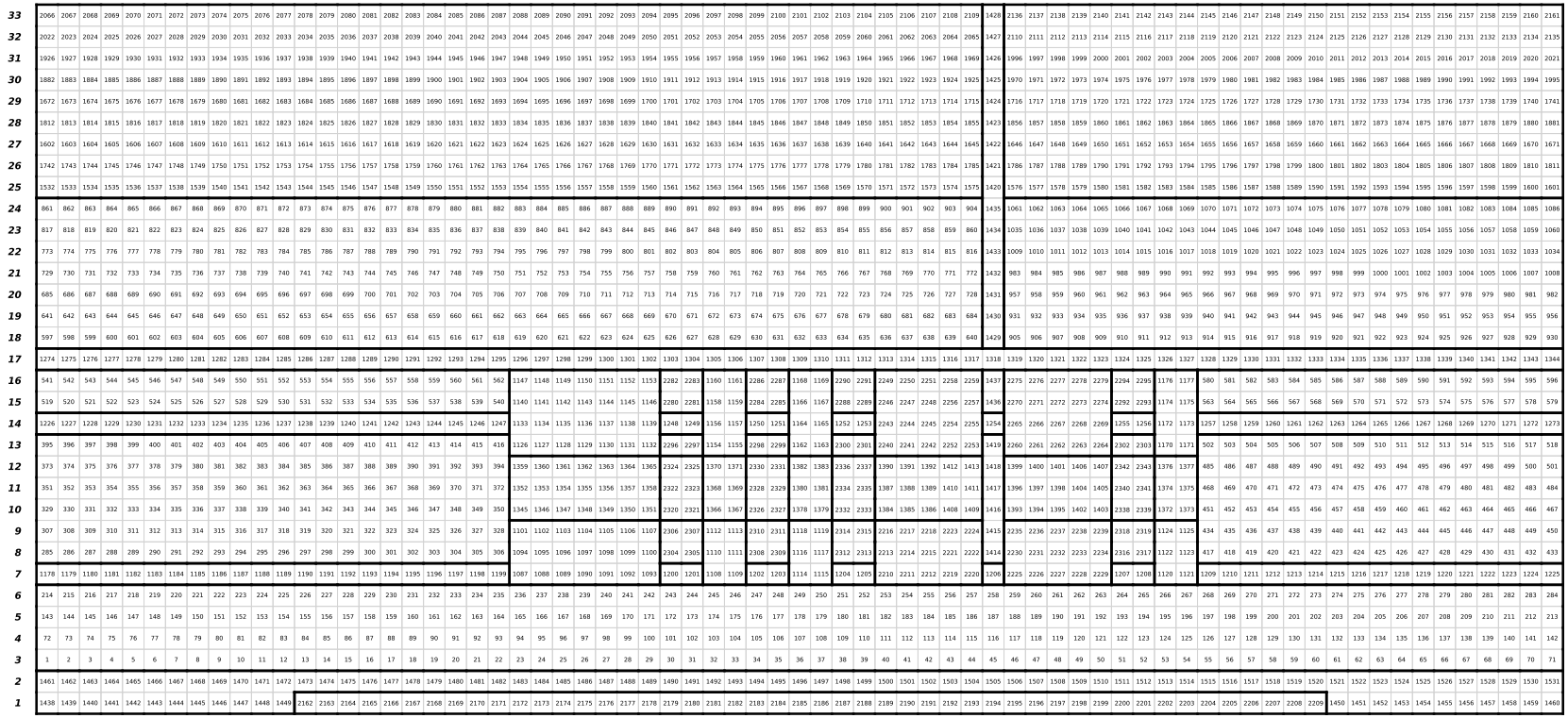


Figure PA-13. BRAGFLO Grid Indices and Cell Numbers

PA-4.2.2 Material Properties

Material properties are assigned to each cell in the grid in Figure PA-12. Most properties are constants, and time-varying property values are implemented by changing the material properties at defined simulation times. For example, in scenarios involving a borehole, the properties of grid cells comprising the borehole are changed from those of geologic strata to those of the borehole materials, at the time of the simulated intrusion. Figures PA-14 through PA-23 depict the material maps used by BRAGFLO for the E0, E1, E2, and E1E2 scenarios described in PA-3.4.

PA-4.2.2.1 Permeability and Capillary Pressure

For the brine conservation equation (Equation PA.19), the intrinsic permeability of the material is used. For the gas conservation equation (Equation PA.18), the permeability K is modified to account for the Klinkenberg effect (Klinkenberg 1941). Specifically:

$$K_g = 1 + \frac{bK^a}{P_g} \tag{PA.29}$$

where a and b are gas and formation-dependent constants. Values of $a = -0.3410$ and $b = 0.2710$ were determined from data obtained for MB 139 (Christian-Frear 1996) and used for all regions in Figure PA-12.

In the solution of Equations (PA.18) through (PA.24), saturations S_b and S_g are functions of location and time. Thus, capillary pressure P_c, and relative permeabilities k_{rb}, and k_{rg} are functions of the form $P_c(x, y, t)$, $k_{rb}(x, y, t)$, and $k_{rg}(x, y, t)$. In the computational implementation of the solution of the preceding equations, flow of phase l out of a computational cell cannot occur when $S_l(x, y, t) \leq S_{lr}(x, y, t)$, where S_{lr} denotes the residual saturation for phase l. The values used for S_{lr}, $l = b, g$ are summarized in Table PA-5.

The primary model used in PA for capillary pressure P_c, and relative permeability k_{rl}, is a modification of the Brooks-Corey model (Brooks and Corey 1964). In this model, P_c, k_{rb}, and k_{rg} are defined by:

$$P_c = \left(\min \left[\frac{P_t(k)}{S_{e2}^{1/\lambda}} \right], P_{c,max} \right) \tag{PA.30}$$

$$k_{rb} = S_{e1}^{(2+3\lambda)/\lambda} \tag{PA.31}$$

$$k_{rg} = (1 - S_{e2})^2 \left(1 - S_{e2}^{(2+\lambda)/\lambda} \right) \tag{PA.32}$$

where

λ = pore distribution parameter (dimensionless)

$P_t(k)$ = capillary threshold pressure (Pa) as a function of intrinsic permeability *k* (Webb 1992)

$$= ak^{\eta} \quad \text{(PA.33)}$$

S_{e1} = effective brine saturation (dimensionless) without correction for residual gas saturation

$$= {(S_b - S_{br})}/{(1 - S_{br})} \quad \text{(PA.34)}$$

S_{e2} = effective brine saturation (dimensionless) with correction for residual gas saturation

$$= {(S_b - S_{br})}/{(1 - S_{gr} - S_{br})} \quad \text{(PA.35)}$$

The values used for λ, a, η, S_{br}, S_{gr}, and k are summarized in Table PA-5. The statement that the Brooks-Corey model is in use means that P_c, k_{rb}, and k_{rg} are defined by Equation (PA.30), Equation (PA.31), and Equation (PA.32).

In the anhydrite MBs, either the Brooks-Corey model or the van Genuchten-Parker model is used as determined by the subjectively uncertain parameter S_MB139:RELP_MOD (Feng and Kicker (2025a), Table 3). In the van Genuchten-Parker model, P_c, k_{rb}, and k_{rg} are defined by (van Genuchten 1978):

$$P_c = \min\left[\max\left\{P_{VGP}\left(S_{e2}^{-\frac{1}{m}} - 1\right)^{1-m}, P_{c,min}\right\}, P_{c,max}\right] \quad \text{(PA.36)}$$

$$k_{rb} = S_{e1}^{1/2}\left[1 - \left(1 - S_{e1}^{1/m}\right)^{m}\right]^2 \quad \text{(PA.37)}$$

$$k_{rg} = (1 - S_{e2})^{1/2}\left(1 - S_{e2}^{1/m}\right)^{2m} \quad \text{(PA.38)}$$

where $m = \lambda/(1+\lambda)$ and the capillary pressure parameter P_{VGP} is determined by requiring that the capillary pressures defined in Equation (PA.30) and Equation (PA.36) are equal at an effective brine saturation of S_{e2} = 0.5 (Webb 1992), or:

$$P_{VGP} = P_t 2^{1/\lambda}\left(0.5^{-1/m} - 1\right)^{m-1} \quad \text{(PA.39).}$$

The van Genuchten-Parker model is only used for the anhydrite MBs in the Salado and uses the same values for λ, S_{br}, and S_{gr} as the Brooks-Corey model (Table PA-5).

Capillary pressure, P_c, for both the van Genuchten-Parker and Brooks-Corey models becomes unbounded as brine saturation, S_b, approaches the residual brine saturation, S_{br}. To avoid unbounded values, P_c is capped at $P_{c,max} = 1 \times 10^8$ Pa in selected materials (Table PA-6). For van Genuchten-Parker, P_c is bounded below at $P_{c,min}$ = 101,325 Pa in the anhydrite MBs (Table PA-6).

An open cavity model (RELP_MOD = 11) is used for the open borehole (BH_OPEN material, Table PA-8) in the first 200 years after a drilling intrusion, open cavities (CAVITY_1,…, CAVITY_5) for the −5 to 0 year portion of the simulation (see Section PA-4.2.3), and for the abandoned panel closure, south and west operations areas, experimental area and west drifts (t = 0 to 10,000 years) which are modeled without a time-dependent creep closure:

$$k_{rl} = 0 \text{ for } S_l < S_{lr} \quad \text{(PA.40)}$$

$$k_{rl} = {(S_l - S_{lr})}/{tol} \text{ for } S_{rl} \le S_l \le S_{rl} + tol \quad \text{(PA.41)}$$

$$k_{rl} = 1 \;\; for \;\; S_l > S_{rl} + tol \quad \text{(PA.42)}$$

where *l* = gas or brine. The transition width *tol* is defined in BRAGFLO as:

$$tol = C_{tol}(1 - S_{lr} - S_{gr})$$

where S_{lr} and S_{gr} are the residual brine and gas saturations, respectively, and C_{tol} is a dimensionless scaling factor equal to 0.01 in the PA. Thus, the width of the linear transition region depends on the available mobile saturation $(1 - S_{lr} - S_{gr})$, and the slope of the transition is $1/tol$. Thus, the relative permeabilities are approximately 1 for saturations away from the residual saturation and the capillary pressure is always zero.

PA-4.2.2.2 Initial Porosity and Pore Compressibility

Values for initial porosity, ϕ_0, and pore compressibility, c_ϕ, (Equation (PA.24)) are given in Table PA-5. Initial porosity ϕ_0 for the DRZ is a function of the uncertain parameter for initial halite porosity ϕ_{0H} (S_HALITE:POROSITY; see Table PA-17) and is given by Martell (1996a) and Bean et al. (1996), Section 4:

$$\phi_0 = \phi_{0H} + 0.0029 \quad \text{(PA.43)}$$

Pore compressibility c_ϕ for halite is computed from halite bulk compressibility c_r (S_HALITE:COMP_RCK; see Table PA-17) and halite initial porosity ϕ_{0H} by:

$$c_\phi = {c_r}/{\phi_{0H}} \quad \text{(PA.44)}$$

Initial porosity ϕ_0 and pore compressibility of the Castile brine reservoir are calculated as described in Section PA-4.2.11.

PA-4.2.2.3 Material Maps

Material maps associate material properties with each cell in the computational grid. Figure PA-12 provides a summary of regions in the grid. Figures PA-14 through PA-23 detail the scenario- and time-dependent assignments of materials.

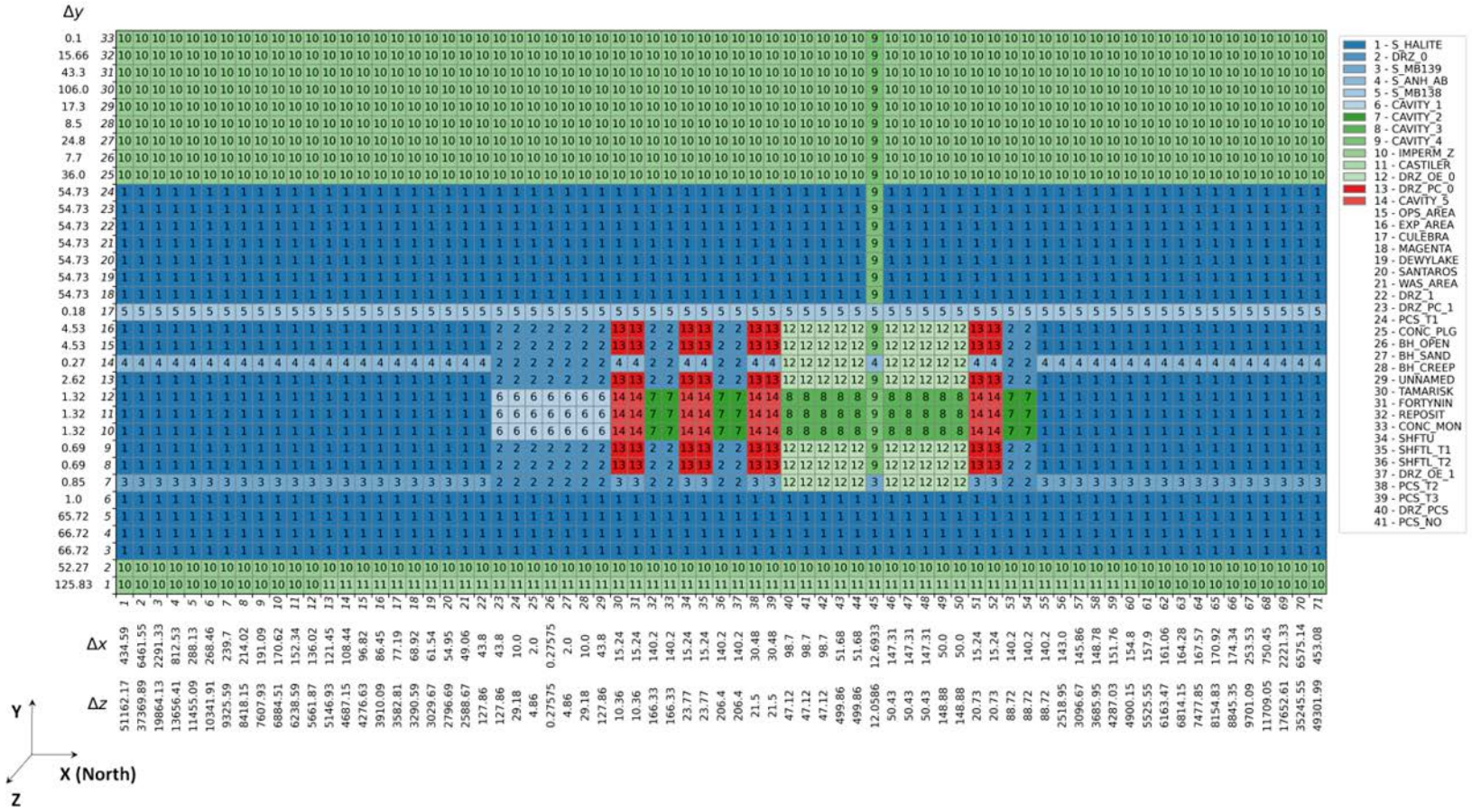


Figure PA-14. CRA-2026 PA BRAGFLO Grid and Material Map; Years −5 to 0 (all scenarios) (Δx, Δy, and Δz Dimensions in Meters)

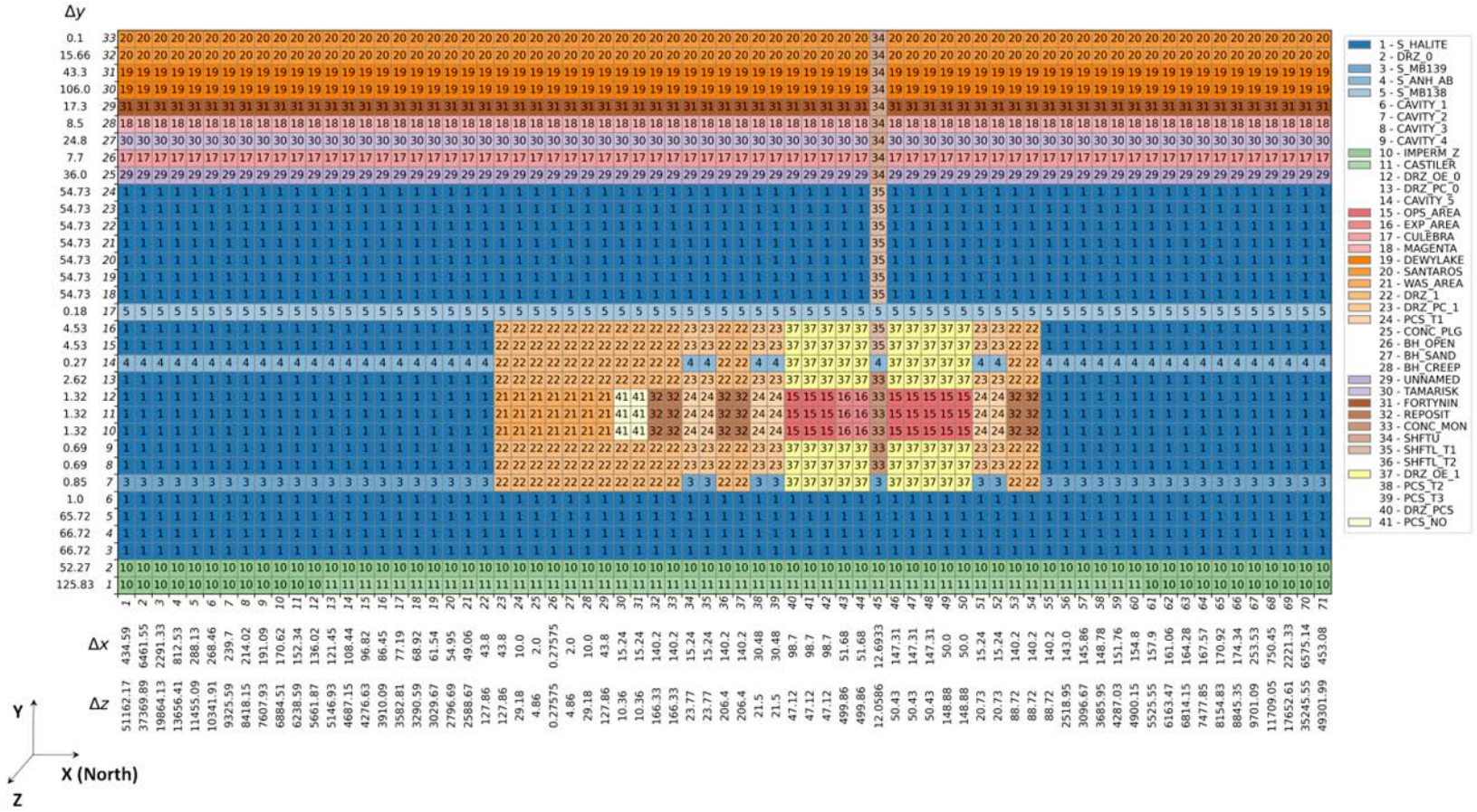


Figure PA-15. CRA-2026 PA BRAGFLO Grid and Material Map; Years 0 to 100 (all scenarios) (Δx, Δy, and Δz Dimensions in Meters)

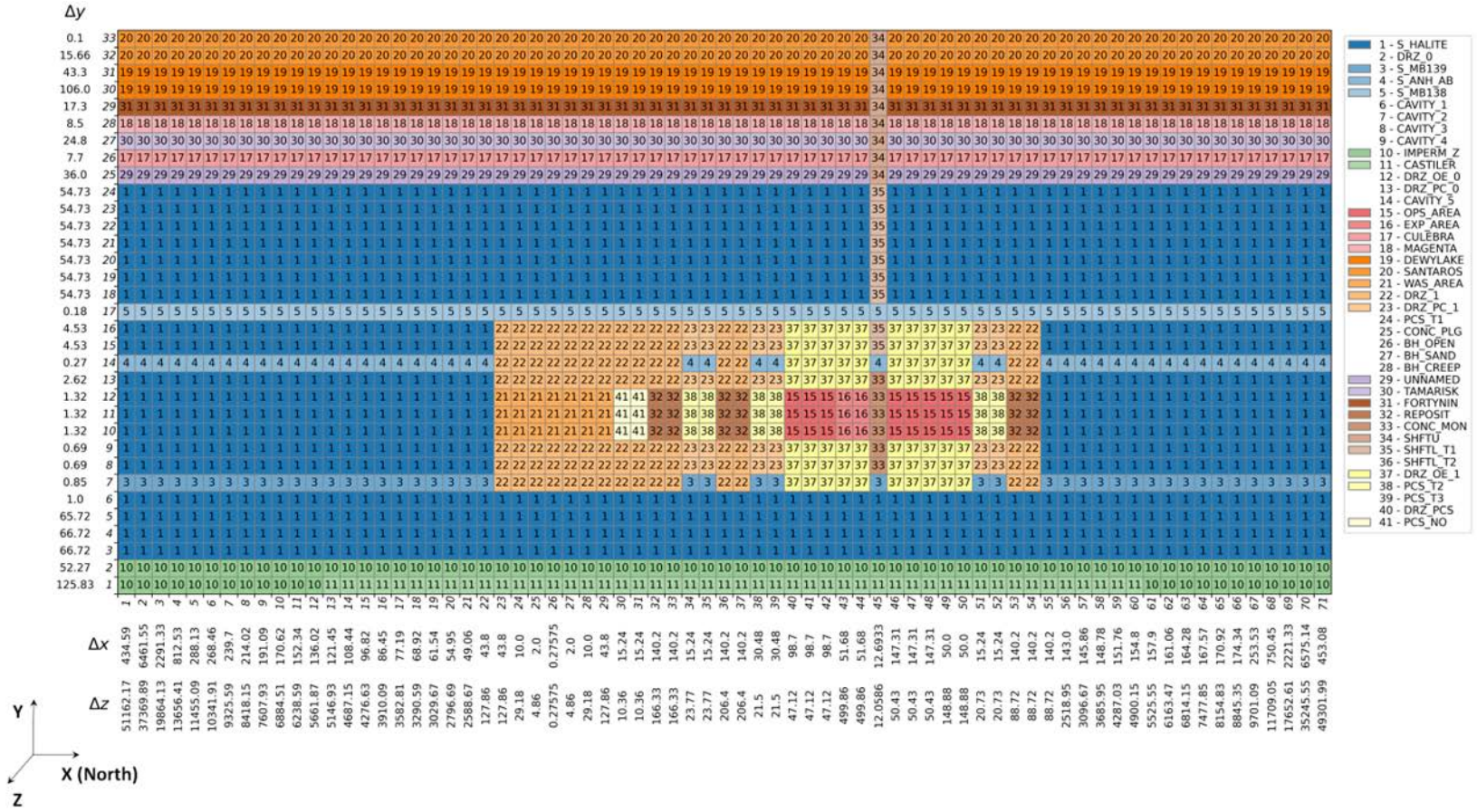


Figure PA-16. CRA-2026 PA BRAGFLO Grid and Material Map; Years 100 to 200 (all scenarios) (Δx, Δy, and Δz Dimensions in Meters).

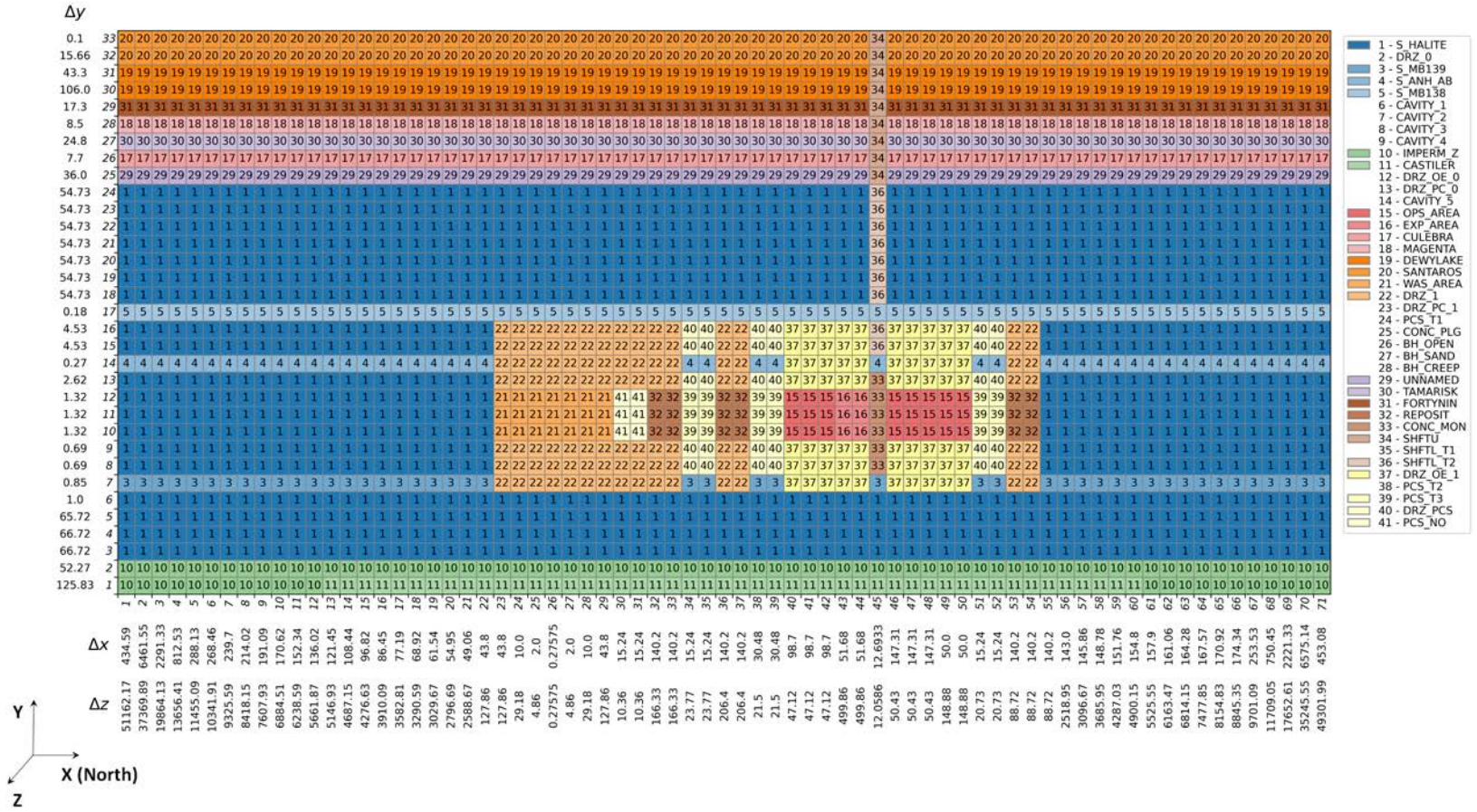


Figure PA-17. CRA-2026 PA BRAGFLO Grid and Material Map; Years 200 to 10,000 (E0 scenario), Years 200 to First Intrusion Time (E1, E2, and E1E2 scenario) (Δx, Δy, and Δz Dimensions in Meters).

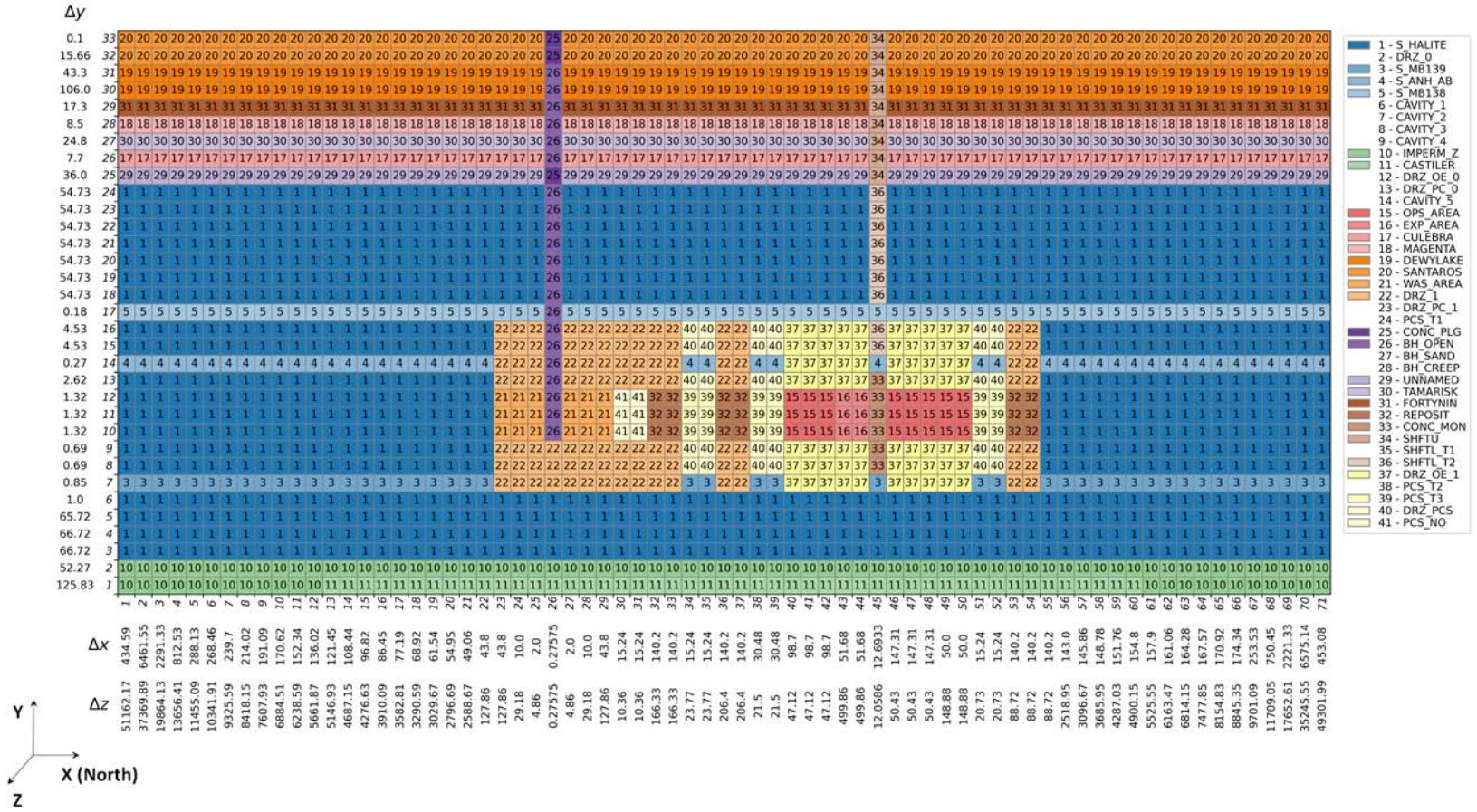


Figure PA-18. CRA-2026 PA BRAGFLO Grid and Material Map; From E2 Intrusion to 200 Years After Intrusion (E2 and E1E2 scenario) (Δx, Δy, and Δz Dimensions in Meters).

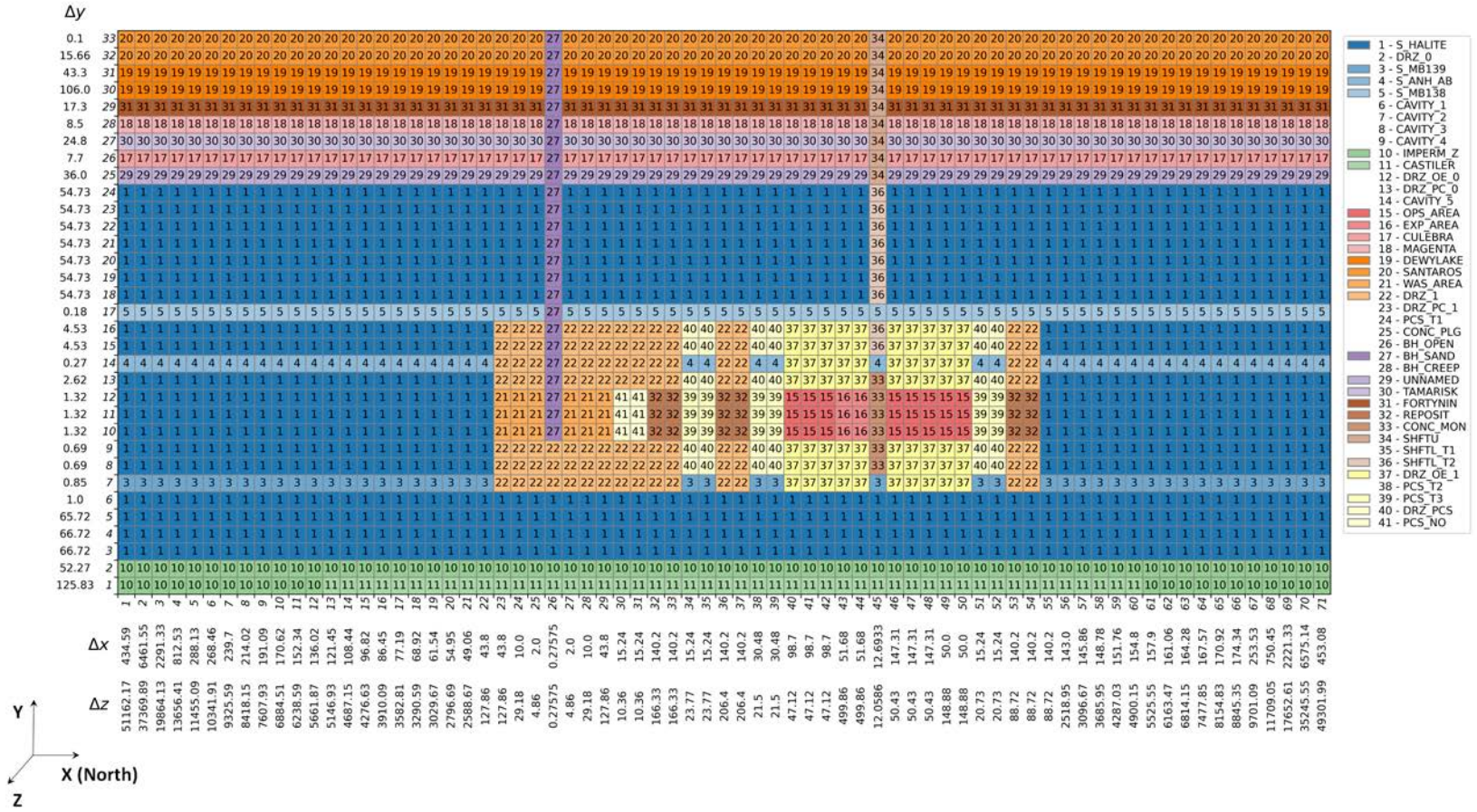


Figure PA-19. CRA-2026 PA BRAGFLO Grid and Material Map; From 200 Years After E2 Intrusion to 10,000 Years (E2 scenario), From 200 Years After E2 Intrusion to E1 Intrusion (E1E2 scenario) (Δx, Δy, and Δz Dimensions in Meters).

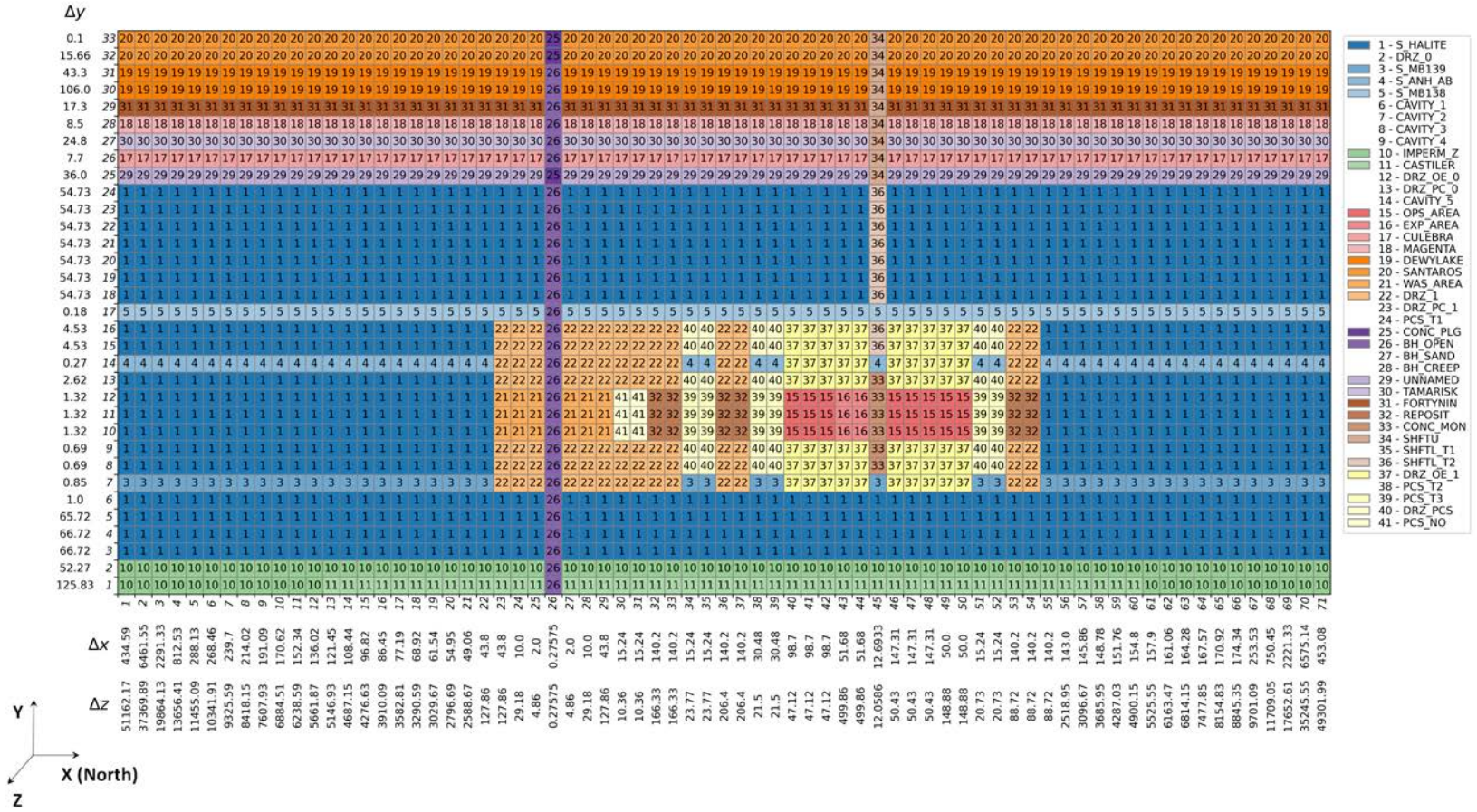


Figure PA-20. CRA-2026 PA BRAGFLO Grid and Material Map; From E1 Intrusion to 200 Years After E1 Intrusion (E1 scenario) (Δx, Δy, and Δz Dimensions in Meters).

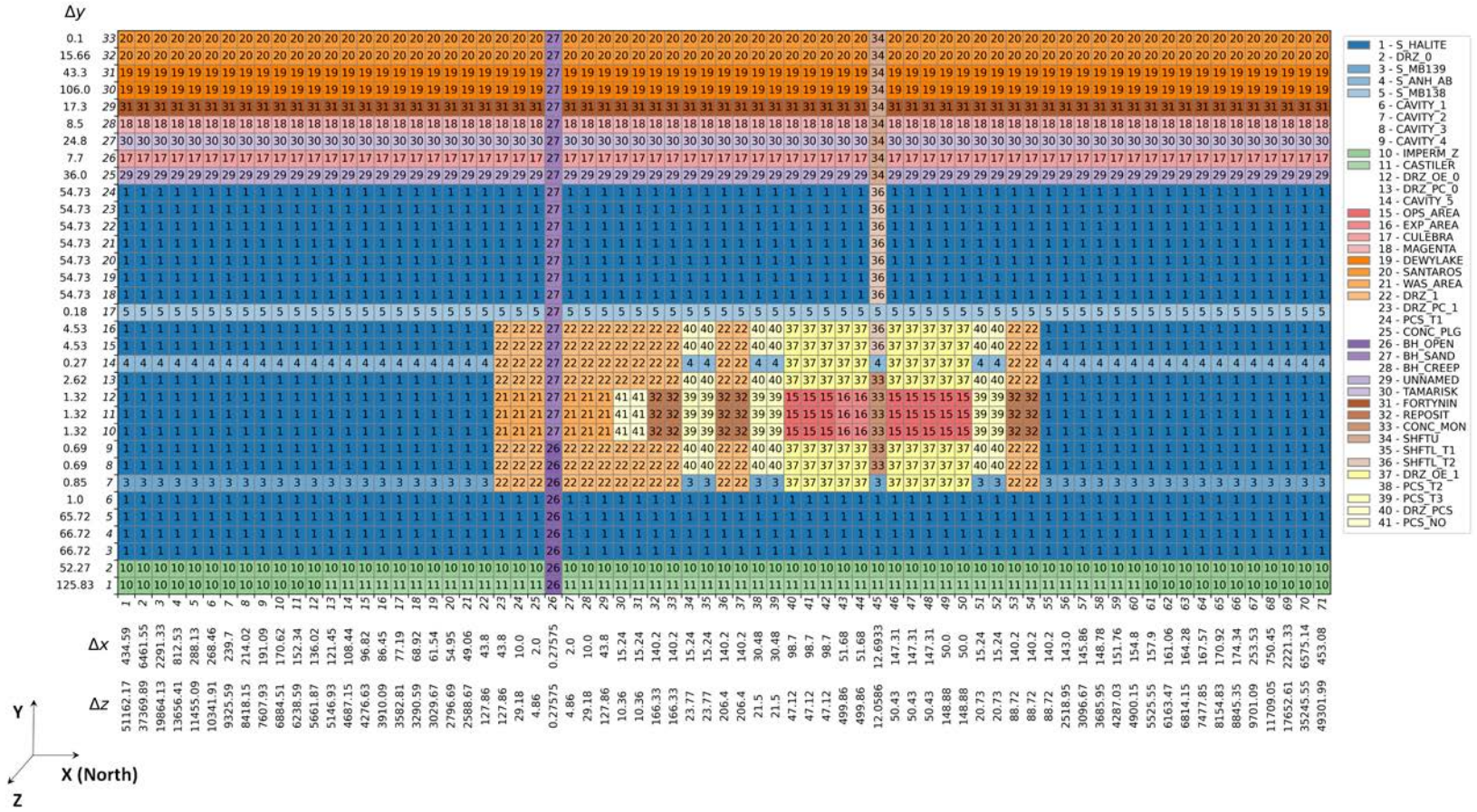


Figure PA-21. CRA-2026 PA BRAGFLO Grid and Material Map; From E1 Intrusion to 200 Years After E1 Intrusion (E1E2 scenario) (Δx, Δy, and Δz Dimensions in Meters).

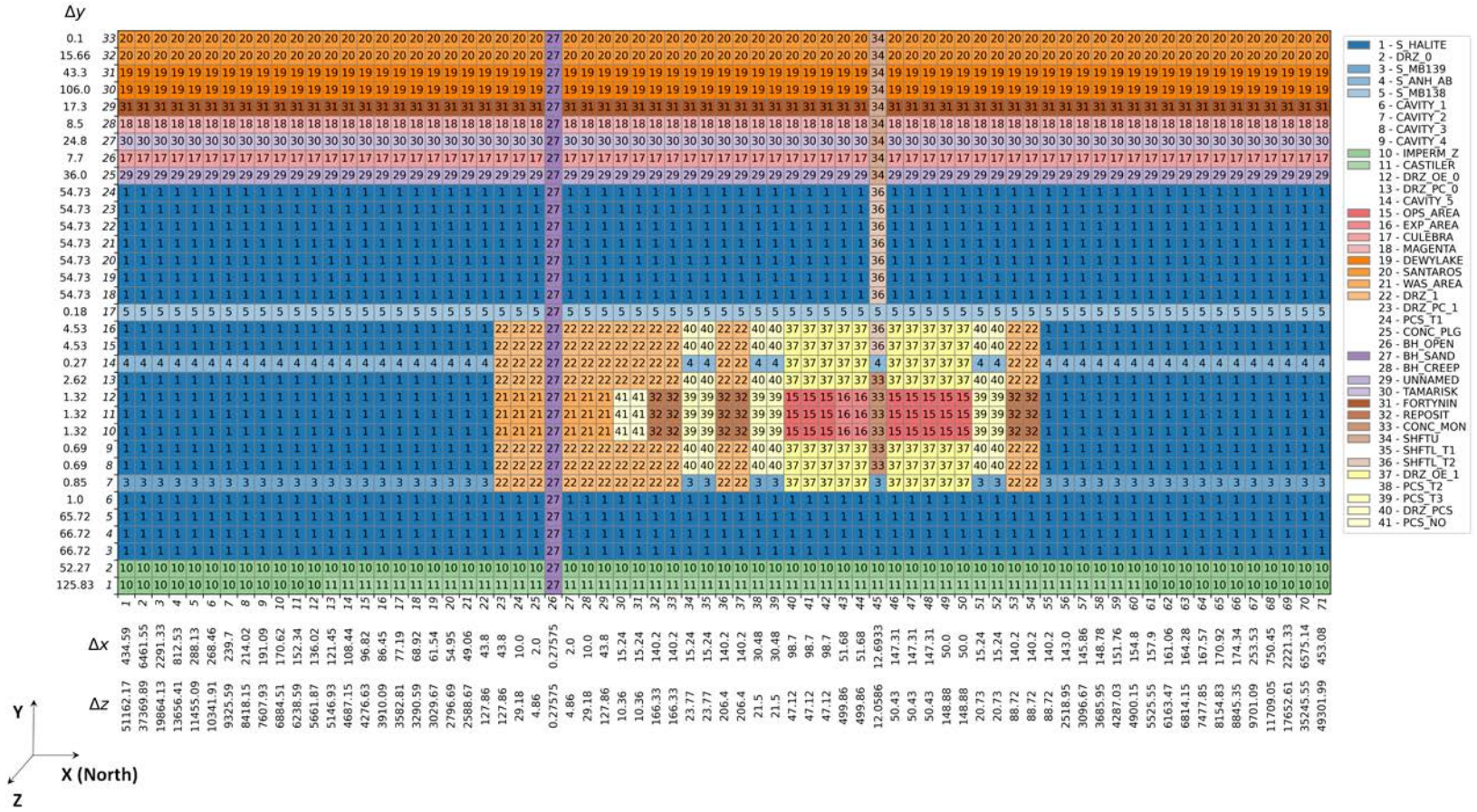


Figure PA-22. CRA-2026 PA BRAGFLO Grid and Material Map; From 200 Years After E1 Intrusion to 1,200 Years After E1 Intrusion (E1 and E1E2 scenario) (Δx, Δy, and Δz Dimensions in Meters).

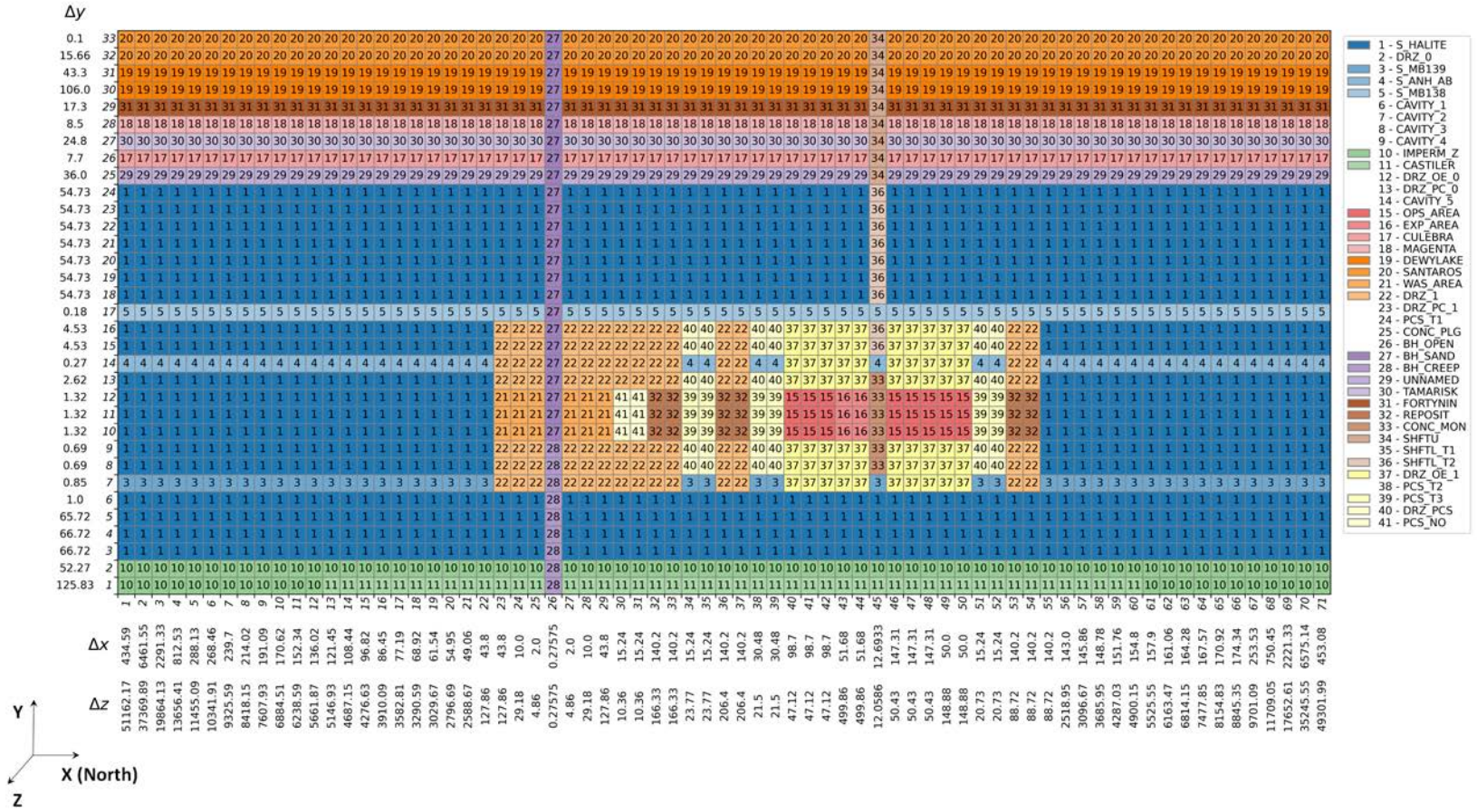


Figure PA-23. CRA-2026 PA BRAGFLO Grid and Material Map; From 1,200 Years After E1 Intrusion to 10,000 Years (E1 and E1E2 scenario) (Δx, Δy, and Δz Dimensions in Meters).

PA-4.2.2.4 Two-Phase Flow Parameters

This section summarizes the two-phase flow parameters used to simulate gas and brine movement within the repository and surrounding formations. These parameters govern the relationships among phase pressures, saturations, and relative permeabilities and are implemented through constitutive models for capillary pressure and relative permeability. Table PA-5 summarizes the parameter values used in the CRA-2026 PA, and Table PA-6 identifies the functional forms of the relative permeability and capillary pressure models applied to the various materials.

Table PA-5. Parameter Values Used in Representation of Two-Phase Flow

Material Name	Material Description	Brooks-Corey Pore Distribution (PORE_DIS)[a] l	Threshold Pressure Linear Parameter (PCT_A)[a] a	Threshold Pressure Exponential Parameter (PCT_EXP)[a] h	Residual Brine Saturation (SAT_RBRN)[a] S_{br}	Residual Gas Saturation (SAT_RGAS)[a] S_{gr}	Porosity (POROSITY)[a] f_0	Pore Compressibility C_ϕ, Pa^{-1}	Intrinsic Permeability (PRMX_LOG)[a] k, m^2
S_HALITE	Salado halite, intact	0.7	0.56	−0.346	0.3	0.2	HALPOR[b]	f(HALCROCK, HALPOR)[d]	10^x, x = HALPRM[b]
IMPERM_Z	Impermeable zones	0.7	0.0	0.0	0.0	0.0	0.005	0.0	1.0×10^{-35}
CASTILER	Castile Brine Reservoir	0.7	0.56	−0.346	0.2	0.2	f(BPCOMP)[g]	1.25628×10^{-8}	10^x, x = BPPRM[b]
CULEBRA	Culebra Member of Rustler	0.6436	0.26	−0.348	0.08363	0.07711	0.151	6.622517×10^{-10}	9.59401×10^{-15}
MAGENTA	Magenta Member of Rustler	0.6436	0.26	−0.348	0.08363	0.07711	0.138	1.915942×10^{-9}	2.09894×10^{-15}
DEWYLAKE	Dewey Lake Redbeds	0.6436	0.0	0.0	0.08363	0.07711	0.143	6.993007×10^{-8}	5.01187×10^{-17}
SANTAROS	Santa Rosa Formation	0.6436	0.0	0.0	0.08363	0.07711	0.175	5.714286×10^{-8}	1.0×10^{-10}
UNNAMED	Los Medaños Member of Rustler	0.7	0.0	0.0	0.2	0.2	0.181	0.0	1.0×10^{-35}

Material Name	Material Description	Brooks-Corey Pore Distribution (PORE_DIS)[a] l	Threshold Pressure Linear Parameter (PCT_A)[a] a	Threshold Pressure Exponential Parameter (PCT_EXP)[a] h	Residual Brine Saturation (SAT_RBRN)[a] S_{br}	Residual Gas Saturation (SAT_RGAS)[a] S_{gr}	Porosity (POROSITY)[a] f_0	Pore Compressibility C_ϕ, Pa^{-1}	Intrinsic Permeability (PRMX_LOG)[a] k, m^2
TAMARISK	Tamarisk Member of Rustler	0.7	0.0	0.0	0.2	0.2	0.064	0.0	1.0×10^{-35}
FORTYNIN	Forty-niner Member of Rustler	0.7	0.0	0.0	0.2	0.2	0.082	0.0	1.0×10^{-35}
S_MB138	Salado marker bed 138	ANHBCEXP[b]	0.26	−0.348	ANRBSAT[b]	ANRGSSAT[b]	0.011	f(ANHCOMP)[d]	10^x, x = ANHPRM[b]
S_ANH_AB	Salado anhydrite beds A and B	ANHBCEXP[b]	0.26	−0.348	ANRBSAT[b]	ANRGSSAT[b]	0.011	f(ANHCOMP)[d]	10^x, x = ANHPRM[b]
S_MB139	Salado marker bed 139	ANHBCEXP[b]	0.26	−0.348	ANRBSAT[b]	ANRGSSAT[b]	0.011	f(ANHCOMP)[d]	10^x, x = ANHPRM[b]
CAVITY_1	Waste panel, −5 to 0 yr	NA[e]	NA[e]	NA[e]	0.0	0.0	1.0	0.0	1.0×10^{-10}
WAS_AREA	Waste panel, 0 to 10,000 yr	2.89	0.0	0.0	WRBRNSAT[b]	WRGSSAT[b]	0.848[f]	0.0	2.4×10^{-13}
CAVITY_2	Rest-of-Repository waste panels, −5 to 0 yr	NA[e]	NA[e]	NA[e]	0.0	0.0	1.0	0.0	1.0×10^{-10}
REPOSIT	Rest-of-Repository waste panels, 0 to 10,000 yr	2.89	0.0	0.0	WRBRNSAT[b]	WRGSSAT[b]	0.848[f]	0.0	2.4×10^{-13}
CAVITY_3	Operations and experimental areas, −5 to 0 yr	NA[e]	NA[e]	NA[e]	0.0	0.0	1.0	0.0	1.0×10^{-10}
OPS_AREA	Operations area, 0 to 10,000 yr	NA[e]	NA[e]	NA[e]	0.0	0.0	0.18	0.0	1.0×10^{-11}
EXP_AREA	Experimental area, 0 to 10,000 yr	NA[e]	NA[e]	NA[e]	0.0	0.0	0.18	0.0	1.0×10^{-11}

Material Name	Material Description	Brooks-Corey Pore Distribution (PORE_DIS)[a] l	Threshold Pressure Linear Parameter (PCT_A)[a] a	Threshold Pressure Exponential Parameter (PCT_EXP)[a] h	Residual Brine Saturation (SAT_RBRN)[a] S_{br}	Residual Gas Saturation (SAT_RGAS)[a] S_{gr}	Porosity (POROSITY)[a] f_0	Pore Compressibility C_ϕ, Pa^{-1}	Intrinsic Permeability (PRMX_LOG)[a] k, m^2
CAVITY_4	Shaft, -5 to 0 yr	NA[e]	NA[e]	NA[e]	0.0	0.0	1.0	0.0	1.0×10^{-10}
CONC_MON	Concrete monolith portion of shaft seals, 0 to 10,000 yr	0.94	0.0	0.0	SHURBRN[b]	SHURGAS[b]	0.05	1.2×10^{-9}	1.0×10^{-14}
SHFTU	Upper portion of shaft seals, 0 to 10,000 yr	CONBCEXP[b]	0.0	0.0	SHURBRN[b]	SHURGAS[b]	0.291	2.05×10^{-8}	10^x, x = SHUPRM[b]
SHFTL_T1	Lower portion of shaft seals, 0 to 200 yr	CONBCEXP[b]	0.0	0.0	SHURBRN[b]	SHURGAS[b]	0.113	4.28×10^{-9}	10^x, x = SHLPRM1[b]
SHFTL_T2	Lower portion of shaft seals, 200 to 10,000 yr	CONBCEXP[b]	0.0	0.0	SHURBRN[b]	SHURGAS[b]	0.113	4.28×10^{-9}	10^x, x = SHLPRM2[b]
CAVITY_5	Panel closures, −5 to 0 yr	NA[e]	NA[e]	NA[e]	0.0	0.0	1.0	0.0	1.0×10^{-10}
PCS_T1	Panel closures, 0 to 100 yr	T1PDIS[b]	0.0	0.0	T1SRBRN [b]	T1SRGAS [b]	T1POROS[b]	f(T1POROS)[b, d]	10^x, x = T1PRMX[b]
PCS_T2	Panel closures, 100 to 200 yr	T1PDIS[b]	0.0	0.0	T1SRBRN [b]	T1SRGAS [b]	T2POROS[b]	f(T2POROS)[b, d]	See Equation (PA.58)
PCS_T3	Panel closures, 200 to 10,000 yr	T1PDIS[b]	0.0	0.0	T1SRBRN [b]	T1SRGAS [b]	T3POROS[b]	f(T3POROS)[b, d]	See Equation (PA.59)
PCS_NO	Abandoned panel closure areas, 0 to 10,000 yr	NA[e]	NA[e]	NA[e]	0.0	0.0	0.18	0.0	1.0×10^{-11}
DRZ_0	Disturbed rock zone, −5 to 0 yr	0.7	0.0	0.0	0.0	0.0	f(HALPOR) [b, c]	7.41×10^{-10} / f(HALPOR) [b, c]	1.0×10^{-17}

Material Name	Material Description	Brooks-Corey Pore Distribution (PORE_DIS)[a] l	Threshold Pressure Linear Parameter (PCT_A)[a] a	Threshold Pressure Exponential Parameter (PCT_EXP)[a] h	Residual Brine Saturation (SAT_RBRN)[a] S_{br}	Residual Gas Saturation (SAT_RGAS)[a] S_{gr}	Porosity (POROSITY)[a] f_0	Pore Compressibility C_ϕ, Pa^{-1}	Intrinsic Permeability (PRMX_LOG)[a] k, m^2
DRZ_1	Disturbed rock zone, 0 to 10,000 yr	0.7	0.0	0.0	0.0	0.0	f(HALPOR) [b, c]	7.41×10^{-10} / f(HALPOR) [b, c]	10^x, x = DRZPRM[b]
DRZ_PC_0	Disturbed rock zone around panel closures, −5 to 0 yr	0.7	0.0	0.0	0.0	0.0	f(HALPOR) [b, c]	7.41×10^{-10} / f(HALPOR) [b, c]	1.0×10^{-17}
DRZ_PC_1	Disturbed rock zone around panel closures, 0 to 200 yr	0.7	0.0	0.0	0.0	0.0	f(HALPOR) [b, c]	7.41×10^{-10} / f(HALPOR) [b, c]	10^x, x = DRZPRM[b]
DRZ_PCS	Disturbed rock zone around panel closures, 200 to 10,000 yr	0.7	0.0	0.0	0.0	0.0	f(HALPOR)[b, c]	7.41×10^{-10} / f(HALPOR) [b, c]	10^x, x = min(DRZPRM[b], DRZPCPRM[b])
DRZ_OE_0	Disturbed rock zone around operations and experimental areas, -5 to 0 yr	0.7	0.0	0.0	0.0	0.0	f(HALPOR)[b, c]	7.41×10^{-10} / f(HALPOR) [b, c]	1.0×10^{-17}
DRZ_OE_1	Disturbed rock zone around operations and experimental areas, 0 to 10,000 yr	0.7	0.0	0.0	0.0	0.0	f(HALPOR)[b, c]	7.41×10^{-10} / f(HALPOR)[b, c]	10^x, x = DRZPRM[b]
CONC_PLG	Concrete borehole plugs, from intrusion to 200 yr after intrusion	0.94	0.0	0.0	0.0	0.0	0.32	1.1875×10^{-9}	10^x, x = PLGPRM[b]

Material Name	Material Description	Brooks-Corey Pore Distribution (PORE_DIS)[a] l	Threshold Pressure Linear Parameter (PCT_A)[a] a	Threshold Pressure Exponential Parameter (PCT_EXP)[a] h	Residual Brine Saturation (SAT_RBRN)[a] S_{br}	Residual Gas Saturation (SAT_RGAS)[a] S_{gr}	Porosity (POROSITY)[a] f_0	Pore Compressibility C_ϕ, Pa^{-1}	Intrinsic Permeability (PRMX_LOG)[a] k, m^2
BH_OPEN	Borehole, from intrusion to 200 yr after intrusion	0.7	0.0	0.0	0.0	0.0	0.32	0.0	1.0×10^{-9}
BH_SAND	Borehole, from 200 yr after intrusion to 10,000 yr	0.94	0.0	0.0	0.0	0.0	0.32	0.0	10^x, x = BHPRM[b]
BH_CREEP	Borehole below repository, from 1,000 yr after intrusion to 10,000 yr	0.94	0.0	0.0	0.0	0.0	0.32	0.0	$10^{(x-1)}$, x = BHPRM[b]

a Parenthetical parameter names are property names for the corresponding material, as indicated in Table PA-17.

b Uncertain variable; see Table PA-17.

c See Equation (PA.43).

d See Equation (PA.44).

e These materials use relative permeability model = 11; see Table PA-6.

f Initial value of porosity ϕ_0; porosity changes dynamically to account for creep closure (see Section PA-4.2.4).

g See Section PA-4.2.11.

h See Equation (PA.60).

Table PA-6. Models for Relative Permeability and Capillary Pressure in Two-Phase Flow

Material	Relative Permeability[a] (RELP_MOD)	Capillary Pressure[b] (CAP_MOD)	Material	Relative Permeability[a] (RELP_MOD)	Capillary Pressure[b] (CAP_MOD)
BH_OPEN	11	1	FORTYNIN	4	1
BH_SAND	4	1	IMPERM_Z	4	1
BH_CREEP	4	1	MAGENTA	4	2
CASTILER	4	2	OPS_AREA	11	1
CAVITY_1	11	1	PCS_NO	11	1
CAVITY_2	11	1	PCS_T1	4	1
CAVITY_3	11	1	PCS_T2	4	1
CAVITY_4	11	1	PCS_T3	4	1
CAVITY_5	11	1	REPOSIT	12	1
CONC_MON	4	2	SANTAROS	4	1
CONC_PLG	4	1	SHFTU	4	1
CULEBRA	4	2	SHFTL_T1	4	1
DEWYLAKE	4	1	SHFTL_T2	4	1
DRZ_0	4	1	S_ANH_AB	ANHBCVGP[c]	6
DRZ_1	4	1	S_HALITE	4	2
DRZ_OE_0	4	1	S_MB138	ANHBCVGP[c]	6
DRZ_OE_1	4	1	S_MB139	ANHBCVGP[c]	6
DRZ_PC_0	4	1	TAMARISK	4	1
DRZ_PC_1	4	1	UNNAMED	4	1
DRZ_PCS	4	1	WAS_AREA	12	1
EXP_AREA	11	1			

[a] Relative permeability model, where 4 = Brooks-Corey model given by Equation (PA.30), Equation (PA.31), and Equation (PA.32), 11 = open cavity model given by Equation (PA.40), Equation (PA.41), and Equation (PA.42), 12 = Brooks-Corey model modified to account for cutoff saturation, and ANHBCVGP = use of Brooks-Corey or van Genuchten-Parker model treated as a subjective uncertainty (see parameter S_MB139:PORE_DIS in Feng and Kicker (2025a), Table 3).

[b] Capillary pressure model, where: 1 = capillary pressure P_c is unbounded; 2 = P_c bounded above by 1×10^8 Pa as S_b approaches S_{br}; 6 = P_c bounded above by 1×10^8 Pa as S_b approaches S_{br} for relative permeability model 4; or P_c bounded above by 1×10^8 Pa as S_b approaches S_{br} and P_c bounded below by 101,325 Pa as S_b approaches $1-S_{gr}$ for relative permeability model 1.

[c] See ANHBCVGP in Table PA-17.

PA-4.2.3 Initial Conditions

In each two-phase flow simulation, a short period representing disposal operations is simulated. This period is called the start-up period and spans 5 years from $t = -5$ years to 0 years, corresponding to the amount of time a typical panel is expected to remain open during disposal operations. All grid locations require initial brine pressure and gas saturation at the beginning of the simulation (t = –5 years).

The Rustler and overlying units (Figure PA-12) are modeled as horizontal with spatially constant initial pressure in each layer. Table PA-7 summarizes the initial brine pressures P_b and gas saturations S_g at t = –5 years for each modeled layer of the Rustler Formation, prior to the start of simulations.

Table PA-7. Initial Conditions in the Rustler

Name	Mesh Row (Figure PA-12)	$P_b(x, y, -5)$, Pa	$S_g(x, y, -5)$
Santa Rosa	33	1.013250×10^5	$1 - S_b = 0.916$ (S_b = SANTAROS:SAT_IBRN)[a]
Santa Rosa	32	1.013250×10^5	$1 - S_b = 0.916$ (S_b = SANTAROS:SAT_IBRN)[a]
Dewey Lake	31	1.013250×10^5	$1 - S_b = 0.916$ (S_b = SANTAROS:SAT_USAT)[a]
Dewey Lake[c]	30	7.355092×10^5	$1 - S_b = 0.916$ (S_b = SANTAROS:SAT_USAT)[a]
Forty-niner[c]	29	1.47328×10^6	0[b]
Magenta	28	9.465×10^5 (MAGENTA:PRESSURE)	0[b]
Tamarisk[c]	27	1.82709×10^6	0[b]
Culebra	26	9.141×10^5 (CULEBRA:PRESSURE)	0[b]
Los Medaños [c]	25	2.28346×10^6	0[b]

[a] Material:property parameter names used in the simulations are given in parentheses (see Feng and Kicker 2025a).

[b] The Rustler Formation layers listed above are assumed to be fully saturated with brine (i.e., initial gas saturation S_g=0).

[c] For the Dewey Lake, Forty-niner, and Tamarisk layers, initial brine pressures are calculated using a brine density of 1,220 kg/m³. Pressures are set to approximate hydrostatic equilibrium with θ = 0 at a reference point located at the top of the Dewey Lake (see Equation PA.26 and discussion following).

The Salado (Mesh Rows 3–24 in Figure PA-12) is assumed to dip uniformly θ = 1 degree downward from north to south (right to left in Figure PA-12). Brine is assumed to start in hydrostatic equilibrium everywhere except inside the repository excavations and the shaft. This initial brine pressure is based on an uncertain reference pressure. $P_{b,ref}$ (SALPRES; see Table PA-17), measured at the center of the shaft at the elevation of the middle of MB 139, which is the center of Cell 1206 in Figure PA-13. This gives rise to the initial conditions for brine pressure, P_b and brine density, ρ_b:

$$P_b(x, y, -5) = P_{b,ref} + \frac{1}{c_b} \ln\left[\frac{\rho_b(x, y, -5)}{\rho_{b0}}\right] \quad \text{(PA.45)}$$

$$\rho_b(x, y, -5) = \frac{1}{g\, c_b \left[y_e - \Phi\left(x_{ref}, y_{ref}, -5\right) + \frac{1}{g\, c_b\, \rho_{b0}} \right]} \quad \text{(PA.46)}$$

$$\Phi\left(x_{ref}, y_{ref}, -5\right) = y_{ref} + \frac{1}{g\, c_b}\left[\frac{1}{\rho_{b0}} - \frac{1}{\rho_b\left(x_{ref}, y_{ref}, -5\right)}\right] \quad \text{(PA.47)}$$

$$\rho_b\left(x_{ref}, y_{ref}, -5\right) = \rho_{b0} \exp\left[-c_b\left(P_{b,ref} - P_{b0}\right)\right] \quad \text{(PA.48)}$$

$$y_e = y_{ref} + h(x, y) \quad \text{(PA.49)}$$

where

$h(x, y)$ is defined in Equation (PA.26)

ρ_{b0} = 1,220 kg/m^3 (BRINESAL:DNSFLUID)

c_b = 3.1×10^{-10} Pa^{-1} (BRINESAL:COMPRES)

g = 9.80665 meters per second squared (m/s^2)

$P_{b,ref}$ = 1.01325×10^5 Pa (BRINESAL:REF_PRES)

P_{b0} = sampled far-field pressure in the undisturbed halite (S_HALITE:PRESSURE)

In the Salado, initial gas saturation $S_g(x, y, -5) = 0$ (see Nemer and Clayton 2008, Section 4.1.6). The Castile (mesh rows 1 and 2) is modeled as horizontal, and the initial brine pressure is spatially constant. Outside the brine reservoir, pressure is hydrostatic. Within the reservoir, initial pressure $P_b(x, y, -5)$ is uncertain (see parameter CASTILER:PRESSURE in Feng and Kicker (2025a), Table 3). Initial gas saturation $S_g(x, y, -5) = 0$.

Within the shaft (materials SHFTU, SHFTL_T1, SHFTL_T2, and CONC_MON), abandoned panel closure areas (PCS_NO), and panel closures (PCS_T1), $P_b(x, y, -5) = 1.01325 \times 10^5$ Pa and $S_g(x, y, -5) = 1$. Within the excavated area (materials WAS_AREA, REPOSIT, OPS_AREA, EXP_AREA), $P_b(x, y, -5) = 1.01325 \times 10^5$ Pa and $S_g(x, y, -5) = 1$.

At the end of the initial 5-year start-up period and the beginning of the regulatory period ($t = 0$ years), brine pressure and gas saturation are reset in the shaft, panel closures, abandoned panel closure area, and excavated areas. In the shaft (materials SHFTU, SHFTL_T1, SHFTL_T2, and CONC_MON), $P_b(x, y, 0) = 1.01325 \times 10^5$ Pa and $S_g(x, y, 0) = 1 \times 10^{-7}$. In the panel closures, $P_b(x, y, 0) = 1.01325 \times 10^5$ Pa and $S_g(x, y, 0) = 1 -$ PCS_T1:SAT_RBRN, where PCS_T1:SAT_RBRN is uncertain (see Feng and Kicker (2025a), Table 3). In the waste disposal regions (materials WAS_AREA and REPOSIT), $P_b(x, y, 0) = 1.24 \times 10^5$ Pa and $S_g(x, y, 0) = 0.985$. The initial pressure in the waste-disposal regions exceeds atmospheric pressure to account for early-time gas generation prior to the start of the regulatory period. This pressure increase is computed within the Salado flow calculation based on the repository inventory and volume, following the methodology implemented in the BRAGFLO initialization, rather than being specified directly as an independent analysis input (King 2021a). In the other excavated areas, including the abandoned panel closure area, $P_b(x, y, 0) = 1.01325 \times 10^5$ Pa and $S_g(x, y, 0) = 1.0$.

PA-4.2.4 Creep Closure of Repository

Salt creep occurs naturally in the Salado halite in response to deviatoric stress. Inward creep of rock is generally referred to as creep closure. Creep closure of excavated regions begins immediately upon the application of excavation-induced deviatoric stress. If the rooms were empty, closure would proceed until the void volume created by the excavation was eliminated as the surrounding formation returned to a uniform stress state. In the waste-disposal region, inward creep of salt causes consolidation of the waste, and this consolidation continues until the load on the surrounding rock reaches lithostatic conditions and the deviatoric stress is removed, at which point salt creep and waste consolidation cease. The amount of waste consolidation and the time required to consolidate are governed by waste properties (e.g., waste strength, modulus), the surrounding rock properties, the dimensions and location of the room, and the relative quantities of brine and gas present.

The porosity of the waste disposal regions and neighboring access drifts (i.e., materials WAS_AREA, REPOSIT, and PCS_NO in the material maps in PA-4.2.2) is assumed to change through time due to creep closure of the halite surrounding the excavations. The equations for two-phase flow in PA-4.2.1 do not incorporate this type of deformation. Changes in repository porosity due to halite deformation are modeled in a separate analysis (Appendix PORSURF-2026, PORSURF-3.0). Interpolation procedures are then used to define porosity (ϕ) within the repository as a function of time, pressure, and gas generation rate (Appendix PORSURF, PORSURF-4.0). Non-waste-filled areas (i.e., materials OPS_AREA, EXP_AREA) are modeled with a constant porosity (Appendix PORSURF-2026, PORSURF-5.0).

PA-4.2.5 Fracturing of MBs and DRZ

Fracturing within the anhydrite MBs (i.e., regions MB 138, Anhydrite AB, and MB 139 in Figure PA-12) and in the DRZ (region DRZ in Figure PA-12) is assumed to occur at brine pressures slightly above lithostatic pressure, and is implemented through a pressure-dependent compressibility $c_r(P_b)$ (Mendenhall and Gerstle 1995). Specifically, MB fracturing begins at a brine pressure of:

$$P_{bi} = P_{b0} + \Delta P_i \tag{PA.50}$$

where P_{bi} and P_{b0} are spatially dependent (i.e., $P_{b0} = P(x, y, 0)$ as in Section PA-4.2.3) and $\Delta P_i = 2 \times 10^5$ Pa (see S_MB138:PI_DELTA in Feng and Kicker (2025a), Table 21).

Fracturing ceases at a pressure of:

$$P_{ba} = P_{b0} + \Delta P_a \tag{PA.51}$$

and a fully fractured porosity of:

$$\phi(P_{ba}) = \phi_a = \phi_0 + \Delta\phi_a \tag{PA.52}$$

where $\Delta P_a = 3.8 \times 10^6$ Pa (see S_MB138:PF_DELTA in Feng and Kicker (2025a), Table 21), ϕ_0 is spatially dependent (Table PA-5), and $\Delta\phi_a$ = 0.039, 0.239, and 0.039 for anhydrite materials S_MB138, S_ANH_AB, and S_MB139, respectively (see, e.g., S_MB138:DPHIMAX in Feng and Kicker (2025a), Table 21).

Once fractured, compressibility c_r becomes a linear function:

$$c_r(P_b) = c_{ri} + \left(\frac{P_b - P_{bi}}{P_{ba} - P_{bi}}\right)\left(c_{ra} - c_{ri}\right) \tag{PA.53}$$

of brine pressure for $P_{bi} \le P_b \le P_{ba}$, with c_{ra} defined so that the solution ϕ of:

$$\frac{d\phi}{dP_b} = c_{ra}\left(P_b\right)\phi, \text{ where } \phi\left(P_{bi}\right) = \phi_0 \exp\left[c_r\left(P_{bi} - P_{b0}\right)\right] \tag{PA.54}$$

satisfies $\phi(P_{ba}) = \phi_a$; specifically, c_{ra} is given by:

$$c_{ra} = c_{ri}\left[1 - 2\frac{P_{ba} - P_{b0}}{P_{ba} - P_{bi}}\right] + \left[\frac{2}{P_{ba} - P_{bi}}\right]\ln\left(\frac{\phi_a}{\phi_0}\right) \tag{PA.55}$$

The permeability, $k_f(P_b)$, of fractured material at brine pressure, P_b, is related to the permeability of unfractured material at brine pressure, P_{bi}, by:

$$k_f(P_b) = k\left[\frac{\phi(P_b)}{\phi(P_{bi})}\right]^n \quad \text{(PA.56)}$$

where k is the permeability of unfractured material (i.e., at P_{bi}) and n is defined so that $k_f(P_{ba})$ = 1×10^{-9} m^2 (i.e., n is a function of k, which is uncertain; see parameter S_MB139:PRMX_LOG in Feng and Kicker (2025a), Table 3). When fracturing occurs, $k_f(P_b)$ is used instead of k in the definition of the permeability for the fractured areas of the anhydrite MBs.

Fracturing is also modeled in the DRZ region in Figure PA-12. The fracture model implementation is the same as for the anhydrite materials. In the DRZ, the fractures form in halite rather than anhydrite, and the limited size of the DRZ and its closeness to nearby interbeds make this modeling approach appropriate for representing its behavior.

PA-4.2.6 Gas Generation and Brine Production

Gas and brine sources and sinks are described in detail in Appendix GEOCHEM-2026, Section 2.0. For two-phase flow, the gas and brine sources and sinks are accounted for by the net gas generation rate q_{rg} in Equation (PA.18) (see Appendix GEOCHEM-2026, Equation GEOCHEM.10) and net brine production rate q_{rb} in Equation (PA.19) (see Appendix GEOCHEM-2026, Equation GEOCHEM.11).

Gas is generated by chemical reactions and alpha radiolysis of brine. Water is consumed by iron corrosion, hydration of MgO, and radiolysis. Water is produced by microbial degradation of CPR and by the conversion of hydromagnesite to brucite. Chemical reactions and radiolysis are assumed to take place only within the waste disposal regions of the repository (i.e., WAS_AREA and REPOSIT in the material maps of PA-4.2.2) and all the generated gas is assumed to have the same properties as H_2 (see Appendix MASS-2026, Section MASS-2.2). Reactant materials are assumed to be homogeneously distributed throughout the waste disposal regions, i.e., the concentrations of Fe-base metals, CPR materials, radionuclides that participate in brine radiolysis, and MgO in the waste area are not spatially dependent. Five radionuclides, which account for more than 98% of the decay heat of the inventory through the life of the repository, contribute to radiolysis: ^{241}Am, ^{238}Pu, ^{239}Pu, ^{240}Pu and ^{242}Pu (Kicker 2025, Section 6.0).

PA-4.2.7 Capillary Action in the Waste

Capillary action (wicking) results in a material carrying fluid above the level it would normally seek in response to gravity. This phenomenon is accounted for by defining an effective brine saturation, $S_{b,eff}$, given by:

$$S_{b,eff} = \mathrm{Max}\left[\mathrm{Min}\left(S_b - S_{min} + S_{wick}\left(1 - \exp\left[200\alpha\left(\mathrm{Max}\left(S_b - S_{min}, 0\right)\right)^2\right]\right), 1\right), 0\right] \quad \text{(PA.57)}$$

where

S_b = brine saturation

S_{wick} = wicking saturation

S_{min} = minimum brine saturation at which the code can run in the waste-filled areas

α = smoothing parameter = -1000

The effective brine saturation $S_{b,eff}$ is used in cells containing waste (materials WAS_AREA and REPOSIT) to calculate chemical reaction rates (Section PA-4.2.6).

The effective saturation, $S_{b,eff}$ given by Equation (PA.57) approaches zero as S_b approaches a small value S_{min} = 0.015 (Nemer and Clayton 2008, Section 5.2.2). The smoothing provided by the exponential factor avoids a discontinuity in the derivative of effective saturation, thereby facilitating the numerical solutions. The wicking saturation, S_{wick}, is an uncertain variable (see WAS_AREA:SAT_WICK in Feng and Kicker (2025a), Table 3).

PA-4.2.8 Shafts

The disposal system includes five shafts that connect the repository region to the surface: the air-intake shaft, salt-handling shaft, waste-handling shaft, exhaust shaft, and utility shaft. In PA, all shafts are modeled as a single vertical feature in the grid for two-phase flow (column 45 in Figure PA-12). The rationale for this modeling treatment is set forth by Sandia National Laboratories (SNL 1992, Volume 5, Section 2.3).

The planned design of the shaft seals involves numerous materials, including earth, crushed salt, clay, asphalt, and Salado Mass Concrete (SMC) (US DOE 1996, Appendix SEAL). The design is intended to control both short-term and long-term fluid flow through the Salado portion of the shafts. A simplified shaft seal model was developed prior to the CRA-2004 PA (Stein and Zelinski, 2003) and is briefly discussed below.

A conceptual representation of the simplified shaft seal system is shown in Figure PA-24. The simplified model divides the shaft into three sections: an upper section (shaft seal above the Salado), a lower section (within the Salado), and a concrete monolith section within the repository horizon. A detailed discussion of how the material properties were assigned for the simplified shaft seal model is included in James and Stein (2003). The permeability value used to represent the upper and lower sections is defined as the harmonic mean of the component materials' permeability in the detailed shaft seal model (including permeability adjustments made for the DRZ assumed to surround the lower shaft seal section within the Salado). Porosity is defined as the thickness-weighted mean porosity of the component materials. Other material properties are described in James and Stein (2003). The fifth utility shaft was added to the combined shaft model in CRA-2019 (U.S. DOE 2019). There have been no changes to the shaft model since CRA-2019. Matteo and Reedlunn (2020) estimated the impact of the utility shaft's increased diameter on the hydrologic performance of the shaft seal, and concluded there would be no significant impact on mass transport calculations in the WIPP PA.

The lower section of the shaft experiences a change in material properties at 200 years. This change simulates the consolidation of seal materials within the Salado and significantly decreases permeability. This time was chosen as a conservative estimate of the time required for this section of the shaft to become consolidated. The concrete monolith section of the shaft is modeled as highly permeable for 10,000 years to ensure the shaft isn't a barrier to lateral fluid flow. In three thin regions at the stratigraphic position of the anhydrite MBs, the shaft seal is modeled as MB material. This model feature is included to allow fluids flowing in the DRZ and MB fractures to access the interbeds to the north of the repository "around" the shaft seals. Because these layers are so thin, they have virtually no effect on the effective permeability of the shaft seal itself.

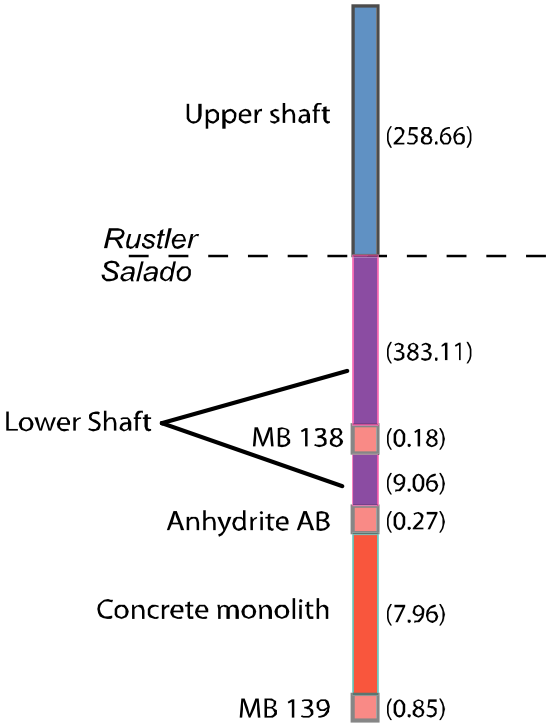
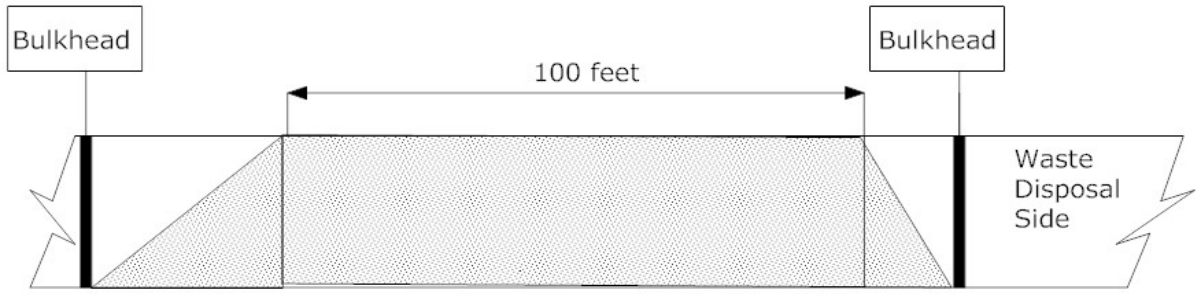


Figure PA-24. Schematic View of the Simplified Shaft Model (numbers on right indicate length in meters)

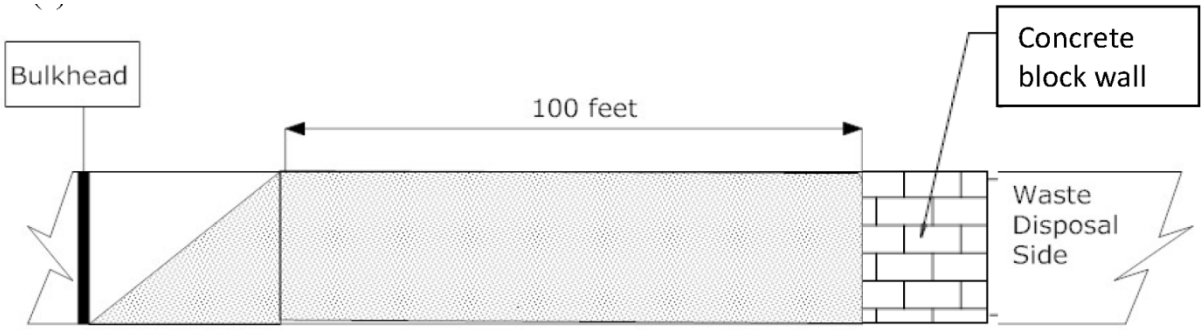
PA-4.2.9 Panel Closures

Waste panel closures are assumed to be emplaced for all waste panels except Panels 3, 4, 5, and 6. Panel closures (PCS) comprise 100 feet of ROM salt with barriers at each end (Figure PA-25). Ventilation bulkheads are similar to those used within waste panels as room closures to restrict airflow and prevent personnel access to waste-filled areas during the operational phase of the repository. Ventilation bulkheads are expected to have no significant effect on the long-term performance of the panel closures and are therefore not included in the representation of the PCS. Explosion walls fabricated from concrete blocks have been installed at the entrance to Panels 1, 2, and 5. Because concrete behaves in a brittle, non-plastic manner, these walls are expected to lose their structural integrity within the first 100 years. The explosion walls are

expected to have no significant effect on long-term panel closure performance, and are therefore not included in the representation of the PCS. Consequently, the PCS are modeled as consisting of 100 feet of ROM salt.



(a) Panel closure with 100 feet of ROM salt between two ventilation bulkheads



(b) Panel closure with 100 feet of ROM salt between a ventilation bulkhead and an explosion wall

Figure PA-25. Schematic Diagram of the ROMPCS (adapted from U.S. DOE 2011)

Material properties to represent the PCS were developed to account for the following physical processes and accepted rock mechanics principles:

1. Creep closure of the salt rock surrounding panel entries will cause consolidation of the ROM salt emplaced there.
2. Eventually, the ROM salt comprising the closures will approach a condition similar to intact salt.
3. As ROM salt reaches higher fractional densities during consolidation, back stress will be imposed on the surrounding rock mass, leading to eventual healing of the DRZ.
4. DRZ healing above and below the ROM salt panel closures will reduce DRZ porosity and permeability in those areas.

During the operational period (i.e., from −5 yr to 0 yr), PCS are represented by cavities. After closure, three materials (PCS_T1, PCS_T2, and PCS_T3) are specified for three time periods (see Camphouse et al. 2012a, Camphouse 2013a, and Camphouse et al. 2013) to represent the temporal effects of the physical processes listed above (see Table PA-5).

For the first 200 years post-closure, the DRZ above and below the PCS maintains the same properties as specified for the DRZ surrounding the disposal rooms (material DRZ_1). After 200 years, the DRZ above and below the PCS is modeled as having healed and is represented by material DRZ_PCS (see Table PA-5). The healing of the DRZ region above and below the PCS will not yield a higher permeability than that of the DRZ above the waste rooms. Accordingly, permeability is constrained so that DRZ_PCS:PRMX ≤ DRZ_1:PRMX, and likewise in the y- and z-directions.

Permeability and porosity values are obtained through sampling for PCS material PCS_T1 (Camphouse et al. 2012b). Porosity values are sampled for materials PCS_T2 and PCS_T3 and used to calculate their permeability. The relationship used to calculate the permeability of material PCS_T2 is of the form (Camphouse et al. 2012):

$$k_2 = 10^{(-21.187(1-\phi_2)+1.5353+\alpha)} \quad \text{(PA.58)}$$

where k_2 is the calculated permeability for PCS_T2, ϕ_2 is the sampled PCS_T2 porosity value, and α is sampled from a normal distribution having a mean of 0, a standard deviation of 0.86, and truncated at ±2 standard deviations (parameter PCS_T2:POR2PERM in Feng and Kicker (2025a), Table 3). An analogous relationship is used for PCS_T3:

$$k_3 = 10^{(-21.187(1-\phi_3)+1.5353+\alpha)} \quad \text{(PA.59)}$$

where α is the same value as in Equation (PA.58). Other parameters representing the PCS and associated DRZ are listed in Feng and Kicker (2025a), Table 11.

Overlap in the porosity ranges for materials PCS_T1 and PCS_T2 potentially results in an increase in panel closure porosity at the transition from PCS_T1 to PCS_T2 at 100 years, a non-physical result. To prevent this possibility, the porosity for PCS_T2 is conditionally sampled so that PCS_T2:POROSITY ≤ PCS_T1:POROSITY for all vectors (King and Zeitler 2025, Section 5.3). For similar reasons, the porosity for material PCS_T3 is conditionally sampled so that PCS_T3:POROSITY ≤ PCS_T2:POROSITY. Similar constraints are placed on the calculated permeabilities for materials PCS_T2 and PCS_T3. The calculated permeability value for PCS_T2 is constrained such that PCS_T2:PRMX ≤ PCS_T1:PRMX. If the calculated permeability for PCS_T2 is greater than the sampled permeability for PCS_T1, then PCS_T2 retains the sampled PCS_T1 permeability. The same is true for the calculated permeabilities in the y- and z-directions. A similar constraint is applied to the calculated permeability for PCS_T3 to prevent non-physical instantaneous increases in panel closure permeability at 200 years. The constraint placed on the calculated permeability for PCS_T3 is that PCS_T3:PRMX ≤ PCS_T2:PRMX, and likewise in the y and z directions. If the calculated permeability for PCS_T3 is greater than the permeability for PCS_T2, then PCS_T3 retains the sampled PCS_T2 permeability.

PA-4.2.10 Borehole Model

The major disruptive event in PA is the penetration of the repository by a drilling intrusion. The drilling intrusion is assumed to produce a borehole with a diameter of 12.25 in. (0.31115 m)

(Vaughn 1996; Howard 1996). The same grid (Figure PA-12) is used for undisturbed and borehole intrusion scenarios by modifying the material properties of a column of cells with lateral dimensions appropriate for a borehole cross-section.

In the undisturbed (E0) scenario, grid cells corresponding to the intrusion location have the material properties of the neighboring stratigraphic or excavated modeling unit. In scenarios simulating a drilling disturbance (E1, E2, E1E2), cells corresponding to the borehole start with the same material properties as in the undisturbed scenario. At the time of intrusion, these cells are reassigned borehole material properties as indicated in the material maps in Section PA-4.2.2. Borehole fill is assumed to be incompressible, capillary effects are ignored, residual gas and brine saturations are set to zero, and porosity is set to 0.32 (see materials CONC_PLG, BH_OPEN, BH_SAND, and BH_CREEP in Table PA-5). Permeability of borehole materials is summarized in Table PA-8. When a borehole that penetrates pressurized brine in the Castile is simulated (i.e., an E1 intrusion), the permeability modifications indicated in Table PA-8 extend from the ground surface (i.e., Grid Cell 2091 in Figure PA-13) to the base of the pressurized brine (i.e., Grid Cell 2175 in Figure PA-13). When a borehole that does not penetrate pressurized brine in the Castile is under consideration (i.e., an E2 intrusion), the permeability modifications indicated in Table PA-8 stop at the floor of the intruded waste panel (i.e., Grid Cell 1348 in Figure PA-13).

Table PA-8. Permeabilities for Drilling Intrusions Through the Repository

Time After Intrusion	Assigned Permeabilities
0–200 years	Concrete plugs are assumed to be emplaced at the Santa Rosa (i.e., a surface plug with a length of 15.76 m; corresponds to Grid Cells 2091 and 2047 in Figure PA-13) and the Los Medaños Member of the Rustler (i.e., a plug at the top of the Salado with a length of 36 m; corresponds to Grid Cell 1557 in Figure PA-13). Concrete plugs are assumed to have a permeability log-uniformly sampled between 10^{-19} m^2 to $10^{-17}$$m^2$ (see parameter CONC_PLG:PRMX_LOG in Feng and Kicker (2025a), Table 5). The open portions of the borehole are assumed to have a permeability of 1×10^{-9} m^2 (see parameter BH_OPEN:PRMX_LOG in Feng and Kicker (2025a), Table 5).
200–1,200 years	Concrete plugs are assumed to fail after 200 years (U.S. DOE 1995). An entire borehole is assigned a permeability typical of silty sand log-uniformly sampled between $10^{-16.3}$ m^2 and 10^{-14} m^2 (see parameter BH_SAND:PRMX_LOG in Feng and Kicker (2025a), Table 3).
> 1,200 years	Permeability of borehole reduced by one order of magnitude in the Salado beneath the repository due to creep closure of borehole (Thompson et al. 1996) (i.e., k = $10^x/10$, x = BHPRM, in Grid Cells 2175, 1486, 26, 97, 168, 239, 1090, 1097, 1104 in Figure PA-13) (see parameter BH_CREEP:PRMX_LOG in Feng and Kicker (2025a), Table 8).

PA-4.2.11 Castile Brine Reservoir

High-pressure Castile brine was encountered in several WIPP-area boreholes, including the WIPP-12 borehole within the controlled area and the ERDA-6 borehole northeast of the site.

Consequently, the conceptual model for the Castile includes the possibility that brine reservoirs underlie the repository (McCormick et al. 2024, Section 18). The E1 and E1E2 scenarios include penetration of both the repository and a brine source in the Castile.

Where they exist, sources of Castile brine in the northern Delaware Basin are believed to be fractured systems, with high-angle fractures spaced widely enough that a borehole can penetrate through a volume of rock containing a brine reservoir without intersecting any fractures, and therefore not producing brine. Castile brine sources occur in the upper portion of the Castile (Popielak et al. 1983). Appreciable volumes of brine have been produced from several reservoirs in the Delaware Basin, but there is little direct information on the areal extent of the brine sources or the existence of the interconnection between them. Data from WIPP-12 and ERDA-6 indicate that fractures exhibit a range of apertures and permeabilities, and that they deplete at different rates. Brine occurrences in the Castile behave as reservoirs; that is, they are bounded systems.

Two regions are specified in the disposal system geometry of the Castile horizon: the Castile (Rows 1 and 2 in Figure PA-12) and a reservoir (Row 1, Columns 13 to 60 in Figure PA-12). The Castile region has an extremely low permeability, which prevents it from participating in fluid flow processes. Unless a borehole connects the repository with a brine reservoir in the Castile, the Castile is conceptually unimportant to PA because of its expected low permeability.

It is unknown whether a brine source exists below the repository. As a result, a range of probabilities for a borehole hitting a pressurized brine source is used (see Section PA-3.2.3). In addition to stochastic uncertainty in the location and hence the probability of intersecting pressurized brine, there is also uncertainty in the properties of these sources.

Bulk compressibility (CASTILER:COMP_RCK), initial pressure (CASTILER:PRESSURE), and permeability (CASTILER:PRMX_LOG) are described by probability distributions (see Table PA-17). Initial porosity, ϕ_0, is computed from bulk compressibility, c_b (Pa^{-1}), by:

$$\phi_0 = \frac{c_b}{c_\phi} \tag{PA.60}$$

where pore compressibility c_ϕ is set to a constant 1.25628×10^{-8} Pa^{-1} so that the resulting minimum and maximum porosity values (0.001592 and 0.00796, respectively) multiply the bulk volume representing the reservoir (7.41204×10^{8} m^3) to yield the range of reservoir brine volume, between 1.18×10^{6} m^3 and 5.9×10^{6} m^3 (Section PA-1.3.8).

PA-4.2.12 Numerical Solution

Determining gas and brine flow in the vicinity of the repository requires solving the two nonlinear PDEs in Equations (PA.18) through (PA.24) over the computational domain in Figure PA-12, along with evaluating appropriate auxiliary conditions. The actual unknown functions in this solution are P_b and S_g, although the constraint conditions also give rise to values for P_g and

S_b. As two dimensions in space and one dimension in time are in use, P_b, P_g, S_b, and S_g are functions of the form $P_b(x, y, t)$, $P_g(x, y, t)$, $S_b(x, y, t)$, and $S_g(x, y, t)$.

Solving Equations (PA.18) through (PA.24) requires both initial-value and boundary-value conditions for P_b and S_g. The initial value conditions for P_b and S_g are given in Section PA-4.2.3. As indicated there, the calculation starts at time t = −5 years, with a possible resetting of values at t = 0 years, which corresponds to final waste emplacement and sealing of the repository. The boundary conditions are such that no brine or gas moves across the exterior grid boundary (Table PA-9). This Neumann-type boundary condition is maintained for all time.

Table PA-9. Boundary Value Conditions for P_g and P_b

Boundaries below (Row 1, y = 0 m) and above (Row 33, y = 1039.05 m) system for 0 ≤ x ≤ 26622.56 m (Columns 1-71) and −5 yr ≤ t. Below, **j** refers to the unit normal vector in the positive y direction.

$\left(\nabla P_g + \rho_g g \nabla h\right)_{(x,y,t)} \cdot \mathbf{j} = 0 \text{ Pa} / m$	No gas flow condition
$\left(\nabla P_b + \rho_b g \nabla h\right)_{(x,y,t)} \cdot \mathbf{j} = 0 \text{ Pa} / m$	No brine flow condition

Boundaries at left (Column 1, x = 0 m) and right (Column 71, x = 26622.56 m) of system for 0 ≤ y ≤ 1039.05 m (Rows 1-33) and −5 yr ≤ t. Below, **i** refers to the unit normal vector in the positive x-direction.

$\left(\nabla P_g + \rho_g g \nabla h\right)_{(x,y,t)} \cdot \mathbf{i} = 0 \text{ Pa} / m$	No gas flow condition
$\left(\nabla P_b + \rho_b g \nabla h\right)_{(x,y,t)} \cdot \mathbf{i} = 0 \text{ Pa} / m$	No brine flow condition

BRAGFLO allows the user to maintain a specified pressure and/or saturation within any grid cell. This is not a boundary condition and is not required to close the problem. This feature is used to specify Dirichlet-type conditions at the surface grid blocks (Columns 1-71, Row 33, Figure PA-12) and at the far-field locations in the Culebra and Magenta (Columns 1 and 71, Row 26, and Columns 1 and 71, Row 28, Figure PA-12). These auxiliary conditions are summarized in Table PA-10.

Table PA-10. Auxiliary Dirichlet Conditions for S_g and P_b

Surface Grid Blocks	Condition
$S_g(i, j, t) = 0.08363$	Columns 1–44, 46–71, Row 33, −5 yr ≤ t Saturation is not forced at the shaft cell on the surface because its saturation is reset to 0.9999 at t = 0 yr.
$P_b(i, j, t) = 1.01 \times 10^5 \text{ Pa}$	Columns 1–71, row 33, –5 yr ≤ t
Culebra and Magenta Far Field	**Condition**
$P_b(i, 26, t) = 9.14 \times 10^5 \text{ Pa}$	i = 1 and 71, j = 26, –5 yr ≤ t (Culebra)
$P_b(i, 28, t) = 9.47 \times 10^5 \text{ Pa}$	i = 1 and 71, j = 28, –5 yr ≤ t (Magenta)

A fully implicit finite-difference procedure is used to solve Equations (PA.18) through (PA.24). The associated discretization of the gas mass balance equation is given by:

$$\frac{1}{\Delta x_i}\left\{\frac{1}{x_{i+1}-x_i}\left[\frac{\alpha\rho_g k_x k_{rg}}{\mu_g}\right]_{i+1/2,\,j}^{n+1}\left(\Phi_{g_{i+1,\,j}}^{x-}-\Phi_{g_{i,\,j}}^{x+}\right)^{n+1}\right.$$

$$\left.-\frac{1}{x_i-x_{i-1}}\left[\frac{\alpha\rho_g k_x k_{rg}}{\mu_g}\right]_{i-1/2,\,j}^{n+1}\left(\Phi_{g_{i,\,j}}^{x-}-\Phi_{g_{i-1,\,j}}^{x+}\right)^{n+1}\right\}$$

$$+\frac{1}{\Delta y_j}\left\{\frac{1}{y_{j+1}-y_j}\left[\frac{\alpha\rho_g k_y k_{rg}}{\mu_g}\right]_{i,\,j+1/2}^{n+1}\left(\Phi_{g_{i,\,j+1}}^{y-}-\Phi_{g_{i,\,j}}^{y+}\right)^{n+1}\right.$$

$$\left.-\frac{1}{y_j-y_{j-1}}\left[\frac{\alpha\rho_g k_y k_{rg}}{\mu_g}\right]_{i,\,j-1/2}^{n+1}\left(\Phi_{g_{i,\,j}}^{y-}-\Phi_{g_{i,\,j-1}}^{y+}\right)^{n+1}\right\}$$

$$+\alpha_{i,\,j}q_{g_{i,\,j}}^{n+1}+\alpha_{i,\,j}q_{rg_{i,\,j}}^{n+1}-\frac{\left(\alpha\phi\rho_g S_g\right)_{i,\,j}^{n+1}-\left(\alpha\phi\rho_g S_g\right)_{i,\,j}^{n}}{\Delta t}=0 \qquad \text{(PA.61)}$$

where Φ represents the phase potentials given by:

$$\Phi_{g_{i,\,j}}^{x+}=P_{g_{i,\,j}}+\rho_{g_{i+1/2,\,j}}g\,h_{i,\,j},\quad \Phi_{g_{i,\,j}}^{x-}=P_{g_{i,\,j}}+\rho_{g_{i-1/2\,j}}g h_{i,\,j}$$

and

$$\Phi_{g_{i,\,j}}^{y+}=P_{g_{i,\,j}}+\rho_{g_{i,\,j+1/2}}g\,h_{i,\,j},\quad \Phi_{g_{i,\,j}}^{y-}=P_{g_{i,\,j}}+\rho_{g_{i,\,j-1/2}}g h_{i,\,j}$$

the subscripts are defined by

i = x-direction grid index

j = y-direction grid index

$i\pm 1/2$ = x-direction grid block interface

$j\pm 1/2$ = y-direction grid block interface

x_i = grid block center in the x-coordinate direction (m)

y_j = grid block center in the y-coordinate direction (m)

Δx_i = grid block length in the x-coordinate direction (m)

Δy_j = grid block length in the y-coordinate direction (m)

the superscripts are defined by

n = index in the time discretization, known solution time level

n+1 = index in the time discretization, unknown solution time level

and the interblock densities are defined by

$$\rho_{g_{i+1/2,\,j}} = \frac{\Delta x_{i+1,\,j}}{\Delta x_{i,\,j} + \Delta x_{i+1,\,j}} \rho_{g_{i,\,j}} + \frac{\Delta x_{i,\,j}}{\Delta x_{i,\,j} + \Delta x_{i+1,\,j}} \rho_{g_{i+1,\,j}}$$

$$\rho_{g_{i-1/2,\,j}} = \frac{\Delta x_{i,\,j}}{\Delta x_{i-1,\,j} + \Delta x_{i,\,j}} \rho_{g_{i-1,\,j}} + \frac{\Delta x_{i-1,\,j}}{\Delta x_{i-1,\,j} + \Delta x_{i,\,j}} \rho_{g_{i,\,j}}$$

$$\rho_{g_{i,\,j+1/2}} = \frac{\Delta y_{i,\,j+1}}{\Delta y_{i,\,j} + \Delta y_{i,\,j+1}} \rho_{g_{i,\,j}} + \frac{\Delta y_{i,\,j}}{\Delta y_{i,\,j} + \Delta y_{i,\,j+1}} \rho_{g_{i,\,j+1}}$$

$$\rho_{g_{i,\,j-1/2}} = \frac{\Delta y_{i,\,j}}{\Delta y_{i,\,j-1} + \Delta y_{i,\,j}} \rho_{g_{i,\,j-1}} + \frac{\Delta y_{i,\,j-1}}{\Delta y_{i,\,j-1} + \Delta y_{i,\,j}} \rho_{g_{i,\,j}}$$

The interface values of k_{rg} in Equation (PA.61) are evaluated using upstream-weighted values (i.e., the relative permeabilities at each grid-block interface are defined to be the relative permeabilities at the center of the adjacent grid block with the highest potential). Further, interface values for $\alpha\rho_g k_x/\mu_g$ and $\alpha\rho_g k_y/\mu_g$ are obtained by harmonic averaging of adjacent grid block values for these expressions. All materials are isotropic; i.e., $k_x = k_y = k_z$.

The discretization of the brine mass balance equation is obtained by replacing the subscript for gas, *g*, by the subscript for brine, *b*, and using the permeability not modified for the Klinkenberg effect. As a reminder, P_g and S_b are replaced in the numerical implementation by the substitutions given by Equation (PA.21) and Equation (PA.20), respectively.

Wells are not used in the conceptual model for long-term Salado flow calculations, but they are used for DBR calculations. Thus, for long-term Salado flow calculations, the terms q_g and q_b are zero. For long-term Salado flow calculations, the wellbore is not treated by specifying sources

and sinks but rather is explicitly modeled within the grid as a distinct material region (i.e., Upper Borehole and Lower Borehole in Figure PA-12).

The resultant coupled system of nonlinear brine and gas mass balance equations is integrated in time using the Newton-Raphson method with upstream weighting of the relative permeabilities, as previously indicated. The primary unknowns at each computational cell center are brine pressure and gas saturation.

PA-4.2.13 Gas and Brine Flow across Specified Boundaries

Darcy velocity vectors $\boldsymbol{v}_g(x, y, t)$ and $\boldsymbol{v}_b(x, y, t)$ for gas and brine flow ($m^3/m^2/s$ = m/s), representing the volumetric flux per unit area as defined by Darcy's Law, are defined by the expressions:

$$\boldsymbol{v}_g(x,y,t) = K_g k_{rg} \left(\nabla P_g + \rho_g g \nabla h\right) / \mu_g \tag{PA.62}$$

and

$$\boldsymbol{v}_b(x,y,t) = K k_{rb} (\nabla P_b + \rho_b g \nabla h) / \mu_b \tag{PA.63}$$

Values for $\boldsymbol{v}_g$ and $\boldsymbol{v}_b$ are obtained and saved as the numerical solutions of Equations (PA.18) through (PA.24) are carried out. Cumulative flow of gas, $C_g(t, B)$, and brine, $C_b(t, B)$, from time 0 to time t across an arbitrary boundary B is then given by:

$$C_l(t,B) = \int_0^t \left[\int_B \alpha(x,y) \boldsymbol{v}_l(x,y,t) \cdot \boldsymbol{n}(x,y) ds \right] dt \tag{PA.64}$$

for $l = g, b$, where $\alpha(x, y)$ is the geometry factor defined in Equation (PA.25), $n(x, y)$ is an outward-pointing unit normal vector, and $\int_B ds$ denotes a line integral. As an example, B could correspond to the boundary of the waste disposal regions in Figure PA-12. The integrals defining $C_g(t, B)$ and $C_b(t, B)$ are evaluated using the Darcy velocities defined by Equation (PA.62) and Equation (PA.63). Due to the dependence of gas volume on pressure, $C_g(t, B)$ is typically calculated in moles or cubic meters at standard temperature and pressure, which requires an appropriate change of units for $\boldsymbol{v}_g$ in the calculation of $C_l(t,B)$.

PA-4.2.14 Additional Information

Additional information on the BRAGFLO code and its use in the CRA-2026 PA can be found in the BRAGFLO design document and user's manual (WIPP Performance Assessment 2025 and the analysis package for the Salado flow in the CRA-2026 PA (Day and King 2025).

PA-4.3 Radionuclide Source Term

Appendix TRU WASTE Table TRU WASTE-4 lists the radionuclide content of the waste to be emplaced in the WIPP. Screening algorithms are applied (Kicker 2025) to exclude radionuclides not regulated under 40 CFR 191, or that contribute negligibly to potential radionuclide releases. After screening, the resulting 39 radionuclides (Kicker 2025, Table 5) are decayed to a common year of assumed repository closure (2083). From these 39 radionuclides, three subsets are defined (see Sections PA-4.3.1, PA-4.3.4, and PA-4.3.5) that specify radionuclides considered in groundwater transport and in releases directly to the surface (Table PA-11).

Table PA-11. Radionuclides Considered in Releases

Release Pathway	Radionuclide
Groundwater transport	^{241}Am, ^{238}Pu, ^{239}Pu, ^{240}Pu, ^{241}Pu, ^{242}Pu, ^{229}Th, ^{230}Th, ^{233}U, ^{234}U
Direct release as solids (i.e., by cuttings, cavings, or spallings)	^{241}Am, ^{244}Cm, ^{137}Cs, ^{238}Pu, ^{239}Pu, ^{240}Pu, ^{241}Pu, ^{90}Sr, ^{233}U, ^{234}U
Direct release in brine (DBR)	^{241}Am, ^{243}Am, ^{252}Cf, ^{243}Cm, ^{244}Cm, ^{245}Cm, ^{248}Cm, ^{137}Cs, ^{237}Np, ^{231}Pa, ^{147}Pm, ^{238}Pu, ^{239}Pu, ^{240}Pu, ^{241}Pu, ^{242}Pu, ^{244}Pu, ^{90}Sr, ^{229}Th, ^{230}Th, ^{232}Th, ^{233}U, ^{234}U, ^{235}U, ^{236}U, ^{238}U

PA-4.3.1 Determination of Oxidation State

The oxidation state controlling the solubility of a radionuclide is considered epistemically uncertain. For elements Pu, Np, and U, a low or high oxidation state is selected by the parameter GLOBAL:OXSTAT (Feng and Kicker 2025a, Table 3). Because OXSTAT is used for all elements, oxidation state is correlated among radionuclides. OXSTAT is randomly sampled from a uniform distribution ranging between 0 and 1. If OXSTAT is less than an element's OXCUTOFF value, the low oxidation state is selected. Appendix SOTERM-2026, Section SOTERM-6.3 summarizes oxidation states for each element.

PA-4.3.2 Mobile Concentration Limits

For transport in the Salado, radionuclides are mobilized as dissolved and colloidal forms in brine. Four types of colloids are considered: humic, mineral fragment, intrinsic, and microbial. The mobile concentration limit of an element is the maximum concentration (mol/L) of dissolved isotopes and their colloids. For a radionuclide, the mobile concentration limit is obtained by multiplying the element's mobile concentration limit by the radionuclide's mole fraction (Docherty and Kim 2025, Section 3.1.5). The basis for the mobile concentration limit is detailed in Appendix SOTERM-2026 and in Appendix GEOCHEM-2026, Sections GEOCHEM-4.0 and GEOCHEM-5.0. Mobile concentration limits are computed using the code PANEL (Section PA-6.3.3).

Mobile concentration limits of Cm, Cf, and Pm are set equal to the mobile concentration limit of Am; the mobile concentration limit of Pa is equal to the mobile concentration limit of Np; and the mobile concentration limits of Cs and Sr are equal to 1.0 mol/L (Docherty and Kim 2025, Section 3.1.4).

For each element *k* (Am, Pu, Th, Np, and U), the mobile concentration limit S_k is the sum of the dissolved and colloidal contributions:

$$S_k = S_{k,diss} + S_{k,hum} + S_{k,mic} + S_{k,min} + S_{k,int} \quad \text{(PA.65)}$$

The dissolved solubility $S_{k,diss}$ (mol/L) is calculated from a baseline solubility $BSOL$ and a solubility uncertainty factor $VSOL$:

$$S_{k,diss}(Ox, Br, BV) = BSOL(Ox, Br, BV) \times 10^{VSOL(Ox)} \quad \text{(PA.66)}$$

where $BSOL(Ox, Br, BV)$ is a function of oxidation state Ox, brine type $Br = \{Castile, Salado\}$ (Appendix SOTERM-2026, Section SOTERM-3.2), brine volume BV, and the solubility uncertainty factor $VSOL(Ox)$ is a function of oxidation state Ox. Baseline solubilities $BSOL(Ox, Br, BV)$ are documented in Domski (2025c) for $Ox = III, IV, V$, and Kaplan et al. (2025) for $Ox = VI$. Brine volumes BV are 1x, 2x, 3x, 4x, and 5x of a minimum brine volume (6,314 m^3) (parameter GLOBAL:DBRMINBV in Feng and Kicker (2025a), Table 36). For $Ox = III, IV$ uncertainty factors $VSOL(Ox)$ are recorded in Domski (2025b). For $Ox = V, VI$, the uncertainty factors $VSOL(Ox)$ are set to 0 (Appendix GEOCHEM-2026, Sections GEOCHEM-4.4.2.3 and GEOCHEM-4.4.2.4).

The humic colloidal contribution $S_{k,hum}$ (mol/L) is calculated as:

$$S_{k,hum} = \min\left(S_{k,diss}(Ox, Br, BV) \times PHUM(Ox, Br), CAPHUM_k\right) \quad \text{(PA.67)}$$

where $PHUM(Ox, Br)$ is a proportionality constant, and $CAPHUM$ is the maximum contribution on humic colloids. The microbial colloidal contribution $S_{k,mic}$ is calculated by:

$$S_{k,mic} = \min\left(S_{k,diss}(Ox, Br, BV) \times PROPMIC_k(Ox), CAPMIC_k(Ox)\right) \quad \text{(PA.68)}$$

where $PROPMIC(Ox)$ is a proportionality constant, and *CAPMIC* is the maximum contribution on microbial colloids. The mineral fragment colloidal contribution $S_{k,min}$ and the intrinsic colloidal contribution $S_{k,int}$ are defined by constants *CONCMIN* and *CONCINT*, respectively:

$$S_{k,min} = CONCMIN_k \quad \text{(PA.69)}$$

$$S_{k,int} = CONCINT_k \quad \text{(PA.70)}$$

Appendix GEOCHEM-2026, Table GEOCHEM-29 lists parameter values for the colloid parameters.

PA-4.3.3 Radionuclides for Transport in the Salado

Radionuclides considered in groundwater transport in the Salado differ between the E0, E1, and E2 scenarios, and the E1E2 scenario, due to different methods for calculating the radionuclides entering the Culebra through a borehole.

For the E0, E1, and E2 scenarios, 10 of the 39 radionuclides are considered for groundwater transport through the Salado (Section PA-4.4) (Kicker 2025, Table 8):

$$\left({}^{242}\mathrm{Pu}, {}^{238}\mathrm{Pu}\right) \rightarrow {}^{234}\mathrm{U} \rightarrow {}^{230}\mathrm{Th} \tag{PA.71}$$

$${}^{239}\mathrm{Pu} \tag{PA.72}$$

$${}^{240}\mathrm{Pu} \tag{PA.73}$$

$${}^{241}\mathrm{Pu} \rightarrow {}^{241}\mathrm{Am} \rightarrow {}^{233}\mathrm{U} \rightarrow {}^{229}\mathrm{Th} \tag{PA.74}$$

The radionuclides considered account for 99.967% of the inventory release that could contribute to releases over 10,000 years. The subset of 10 radionuclides is further reduced by combining those with similar decay and transport properties. In particular, ^{241}Am, ^{234}U, ^{230}Th, and ^{239}Pu are used as surrogates for the groups {^{241}Am, ^{241}Pu}, {^{234}U, ^{233}U}, {^{230}Th, ^{229}Th}, and {^{242}Pu, ^{240}Pu, ^{239}Pu}, respectively, while ^{238}Pu is retained without lumping. Initial inventories of the surrogate radionuclides are adjusted to account for the additional radionuclide(s) represented in each group, including half-life scaling where appropriate (see Kicker 2025, Section 7.0). The outcome of this process was the following set of five lumped radionuclides in three simplified decay chains:

$${}^{241}\mathrm{Am}; \quad {}^{238}\mathrm{Pu} \rightarrow {}^{234}\mathrm{U} \rightarrow {}^{230}\mathrm{Th}; \quad {}^{239}\mathrm{Pu} \tag{PA.75}$$

For the E1E2 scenario, the same 10 radionuclides used in the E0, E1, and E2 scenarios are employed for lumping into the five simplified radionuclides (Docherty and Kim 2025, Section 3.1.9). In this case, transport calculations are performed on the 10 individual radionuclides leaving the repository through the borehole, reflecting the simpler transport method for this scenario (Section PA-4.5). After transport, the concentrations of these 10 radionuclides are converted into the five lumped radionuclides defined in Equation (PA.75). This approach differs from the NUTS method used in the E0, E1, and E2 scenarios, which performs the lumping before transport calculations.

Mobile concentrations for transport in the Salado are computed by the code NUTS (Section PA-4.4) for the E0, E1, and E2 scenarios, and by the code PANEL (Section PA-4.5) for the E1E2 scenario. Docherty and Kim (2025) provide details of the calculation of mobile concentrations.

PA-4.3.4 Radionuclides for Direct Solid Releases

Ten of the 39 radionuclides are considered in solid waste materials released by cuttings, cavings, or spallings (Kicker 2025, Table 10): ^{241}Am, ^{244}Cm, ^{137}Cs, ^{238}Pu, ^{239}Pu, ^{240}Pu, ^{241}Pu, ^{90}Sr, ^{232}U, and ^{234}U. Together, these radionuclides represent 99.85% of the inventory (Ci) at the time of closure. Total concentrations (EPA units/m^3 solid) of these radionuclides, accounting for decay and ingrowth, are computed for each waste stream using the code EPAUNI (Kim and Kicker 2025). For cuttings and cavings, a subset of waste streams is selected (PA-3.2.5) to compute the concentration $\bar{C}_r$ in a release (PA.275). For spallings, the concentration in the release is the average concentration in CH-TRU waste (PA-6.4.2.5).

PA-4.3.5 Radionuclides for Direct Releases in Brine

Twenty six of the 39 radionuclides are accounted for in the activity in direct brine releases (Docherty and Kim 2025, Section 3.1.8). This set includes four unregulated radionuclides (^{252}Cf, ^{244}Cm, ^{147}Pm, and ^{241}Pu) because their decay products contribute to the calculated DBR activity. Mobile concentrations (EPA units/m^3 brine) of these radionuclides, accounting for inventory, decay, and ingrowth, are computed by the code PANEL (Section PA-6.3.3) for the five assumed volumes of brine in a waste panel (see parameter GLOBAL:DBRMINBV in Feng and Kicker 2025a, Table 36). The concentration in a DBR release, C_{bl} (Equation (PA.276)) is found by interpolation on time and brine volume (PA-6.4.2.6).

PA-4.4 Radionuclide Transport in the Salado: NUTS

This section describes the model used to compute radionuclide transport in the Salado for E0, E1, and E2 scenarios (Section PA-2.2.2) that is implemented in the NUTS code. The PANEL code is used to compute transport in the E1E2 scenario, and the details of this model are provided in Section PA-4.5.

Radionuclide transport is modeled in all regions where BRAGFLO computes brine and gas flow, using the NUTS code. For each realization, input is the corresponding BRAGFLO output of fluid velocity, porosity, saturation, and other parameters such as grid geometry. Radionuclides that are transported vertically due to an intrusion or up the shaft are assumed to enter the most transmissive lateral unit, the Culebra. Therefore, radionuclide transport through the Dewey Lake to the accessible environment and to the land surface due to long-term flow is set to zero.

The PA uses NUTS in two different modes. First, the code is used in a computationally fast *screening* mode to identify the realizations for which it is unnecessary to do full transport calculations because the amount of contaminated brine that reaches the Culebra or the LWB within the Salado is insufficient to significantly contribute to the total integrated release of radionuclides from the disposal system (the SCREEN_NUTS code is also used in the screening process). For the remaining realizations, which have the possibility of consequential release, a more computationally intensive calculation of each radionuclide's full transport is performed (see Section PA-6.3.2).

Radionuclide transport is assumed to occur only by advection, with molecular and mechanical dispersion neglected. Sorptive and other retarding effects are conservatively disregarded. Equilibrium chemistry is assumed. These and other assumptions for radionuclide transport in the Salado are discussed further in Appendix MASS-2026, Section MASS-11.4.

Colloidal actinides are subject to retardation through chemical and physical interactions, including attachment to solid surfaces, clogging of small pore throats (i.e., by sieving), and other physical processes that may impede their transport. There will be some interaction of colloids with solid surfaces in the anhydrite interbeds. Given the low permeability of intact interbeds, pore apertures will likely be small, leading to some sieving. However, colloidal particles, if not retarded, are transported slightly more rapidly than the average velocity of the bulk liquid flow due to size exclusion from pore walls (i.e., hydrodynamic chromatography). Because the effects on transport of slightly increased average pore velocity and retarded interactions with solid surfaces and sieving offset one another, the DOE assumes residual effects of these opposing processes will be either small or beneficial and does not incorporate colloidal retardation or sieving when modeling actinide transport in the Salado interbeds.

Fractures, channeling, and viscous fingering may also impact transport in Salado interbeds, which contain natural fractures. Because of the low permeability of unfractured anhydrite, most fluid flow in interbeds will occur in fractures. In situ tests have been conducted to characterize the properties of naturally fractured interbeds at WIPP, providing measured data on fracture characteristics under existing conditions. However, uncertainty remains in the characteristics of the fracture network that may develop under the elevated gas pressures expected in the repository. The PA modeling system accounts for the possible effects of fracturing on porosity and permeability using a fracturing model (see Section PA-4.2.5). The processes and effects associated with fracture dilation or fracture propagation not already captured by the PA fracture model are negligible (U.S. DOE 1996, Appendix MASS, Section MASS.13.3, and Appendix MASS, Attachment 13.2). Of those processes not already incorporated, channeling has the greatest potential effect.

PA-4.4.1 Mathematical Description

The following system of PDEs is used to model radionuclide transport in the Salado:

$$-\nabla\cdot\alpha\boldsymbol{v}_b C_{bl} + \alpha S_l = \alpha\frac{\partial}{\partial t}\left(\phi S_b C_{bl}\right) + \left(\alpha\phi S_b C_{bl}\right)\lambda_l - \alpha\phi S_b \sum_{p\in P(l)} C_{bp}\lambda_p \qquad \text{(PA.76)}$$

$$-S_l = \frac{\partial}{\partial t}\left(C_{sl}\right) + C_{sl}\lambda_l - \sum_{p\in P(l)} C_{sp}\lambda_p \qquad \text{(PA.77)}$$

for l = 1, 2, …, n_R, where

$\boldsymbol{v}_b$ = Darcy velocity vector (m/s) for brine (supplied by BRAGFLO from solution of Equation (PA.63))

C_{bl} = concentration (kg/m^3) of radionuclide *l* in brine

C_{sl} = concentration (kg/m^3) of radionuclide *l* in solid phase (i.e., not in brine), with concentration defined with respect to total (i.e., bulk) formation volume (only used in waste-filled regions; see Figure PA-12)

S_l = linkage term (kg/m^3/s) due to dissolution/precipitation between radionuclide *l* in brine and in solid phase (see Equation (PA.78))

ϕ = porosity (supplied by BRAGFLO from solution of Equations (PA.18) through (PA.24))

S_b = brine saturation (supplied by BRAGFLO from solution of Equations (PA.18) through (PA.24))

λ_l = decay constant (s^{-1}) for radionuclide *l*

$P(l)$ = {*p*: radionuclide *p* is a parent of radionuclide *l*}

n_R = number of radionuclides,

and α is the dimension-dependent geometry factor in Equation (PA.25). Although omitted for brevity, the terms α, $\boldsymbol{v}_b$, C_{bl}, C_{sl}, S_l, S_b, and ϕ are functions $\alpha(x, y)$, $\boldsymbol{v}_b(x, y, t)$, $C_{bl}(x, y, t)$, $C_{sl}(x, y, t)$, $S_l(x, y, t)$, $S_b(x, y, t)$, and $\phi(x, y, t)$ of time *t* and the spatial variables *x* and *y*. Equation (PA.76) and Equation (PA.77) are defined and solved on the same computational grid (Figure PA-12) used for the solution of Equations (PA.18) through (PA.24)). The solution is carried out for the five radionuclides indicated in Equation (PA.75).

Radionuclides are assumed to be present in both brine (Equation (PA.76)) and in an immobile solid phase (Equation (PA.77)), although radionuclide transport takes place only by brine flow (Equation (PA.76)). Mobile concentrations of radionuclides comprise both dissolved radionuclides and radionuclides associated with colloids (PA-4.3.1). Mobile concentration limits are calculated for Salado and Castile brines, and using the minimum brine volume (parameter GLOBAL:DBRMINBV in Feng and Kicker (2025a), Table 36). Using the minimum brine volume is conservative as it maximizes the concentration of actinides potentially transported through the Salado.

The maximum radionuclide concentration is assumed to equilibrate instantly between dissolved and colloidal species. Then each radionuclide equilibrates between the brine and solid phases based on its mobile concentration limit and the radionuclide inventory. The linkage between the brine and solid phases in Equation (PA.76) and Equation (PA.77) is accomplished by the term S_l, where:

$$S_l = \begin{cases} S_{Tl} - C_{bl}\,, & \text{if } 0 \le S_{Tl} - C_{bl} \le \frac{C_{sl}}{\phi S_b} \\ \frac{C_{sl}}{\phi S_b}, & \text{if } 0 \le \frac{C_{sl}}{\phi S_b} < S_{Tl} - C_{bl} \\ S_{Tl} - C_{bl}\,, & \text{if } C_{bl} > S_{Tl} \end{cases} \quad \text{(PA.78)}$$

In Equation (PA.78), S_{Tl} is the mobile concentration limit of radionuclide *l*, obtained from the element mobile concentration limit and the radionuclide mole fraction (Docherty and Kim 2025). Equation (PA.78) enforces the mobile concentration limit by transferring radionuclide mass between the dissolved and solid phases, subject to the available precipitated inventory. When the dissolved concentration is below the mobile concentration limit, mass may be released from the solid phase into brine; when it exceeds the limit, excess dissolved radionuclide is transferred to the solid phase.

The velocity vector $\boldsymbol{v}_b$ in Equation (PA.76) is defined in Equation (PA.63) and is obtained from the numerical solution of Equations (PA.18) through (PA.24). If *B* denotes an arbitrary boundary (e.g., the LWB) in the domain of Equation (PA.76) then the cumulative transport of $C_l(t, B)$ of radionuclide *l* from time 0 to time *t* across *B* is given by:

$$C_l(t,B) = \int_0^t \left[\int_B \boldsymbol{v}_b(x,y,t) C_{bl}(x,y,t) \alpha(x,y) \cdot \boldsymbol{n}(x,y) ds \right] dt \quad \text{(PA.79)}$$

where $\boldsymbol{n}(x, y)$ is an outward-pointing unit normal vector and $\int_B ds$ denotes a line integral over *B*.

PA-4.4.2 Numerical Solution

Equation (PA.76) and Equation (PA.77) are numerically solved by the NUTS program (WIPP Performance Assessment 2022c) on the same computational grid (Figure PA-12) used by BRAGFLO for the solution of Equations (PA.18) through (PA.24)). In the solution procedure, Equation (PA.76) and Equation (PA.77) are numerically solved with $S_l = 0$ for each time step, with the instantaneous updating of concentrations indicated in Equation (PA.78) and the appropriate modification to C_{sl} in Equation (PA.76) taking place after the time step.

The initial value and boundary value conditions used with Equation (PA.76) and Equation (PA.77) are given in Table PA-12. At time $t = 0$ (corresponding to the year 2083), the total inventory of each radionuclide is assumed to be in brine; the solubility constraints associated with Equation (PA.78) then immediately adjust the values for $C_{bl}(x, y, t)$ and $C_{sl}(x, y, t)$ for consistency with the constraints imposed by the radionuclide concentration limit and the available radionuclide inventory.

Table PA-12. Initial and Boundary Conditions for $C_{bl}(x, y, t)$ and $C_{sl}(x, y, t)$

Initial Conditions for $C_{bl}(x, y, t)$ and $C_{sl}(x, y, t)$	**Condition**
$C_{bl}(x, y, 0) = {A_l(0)}/{V_b(0)}$ if (x, y) is a point in the waste-filled regions of the repository. $A_l(0)$ is the amount (kg) of radionuclide *l* present at time *t* = 0 and $V_b(0)$ is the amount (m^3) of brine in the repository at time *t* = 0 (from solution of Equations (PA.18) through (PA.24) with BRAGFLO) for all (x, y). **=** 0 otherwise.	$C_{sl}(x, y, 0) = 0$ for all points in the computational domain.
Boundary Conditions for $C_{bl}(x, y, t)$	**Condition**
On the outer boundary of the computational grid (Figure PA-12), a Neumann boundary condition is applied for the concentration of the dissolved phase in the next column	$\nabla C_{bl} = 0$.

The n_R PDEs in Equation (PA.76) and Equation (PA.77) are discretized in two dimensions and then developed into a linear system of algebraic equations for numerical implementation. The following conventions are used in the representation of each discretized equation:

- The subscript *b* is dropped from C_{bl}, so that the unknown function is represented by C_l.
- A superscript *n* denotes time t_n, with the assumption that the solution C_l is known at time t_n and is to be propagated to time t_{n+1}.
- The grid indices are *i* in the x-direction and *j* in the y-direction and are the same as the BRAGFLO grid indices.
- Fractional indices refer to quantities evaluated at grid block interfaces.
- Each time step by NUTS is equal to five BRAGFLO time steps because BRAGFLO stores results (here, $\boldsymbol{v}_b$, ϕ, and S_b) every five time steps.

The following finite-difference discretization is used for the l^{th} equation in each grid block (*i*, *j*):

$$q^{n+1}_{b,i+1/2,j}C^{n+1}_{l,i+1/2,j} - q^{n+1}_{b,i-1/2,j}C^{n+1}_{l,i-1/2,j} + q^{n+1}_{b,i,j+1/2}C^{n+1}_{l,i,j+1/2} - q^{n+1}_{b,i,j-1/2}C^{n+1}_{l,i,j-1/2} =$$

$$\frac{V_{R,i,j}}{\Delta t}\left[\left\{\phi_{i,j}S_{b_{i,j}}C_{l,i,j}\right\}^{n+1} - \left\{\phi_{i,j}S_{b_{i,j}}C_{l,i,j}\right\}^{n}\right] \qquad \text{(PA.80)}$$

$$+V_{R,i,j}\left\{\phi_{i,j}S_{b_{i,j}}C_{l,i,j}\right\}^{n+1}\lambda_l - V_{R,i,j}\left(\phi_{i,j}S_{b_{i,j}}\right)^{n+1}\sum_{p\in P(l)}C^{n+1}_{p,i,j}\lambda_p$$

where q_b is the grid block interfacial brine flow rate (m^3/s) and V_R is the grid block volume (m^3) from Figure PA-12. The quantity q_b is based on $\boldsymbol{v}_b$ in Equation (PA.63) and α in Equation (PA.25).

The interfacial values of concentration in Equation (PA.80) are discretized using the one-point upstream weighting method (Aziz and Settari 1979), which results in:

$$q^{n+1}_{b,i+1/2,j}\left(\omega_{i+1}C^{n+1}_{l,i,j}+\left(1-\omega_{i+1}\right)C^{n+1}_{l,i+1,j}\right)-q^{n+1}_{b,i-1/2,j}\left(\omega_i C^{n+1}_{l,i-1,j}+\left(1-\omega_i\right)C^{n+1}_{l,i,j}\right)$$
$$+q^{n+1}_{b,i,j+1/2}\left(\omega_{j+1}C^{n+1}_{l,i,j}+\left(1-\omega_{j+1}\right)C^{n+1}_{l,i,j+1}\right)-q^{n+1}_{b,i,j-1/2}\left(\omega_j C^{n+1}_{b,i,j-1}+\left(1-\omega_j\right)C^{n+1}_{l,i,j}\right)= \tag{PA.81}$$
$$\frac{V_{R,i,j}}{\Delta t}\left[\left\{\phi_{i,j}S_{b_{i,j}}C_{l,i,j}\right\}^{n+1}-\left\{\phi_{i,j}S_{b_{i,j}}C_{l,i,j}\right\}^{n}\right]+V_{R,i,j}\left\{\phi_{i,j}S_{b_{i,j}}C_{l,i,j}\right\}^{n+1}\lambda_l$$
$$-V_{R,i,j}\left(\phi_{i,j}S_{b_{i,j}}\right)^{n+1}\sum_{p\in P(l)}C^{n+1}_{p,i,j}\lambda_p$$

where ω derives from the upstream weighting for flow between adjacent grid blocks and is defined by:

$$\omega_i=\begin{cases}1 & \text{if flow is from grid block } (i-1,j) \text{ to grid block } (i,j)\\ 0 & \text{otherwise}\end{cases}$$

$$\omega_j=\begin{cases}1 & \text{if flow is from grid block } (i,j-1) \text{ to grid block } (i,j)\\ 0 & \text{otherwise}\end{cases}$$

By collecting similar terms, Equation (PA.81) can be represented by the linear equation:

$$AC^{n+1}_{l,i,j-1}+BC^{n+1}_{l,i-1,j}+DC^{n+1}_{l,i,j}+EC^{n+1}_{l,i+1,j}+FC^{n+1}_{l,i,j+1}=R_{l,i,j} \tag{PA.82}$$

where

$$A=-\omega_j q^{n+1}_{b,i,j-1/2} \qquad B=-\omega_j q^{n+1}_{b,i-1/2,j}$$
$$E=\left(1-\omega_{i+1}\right)q^{n+1}_{b,i+1/2,j} \qquad F=\left(1-\omega_{j+1}\right)q^{n+1}_{b,i,j+1/2}$$

$$D=-\left(1-\omega_j\right)q^{n+1}_{b,i,j-1/2}-\left(1-\omega_i\right)q^{n+1}_{b,i-1/2,j}+\omega_{j+1}q^{n+1}_{b,i,j+1/2}+\omega_{i+1}q^{n+1}_{b,i+1/2,j}$$
$$-\left(\frac{V_{R,i,j}}{\Delta t}-V_{R,i,j}\lambda_l\right)\left\{\phi_{i,j}S_{b_{i,j}}\right\}^{n+1}$$

$$R_{l,i,j} = -\frac{V_{R,i,j}}{\Delta t}\left\{\phi_{i,j} S_{b_{i,j}} C_{l,i,j}\right\}^{n} - V_{R,i,j}\left(\phi_{i,j} S_{b_{i,j}}\right)^{n+1} \sum_{p \in P(l)} C_{p,i,j}^{n+1} \lambda_p$$

Given the form of Equation (PA.82), the solution of Equation (PA.76) and Equation (PA.77) has now been reduced to the solution of $n_R \times n_G$ linear algebraic equations in $n_R \times n_G$ unknowns, where n_R is the number of equations for each grid block (i.e., the number of radionuclides) and n_G is the number of grid blocks into which the spatial domain is discretized.

The system of PDEs in Equation (PA.76) and Equation (PA.77) is strongly coupled because of the contribution from parental decay to the equation governing the immediate daughter. Consequently, a sequential method is used to solve for the radionuclide concentrations by starting at the top of a decay chain and working down from parent to daughter. This implies that when solving Equation (PA.82) for the l^{th} isotope concentration, all parent concentrations occurring in the right-hand-side term R are known. The system of equations is then linear in the concentrations of the l^{th} isotope. As a result, solving Equation (PA.82) is reduced from the solution of one algebraic equation at each time step with $n_R \times n_G$ unknowns to the solution of n_R algebraic equations, each with n_G unknowns at each time step, which can result in a significant computational savings.

The matrix resulting from one-point upstream weighting has the following structural form for a 3×3 system of grid blocks, and a similar structure for a larger number of grid blocks:

	1	2	3	4	5	6	7	8	9
1	X	X	0	X					
2	X	X	X	0	X				
3	0	X	X	0	0	X			
4	X	0	0	X	X	0	X		
5		X	0	X	X	X	0	X	
6			X	0	X	X	0	0	X
7				X	0	0	X	X	0
8					X	0	X	X	X
9						X	0	X	X

where X designates possible nonzero matrix entries, and 0 designates zero entries within the banded structure. All entries outside of the banded structure are zero. Because of this structure, a banded direct elimination solver (Aziz and Settari 1979, Section 8.2.1) is used to solve the linear system for each radionuclide. The bandwidth is minimized by first indexing equations in the coordinate direction with the minimum number of grid blocks. The coefficient matrix is stored in this banded structure, and all infill coefficients calculated during the elimination procedure are contained within the banded structure. Therefore, for the matrix

system in two dimensions, a pentadiagonal matrix of dimension $I_{BW} \times n_G$ is inverted instead of a full $n_G \times n_G$ matrix, where I_{BW} is the bandwidth.

The numerical implementation of Equation (PA.77) enters the solution process through updates to the radionuclide concentrations in Equation (PA.81) between each time step, as indicated in Equation (PA.78). The numerical solution of Equation (PA.76) and Equation (PA.77) also generates the concentrations required to numerically evaluate the integral that defines $C_l(t, B)$ in Equation (PA.79).

PA-4.4.3 Additional Information

Additional information on NUTS and its use in WIPP PA can be found in the NUTS user's manual (WIPP Performance Assessment 2022c) and in the analysis package of actinide mobilization and Salado transport calculations for the CRA-2026 PA (Docherty and Kim 2025).

PA-4.5 Radionuclide Transport in the Salado: PANEL

This section describes the model used to compute radionuclide transport in the Salado for the E1E2 scenario. The model for transport in the E0, E1, and E2 scenarios is described in Section PA-4.4.

PA-4.5.1 Mathematical Description

A relatively simple mixed-cell model is used for radionuclide transport in the vicinity of the repository after an E1E2 intrusion, assuming that connecting flow between two drilling intrusions into the same waste panel occurs. With this model, the amount of radionuclide *l* contained in a waste panel is represented by:

$$\frac{dA_l}{dt} = -r_b C_{bl} - \lambda_l A_l + \sum_{p \in P(l)} \lambda_p A_p \qquad \text{(PA.83)}$$

where

$A_l(t)$ = amount (mol) of radionuclide *l* in waste panel at time *t*

$C_{bl}(t)$ = concentration (mol/m^3) of radionuclide *l* in brine in waste panel at time *t* (Equation (PA.84))

$r_b(t)$ = rate (m^3/s) at which brine flows out of the repository at time *t* (supplied by BRAGFLO from solution of Equation (PA.64)); taken to be the rate of brine flowing up the borehole at MB138, i.e., at the boundary between cell 1150 and cell 1299 in Figure PA-13.

λ_l = decay constant (s^{-1}) for radionuclide *l* (same definition as for Equation (PA.76))

$P(l)$ = {*p*: radionuclide *p* is a parent of radionuclide *l*} (same definition as for Equation (PA.76))

The concentration C_{bl} in Equation (PA.83) is defined by:

$$C_{bl}(t) = Min\left(S_T[Br, Ox, El]\, MF_l(t), {}^{A_l(t)}\Big/_{V_b(t)} \right) \quad \text{(PA.84)}$$

where

$MF_l(t)$ = mole fraction of radionuclide *l* in waste panel at time *t*

$$= \frac{A_l(t)}{\sum_{k \in El(l)} A_k(t)} \quad \text{(PA.85)}$$

$V_b(t)$ = volume (m^3) of brine in waste panel at time *t* (supplied by BRAGFLO from solution of Equations (PA.18) through (PA.24))

and $S_T[Br, Ox, El]$ is the mobile concentration limit of element *El*, expressed in units of mol/L (Section PA-4.3.2). $C_{bl}(t)$ is defined to be the radionuclide mobile concentration limit when the waste panel contains enough inventory to reach that value. If the available inventory is insufficient, $C_{bl}(t)$ is instead defined as the concentration produced by dissolving all radionuclides in the waste panel (Equation (PA.84)). The dissolved and colloidal components equilibrate instantly for each element.

Given $r_b(\tau)$ and $C_{bl}(\tau)$, evaluation of the integral:

$$R_l(t) = \int_0^t C_{bl}(\tau)\, r_b(\tau) d\tau \quad \text{(PA.86)}$$

provides the cumulative release $R_l(t)$ of radionuclide *l* from the waste panel through time *t*.

PA-4.5.2 Numerical Solution

Equation (PA.83) is numerically evaluated by the PANEL model (WIPP Performance Assessment 2022d) using a discretization based on time steps of 50 years or less. Specifically, Equation (PA.83) is evaluated with the approximation

$$A_l(t_{n+1}) = A_l(t_n) - \left[\int_{t_n}^{t_{n+1}} r_b(\tau) d\tau \right] C_{bl}(t_n) - A_l(t_n) \exp(-\lambda_l \Delta t) + G_l(t_n, t_{n+1}) \quad \text{(PA.87)}$$

where

$G_l\left(t_n, t_{n+1}\right)$ = gain in radionuclide *I* due to the decay of precursor radionuclides between t_n and t_{n+1}.

As the solution progresses, values for $C_{bl}(t_n)$ are updated in consistency with Equation (PA.84), and the products $r_b(t_n)C_{bl}(t_n)$ are accumulated to provide an approximation to R_l in Equation (PA.86) with $\Delta t = t_{n+1} - t_n = 50$ yr.

The term $G_l(t_n, t_{n+1})$ in Equation (PA.87) is evaluated with the Bateman equations (Bateman 1910), with PANEL programmed to handle decay chains of up to five (four decay daughters for a given radionuclide). As a single example, if radionuclide *I* is the third radionuclide in a decay chain (i.e., *I* = 3) and the two preceding radionuclides in the decay chain are designated by *I* = 1 and *I* = 2, then:

$$G_3\left(t_n, t_{n+1}\right) = \frac{\lambda_2 A_2\left(t_n\right)}{\left(\lambda_3 - \lambda_2\right)}\left[\exp\left(-\lambda_2 \Delta t\right) - \exp\left(-\lambda_3 \Delta t\right)\right] + \lambda_1 \lambda_2 A_1\left(t_n\right)\left\{\frac{\exp\left(-\lambda_1 \Delta t\right)}{\left(\lambda_2 - \lambda_1\right)\left(\lambda_3 - \lambda_1\right)} + \frac{\exp\left(-\lambda_2 \Delta t\right)}{\left(\lambda_3 - \lambda_2\right)\left(\lambda_1 - \lambda_2\right)} + \frac{\exp\left(-\lambda_3 \Delta t\right)}{\left(\lambda_1 - \lambda_3\right)\left(\lambda_2 - \lambda_3\right)}\right\} \quad \text{(PA.88)}$$

PA-4.5.3 Additional Information

Additional information on PANEL and its use in the CRA-2026 PA calculations can be found in the PANEL user's manual (WIPP Performance Assessment 2022d), the analysis package for actinide mobilization, and Salado transport calculations (Docherty and Kim 2025).

PA-4.6 Cuttings and Cavings to Surface: CUTTINGS_S

Cuttings are waste solids contained in the cylindrical volume created by the cutting action of the drill bit passing through the waste, while cavings are additional waste solids eroded from the borehole by the upward-flowing drilling fluid within the borehole. The releases associated with these processes are computed within the CUTTINGS_S code (WIPP Performance Assessment 2021a). The mathematical models for cuttings and cavings are described in this section.

PA-4.6.1 Cuttings

The uncompacted volume of cuttings removed and transported to the surface in the drilling fluid, V_{cut}, is given by:

$$V_{cut} = AH_i = \pi D^2 H_i / 4 \quad \text{(PA.89)}$$

where A is the drill bit area (m^2), H_i is the initial (or uncompacted) repository height (3.96 m) (see parameter BLOWOUT:HREPO in Feng and Kicker 2025a, Table 4), and D is the drill-bit diameter (0.31115 m) (see parameter BOREHOLE:DIAMMOD in Feng and Kicker 2025a, Table 4). For drilling intrusions through RH-TRU waste, H_i = 0.509 m is used (see parameter REFCON:HRH in Feng and Kicker 2025a, Table 35).

PA-4.6.2 Cavings

Cavings are caused by the shearing action of the drilling fluid on the waste as it flows up the borehole annulus. Like the cuttings release, the cavings release is assumed to be independent of the conditions that exist in the repository during a drilling intrusion.

The final diameter of the borehole depends on the diameter of the drill bit and on the extent to which the actual borehole diameter exceeds the drill-bit diameter. Although several factors affect erosion within a borehole (Chambre Syndicale de la Recherche et de la Production du Petrole et du Gaz Naturel 1982), the most important is the fluid shear stress on the borehole wall (i.e., the shearing force per unit area, N/m^2) resulting from circulating drilling fluids (Darley 1969; Walker and Holman 1971). As a result, cavings are estimated using a model that accounts for the effect of shear stress on the borehole diameter. In particular, the borehole diameter is assumed to grow until the shear stress on the borehole wall is equal to the shear strength of the waste, which is the limit below which waste erosion ceases.

The final eroded diameter D_f (m) of the borehole through the waste determines the total volume V (m^3) of uncompacted waste removed to the surface by circulating drilling fluid. Specifically:

$$V = V_{cut} + V_{cav} = \pi D_f^2 \frac{H_i}{4} \tag{PA.90}$$

where V_{cav} is the volume (m^3) of waste removed as cavings.

Most borehole erosion is believed to occur in the vicinity of the drill collar (Figure PA-26) because of decreased flow area and consequent increased mud velocity (Rechard et al. 1990, Letters 1a and 1b, App. A). An important determinant of the extent of this erosion is whether the flow of the drilling fluid in the vicinity of the collar is laminar or turbulent. Reynolds numbers distinguish between laminar and turbulent flow. The Reynolds number is the ratio between inertial and viscous (or shear) forces in a fluid, and can be expressed as (Fox and McDonald 1985):

$$\mathrm{Re} = {}^{\rho_f D_e \nu}/_{\eta} \tag{PA.91}$$

where Re is the Reynolds number (dimensionless), ρ_f is the fluid density (1.21×10^3 kg/m^3; see parameter DRILLMUD:DNSFLUID in Feng and Kicker (2025a), Table 4), $\nu = \|\mathbf{v}\|$ is the fluid

speed (0.7089 m s^{-1} based on 40 gal/min/in of drill diameter (Berglund 1992)), D_e is the equivalent diameter (m), and η is the fluid viscosity (kg m^{-1} s^{-1}).

Typically, ρ_f, ν, and η are averages over a control volume with an equivalent diameter of D_e, which is defined as:

$$D_e = 2(R - R_i) \quad \text{(PA.92)}$$

where R_i is the inner diameter of the annulus, as shown in Figure PA-26. The diameter of the drill collar (i.e., $2R_i$ in Figure PA-26) is 8.0 in = 0.2032 m (Brunell and Kicker 2025). The determination of η is discussed below. Reynolds numbers less than 2100 are assumed to indicate laminar flow, while Reynolds numbers greater than 2100 are associated with turbulent flow (Walker 1976).

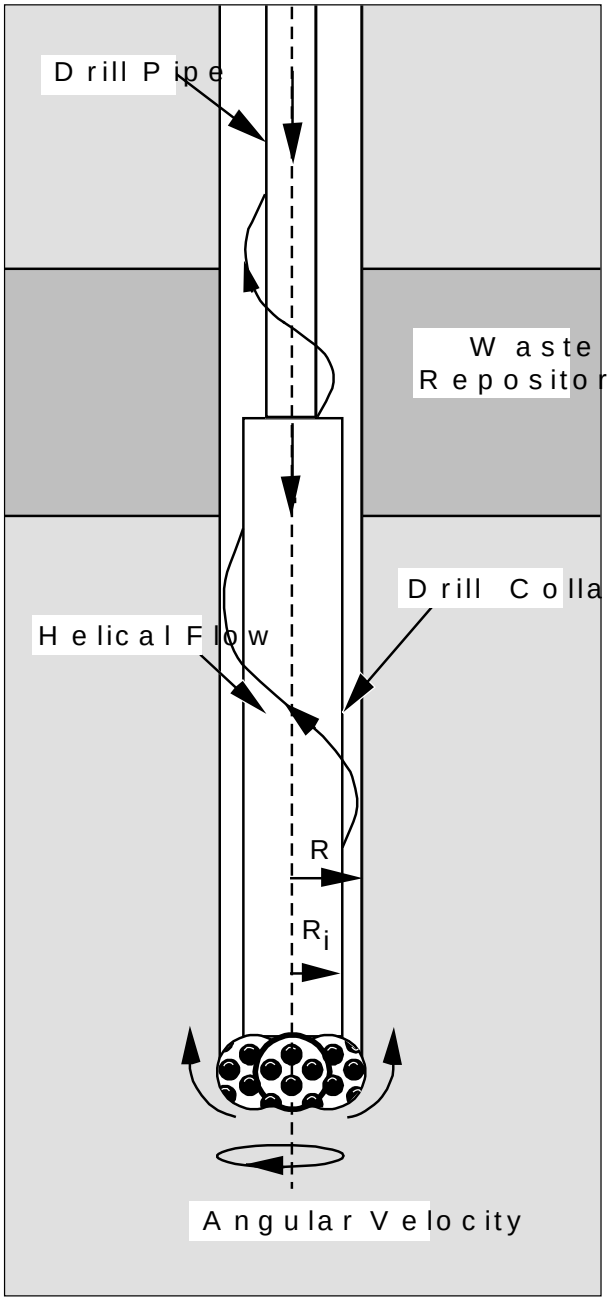


Figure PA-26. Detail of Rotary Drill String Adjacent to Drill Bit

Drilling fluids are modeled as non-Newtonian, which means that the viscosity, η, is a function of the shear rate within the fluid (i.e., the rate at which the fluid velocity changes normal to the flow direction, m/s/m). PA uses a model proposed by Oldroyd (1958) to estimate the viscosity of drilling fluids. As discussed in the *Drilling Mud and Cement Slurry Rheology Manual* (Chambre Syndicale de la Recherche et de la Production du Petrole et du Gaz Naturel 1982), the Oldroyd model leads to the following expression for the Reynolds number associated with the helical flow of a drilling fluid within an annulus:

$$\mathrm{Re} = \frac{0.8165 \rho_f D_e v}{\eta_\infty} \quad \text{(PA.93)}$$

where ρ_f and v are defined as in Equation (PA.91), D_e is defined by Equation (PA.92), and η_∞ is the asymptotic value for the derivative of the shear stress (τ , kg m^{-1} s^{-2}) with respect to the shear rate (Γ, s^{-1}) obtained as the shear rate increases (i.e., $\eta_\infty = d\tau/d\Gamma$ as $\Gamma \to \infty$). Equation (PA.93) determines whether drilling fluids in the area of the drill collar are undergoing laminar or turbulent flow.

The Oldroyd model assumes that the shear stress τ is related to the shear rate Γ through the relationship:

$$\tau = \eta_0 \left(\frac{1 + \sigma_2 \Gamma^2}{1 + \sigma_1 \Gamma^2} \right) \Gamma \quad \text{(PA.94)}$$

where η_0 is the asymptotic value of the viscosity (kg m^{-1} s^{-1}) that results as the shear rate Γ approaches zero, and σ_1 and σ_2 are constants (s^2). Combining $\eta_\infty = d\tau/d\Gamma$ with Equation (PA.94) and taking the limit as $\Gamma \to \infty$ leads to:

$$\eta_\infty = \eta_0 \left(\frac{\sigma_2}{\sigma_1} \right) \quad \text{(PA.95)}$$

PA uses the values of η_0 = 1.834 × 10^{-2} kg m^{-1} s^{-1}, σ_1 = 1.082 × 10^{-6} s^2, and σ_2 = 5.410 × 10^{-7} s^2 (Berglund 1996), from which the viscosity in the limit of infinite shear rate is found to be η_∞ = 9.17 × 10^{-3} kg m^{-1} s^{-1}. The quantity η_∞ is comparable to the plastic viscosity of the fluid (Chambre Syndicale de la Recherche et de la Production du Petrole et du Gaz Naturel 1982).

As previously indicated, different models are used to determine the eroded diameter D_f of a borehole depending on whether flow in the vicinity of the drill collar is laminar or turbulent. The model for borehole erosion in the presence of laminar flow is described next, followed by the model for borehole erosion in the presence of turbulent flow.

PA-4.6.2.1 Laminar Flow Model

As shown by Savins and Wallick (1966), the shear stresses associated with the laminar helical flow of a non-Newtonian fluid, as a function of the normalized radius, r, can be expressed as:

$$\tau(R, r) = \sqrt{\left(\frac{C}{r^2} \right)^2 + \left[\frac{RJ}{2r} \left(r^2 - \lambda^2 \right) \right]^2} \quad \text{(PA.96)}$$

for $R_i/R \le r \le 1$, where R_i and R are the inner and outer radii within which the flow occurs, as indicated in Figure PA-26; $\tau(R, r)$ is the shear stress (kg m^{-1} s^{-2}) at a radial distance ΔR beyond the inner boundary (i.e., at $r = (R_i + \Delta R)/R$); and the variables C, J, and λ depend on R and satisfy

conditions of Equation (PA.98), Equation (PA.99), and Equation (PA.100). The shear stress at the outer radius *R* is given by:

$$\tau(R,1)=\sqrt{C^2+\left[\frac{RJ}{2}\left(1-\lambda^2\right)\right]^2} \tag{PA.97}$$

As previously indicated, the borehole radius *R* is assumed to increase because of erosional processes until a value of *R* is reached at which $\tau(R,1)$ is equal to the shear strength of the waste. In PA, the shear strength of the waste is represented by the uncertain parameter BOREHOLE:TAUFAIL (see Feng and Kicker (2025a), Table 3). Computationally, determining the eroded borehole diameter *R* associated with a particular value of the waste shear strength requires repeated evaluation of $\tau(R,1)$ as indicated in Equation (PA.97).

The quantities *C*, *J*, and λ must satisfy the following three conditions (Savins and Wallick 1966) for Equation (PA.97) to be valid:

$$\int_{R_i/R}^{1}\left(\frac{r^2-\lambda^2}{r\eta}\right)dr=0 \tag{PA.98}$$

$$C\int_{R_i/R}^{1}\left(\frac{1}{r^3\eta}\right)dr=\Delta\Omega \tag{PA.99}$$

$$J\int_{R_i/R}^{1}\left[\frac{\left(R_i/R\right)^2-r^2}{\eta}\right]\left[\frac{r^2-\lambda^2}{r}\right]dr=-\frac{2Q}{\pi R^4} \tag{PA.100}$$

where η, the drilling fluid viscosity (kg m^{-1} s^{-1}), is a function of *R* and r; $\Delta\Omega$ is the drill string angular velocity (rad s^{-1}); and *Q* is the drilling fluid flow rate (m^3 s^{-1}).

The viscosity η in Equation (PA.98), Equation (PA.99), and Equation (PA.100) is introduced into the analysis by assuming that the drilling fluid follows the Oldroyd model for shear stress in Equation (PA.94). By definition of the viscosity η:

$$\tau=\eta\Gamma \tag{PA.101}$$

and from Equation (PA.94):

$$\Gamma^2=\frac{\eta-\eta_0}{\eta_0\sigma_2-\eta\sigma_1} \tag{PA.102}$$

thus the expression in Equation (PA.96) can be reformulated as:

$$\frac{\eta^2(\eta-\eta_0)}{\eta\sigma_2-\eta\sigma_1}=\left(\frac{C}{r^2}\right)^2+\left[\frac{RJ}{2r}\left(r^2-\lambda^2\right)\right]^2 \quad \text{(PA.103)}$$

As discussed by Savins and Wallick (1966) and Berglund (1992), the expressions in Equation (PA.98), Equation (PA.99), Equation (PA.100), and Equation (PA.102) can be numerically evaluated to obtain *C*, *J*, and λ for use in Equation (PA.96) and Equation (PA.97). The drill string angular velocity $\Delta\Omega$ (see BOREHOLE:DOMEGA in Feng and Kicker (2025a), Table 3) is uncertain, and:

$$Q = v(\pi R^2 - \pi R_i^2) \quad \text{(PA.104)}$$

where v = 0.7089 m s^{-1} as used in Equation (PA.91), and η_0, σ_1, and σ_2 are defined as for Equation (PA.94) and Equation (PA.95).

PA-4.6.2.2 Turbulent Flow Model

The model for borehole erosion in the presence of turbulent flow is now described. Unlike the theoretically derived relationship for erosion in laminar flow, the model for borehole erosion in turbulent flow is empirical. In particular, pressure loss for axial flow in an annulus under turbulent flow conditions can be approximated by (Chambre Syndicale de la Recherche et de la Production du Petrole et du Gaz Naturel 1982):

$$\Delta P = \frac{2fL\rho_f v^2}{0.8165 D_e} \quad \text{(PA.105)}$$

where: ΔP is the pressure change (Pa); f is the Fanning friction factor (dimensionless); L is the distance (m) over which pressure change ΔP occurs; ρ_f is the fluid density (kg/m^3) and $v = \|\mathbf{v}\|$ is the fluid speed (m s^{-1}) as defined for Equation (PA.91); and D_e is the equivalent diameter (m) (Equation (PA.92)).

For turbulent pipe flow, f is empirically related to the Reynolds number Re defined in Equation (PA.91) by (Whittaker 1985):

$$\frac{1}{\sqrt{f}} = -4\log_{10}\left(\frac{\varepsilon}{3.72D}+\frac{1.255}{\mathrm{Re}\sqrt{f}}\right) \quad \text{(PA.106)}$$

where D is the inside diameter (m) of the pipe and ε is a "roughness term" equal to the average depth (m) of pipe wall irregularities. In the absence of a similar equation for flow in an annulus, Equation (PA.106) defines f for use in Equation (PA.105), with D replaced by the effective diameter $D_e = 2(R - R_i)$ (Equation (PA.92)) and ε equal to the average depth of irregularities in the waste-borehole interface. In the present analysis, ε = 0.025 m (parameter

WAS_AREA:ABSROUGH in Feng and Kicker (2025a), Table 25), which exceeds the value often selected in calculations involving very rough concrete or riveted steel piping (Streeter 1958).

The pressure change ΔP in Equation (PA.105) and the corresponding shear stress τ at the walls of the annulus are approximately related by:

$$(\Delta P)\pi\left(R^2 - R_i^2\right) = 2\pi L\tau\left(R + R_i\right) \quad \text{(PA.107)}$$

where $\pi(R^2 - R_i^2)$ is the cross-sectional area of the annulus (see Figure PA-26) and $2\pi L(R + R_i)$ is the total surface area of the annulus.

Rearranging Equation (PA.105) and using the relationships in Equation (PA.92) and Equation (PA.107) yields:

$$\tau(R) = \frac{f\rho_f v^2}{2(0.8165)} \quad \text{(PA.108)}$$

which defines the shear stress at the surface of a borehole of radius *R*.

To account for drill string rotation when fluid flow in the vicinity of the drill collars is turbulent, a correction factor (i.e., a rotation factor), F_r, is applied to fluid speed v (Abdul Khader and Rao 1974; Bilgen et al. 1973). Specifically, F_r is defined by:

$$F_r = \frac{v_{2100}}{v} \quad \text{(PA.109)}$$

The quantity v_{2100} is the norm of the fluid velocity required for the eroded diameters to be the same for turbulent and laminar flow at a Reynolds number of Re = 2,100, where PA assumes that the transition between turbulent and laminar flow takes place. The quantity v_{2100} is obtained by solving:

$$\tau_{fail} = \frac{f\rho_f v_{2100}^2}{2(0.8165)} \quad \text{(PA.110)}$$

for v_{2100} with *D* in the definition of *f* in Equation (PA.106) assigned the final diameter value that results for laminar flow at a Reynolds number of Re = 2,100 (that is, the *D* in $D_e = 2(R - R_i) = D - 2R_i$ obtained from Equation (PA.91) and Equation (PA.92) with Re = 2,100). The modified definition of τ is:

$$\tau(R) = \frac{f\rho_f (F_r v)^2}{2(0.8165)} \quad \text{(PA.111)}$$

The radius R enters Equation (PA.111) by $D = 2(R - R_i)$ in the definition of f in Equation (PA.106). As with laminar flow, the borehole radius R is assumed to increase until a value of $\tau(R)$ is reached that equals the sample value for the shear strength of the waste (BOREHOLE:TAUFAIL; see Feng and Kicker (2025a), Table 3). Computationally, the eroded borehole diameter is determined by solving Equation (PA.111) for R under the assumption that $\tau(R)$ equals the assumed shear strength of the waste τ_{fail}.

PA-4.6.2.3 Calculation of R_f

The following algorithm was used to determine the final eroded radius R_f of a borehole and incorporates a possible transition from turbulent to laminar fluid flow within a borehole:

Step 1. Use Equation (PA.93) to determine an initial Reynolds number Re, with R initially set to the drill-bit radius, R_0 = 0.31115 m (parameter BOREHOLE:DIAMMOD in Feng and Kicker (2025a), Table 4).

Step 2. If Re < 2,100, the flow is laminar and the procedure in Section PA-4.6.2.1 is used to determine R_f. Because any increase in the borehole diameter decreases the Reynolds number, the flow remains laminar and there is no need to consider turbulent flow. Consequently, the R_f determined in this step is the final eroded radius of the borehole.

Step 3. If Re $\geq$ 2,100, then the flow is turbulent, and the procedure discussed in Section PA-4.6.2.2 is used to determine R_f. Once R_f is determined, the associated Reynolds number Re is recalculated using Equation (PA.93) and $R = R_f$. If the recalculated Re > 2,100, a transition from turbulent to laminar flow cannot occur, and the final eroded radius R_f is determined in this step. If not, go to Step 4.

Step 4. If the Reynolds number Re with the new R_f in Step 3 satisfies the inequality Re $\leq$ 2,100, a transition from turbulent to laminar flow is assumed to have taken place. In this case, R_f is recalculated assuming laminar flow, with the outer borehole radius R initially set to the radius corresponding to Re = 2,100. In particular, the initial value for R is given by the radius at which the transition from laminar to turbulent flow takes place:

$$R = R_i + \frac{2100\eta_\infty}{2(0.8165)v\rho} \qquad \text{(PA.112)}$$

which is obtained from Equation (PA.93) by solving for R with Re = 2,100. A new value for R_f is then calculated with the procedure discussed in Section PA-4.6.2.1 for laminar flow, with this value of R_f replacing the value from Step 3 as the final eroded diameter of the borehole.

Step 5. Once R_f is known, the amount of waste removed to the surface is determined using Equation (PA.90) with $D_f = 2R_f$.

PA-4.6.3 Additional Information

Additional information on CUTTINGS_S can be found in the CUTTINGS_S design document (WIPP Performance Assessment 2021a). Information about the use of CUTTINGS_S in the CRA-2026 is found in the analysis package for cuttings, cavings, and spallings releases (Brunell and Kicker 2025).

PA-4.7 Spallings to Surface: DRSPALL and CUTTINGS_S

Spallings are waste solids introduced into a borehole by the movement of gas towards the lower-pressure borehole. Spallings could occur when pressure differences between the repository and the wellbore cause solid stresses in the waste exceeding the waste material strength and gas velocities sufficient to mobilize failed waste material. In engineering literature, the term "spalling" describes the dynamic fracture of a solid material, such as rock or metal (Antoun et al. 2003). In the WIPP PA, the spallings model describes a series of processes, including tensile failure of solid waste, fluidization of failed material, entrainment into the wellbore flow, and transport up the wellbore to the land surface.

The spallings model is described in the following sections. Presented first are the primary modeling assumptions used to build the conceptual model. Next, the mathematical model and its numerical implementation in the computer code DRSPALL are described. Finally, the calculation of spallings in the WIPP PA by means of the codes DRSPALL and CUTTINGS_S is discussed.

PA-4.7.1 Summary of Assumptions

Assumptions underlying the spallings model include the future state of the waste, specifications of drilling equipment, and the driller's actions at the time of intrusion. Consistent with the other PA models, the spallings model assumes massive degradation of the emplaced waste through mechanical compaction, corrosion, and biodegradation. Waste is modeled as a homogeneous, isotropic, weakly consolidated material with uniform particle size and shape. The rationale for selecting the spallings model material properties is addressed in detail by Hansen et al. (1997; 2003).

Drilling equipment specifications, such as bit diameter and drilling mud density, are based on surveys of drillers in the Delaware Basin (Hansen et al. 2003). Assumptions about the driller's actions during the intrusion are conservative. Typically, the drilling mud density is controlled to maintain a slightly "overbalanced" condition so that the mud pressure is always slightly higher than the fluid pressures in the formation. If the borehole suddenly passes through a high-pressure zone, the well can quickly become "underbalanced," and the resulting fluid pressure gradient drives formation fluids into the wellbore. This situation, known as a *kick*, is of great concern to drillers because a violent kick can cause a blowout of mud, gas, and oil from the wellbore, resulting in equipment damage and worker injury.

Standard drilling practice is to watch diligently for kicks. The first indicator of a kick is typically an increase in the mud return rate, which leads to an increase in mud pit volume (Frigaard and Humphries 1997). Mud logging monitors detect whether the kick is air, H_2S, or brine. If the kick fluid is air, the standard procedure is to stop drilling and continue pumping mud in order to circulate the air pocket out. If the mud return rate continues to grow after drilling has stopped and the driller believes that the kick is sufficiently large to cause damage, the well may be shut in by closing the blowout preventer. Once shut in, the well pressure may be bled off slowly and mud weight eventually increased and circulated to offset the higher formation pressure before drilling continues. The spallings model simulates an underbalanced system in which a gas kick is assumed to occur and the kick proceeds without intervention by the driller. Therefore, drilling and pumping continue during the entire blowout event.

PA-4.7.2 Mathematical Description

The spallings model calculates transient fluid flow in the repository and wellbore before, during, and after a drilling intrusion. To simplify the calculations, both the wellbore and the repository are modeled by one-dimensional geometries. Wellbore fluid flow assumes a compressible Newtonian fluid consisting of a mixture of mud, gas, salt, and waste solids in which the viscosity of the mixture varies with the fraction of waste solids. In the repository, flow is viscous, isothermal, compressible single-phase (gas) flow in the porous medium.

The wellbore and repository flows are coupled by a cylinder of porous media before penetration, and by a cavity representing the bottom of the borehole after penetration. Schematic diagrams of the flow geometry prior to and after penetration are shown in Figure PA-27 and Figure PA-28, respectively. The drill bit moves downward as a function of time, removing salt or waste material. After penetration, waste solids freed by drilling, tensile failure, and associated fluidization may enter the wellbore flow stream at the cavity forming the repository-wellbore boundary.

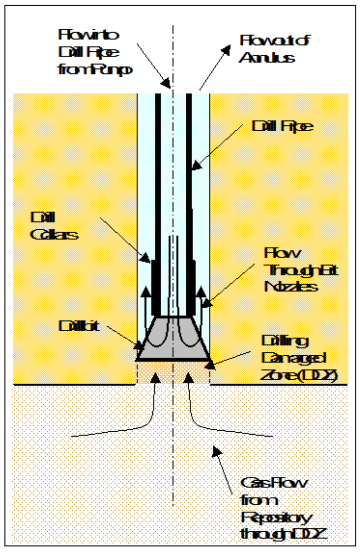


Figure PA-27. Schematic Diagram of the Flow Geometry Prior to Repository Penetration (from U.S. DOE 2004)

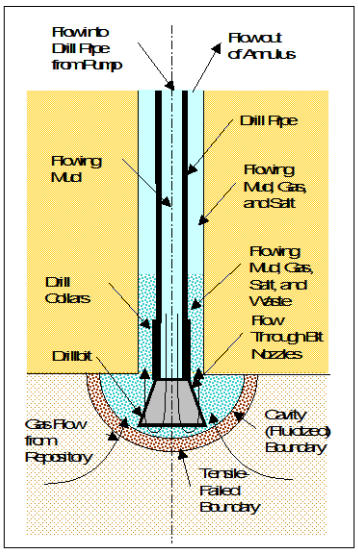


Figure PA-28. Schematic Diagram of the Flow Geometry After Repository Penetration (from U.S. DOE 2004)

PA-4.7.2.1 Wellbore Flow Model

Flow in the well is modeled as one-dimensional pipe flow with cross-sectional areas corresponding to the appropriate flow area at each position in the well, as shown in Figure PA-29 and Figure PA-30. This model is conceptually similar to that proposed by Podio and Yang (1986) for use in the oil and gas industry. Drilling mud is added at the wellbore entrance by the pump. Flow through the drill bit is treated as a choke with a cross-sectional area appropriate for the bit nozzle area. At the annulus output to the surface, the mixture is ejected at a constant

atmospheric pressure. The gravitational body force acts in its appropriate direction based on position before or after the bit.

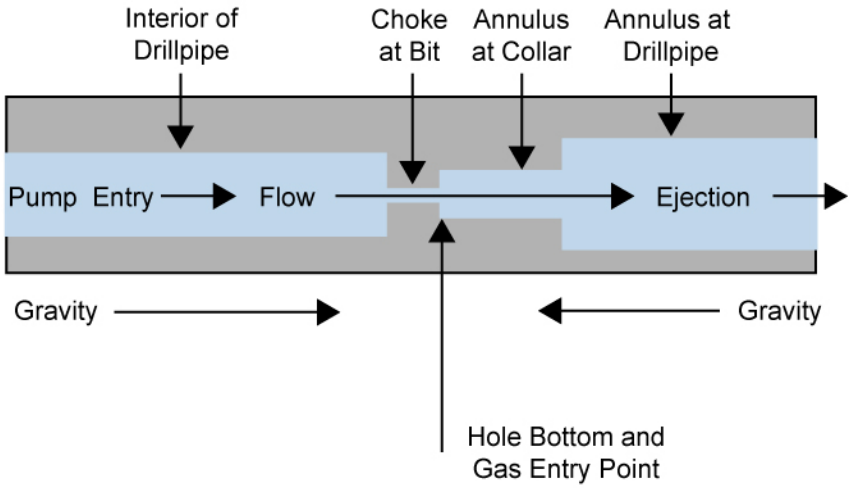


Figure PA-29. Effective Wellbore Flow Geometry Before Bit Penetration (adapted from U.S. DOE 2004)

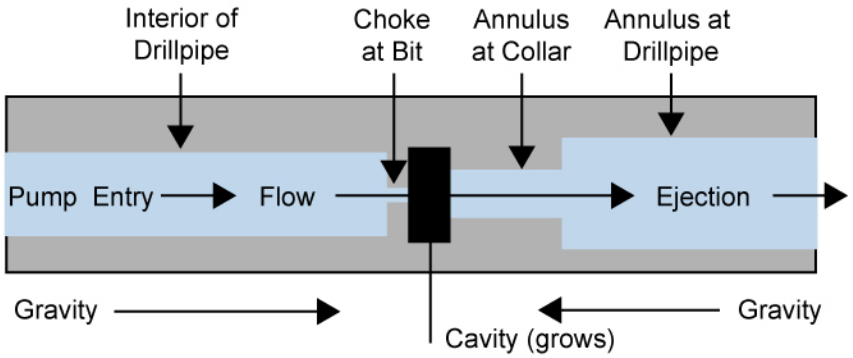


Figure PA-30. Effective Wellbore Flow Geometry After Bit Penetration (adapted from U.S. DOE 2004)

Prior to drill bit penetration into the repository, gas from the repository can flow through drilling-damaged salt into the well. After penetration, the cavity at the bottom of the wellbore couples the wellbore flow and the repository flow models; gas and waste material can exit the repository domain into the cavity. The cavity radius increases as waste materials are moved into the wellbore.

The system of equations representing flow in the wellbore consists of four equations for mass conservation, one for each phase (salt, waste, mud, and gas); one equation for conservation of total momentum; two equations relating gas and mud density to pressure; the definition of density for the fluid mixture; and one constraint imposed by the fixed volume of the wellbore. The conservation of mass and momentum is described by:

$$\frac{\partial}{\partial t}\left(\rho_q V_q\right)+\frac{\partial}{\partial z}\left(\rho_q V_q u\right)=S_q \quad \text{(PA.113)}$$

$$\frac{\partial}{\partial t}\left(\rho V u\right)+\frac{\partial}{\partial z}\left(\rho V u^2\right)=-V\left(\frac{\partial P}{\partial z}-\rho g+F\right)+S_{mom} \quad \text{(PA.114)}$$

where

q = phase (w for waste, s for salt, m for mud, and g for gas)

V_q = volume (m^3) of phase q

V = total volume (m^3)

ρ_q = density (kg/m^3) of phase q, constant for salt and waste (2,180 and 2,650 kg/m^3, respectively) and pressure-dependent for gas and mud (see Equation (PA.115) and Equation (PA.116))

ρ = density of fluid mixture (kg/m^3) determined by Equation (PA.117)

u = velocity (m/s) of fluid mixture in wellbore

t = time (s)

z = distance (m) from inlet at top of well

S_q = rate of mass (kg/s) in phase q entering and exiting wellbore domain at position z (Equation (PA.128))

S_{mom} = rate of momentum ($kg\ m/s^2$) entering and exiting wellbore domain at position z (Equation (PA.131))

P = pressure (Pa) at position z

g = standard acceleration due to gravity (9.8067 m/s^2)

F = friction loss using pipe flow model ($kg/m^2/s^2$) determined by Equation (PA.119)

Gas is treated as isothermal and ideal, so the pressure and density are related by Boyle's law:

$$\frac{\rho}{\rho_{g,0}}=\frac{P}{P_{atm}} \quad \text{(PA.115)}$$

where $\rho_{g,0}$ is the density of H_2 gas at atmospheric pressure and 298 K (8.24182×10^{-2} kg/m^3).

The mud is assumed to be a compressible fluid, so:

$$\rho_m = \rho_{m,0}\left[1 + c_m\left(P - P_{atm}\right)\right] \quad \text{(PA.116)}$$

where $\rho_{m,0}$ is the density of the mud at atmospheric pressure (1,210 kg/m^3) and c_m is the compressibility of the mud (3.1×10^{-10} Pa^{-1}).

The density of the fluid mixture is determined from the densities and volumes occupied by the phases:

$$\rho = \frac{\rho_g V_g + \rho_m V_m + \rho_s V_s + \rho_w V_w}{V} \quad \text{(PA.117)}$$

The volume of each phase is constrained by the fixed total volume of the wellbore:

$$V = V_g + V_m + V_s + V_w \quad \text{(PA.118)}$$

The friction loss is a standard formulation for pipe flow (Fox and McDonald 1985), where the head loss per unit length is given as:

$$F = \frac{\Delta P}{L} = \frac{f \rho u^2}{2 d_h} \quad \text{(PA.119)}$$

where the hydraulic diameter d_h is given by:

$$d_h = \frac{4A}{\pi\left(D_i + D_o\right)} \quad \text{(PA.120)}$$

with D_i and D_o being the inner and outer diameters, respectively. In PA, D_o = 0.31115 m throughout the domain. From the bit to the top of the collar, D_i = 0.2032 m; above the collar, D_i = 0.1143 m. The area A is calculated as the area of the annulus between the outer and inner radii:

$$A = \frac{\pi}{4}\left(D_o^2 - D_i^2\right) \quad \text{(PA.121)}$$

Thus, d_h = 0.108 m from the bit to the top of the collar, and d_h = 0.197 m above the collar.

The Darcy friction factor f in Equation (PA.119) is determined by the method of Colebrook (Fox and MacDonald 1985). In the laminar regime, which is assumed to be characterized by Reynolds numbers below 2100 (Walker 1976):

$$f = \frac{64}{\mathrm{Re}} \quad \text{(PA.122)}$$

and in the turbulent regime (Re > 2100):

$$\frac{1}{\sqrt{f}} = -2.0\log_{10}\left(\frac{\varepsilon}{3.72d_h} + \frac{2.51}{\mathrm{Re}\sqrt{f}}\right) \quad \text{(PA.123)}$$

where $\mathrm{Re} = \frac{u\rho d_h}{\eta}$ is the Reynolds number of the mixture, and η is the viscosity calculated in Equation (PA.124). As the wellbore mixture becomes particle-laden, its viscosity is obtained from an empirical relationship that was developed for proppant-slurry transport in channel flows for the oil and gas industry (Barree and Conway 1995

). Viscosity is computed by an approximate slurry formula based on the volume fraction of waste solids:

$$\eta = \eta_0\left(1 - \frac{w}{w_{\max}}\right)^s \quad \text{(PA.124)}$$

where η_0 is a base mixture viscosity (9.17×10^{-3} Pa s), $w = V_w/V$ is the current volume fraction of waste solids, w_{max} is an empirically determined maximal volume fraction above which flow is choked (0.615), and s is an empirically determined constant (–1.5) (Hansen et al. 2003).

PA-4.7.2.1.1 Wellbore Initial Conditions

Initial conditions in the wellbore approximate mixture flow conditions just prior to waste penetration. The wellbore is assumed to contain only mud and salt. Initial conditions for the pressure, fluid density, volume fractions of mud and salt, and the mixture velocity are set by the following algorithm:

Step 1. Set pressure in the wellbore to hydrostatic: $P(z) = P_{atm} - \rho_{m,0}gz$.

Step 2. Set mud density using Equation (PA.116).

Step 3. Set mixture velocity: $u(z) = R_m/A(z)$, where R_m is the volume flow rate of the pump (0.0202 m^3/s), and $A(z)$ is the cross-sectional area of the wellbore.

Step 4. Set volume of salt in each cell: $V_{s,i} = R_{drill}A_{bit}\Delta z_i/u_i$, where R_{drill} is the rate of drilling (0.004445 m/s), $A_{bit} = \pi d_{bit}^2/4$ is the area of the bottom of the wellbore, Δz_i is the i-th zone size, u_i is the mixture velocity in the i-th zone, and d_{bit} is the diameter of the bit (0.31115 m).

Step 5. Set volume fraction of mud in each cell: $V_{m,i} = V_i - V_{s,i}$.

Step 6. Recalculate mixture density using Equation (PA.117), assuming no waste or gas in the wellbore.

The initial conditions set by this algorithm approximate a solution to the wellbore flow (Equation (PA.113) and Equation (PA.114)) for constant flow of mud and salt in the well. The

approximation rapidly converges to a solution for wellbore flow if steady-state conditions are maintained (WIPP Performance Assessment 2021c).

PA-4.7.2.1.2 Wellbore Boundary Conditions

For simplicity, DRSPALL does not model the flow of mud down the pipe to the bit. Mass can enter the wellbore below the drill bit and exit at the wellbore outlet. Below the bit, mud, salt, gas, and waste can enter the wellbore. PA assumes a constant volume of mud flow down the drilling pipe; therefore, the source term for mud, $S_{m,in}$, is set by the volumetric flow rate of the pump R_m (0.0202 m^3/s) and the density of the mud at the bottom of the wellbore:

$$S_{m,in} = \rho_m R_m \tag{PA.125}$$

Until the drill bit penetrates the repository, salt enters the wellbore at a constant rate:

$$S_{s,in} = \rho_s R_{drill} A_{bit} \tag{PA.126}$$

Additional mass enters the wellbore by gas flow from the repository ($S_{g,in}$) and spalling of waste material ($S_{w,in}$); these mass sources are discussed in Section PA-4.7.2.3. The pressure at the outlet of the wellbore is set to atmospheric pressure. Mass exiting the wellbore is determined from the mixture velocity, the area of the outlet A_{out} (0.066 m^2), and the density and volume fraction of each phase at the outlet of the wellbore:

$$S_{q,out} = \rho u_{out} A_{out} \frac{V_q}{V} \tag{PA.127}$$

Finally, the net change in mass and momentum for phase q is:

$$S_q = S_{q,in} - S_{q,out} \tag{PA.128}$$

$$S_{mom,in} = \frac{\rho_{0,m}}{A_p} R_{mudpump} \tag{PA.129}$$

The outlet of the wellbore is set to atmospheric pressure. Momentum exiting the wellbore is determined from the fluid velocity and the area of the outlet A_{out} (0.066 m^2):

$$S_{mom,out} = -\rho A_{out} u_{out}^2 \tag{PA.130}$$

No momentum is added by mass flow into the wellbore from the repository; thus:

$$S_{mom} = S_{mom,in} - S_{mom,out} \tag{PA.131}$$

PA-4.7.2.2 Repository Flow Model

The repository is modeled as a radially symmetric domain. A spherical coordinate system is used for most DRSPALL calculations. In a few circumstances, cylindrical coordinates are used in PA calculations, where spall volumes are large enough that spherical coordinates are not representative of the physical process (Lord et al. 2003). The design document for DRSPALL (WIPP Performance Assessment 2021b) provides details on implementing the repository flow model in cylindrical coordinates.

Flow in the repository is transient, compressible, viscous, and single-phase (gas) flow in a porous medium. Gas is treated as isothermal and ideal. The equations governing flow in the repository are the equation of state for ideal gases (written in the form of Boyle's law for an ideal gas at constant temperature), conservation of mass, and Darcy's law with the Forchheimer correction (Aronson 1986; Whitaker 1996):

$$\frac{\rho_g}{\rho_{g,0}} = \frac{P}{P_{atm}} \tag{PA.132}$$

$$\phi \frac{\partial \rho_g}{\partial t} + \nabla \cdot \left(\rho_g u \right) = 0 \tag{PA.133}$$

$$\nabla P = -\frac{\eta_g}{k} \left(1 + F \right) u \tag{PA.134}$$

where

P = pressure in pore space (Pa)

ρ_g = density of gas (kg/m^3)

u = velocity of gas in pore space (m/s)

ϕ = porosity of the solid (unitless)

η_g = gas viscosity (8.934×10^{-6} Pa s)

k = permeability of waste solid (m^2)

F = Forchheimer correction (unitless)

The Forchheimer correction is included in Equation (PA.134) to account for inertia in the flowing gas, which becomes important at high gas velocities (Ruth and Ma 1992). When the Forchheimer coefficient is zero, Equation (PA.134) reduces to Darcy's law. A derivation of Equation (PA.134) from the Navier-Stokes equations is given by Whitaker (1996); the derivation suggests that F is a linear function of gas velocity for a wide range of Reynolds numbers.

In PA, the Forchheimer correction takes the form:

$$F = \beta_{nd}\rho u \tag{PA.135}$$

where β_{nd} is the non-Darcy coefficient. This coefficient depends on material properties such as tortuosity and internal channel flow area and is empirically determined (Belhaj et al. 2003). DRSPALL uses a value from Li et al. (2001) that measured high-velocity nitrogen flow through porous sandstone wafers, giving the result:

$$\beta_{nd} = \frac{1.15\times10^{-6}}{k\phi} \tag{PA.136}$$

Equation (PA.132), Equation (PA.133), and Equation (PA.134) combine into a single equation for pressure in the porous solid:

$$\frac{\partial P}{\partial t} = \frac{k'}{2\phi\eta_g}\nabla^2 P^2 + \frac{1}{2\phi\eta_g}\nabla P^2 \cdot \nabla k' \tag{PA.137}$$

where

$$k' = \frac{k}{1+F} = \frac{k}{1+\beta_{nd}\rho u} \tag{PA.138}$$

and the Laplacian operator in a radially symmetric coordinate system is given by:

$$\nabla^2 = \frac{1}{r^{n-1}}\frac{\partial}{\partial r}\left(r^{n-1}\frac{\partial}{\partial r}\right) \tag{PA.139}$$

where n = 2 and n = 3 for polar and spherical coordinates, respectively.

The permeability of the waste solid is an uncertain parameter that remains constant for waste material that has not failed and is not fluidized. In a region of waste that has failed, permeability increases by a factor of 1 + F_f, where F_f is the fraction of failed material that has fluidized and determined by the fluidization relaxation time. This factor accounts for the material bulking as it fluidizes.

The initial pressure in the repository is set to a constant value P_{ff}. A no-flow boundary condition is imposed at the outer boundary (r =R):

$$\nabla P(R) = 0 \tag{PA.140}$$

At the inner boundary ($r = r_{cav}$), the pressure is specified as $P(r_{cav},t) = P_{cav}(t)$, where $P_{cav}(t)$ is defined in the next section. The cavity radius r_{cav} increases as drilling progresses and waste material fails and moves into the wellbore; the calculation of r_{cav} is described in Section PA-4.7.2.3.3.

PA-4.7.2.3 Wellbore to Repository Coupling

Prior to penetration, a cylinder of altered-permeability salt material with a diameter equal to the drill bit is assumed to connect the bottom of the wellbore to the repository. At the junction of the repository and this cylinder of salt, a small, artificial cavity is used to determine the boundary pressure for repository flow. After penetration, the cavity merges with the bottom of the wellbore to connect the wellbore to the repository.

PA-4.7.2.3.1 Flow Prior to Penetration

The cylinder of salt connecting the wellbore to the repository is referred to as the drilling damaged zone (DDZ) in Figure PA-27. The permeability of the DDZ, k_{DDZ}, is 1×10^{-14} m^2. The spallings model starts with the bit 0.15 m above the repository; the bit advances at a rate of R_{drill} = 0.004445 m/s.

To couple the repository to the DDZ, the model uses an artificial pseudo-cavity in the small hemispherical region of the repository below the wellbore with the same surface area as the bottom of the wellbore (Figure PA-30). The pseudo-cavity is a numerical construct used to smooth discontinuities in pressure and flow that would otherwise occur when the bit penetrates the repository. The pseudo-cavity contains only gas and is initially at repository pressure. The mass of gas in the cavity m_{cav} is given by:

$$\frac{dm_{cav}}{dt} = S_{rep} - S_{g,in} \tag{PA.141}$$

where

S_{rep} = gas flow from repository into pseudo-cavity (kg/s); see Equation (PA.142)

$S_{g,in}$ = gas flow from pseudo-cavity through DDZ into wellbore (kg/s); see Equation (PA.143)

Flow from the repository into the pseudo-cavity is given by:

$$S_{rep} = \rho_{g,rep} u_{rep} \phi A_{cav} \tag{PA.142}$$

where

$\rho_{g,rep}$ = gas density in repository at cavity surface (kg/m^3) = $\rho_g(r_{cav})$

u_{rep} = gas velocity (m/s) in repository at cavity surface = $u(r_{cav})$

ϕ = porosity of waste (unitless)

A_{cav} = surface area of hemispherical part of the cavity (m^2)

= $\pi d_{bit}^2/4$, where d_{bit} is the diameter of the bit (m)

Flow out of the pseudo-cavity through the DDZ and into the wellbore is modeled as steady-state using Darcy's Law:

$$S_{g,in} = \frac{k_{DDZ}\pi M_w}{2\eta_g RTL}\left(\frac{d_{bit}}{2}\right)^2\left(P_{cav}^2 - P_{BH}^2\right) \quad \text{(PA.143)}$$

where

η_g = viscosity of H_2 gas (8.934×10^{-6} Pa s)

M_w = molecular weight of H_2 gas (0.00202 kg/mol)

R = ideal gas constant (8.314 J/mol K)

T = repository temperature (constant at 300 K (27 °C; 80 °F))

L = length (m) of DDZ (from bottom of borehole to top of repository)

P_{cav} = pressure in pseudo-cavity (Pa)

P_{BH} = pressure at bottom of wellbore (Pa)

A justification for using this steady-state equation is provided in the design document for DRSPALL (WIPP Performance Assessment 2021b). The pseudo-cavity is initially filled with gas at a pressure of P_{ff}. The boundary pressure on the well side (P_{BH}) is the pressure immediately below the bit, determined by Equation (PA.113) and Equation (PA.114). The pressure in the pseudo-cavity (P_{cav}) is determined by the ideal gas law:

$$P_{cav} = \frac{m_{cav}R_0T}{V_{cav}} \quad \text{(PA.144)}$$

where m_{cav} is the number of moles of gas in the cavity, and the cavity volume V_{cav} is given by:

$$V_{cav} = \frac{\pi d_{bit}^3}{24\sqrt{2}} \quad \text{(PA.145)}$$

In PA, the drilling rate into the ground is assumed constant at 0.004445 m/s; thus $L = L_i - 0.004445t$ until $L = 0$, at which time the bit penetrates the waste. The term L_i is the distance from the bit to the waste at the start of calculation (0.15 m).

PA-4.7.2.3.2 Flow After Penetration

After waste penetration, the bottom of the wellbore is modeled as a hemispherical cavity in the repository, the radius of which grows as drilling progresses and as material fails and moves into the cavity. Gas, drilling mud, and waste are assumed to thoroughly mix in this cavity; the resulting mixture flows around the drill collars and then up the annulus between the wellbore and the drill string. Gas flow from the repository into the cavity is given by Equation (PA.142); however, A_{cav} is now dependent on the increasing radius of the cavity (see Section PA-4.7.2.3.3). Mudflow into the cavity from the wellbore is given by Equation (PA.125). Waste can flow into the cavity if the waste fails and fluidizes; these mechanisms are discussed in Section PA-4.7.2.3.4 and Section PA-4.7.2.3.5. Pressure in the cavity is equal to that at the bottom of the wellbore and is computed by Equation (PA.144).

PA-4.7.2.3.3 Cavity Volume After Penetration

The cylindrical cavity created by drilling is mapped to a hemispherical volume at the bottom of the wellbore. This mapping maintains equal surface areas to preserve the gas flux from the repository to the wellbore. The cavity radius from drilling is thus:

$$r_{drill} = \sqrt{\frac{d_{bit}^2 + 4 d_{bit} \Delta H}{8}} \tag{PA.146}$$

where ΔH is the depth of the drilled cylinder. In PA, the drilling rate into the ground is assumed constant at 0.004445 m/s; thus, DH = 0.004445t until $\Delta H = H$, the height of compacted waste (m). Since the initial height of the repository is 3.96 m, H is computed from the porosity ϕ by $H = 3.96\left(1-\phi_0\right)/\left(1-\phi\right)$, where ϕ_0 is the initial porosity of a waste-filled room.

The cavity radius r_{cav} is increased by the radius of failed and fluidized material r_{fluid}, which is the depth to which fluidization has occurred beyond the drilled radius. That is:

$$r_{cav} = r_{drill} + r_{fluid} \tag{PA.147}$$

PA-4.7.2.3.4 Waste Failure

Gas flow from the waste creates a pressure gradient within the waste, which induces elastic stresses in addition to the far-field confining stress. These stresses may lead to tensile failure of the waste material, an assumed prerequisite to spallings releases. While the fluid calculations using Equation (PA.132), Equation (PA.133), and Equation (PA.134) are fully transient, the elastic stress calculations are assumed to be quasi-static (i.e., sound-speed phenomena in the solid are ignored). Elastic effective stresses are (Jaeger and Cook 1969):

$$\sigma_r\left(r\right) = \sigma_{sr}\left(r\right) + \sigma_{ff}\left(1 - \left(\frac{r_{cav}}{r}\right)^3\right) + P\left(r_{cav}\right)\left(\frac{r_{cav}}{r}\right)^3 - \beta P\left(r\right) \tag{PA.148}$$

$$\sigma_\theta(r) = \sigma_{s\theta}(r) + \sigma_{ff}\left[1 + \frac{1}{2}\left(\frac{r_{cav}}{r}\right)^2\right] - \frac{P(r_{cav})}{2}\left(\frac{r_{cav}}{r}\right)^3 - \beta P(r) \qquad \text{(PA.149)}$$

where β is Biot's constant (assumed here to be 1.0) and σ_{ff} is the confining far-field stress (assumed constant at 14.8 MPa).

The flow-related radial and tangential stresses (σ_{sr} and $\sigma_{s\theta}$, respectively) are computed by equations analogous to differential thermal expansion (Timoshenko and Goodier 1970):

$$\sigma_{sr}(r) = \frac{2\beta}{r^3}\left(\frac{1-2\upsilon}{1-\upsilon}\right)\int_{r_{cav}}^{r}\left(P(s) - P_{ff}\right)s^2 ds \qquad \text{(PA.150)}$$

$$\sigma_{s\theta}(r) = -\beta\left(\frac{1-2\upsilon}{1-\upsilon}\right)\left(\frac{1}{r^3}\int_{r_{cav}}^{r}\left(P(s) - P_{ff}\right)s^2 ds - \left(P(r) - P_{ff}\right)\right) \qquad \text{(PA.151)}$$

where P_{ff} is the initial repository pressure, and υ is Poisson's ratio (0.38).

Since stresses are calculated as quasi-static, an initial stress reduction caused by an instantaneous pressure drop at the cavity face propagates instantaneously through the waste. Consequently Equation (PA.148) allows an instantaneous early-time tensile failure of the entire repository if the boundary pressure is allowed to change suddenly. This behavior is nonphysical and arises solely from the quasi-static stress assumption, combined with the true transient pore pressure and flow-related stress equations. To prevent this nonphysical behavior, tensile failure propagation is limited by a tensile failure velocity (1,000 m/s; see Hansen et al. 1997). This limit has no quantitative effect on the results, other than preventing nonphysical tensile failure.

At the cavity face, Equation (PA.148) and Equation (PA.150) evaluate to zero, consistent with the quasi-static stress assumption. The quasi-static stress assumption implies that the waste immediately at the cavity face cannot experience tensile failure; however, tensile failure may occur at some distance into the waste material. Consequently, the radial effective stress σ_r is averaged from the cavity boundary into the waste over a characteristic length, L_t (0.04 m). If this average radial stress $\bar{\sigma}_r$ is tensile and its magnitude exceeds the material tensile strength ($|\bar{\sigma}_r|$ > TENSLSTR), the waste is no longer capable of supporting radial stress and fails, permitting fluidization. The waste tensile strength is an uncertain parameter in the analysis (see SPALLMOD:TENSLSTR in Feng and Kicker (2025a), Table 3).

Equation (PA.150) and Equation (PA.151) evaluate shear stresses in the waste. DRSPALL does not use the waste shear stresses to calculate waste failure for spall releases. These stresses are included in this discussion for completeness.

PA-4.7.2.3.5 Waste Fluidization

Failed waste material is assumed to be disaggregated, but not in motion; it remains as a porous, bedded material lining the cavity face, and is treated as a continuous part of the repository

from the perspective of the porous flow calculations. The bedded material may be mobilized and enter the wellbore if the gas velocity in the failed material (see Equation (PA.134)) exceeds a minimum fluidization velocity, U_f. The minimum fluidization velocity is determined by solving the following quadratic equation (Cherimisinoff and Cherimisinoff 1984; Ergun 1952):

$$\frac{1.75}{a\phi^3}\left(\frac{d_p U_f \rho_g}{\eta_g}\right)^2 + 150\left(\frac{1-\phi}{a^2\phi^3}\right)\left(\frac{d_p U_f \rho_g}{\eta_g}\right) = \frac{d_p^3 \rho_g \left(\rho_w - \rho_g\right) g}{\eta_g^2} \qquad \text{(PA.152)}$$

where

a = particle shape factor (unitless)

d_p = particle diameter (m)

Fluidization occurs in the failed material to the depth at which gas velocity does not exceed the fluidization velocity; this depth is denoted by r_{fluid} and is used to determine cavity radius (Section PA-4.7.2.3.3). If fluidization occurs, the gas and waste particles mix into the cavity at the bottom of the wellbore. Because this mixing cannot be instantaneous, which would be nonphysical (much as allowing instantaneous tensile failure propagation would be nonphysical), a small artificial relaxation time, equal to the cavity radius r_{cav} divided by the superficial gas velocity $u(r_{cav})$, is imposed upon the mixing phenomenon. The fluidized material is released into the cavity uniformly over the relaxation time.

PA-4.7.3 Numerical Model

The numerical model implements the conceptual and mathematical models described above (Section PA-4.7.2). Both the wellbore and the repository domain calculations use time-marching finite differences. These are part of a single computational loop and therefore use the same time step. The differencing schemes for the wellbore and repository calculations are similar, but not identical.

PA-4.7.3.1 Numerical Method—Wellbore

The wellbore is zoned for finite differencing, as illustrated in Figure PA-31, which shows zones, zone indices, grid boundaries, volumes, and interface areas. The method is Eulerian: zone boundaries are fixed, and fluid flows across the interfaces by advection. Quantities are zone-centered, and integration is explicit in time.

To reduce computation time, an iterative scheme is employed to update the wellbore flow solution. The finite-difference scheme first solves Equation (PA.113) and Equation (PA.114) for the mass of each phase and the momentum in each grid cell.

The updated solutions to Equation (PA.113) and Equation (PA.114) are then used to compute the volume of each phase, the pressure, and the mixture velocity in each grid cell.

All of the materials (mud, salt, gas, and waste) are assumed to move together as a mixture. Because fluid moves through the cell boundaries, the calculation requires a value for the flow through each cell boundary during a time step. These values are obtained by averaging the fluid velocities at the zone centers, given by:

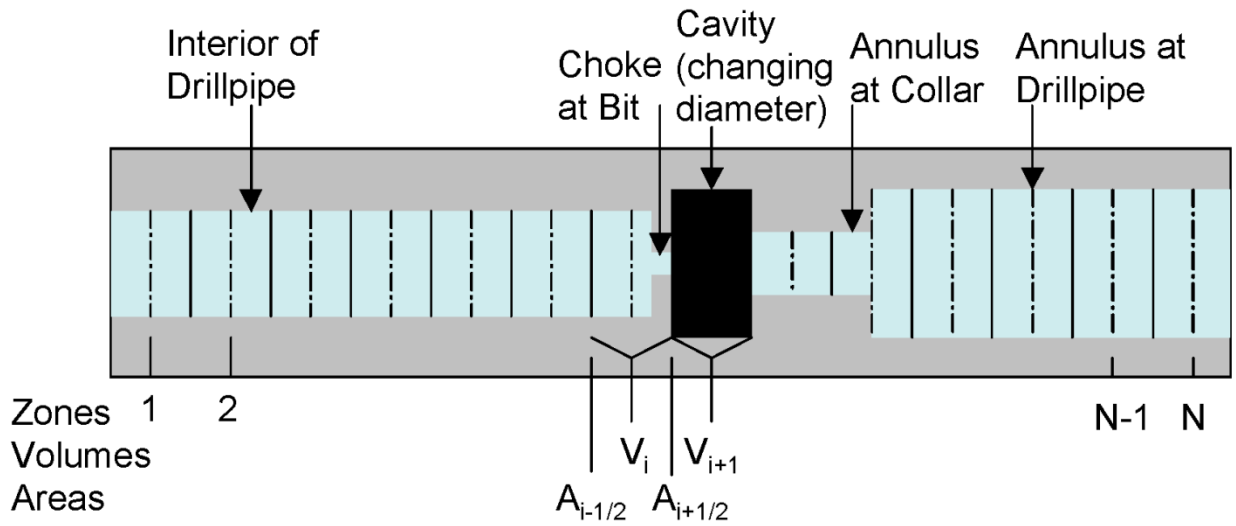


Figure PA-31. Finite-Difference Zoning for Wellbore

$$u_{i+1/2} = \frac{1}{2}\left(u_{i+1}^{n-1} + u_i^{n-1}\right) \tag{PA.153}$$

The mass transport equation, prior to any volume change, becomes:

$$V_i\ \rho_i^* = V_i \rho_i^{n-1} - \left(A_{i+1/2}\rho_{i+1/2}^{n-1}u_{i+1/2} - A_{i-1/2}\rho_{i-1/2}^{n-1}u_{i-1/2}\right)\Delta t + S_{m,i}\Delta t \tag{PA.154}$$

Here, the source terms $S_{m,i}$ correspond to material entering or exiting at the pump, cavity, and surface. The "upwind" zone-centered densities are used for the interface values, $\rho_{i+1/2}^{n-1}$ and $\rho_{i-1/2}^{n-1}$.

Finally, any changed volumes are incorporated, and numerical mass diffusion is added for stability:

$$V_i\rho_i^n = V_i\rho_i^* + \Delta z_i s \sum_{q\in\{w,m,s,g\}} \zeta_q D_{i,q} \tag{PA.155}$$

where

$$D_{i,q} = \left[A_{i+1/2}\left(\left(\rho f_q\right)_{i+1}^{n-1} - \left(\rho f_q\right)_i^{n-1}\right) - A_{i-1/2}\left(\left(\rho f_q\right)_i^{n-1} - \left(\rho f_q\right)_{i-1}^{n-1}\right)\right]$$

and ζ_q is the diffusion coefficient for phase *q*. The density ρf_q for phase *q* being diffused is calculated from the mixture density, r, and the mass fraction, f_q, of phase *q* in the referenced cell ($f_q = \rho V_{q,i}/\rho V_i$). The numerical diffusion coefficient ζ_q is chosen empirically for stability. Separate diffusion coefficients could be used for the different materials (mud, gas, etc.); however, sufficient stability is obtained by diffusing only mud and salt using the same coefficient ($\zeta_m = \zeta_s = 0.0001$ and $\zeta_w = \zeta_g = 0$).

Momentum is differenced as:

$$V_i(\rho u)_i^* = V_i(\rho u)_i^{n-1} - \Delta t\left(A_{i+1/2}(\rho u)_{i+1/2}^{n-1} u_{i+1/2} - A_{i-1/2}(\rho u)_{i-1/2}^{n-1} u_{i-1/2}\right) - V_i \Delta t\left(\frac{P_{i+1}^{n-1} - P_{i-1}^{n-1}}{2\Delta z} - \rho_i^{n-1} g + F_i^{n-1}\right) + S_{mom,i}\Delta t, \quad \text{(PA.156)}$$

where the dissipation term F_i^{n-1} is obtained from Equation (PA.119) and is constrained by:

$$\left|F_i^{n-1}\right| \le \left|\frac{P_{i+1}^{n-1} - P_{i-1}^{n-1}}{2\Delta z} - \rho_i^{n-1} g\right| \quad \text{(PA.157)}$$

and the sign of F_i^{n-1} is chosen to oppose flow. Finally, numerical momentum diffusion is added without distinguishing between phases in the mixture (*r* is the mixture density):

$$V_i\ (\rho u)_i^n = V_i\ (\rho u)_i^* - \zeta_p \Delta x_i\left[A_{i+1/2}\left((\rho u)_{i+1}^{n-1} - (\rho u)_i^{n-1}\right) - A_{i-1/2}\left((\rho u)_i^{n-1} - (\rho u)_{i-1}^{n-1}\right)\right] \quad \text{(PA.158)}$$

In PA, $\zeta_p = 0.01$.

Equation (PA.116), Equation (PA.117), and Equation (PA.118) comprise a simultaneous system of equations for the volumes of gas and mud and the pressure in the wellbore. The volumes of salt and waste are known, since they are considered incompressible. Equation (PA.116), Equation (PA.117), and Equation (PA.118) combine into a quadratic equation for gas volume:

$$aV_g^2 + bV_g - c = 0 \quad \text{(PA.159)}$$

where

$$a = 1 - c_m P_{atm}$$

$$b = c_m P_{atm} V_{g,0} - aV^* + V_{m,0}$$

$$c = V^* c_m P_{atm} V_{g,0}$$

$$V_{g,0} = {}^{m_g}/_{\rho_{g,0}}$$

$$V_{m,0} = {}^{m_m}/_{\rho_{m,0}}$$

$$V^* = V_m + V_g = V - V_s - V_w$$

The volume of the mud phase follows from Equation (PA.116) and the pressure from Equation (PA.115). Once the mixture density in each cell (ρ_i) is updated by Equation (PA.117), the mixture velocity in each cell (u_i) is computed by:

$$u_i = \frac{(\rho u)_i}{\rho_i} \tag{PA.160}$$

where the quantity ρu is determined by Equation (PA.158).

PA-4.7.3.2 Numerical Method—Repository

The time-integration method for the repository flow is implicit, with spatial derivatives evaluated after each time increment. This method requires the inversion of a matrix for the entire repository, which is usually straightforward. The implicit scheme is unconditionally stable. However, it is still necessary to use small time steps to ensure gradient accuracy.

The DRSPALL code implements Darcy flow of an isothermal ideal gas in a porous medium, allowing the simplifying pseudopressure approach. Starting with pseudopressure as defined in the DRSPALL design document (WIPP Performance Assessment 2021b, Equation 4.3.10):

$$\frac{\partial \psi}{\partial t} = \frac{D(\psi)}{r^{m-1}} \frac{\partial}{\partial r}\left(r^{m-1} \frac{\partial \psi}{\partial r} \right) + \frac{D(\psi)}{k'} \frac{\partial k'}{\partial r} \frac{\partial \psi}{\partial r} \tag{PA.161}$$

where k', ϕ, and η are as defined in Section PA-4.7.2.2, ψ is the pseudopressure, and:

$$D(\psi) = \frac{k'}{\phi} \sqrt{\frac{\psi}{\eta}} = \frac{k'p}{\phi\eta} \tag{PA.162}$$

Note also that:

$$\frac{\partial \ln k'}{\partial r} = \frac{1}{k'} \frac{\partial k'}{\partial r} \tag{PA.163}$$

Substituting Equation (PA.163) into Equation (PA.161) yields:

$$\frac{\partial \psi}{\partial t} = \frac{D(\psi)}{r^{m-1}} \frac{\partial}{\partial r}\left(r^{m-1} \frac{\partial \psi}{\partial r} \right) + D(\psi) \frac{\partial \ln(k')}{\partial r} \frac{\partial \psi}{\partial r} \tag{PA.164}$$

Expansion of the first term on the right-hand side of Equation (PA.164) yields:

$$\begin{aligned}\frac{D(\psi)}{r^{m-1}}\frac{\partial}{\partial r}\left(r^{m-1}\frac{\partial\psi}{\partial r}\right) &= D(\psi)\left[\frac{1}{r^{m-1}}\frac{\partial}{\partial r}\left(r^{m-1}\frac{\partial\psi}{\partial r}\right)\right] \\ &= D(\psi)\left[\frac{1}{r^{m-1}}r^{m-1}\frac{\partial}{\partial r}\left(\frac{\partial\psi}{\partial r}\right)+\frac{\partial\psi}{\partial r}\frac{1}{r^{m-1}}\frac{\partial\left(r^{m-1}\right)}{\partial r}\right] \\ &= D(\psi)\left[\frac{\partial^2\psi}{\partial r^2}+\frac{\partial\psi}{\partial r}\frac{1}{r^{m-1}}(m-1)\left(r^{m-2}\right)\frac{\partial r}{\partial r}\right] \\ &= D(\psi)\left[\frac{\partial^2\psi}{\partial r^2}+\frac{(m-1)}{r}\frac{\partial\psi}{\partial r}\right] \end{aligned} \quad \text{(PA.165)}$$

Substituting Equation (PA.165) into Equation (PA.164) gives:

$$\frac{\partial\psi}{\partial t} = D(\psi)\left[\frac{\partial^2\psi}{\partial r^2}+\frac{(m-1)}{r}\frac{\partial\psi}{\partial r}+\frac{\partial\ln(k')}{\partial r}\frac{\partial\psi}{\partial r}\right] \quad \text{(PA.166)}$$

PA-4.7.3.2.1 Finite Difference Discretization

Equation (PA.166) is nonlinear due to the dependence of the parameter *D* on the state variable ψ. Hence, its numerical solution would normally require an iterative scheme such as the Newton-Raphson method. However, as discussed in Lord et al. (2006), $D(\psi)$ is assumed constant over a zone, which simplifies the numerical implementation.

Using an implicit scheme, Equation (PA.166) can be represented in finite difference form by using the central difference method to discretize the right-hand side and the forward difference method to discretize the left-hand side (Özişik 1993, Chapter 12, "Implicit Method").

This gives:

$$\begin{aligned}\frac{\psi_j^{n+1}-\psi_j^n}{\Delta t} = D\left(\psi_j^{n+1}\right)\Bigg[&\frac{\psi_{j+1}^{n+1}-2\psi_j^{n+1}+\psi_{j-1}^{n+1}}{(\Delta r)^2}+\frac{(m-1)}{r_j}\frac{\left(\psi_{j+1}^{n+1}-\psi_{j-1}^{n+1}\right)}{2\Delta r} \\ &+\frac{\left(\ln\left(k'^{n+1}_{j+1}\right)-\ln\left(k'^{n+1}_{j-1}\right)\right)}{2\Delta r}\frac{\left(\psi_{j+1}^{n+1}-\psi_{j-1}^{n+1}\right)}{2\Delta r}\Bigg]\end{aligned} \quad \text{(PA.167)}$$

Using its zone-centered value at the current time, the linearizing approximation $D(\psi)\approx D\left(\psi_j^{n+1}\right)\approx D\left(\psi_j^{n}\right)\approx D_j^n$ is obtained. Equation (PA.167) then becomes:

$$\frac{\psi_j^{n+1}-\psi_j^{n}}{\Delta t}=D_j^n\left[\frac{\psi_{j+1}^{n+1}-2\psi_j^{n+1}+\psi_{j-1}^{n+1}}{\left(\Delta r\right)^2}+\frac{\left(\psi_{j+1}^{n+1}-\psi_{j-1}^{n+1}\right)}{2\Delta r}\left(\frac{\left(m-1\right)}{r_j}+\frac{\left(\ln\left(k'^{n+1}_{j+1}\right)-\ln\left(k'^{n+1}_{j-1}\right)\right)}{2\Delta r}\right)\right]$$

Solving for ψ_j^n and collecting similar terms:

$$\begin{aligned}\psi_j^n&=\psi_j^{n+1}-D_j^n\Delta t\left[\frac{\psi_{j+1}^{n+1}-2\psi_j^{n+1}+\psi_{j-1}^{n+1}}{\left(\Delta r\right)^2}+\frac{\left(\psi_{j+1}^{n+1}-\psi_{j-1}^{n+1}\right)}{2\Delta r}\left(\frac{\left(m-1\right)}{r_j}+\frac{\left(\ln\left(k'^{n+1}_{j+1}\right)-\ln\left(k'^{n+1}_{j-1}\right)\right)}{2\Delta r}\right)\right]\\&=-D_j^n\Delta t\left[\frac{1}{\left(\Delta r\right)^2}-\frac{1}{2\Delta r}\left(\frac{\left(m-1\right)}{r_j}+\frac{\left(\ln\left(k'^{n+1}_{j+1}\right)-\ln\left(k'^{n+1}_{j-1}\right)\right)}{2\Delta r}\right)\right]\psi_{j-1}^{n+1}+\left[1+\frac{2D_j^n\Delta t}{\left(\Delta r\right)^2}\right]\psi_j^{n+1}\\&\quad-D_j^n\Delta t\left[\frac{1}{\left(\Delta r\right)^2}+\frac{1}{2\Delta r}\left(\frac{\left(m-1\right)}{r_j}+\frac{\left(\ln\left(k'^{n+1}_{j+1}\right)-\ln\left(k'^{n+1}_{j-1}\right)\right)}{2\Delta r}\right)\right]\psi_{j+1}^{n+1}\\&=-\frac{D_j^n\Delta t}{\Delta r}\left[\frac{1}{\Delta r}-\frac{\left(m-1\right)}{2r_j}-\frac{\left(\ln\left(k'^{n+1}_{j+1}\right)-\ln\left(k'^{n+1}_{j-1}\right)\right)}{4\Delta r}\right]\psi_{j-1}^{n+1}+\left[1+\frac{2D_j^n\Delta t}{\left(\Delta r\right)^2}\right]\psi_j^{n+1}\\&\quad-\frac{D_j^n\Delta t}{\Delta r}\left[\frac{1}{\Delta r}+\frac{\left(m-1\right)}{2r_j}+\frac{\left(\ln\left(k'^{n+1}_{j+1}\right)-\ln\left(k'^{n+1}_{j-1}\right)\right)}{4\Delta r}\right]\psi_{j+1}^{n+1}\end{aligned}$$

Noting that:

$$\ln\left(k'^{n+1}_{j+1}\right)-\ln\left(k'^{n+1}_{j-1}\right)=\ln\left(k'^{n+1}_{j+1}\Big/k'^{n+1}_{j-1}\right)$$

it follows that:

$$\begin{aligned}\psi_j^n&=-\frac{D_j^n\Delta t}{\Delta r}\left(\frac{1}{\Delta r}-\frac{\left(m-1\right)}{2r_j}-\frac{\ln\left(k'^{n+1}_{j+1}\Big/k'^{n+1}_{j-1}\right)}{4\Delta r}\right)\psi_{j-1}^{n+1}+\left(1+\frac{2D_j^n\Delta t}{\left(\Delta r\right)^2}\right)\psi_j^{n+1}\\&\quad-\frac{D_j^n\Delta t}{\Delta r}\left(\frac{1}{\Delta r}+\frac{\left(m-1\right)}{2r_j}+\frac{\ln\left(k'^{n+1}_{j+1}\Big/k'^{n+1}_{j-1}\right)}{4\Delta r}\right)\psi_{j+1}^{n+1}\end{aligned}$$

Rewriting the equation:

$$\psi_j^n = -\alpha_1 \psi_{j-1}^{n+1} + (1+2\alpha)\psi_j^{n+1} - \alpha_2 \psi_{j+1}^{n+1} \quad \text{(PA.168)}$$

where

$$\alpha = \frac{D_j^n \Delta t}{(\Delta r)^2}$$

$$\alpha_1 = \frac{D_j^n \Delta t}{\Delta r}\left(\frac{1}{\Delta r} - \frac{(m-1)}{2r_j} - Forchterm\right)$$

$$\alpha_2 = \frac{D_j^n \Delta t}{\Delta r}\left(\frac{1}{\Delta r} + \frac{(m-1)}{2r_j} + Forchterm\right)$$

$$Forchterm = \frac{\ln\left(k'^{n+1}_{j+1} \big/ k'^{n+1}_{j-1}\right)}{4\Delta r}$$

and *j* and *n* are the cell and timestep indices, respectively.

Also:

$$\alpha_1 + \alpha_2 = \frac{D_j^n \Delta t}{\Delta r}\left(\frac{1}{\Delta r} - \frac{(m-1)}{2r_j} - \frac{\ln\left(k'^{n+1}_{j+1} \big/ k'^{n+1}_{j-1}\right)}{4\Delta r}\right) + \frac{D_j^n \Delta t}{\Delta r}\left(\frac{1}{\Delta r} + \frac{(m-1)}{2r_j} + \frac{\ln\left(k'^{n+1}_{j+1} \big/ k'^{n+1}_{j-1}\right)}{4\Delta r}\right)$$

$$= \frac{D_j^n \Delta t}{\Delta r}\left(\frac{1}{\Delta r} + \frac{1}{\Delta r}\right)$$

$$= 2\frac{D_j^n \Delta t}{(\Delta r)^2}$$

$$\alpha_1 + \alpha_2 = 2\alpha$$

PA-4.7.3.2.2 Boundary Conditions

For the boundary condition at the inner radius, we use the method given in Thomas (1995, Section 1.6.3, "Cell Centered Grids") for cell-centered grids. Using this method, the difference equation is derived on the second cell in the usual manner (here, the central difference method). The first intact zone is the zone closest to the borehole and is indexed as 1. The boundary condition is implemented by noting that for the first intact cell ($j - 1 = 1$), ψ_1^{n+1} is the cavity pseudopressure, ψ_{cav}^{n+1}, which is known. Therefore, $\psi_1^{n+1} = \psi_{cav}^{n+1}$ can be moved to the left-hand side of Equation (PA.168).

Using $j = 2$, the second cell, Equation (PA.168) gives:

$$\psi_2^n + \alpha_1 \psi_{cav}^{n+1} = (1 + 2\alpha)\psi_2^{n+1} - \alpha_2 \psi_3^{n+1} \quad \text{(PA.169)}$$

The far field boundary condition is a zero-gradient condition. Mathematically, this is:

$$\left.\frac{\partial \psi}{\partial r}\right|_{r=\infty} = 0 \quad \text{(PA.170)}$$

Discretizing using a second-order central difference formulation:

$$\begin{aligned} &\frac{\psi_{N+1}^{n+1} - \psi_{N-1}^{n+1}}{2\Delta r} = 0 \\ &\psi_{N+1}^{n+1} = \psi_{N-1}^{n+1} \end{aligned} \quad \text{(PA.171)}$$

Using Equation (PA.171) to eliminate the fictitious point in the domain discretization of Equation (PA.168), at node point $j = N$ (i.e., the final cell):

$$\begin{aligned} \psi_N^n &= -\alpha_1 \psi_{N-1}^{n+1} + (1+2\alpha)\psi_N^{n+1} - \alpha_2 \psi_{N+1}^{n+1} \\ &= -\alpha_1 \psi_{N-1}^{n+1} + (1+2\alpha)\psi_N^{n+1} - \alpha_2 \psi_{N-1}^{n+1} \\ &= -(\alpha_1 + \alpha_2)\psi_{N-1}^{n+1} + (1+2\alpha)\psi_N^{n+1} \end{aligned}$$

Using $\alpha_1 + \alpha_2 = 2\alpha$, the final condition can be simplified to:

$$\psi_N^n = -(2\alpha)\psi_{N-1}^{n+1} + (1 + 2\alpha)\psi_N^{n+1} \quad \text{(PA.172)}$$

Özişik (1993) shows that the error involved with the central difference representation Equation (PA.172) is second-order accurate, i.e., $O((\Delta r)^2)$; whereas the error involved with a forward difference representation would be first-order accurate, i.e., $O(\Delta r)$. Therefore, the central difference formulation, Equation (PA.172), is used because it decreases numerical discretization errors and provides a more accurate numerical approximation.

PA-4.7.3.2.3 Summary of Finite Difference Equations

From Equation (PA.172), the tri-diagonal linear system of equations is:

$$\begin{aligned} \psi_j^n &= -\alpha_1 \psi_{cav}^{n+1} + (1+2\alpha)\psi_j^{n+1} - \alpha_2 \psi_{j+1}^{n+1} && \text{for } j = 2 \\ \psi_j^n &= -\alpha_1 \psi_{j-1}^{n+1} + (1+2\alpha)\psi_j^{n+1} - \alpha_2 \psi_{j+1}^{n+1} && \text{for } j = 3,\ldots, N-1 \\ \psi_j^n &= -(2\alpha)\psi_{j-1}^{n+1} + (1+2\alpha)\psi_j^{n+1} && \text{for } j = N \end{aligned} \quad \text{(PA.173)}$$

where α, α_1, α_2, *and Forchterm* are defined following Equation (PA.168).

Figure PA-32 illustrates the expansion point (*j*, *n*+1) and the surrounding finite-difference stencil.

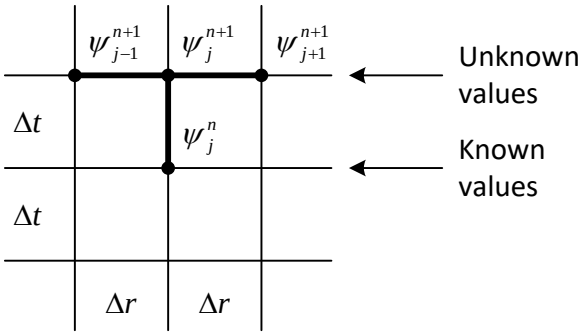


Figure PA-32. Finite Difference Molecules for the Implicit Scheme using Constant Zone Sizes

PA-4.7.3.3 Numerical Method—Wellbore to Repository Coupling

The term u_{rep}, appearing in Equation (PA.142), is the gas velocity in the repository at the waste-cavity interface and is determined from the pressure gradient inside the waste. DRSPALL uses the pressure (*P*1) at the center of the first numerical zone in the waste to determine u_{rep}:

$$u_{rep} = \frac{k\left(P_1 - P_{cav}\right)}{\eta_g \phi \Delta r} \qquad \text{(PA.174)}$$

PA-4.7.4 Implementation in the PA

During development of the spallings model, spall volume was determined to be potentially sensitive to five inputs (Hansen et al. 2003; Lord and Rudeen 2003): repository pressure, local waste permeability, local waste porosity, waste particle diameter and waste tensile strength. All five inputs relate to the repository conditions or the state of the waste at the time of intrusion. Of these parameters, repository pressure (initial repository pressure in Equation (PA.137) and P_{ff} in Equation (PA.150)), had the greatest effect on spall volume.

The computational requirements of DRSPALL discourage calculation of spall volumes for conditions at the time of each simulated intrusion. Instead, DRSPALL calculations were performed for repository pressures of 10, 12, 14, and 14.8 MPa. Sensitivity studies showed that spall does not occur at pressures below 10 MPa; in DRSPALL, the repository pressure cannot exceed the far-field confining stress (14.8 MPa).

The other four inputs (Table PA-13) are considered in the sample of uncertain parameters. Spall volumes are computed for each combination of initial pressure and sample element, for a total of $4 \times 300 = 1{,}200$ calculations. Although repository porosity could have been treated as an initial condition using the time-dependent values computed by BRAGFLO, to reduce the number of computational cases and ensure that extreme porosity values were represented.

Table PA-13. Uncertain Parameters in DRSPALL Calculations

Quantity	Property Name	Implementation
Repository Permeability	REPIPERM	Permeability (m^2) of waste local to the intrusion borehole, implemented by parameter SPALLMOD:REPIPERM (Feng and Kicker 2025a, Table 3). Log-uniform distribution from 2.4×10^{-14} to 2.4×10^{-12}. Defines k in Equation (PA.134).
Repository Porosity	REPIPOR	Porosity (dimensionless) of waste local to the intrusion borehole, implemented by parameter SPALLMOD:REPIPOR (Feng and Kicker 2025a, Table 3). Uniform distribution from 0.35 to 0.66. Defines $\emptyset$ in Equation (PA.133).
Particle Diameter	PARTDIAM	Particle diameter of waste (m) after tensile failure, implemented by parameter SPALLMOD:PARTDIAM (Feng and Kicker 2025a, Table 3). Log-uniform distribution from 0.001 to 0.1 (m). Defines d_p in Equation (PA.152).
Tensile Strength	TENSLSTR	Tensile strength of waste (Pa), implemented by parameter SPALLMOD:TENSLSTR (Feng and Kicker 2025a, Table 3). Uniform distribution from 0.12 MPa to 0.17 MPa. Defines maximum $\bar{\sigma}_r$ for Section PA-4.7.2.3.4.

The spallings submodel of the code CUTTINGS_S uses the DRSPALL results to compute the spall volume for a given initial pressure P. If $P < 10$ MPa or $P > 14.8$ MPa, the spall volume is the value computed at the repository pressure of 10 MPa or 14.8 MPa, respectively. If P falls between 10 and 14.8 MPa, the spall volume is determined by linear interpolation between the DRSPALL results for pressures bracketing P.

PA-4.7.5 Additional Information

Additional information on DRSPALL can be found in the DRSPALL design document (WIPP Performance Assessment 2021b) and in the analysis package for cuttings, cavings, and spallings releases (Brunell and Kicker 2025). Additional information on the construction of spall volumes by the code CUTTINGS_S can be found in the CUTTINGS_S design document (WIPP Performance Assessment 2021a).

PA-4.8 DBR to Surface: BRAGFLO

This section describes the model used to estimate DBR volumes, defined as volumes of brine released to the ground surface at the time of a drilling intrusion into the repository.

A DBR may occur if the brine pressure in the repository at the time of a drilling intrusion exceeds 8 MPa, which corresponds to the hydrostatic pressure exerted by a column of drilling fluid at repository depth (Stoelzel and O'Brien 1996). Exceedance of this pressure threshold alone, however, does not ensure that a DBR will occur. For brine to flow toward and up the

intruding borehole, sufficient mobile brine must be present in the waste. Accordingly, the brine saturation in the intruded waste region must exceed the residual brine saturation of the waste material.

DBRs are estimated for the following cases (see Section PA-6.3.4):

- An initial drilling intrusion into a waste panel located in the lower (down-dip), middle, upper (up-dip), or other repository region.
- A drilling intrusion into a waste panel that is preceded by an E1 intrusion into the same waste panel, an adjacent panel, a nonadjacent panel, or another waste panel.
- A drilling intrusion into a waste panel that is preceded by an E2 intrusion into the same waste panel, an adjacent panel, a nonadjacent panel, or another waste panel.

To evaluate DBR volumes for these cases, calculations are performed using a computational grid that explicitly represents the waste panels and associated repository features (Figure PA-33). The DBR grid is defined in the areal (x–y) plane and is one element thick in the vertical (z) direction, with a constant height. The grid includes representations of salt pillars, disposal rooms, panel closures, open panel-closure regions, waste-containing passageways, and the DRZ. The DRZ representation incorporates a one-degree southerly dip through the excavated regions, consistent with the Salado formation geometry (Equation (PA.26).

DBRs are assumed to occur over a relatively short time interval following a drilling intrusion, ranging from 3 to 4.5 days (see Section PA-4.8.8). Initial conditions for the DBR simulations are obtained by mapping brine pressure and brine saturation from the Salado flow model (Section PA-4.2) onto the DBR computational grid. Volume-averaged pressures and saturations from the Salado flow grid (Figure PA-12) are transferred to corresponding waste regions in the DBR grid using a region-based mapping approach (Figure PA-33). The correspondence between regions in the Salado flow grid and the DBR grid is illustrated in Figure PA-34 and described in detail in Zeitler (2025, Figure 4). DBR volumes are calculated using the BRAGFLO code, which is also used to compute two-phase flow in and around the repository in the Salado flow simulations (Section PA-4.2).

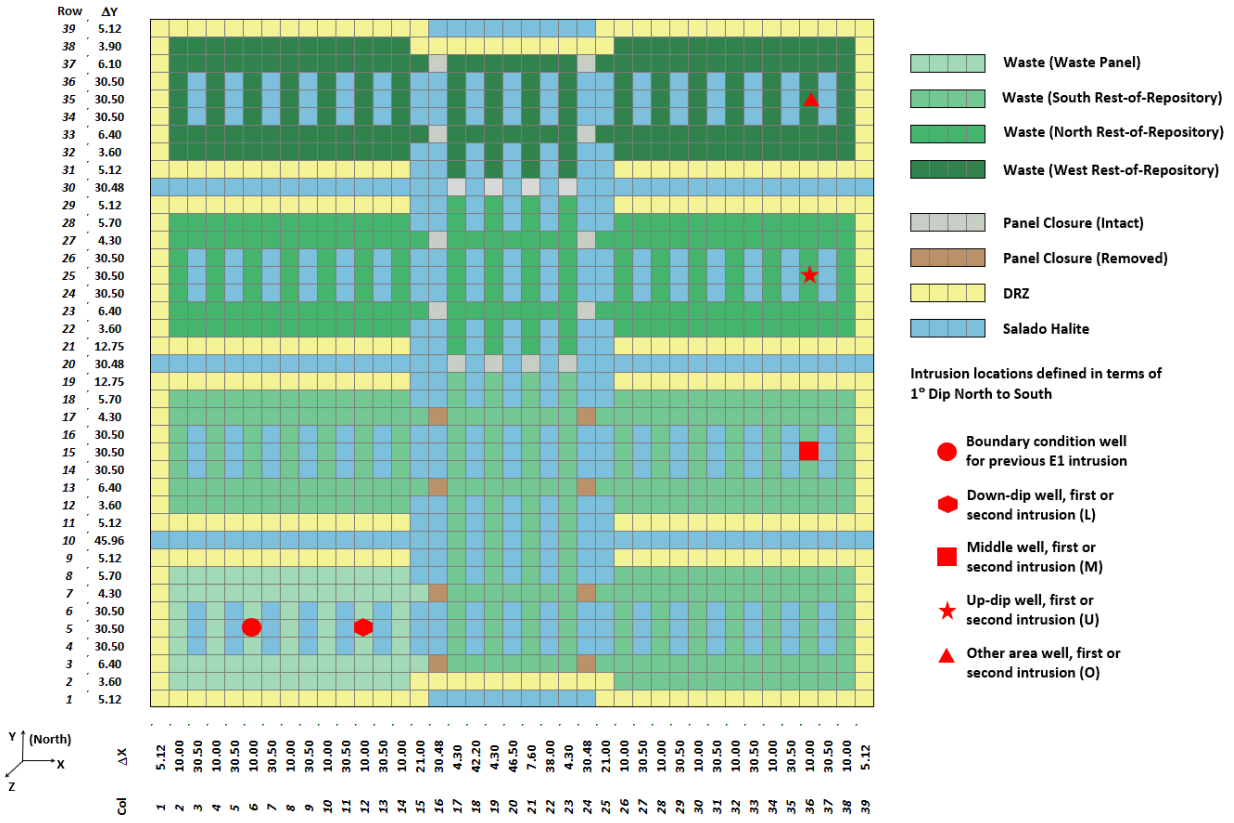


Figure PA-33. CRA-2026 grid for DBR (Δx, Δy, and Δz dimensions in meters)

Conceptually, the DBR volume associated with a drilling intrusion is given by:

$$V_{DBR} = \int_0^{t_e} rDBR(t)dt \qquad \text{(PA.175)}$$

where

V_{DBR} = DBR volume (m^3) for the drilling intrusion

$rDBR(t)$ = rate (m^3/s) at time t at which brine flows up the intruding borehole

t = elapsed time (s) since the drilling intrusion

t_e = time (s) at which DBR ends

The definition of $rDBR(t)$ is discussed in the following sections. Flow within the intruding borehole is represented using two-phase flow relationships (Equations (PA.18) through (PA.24)) and the Poettmann-Carpenter correlation (Poettmann and Carpenter 1952) to determine the flowing bottom-hole pressure at the connection between the borehole and the repository. The duration t_e is based on current drilling practices in the Delaware Basin (Section PA-4.8.8).

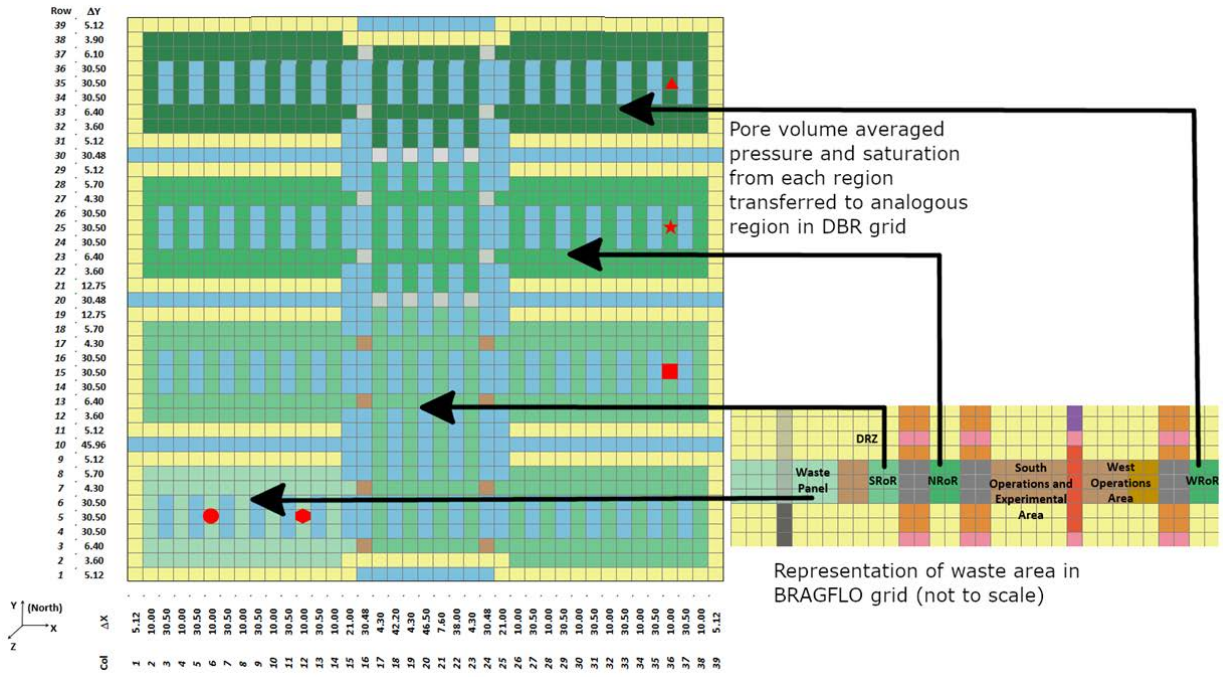


Figure PA-34. Regions Used to Transfer Initial Pressure and Saturation from the BRAGFLO Salado Grid to the DBR Grid.

PA-4.8.1 Material Properties for DBR

The vertical thickness of the DBR computational grid shown in Figure PA-33 is assigned to be equal to the crushed height of the waste, *h* (m), at the time of the drilling intrusion. The crushed height is calculated from the waste compaction relationships used in the BRAGFLO model (Section PA-4.2.4) as:

$$h = h_i \frac{1-\phi_i}{1-\phi} \qquad \text{(PA.176)}$$

where h_i and ϕ_i are the initial height (m) and initial porosity of the waste, respectively, and ϕ is the volume-averaged waste porosity at the time of intrusion (Section PA-4.2.4). The value of *h* is held constant during each DBR simulation.

Panel closure and open panel closure regions in the DBR grid are assigned porosity and permeability values equal to those of the corresponding regions in the Salado flow (BRAGFLO) calculation at the time of intrusion.

Porosity values for disturbed rock zone (DRZ) regions in the DBR grid (Figure PA-33) are initialized using a pore-volume equivalence relationship (Equation PA.177). In this relationship, $h(t_{int})$ is the crushed repository height at the time of intrusion (typically 1–1.5 m and equal to *h* in Equation (PA.176), $h_{DRZ,i}$ is the effective DRZ height (43.5 m) selected so that the DRZ pore volume represented in the DBR grid equals the initial DRZ pore volume represented in the

Salado flow grid (Figure PA-12), and $\phi_{DRZ,i}$ is the initial DRZ porosity (Table PA-5). DRZ porosity is held constant during the DBR simulation, which spans only a few days, and no time-dependent mechanical evolution of the DRZ is modeled over this interval.

$$\phi_{DRZ} = \phi_{DRZ,i} \frac{h_{DRZ,i}}{h(t_{int})} \tag{PA.177}$$

Porosity values for waste and Salado halite regions in the DBR grid are taken directly from the corresponding volume-averaged porosities of those regions in the Salado flow calculation at the time of intrusion. For waste regions, each DBR grid region is assigned the volume-averaged porosity of its corresponding Salado flow region (i.e., the waste panel, the South, North, and West Rest-of-Repository regions) at the time of intrusion.

PA-4.8.2 Initial Conditions for DBR

Initial conditions for the DBR calculations consist of brine pressure, gas saturation, and porosity. Regions in the DBR computational grid (Figure PA-33) are associated with regions in the Salado two-phase flow grid (Figure PA-12) to assign these initial conditions. The correspondence between regions in the Salado flow grid and the DBR grid is illustrated in Figure PA-34. The regional associations are as follows:

- The upper region represents the West RoR area in Figure PA-12.
- The middle region represents the North RoR area in Figure PA-12.
- The lower left region represents the farthest down-dip waste-filled area (Waste Panel) in Figure PA-12 and corresponds to the single down-dip waste panel.
- The balance of the bottom half region represents the South RoR area in Figure PA-12.
- Regions designated as panel closures, open panel-closure areas, the DRZ, and impure halite in Figure PA-33 have initial conditions set equal to the volume-averaged quantities computed for the corresponding material regions in the Salado flow grid at the time of intrusion.

The initial brine pressure $p_b(x, y, 0)$ and gas saturation $S_g(x, y, 0)$ in the grid in Figure PA-33 are assigned by:

$$p_b\left(x, y, 0\right) = \frac{\int_R \tilde{p}_b\left(\tilde{x}, \tilde{y}, t_{int}\right) dV}{\int_R dV} \tag{PA.178}$$

$$S_g\left(x, y, 0\right) = \frac{\int_R \tilde{S}_g\left(\tilde{x}, \tilde{y}, t_{int}\right) dV}{\int_R dV} \tag{PA.179}$$

where (x, y) designates a point in the grid in Figure PA-33, $\tilde{p}_b$ and $\tilde{S}_g$ denote solutions to Equations (PA.18) through (PA.24) in the Salado flow model; $\tilde{x}$ and $\tilde{y}$ denote the variables of integration, t_{int} is the time at which the drilling intrusion occurs, and *R* corresponds to the region in the BRAGFLO computational grid (Figure PA-12) that is mapped into the region in the DBR computational grid (Figure PA-33) that contains the point (*x*, *y*).

Note that t_{int} defines a time in the solution of Equations (PA.18) through (PA.24), whereas $t = 0$ defines the start time for the DBR calculation.

PA-4.8.3 Representation of the Flow Rate *rDBR*(*t*)

A DBR is driven by the difference between the waste panel pressure, p_w (Pa), and the flowing bottomhole pressure, p_{wf} (Pa), in the intruding borehole. The flowing bottomhole pressure p_{wf}, defined as the dynamic pressure at the borehole inlet to the waste panel, is less than the static panel pressure p_w due to friction and acceleration effects. The rate at which brine and gas are transported up the intruding borehole is determined by the difference $p_w - p_{wf}$ and a productivity index J_p for the intruded waste panel (Mattax and Dalton 1990, p. 79):

$$q_p(t) = J_p\left[p_w(t) - p_{wf}\right] \quad \text{(PA.180)}$$

where

$q_p(t)$ = flow rate (m^3/s) at time *t* for phase *p* (*p* = *b* ~ brine, *p* = *g* ~ gas)

J_p = productivity index (m^3/Pa s) for phase *p*

and p_w and p_{wf} are defined above. For a given drilling intrusion, J_p and p_{wf} are treated as constants, whereas $p_w(t)$ varies with time, as indicated by the temporal dependence in Equation (PA.180). Section PA-4.8.4 discusses the determination of J_p (for both gas and brine). The determination of p_{wf} is discussed in Section PA-4.8.6.

Conceptually, the DBR is given by:

$$V_{DBR} = \int_0^{t_e} rDBR(t)dt = \int_0^{t_e} J_b\left[p_w(t) - p_{wf}\right] dt \quad \text{(PA.181)}$$

once J_b (brine), $p_w(t)$ and p_{wf} are determined. Similarly, the total gas release is obtained by replacing J_b (brine) with J_g (gas) in the integral. In the computational implementation, V_{DBR} is determined as part of the numerical solution of the PDE system defining $p_w(t)$, as described in Section PA-4.8.5.

PA-4.8.4 Determination of the Productivity Index J_p

In a radial drainage area with uniform saturation, which is assumed to apply locally for flow into the intruding borehole during a DBR event, the productivity index J_p for each fluid phase p is

obtained from Darcy's law (Mattax and Dalton 1990, p. 79; Williamson and Chappelear 1981; Chappelear and Williamson 1981) as:

$$J_p = \frac{2\pi k k_{rp} h}{\mu_p \left[\ln\left(\frac{r_e}{r_w}\right) + s + c \right]} \quad \text{(PA.182)}$$

where

k = absolute permeability of waste (assumed to be constant through time at 2.4×10^{-13} m^2) (parameter WAS_AREA:PRMX_LOG in Feng and Kicker (2025a), Table 25)

k_{rp} = relative permeability to phase p (calculated with modified Brooks-Corey model in Equation (PA.30), Equation (PA.31), and Equation (PA.32)) and brine and gas saturations, S_b and S_g, obtained by mapping solutions of Equations (PA.18) through (PA.24) obtained with the grid in Figure PA-12 onto the grid in Figure PA-33 (see Section PA-4.8.2)

h = crushed panel height (Equation (PA.176))

μ_p = viscosity of fluid phase (assumed to be constant through time with $\mu_b = 1.8 \times 10^{-3}$ Pa s, and $\mu_g = 8.92 \times 10^{-6}$ Pa s (Kaufmann 1960))

r_e = external drainage radius (for use with the rectangular grid blocks in Figure PA-33, r_e is taken to be the equivalent areal radius; see Equation (PA.183))

r_w = wellbore radius (assumed to be constant through time at 0.1556 m (Gatlin 1960, Table 14.7))

c = –0.50 for pseudo-steady-state flow

s = skin factor, which is used to incorporate flow stimulation caused by cavings and spallings release (see Equation PA.184)

For the rectangular grid blocks used in the DBR grid (Figure PA-33), the external drainage radius is defined as:

$$r_e = \sqrt{(\Delta x)(\Delta y)/\pi} \quad \text{(PA.183)}$$

where Δx is the x dimension (m), and Δy is the y dimension (m) of the grid block containing the down-dip well in Figure PA-33 (Δx = 10 m and Δy = 30.5 m).

The skin factor s is determined from the volume of cuttings, cavings, and spallings associated with a drilling intrusion. Because the amount of material removed depends on local conditions

and repository pressure at the time of intrusion, the resulting skin factor may vary between intrusions. The skin factor is calculated using the petroleum engineering relationship (Lee 1982, pp. 5–7):

$$s = \left(\frac{k}{k_s} - 1 \right) \ln \left(\frac{r_s}{r_w} \right) \tag{PA.184}$$

where

k_s = permeability (m^2) of an open channel because of spallings (assumed to be infinite)

r_s = effective radius (m) of the wellbore that is expanded by the removed cavings and spallings volume

The effective radius, r_s, is obtained by converting the cuttings, cavings, and spallings volume, V_i. into a right circular cylinder of equal volume with height equal to the initial waste height (h_i), and then computing the radius of the cylinder:

$$r_s = \sqrt{\frac{V_i}{h_i \pi}} \tag{PA.185}$$

Substitution of $k_s = \infty$ into Equation (PA.184) yields:

$$s = -(1) \ln \left(\frac{\sqrt{\frac{V_i}{h_i \pi}}}{r_w} \right) \tag{PA.186}$$

PA-4.8.5 Determination of the Waste Panel Pressure $p_w(t)$ and DBR

The repository pressure, $p_w(t)$, in Equation (PA.181) following a drilling intrusion is determined using the same system of nonlinear partial differential equations (PDEs described in Section PA-4.2). These equations are solved numerically using the code BRAGFLO with the computational grid shown in Figure PA-33 and assumptions (i.e., parameter values, initial conditions, and boundary conditions) appropriate for representing brine flow toward an intruding borehole over a relatively short period immediately following the intrusion (e.g., 3 to 4.5 days). Because of the short time intervals considered, the DBR model does not include gas generation or changes in repository height due to creep closure.

Although the DBR volume associated with a drilling intrusion can be conceptually represented by the integral in Equation (PA.181), the numerical solution of the DBR model focuses on computing the time-dependent brine pressure and saturation fields within the repository.

These fields are then used to determine the brine flow rate into the intruding borehole and, ultimately, the DBR volume, as described in the following sections.

With the assumptions specific to DBR calculations, Equations (PA.18) through (PA.24) reduce to the following governing equations:

Gas Conservation $$\nabla \bullet \left[\frac{\alpha \rho_g K_g k_{rg}}{\mu_g} \left(\nabla p_g + \rho_g g \nabla h \right) \right] = \alpha \frac{\partial \left(\phi \rho_g S_g \right)}{\partial t} \quad \text{(PA.187)}$$

Brine Conservation $$\nabla \bullet \left[\frac{\alpha \rho_b K k_{rb}}{\mu_b} \left(\nabla p_b + \rho_b g \nabla h \right) \right] = \alpha \frac{\partial \left(\phi \rho_b S_b \right)}{\partial t} \quad \text{(PA.188)}$$

Saturation Constraint $$S_g + S_b = 1 \quad \text{(PA.189)}$$

Capillary Pressure Constraint $$p_g - p_b = 0 \quad \text{(PA.190)}$$

Gas Density ρ_g determined by RKS equation of state (Equation (PA.27)) (PA.191)

Brine Density $$\rho_b = \rho_0 \exp\left[c_b \left(p_b - p_{b0} \right) \right] \quad \text{(PA.192)}$$

Formation Porosity $$\phi = \phi_0 \exp\left[c_\phi \left(p_b - p_{b0} \right) \right] \quad \text{(PA.193)}$$

All symbols have the same definitions as in Equations (PA.18) through (PA.24).

The two-phase flow model used for DBR calculations differs from the Salado flow model described in Section PA-4.2 primarily in the computational grid (Figure PA-33 and Figure PA-12), initial conditions (Table PA-5 and Section PA-4.8.2), simulated time duration, and boundary conditions (Table PA-14). In the DBR calculations, brine and gas flow associated with an intruding borehole is represented through the specification of appropriate boundary conditions.

Specifically, brine flow up an intruding borehole is incorporated into Equations (PA.187) through (PA.193) by applying a pressure boundary condition at the borehole–repository connection in the waste panel (Figure PA-33). This boundary pressure is determined using the Poettmann–Carpenter wellbore flow model and is imposed as a boundary condition in the DBR calculations (Table PA-14). The details of this determination are described in Section PA-4.8.6. For scenarios that include a prior E1 intrusion, the effects of the earlier intrusion are incorporated by specifying an additional pressure boundary condition at the corresponding borehole location (Table PA-14), as described in Section PA-4.8.7.

Table PA-14. Boundary Conditions for p_b and S_g in DBR Calculations

(x, y) on Upper (Northern) or Lower (Southern) Boundary in Figure PA-33, $t \geq 0$

$\left(\nabla p_g + \rho_g g \nabla h\right)\Big\|_{(x,y,t)} \cdot j = 0 \;\; Pa/m$	No gas flow condition
$\left(\nabla p_b + \rho_b g \nabla h\right)\Big\|_{(x,y,t)} \cdot j = 0 \;\; Pa/m$	No brine flow condition

(x, y) on Right (Eastern) or Left (Western) Boundary in Figure PA-33, $t \geq 0$

$\left(\nabla p_g + \rho_g g \nabla h\right)\Big\|_{(x,y,t)} \cdot i = 0 \;\; Pa/m$	No gas flow condition
$\left(\nabla p_b + \rho_b g \nabla h\right)\Big\|_{(x,y,t)} \cdot i = 0 \;\; Pa/m$	No brine flow condition

(x, y) at Location of Drilling Intrusion under Consideration (see indicated points in Figure PA-33), $t \geq 0$

$p_b(x, y, t) = p_{wf}$ (see Section PA-4.8.6)	Constant pressure condition

(x, y) at Location of Prior Drilling Intrusion (see indicated point in Figure PA-33), $t \geq 0$

$p_b(x, y, t) = p_{wE1}$ (see Section PA-4.8.7)	Constant pressure condition

PA-4.8.6 Boundary Value Pressure p_{wf}

The boundary value pressure p_{wf} at the inlet of the intruding borehole is defined by a system of equations of the following form:

$$\frac{dp}{dh} = G\left(q_b\left[p(0)\right], q_g\left[p(0)\right], p(h), h\right), \quad 0 \leq h \leq 655m \tag{PA.194}$$

$$p(655) = 1.013 \times 10^5 \;\; Pa \tag{PA.195}$$

$$q_b\left[p(0)\right] = J_b\left[p_w - p(0)\right] \tag{PA.196}$$

$$q_g\left[p(0)\right] = J_g\left[p_w - p(0)\right] \tag{PA.197}$$

where $p(h)$ is pressure (Pa) at elevation h in the borehole, with h = 0 m corresponding to the entry point of the borehole into the waste panel and h = 655 m corresponding to the land surface (Figure PA-35); G is a function (Pa/m) characterizing the change of pressure with elevation in the borehole; $p(655)$ is an initial value condition requiring that pressure at the land surface (i.e., the outlet point of the borehole) be equal to atmospheric pressure; $q_b[p(0)]$ and $q_g[p(0)]$ define brine and gas flow rates (m^3/s) into the borehole; J_b and J_g are productivity

indexes (m^3/Pa s) (see Equation (PA.205); and p_w is the pressure (Pa) in the waste panel at the time of the drilling intrusion.

The boundary value pressure p_{wf} is determined by the numerical solution *p* of Equation (PA.194) at *h*=0, subject to the constraints in Equation (PA.195), Equation (PA.196), and Equation (PA.197):

$$p_{wf} = p(0) \tag{PA.198}$$

Equation PA.194 is solved at each DBR time step using the instantaneous repository pressure, $p_w(t_{int})$, for p_w. Pressure $p_w(t_{int})$ is obtained from the solution of Equations (PA.18) through (PA.24) with the computational grid in Figure PA-12 (see Section PA-4.8.5). The production indexes J_b and J_g are defined in Equation (PA.182). Thus, the only quantity remaining to be specified in Equations (PA.194) through (PA.197) is the function *G*.

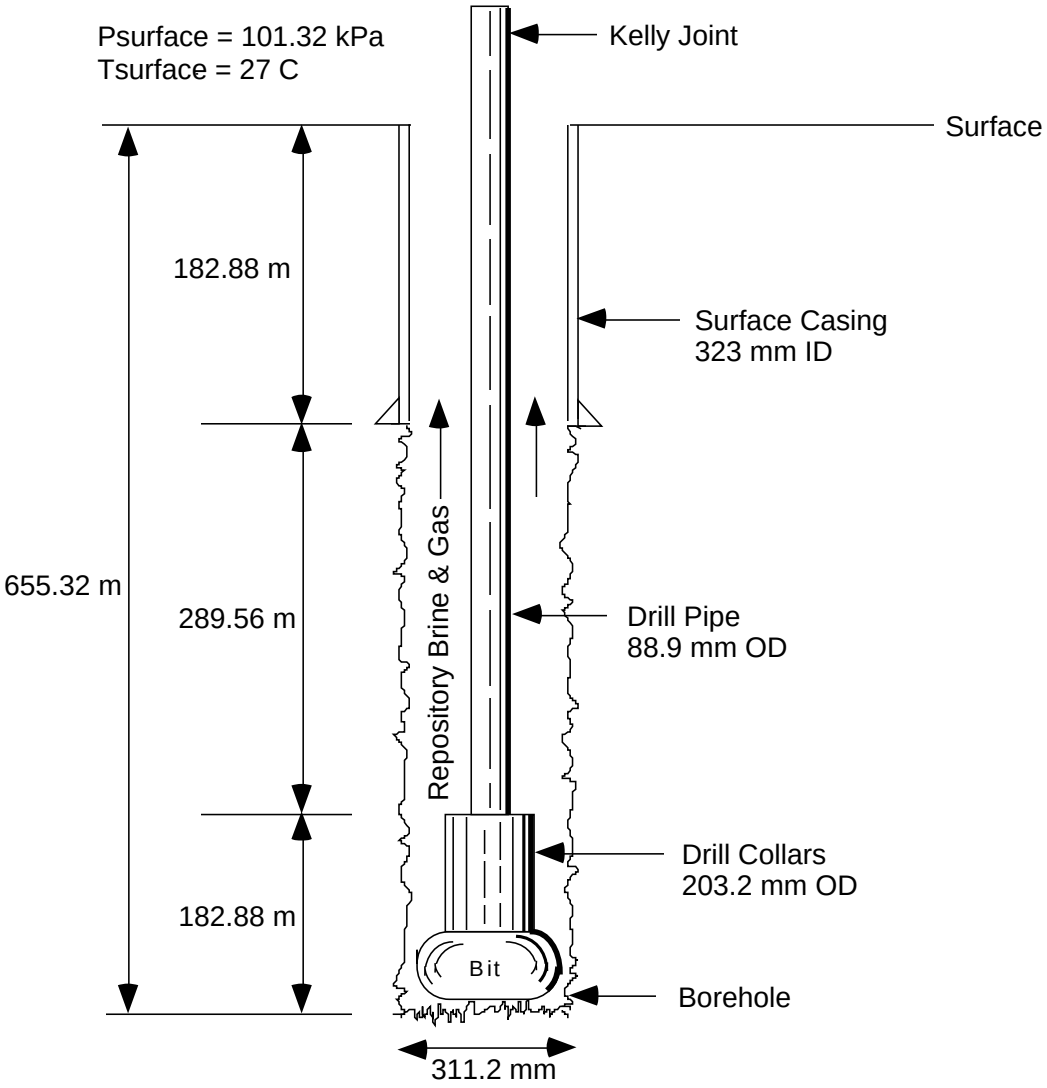


Figure PA-35. Borehole Representation Used for Poettmann-Carpenter Correlation (adapted from U.S. DOE 2004).

Brine and gas flow up a borehole is governed by complex physics dependent on frictional effects and two-phase fluid properties. This phenomenon has been widely studied in the petroleum industry and many modeling procedures have been developed to predict flow rates and pressures in vertical two-phase pipe flow (i.e., to define *G* in Equation (PA.194)) (Brill and Beggs 1986). The Poettmann-Carpenter model (Poettmann and Carpenter 1952; Welchon et al. 1962) was used to define *G* because it accounts for multiphase frictional effects based on empirical (i.e., field) data from flowing wells, is one of the few modeling approaches that included annular flow data in its development and is relatively easy to implement. Specifically, the Poettmann-Carpenter model defines *G* by:

$$G\left(q_b\left[p(0)\right], q_g\left[p(0)\right], p(h), h\right) = gm(h) + f'\left(m(h), D(h), q_b\left[p(0)\right]\right) gm(h) F^2(h) / D^5(h) \quad \text{(PA.199)}$$

where

g = acceleration due to gravity (9.8 m/s^2)

$m(h)$ = density (kg/m^3) of fluids (i.e., gas and brine) in wellbore at elevation h (Note: $m(h)$ is a function of $q_b[p(0)]$ and $q_g[p(0)]$; see Equation (PA.200))

$f'\left\{m(h), D(h) q_b\left[p(0)\right]\right\}$ = empirically defined scale factor (m/s^2) (Note: f' is the scale factor in the Poettmann-Carpenter model for fluid flow in a wellbore (Poettmann and Carpenter 1952); see discussion below)

$F(h)$ = flow rate (m^3/s) of fluids (i.e., gas and brine) in wellbore at elevation h (Note: $F(h)$ is a function of $q_b[p(0)]$ and $q_g[p(0)]$; see Equation (PA.201))

$D(h)$ = effective diameter (m) of wellbore (see Equation (PA.204))

The first term, $gm(h)$, in Equation (PA.199) accounts for the contribution of elevation to pressure; the second term accounts for frictional effects (Poettmann and Carpenter 1952). The fluid density $m(h)$ at elevation h is given by:

$$m(h) = \frac{q_b\left[p(0)\right]\rho_b\left[p(0)\right] + q_g\left[p(0)\right]\rho_g\left[p(0)\right]}{F(h)} \quad \text{(PA.200)}$$

where

$$F(h) = q_b\left[p(0)\right] + \frac{z(h)\,p(h)}{p(0)} q_g\left[p(0)\right] \quad \text{(PA.201)}$$

and

$\rho_b[p(0)]$ = density (kg/m^3) of brine at pressure $p(0)$ and temperature 300.1 K, which is fixed at 1,230 kg/m^3

$\rho_g[p(0)]$ = density (kg/m^3) of H_2 at pressure $p(0)$ and temperature 300.1 K (see Equation (PA.202))

$z(h)$ = z-factor for compressibility of H_2 at elevation h (Note: $z(h)$ is a function of $p(h)$; see Equation (PA.203)), and $q_b[p(0)]$ and $q_g[p(0)]$ are defined in Equations (PA.194) through (PA.197)

The gas density in Equation (PA.200) is obtained from the universal gas law, $PV = nRT$, by:

$$\rho_g\left[p(0)\right] = C_{m,kg}\frac{n}{V} = C_{m,kg}\frac{P}{RT} \quad \text{(PA.202)}$$

where n is the amount of gas (mol) in a volume V, $C_{m,kg}$ is the conversion factor from moles to kilograms for H_2 (i.e., 2.02×10^{-3} kg/mol), $P = p(0)$, $R = 8.3145$ J/mol K, and $T = 300.1$ K. The z-factor is given by:

$$z(h) = 1 + \left(8.54 \times 10^{-8}\ \text{Pa}^{-1}\right) p(h) \quad \text{(PA.203)}$$

and was obtained from calculations performed with the SUPERTRAPP program (Ely and Huber 1992) for pure H_2 and a temperature of 300.1 K (Stoelzel and O'Brien 1996, Figure 4.7.4). The preceding approximation to $z(h)$ was obtained by fitting a straight line between the results for pressures of 0 pounds per square inch absolute (psia) and 3,000 psia and a H_2 mole fraction of 1 in Stoelzel and O'Brien (1996, Figure 4.7.4). The z-factor values used in the DBR calculations were obtained using the more complex, but numerically similar, regression model reported in Stoelzel and O'Brien (1996, Figure 4.7.4). The numerator and denominator in Equation (PA.200) involve rates, with the time units canceling to give $m(h)$ in units of kg/m^3.

The effective diameter $D(h)$ in Equation (PA.199) is defined with the hydraulic radius concept. Specifically:

$$D^5(h) = \left[D_o(h) + D_i(h)\right]^2\left[D_o(h) - D_i(h)\right]^3 \quad \text{(PA.204)}$$

where $D_i(h)$ and $D_o(h)$ are the inner and outer diameters (m) of the wellbore at elevation $h(m)$ (see Figure PA-35). The factor f' in Equation (PA.199) is a function of $m(h)$, $D(h)$, and $q_b[p(0)]$.

The following iterative procedure based on the bisection method was used to approximate solutions to Equations (PA.194) through (PA.197).

Step 1. Estimate $p(0)$ using a bisection algorithm:

The initial guess for $p(0)$ is the midpoint $\frac{1}{2}p_w$ of interval [0, p_w], where p_w is the local repository pressure in the DBR grid region intersected by the drilling intrusion at the time of intrusion used in Equations (PA.194) through (PA.197).

The next guess for $p(0)$ is at the midpoint of either $\left[0, \frac{1}{2} p_w\right]$ or $\left[\frac{1}{2} p_w, p_w\right]$, depending on whether the resultant approximation to $p(655)$ is above or below atmospheric pressure.

Subsequent guesses for $p(0)$ are made in a similar manner.

Step 2. Use $p(0)$, known values for J_b, J_g, and p_w, and Equations (PA.194) through (PA.197) to determine $q_b[p(0)]$ and $q_g[p(0)]$.

Step 3. Use the bisection method with Δh = 25 ft = 7.62 m and appropriate changes in annular diameter (Figure PA-35) to determine $p(655)$ (i.e., $p(h + \Delta h) = p(h) + G(q_b[p(0)], q_g[p(0)], p(h), h), \Delta h)$).

Step 4. Stop if $p(655)$ is within 0.07% of atmospheric pressure (i.e., if $|1.013\times10^5 \text{ Pa} - p(655)| \leq 70$ Pa)). Otherwise, return to Step 1 and repeat process.

The preceding procedure is continued until the specified error tolerance (i.e., 0.07%) has been met. The computational design of the PA has the potential to require more than 30,000 separate DBR calculations (3 replicates × 5 scenarios × 4 drilling locations × 100 vectors × 5 to 6 intrusion times per scenario). In concept, each of these cases requires the solution of Equations (PA.194) through (PA.197) with the iterative procedure just presented to obtain the boundary value condition $p_{wf} = p(0)$ (Table PA-14). To help hold computational costs down, $p(0)$ was calculated for approximately 2,000 randomly generated vectors of the form:

$$\mathbf{v} = \left[p_w, h, S_{br}, S_{gr}, S_b, A_i \right] \quad \text{(PA.205)}$$

where p_w is the repository pressure (used in definition of $q_b[p(0)]$ and $q_g[p(0)]$ in Equations (PA.194) through (PA.197), h is the crushed height of the repository (used in definition of J_p in Equation (PA.182)), S_{br} and S_{gr} are the residual saturations for gas and brine in the repository (used in definition of k_{rp} in Equation (PA.182)), S_b is the saturation of brine in the repository (used in definition of k_{rp} in Equation (PA.182)), and A_i is the equivalent area of material removed by cuttings, cavings, and spallings (used in definition of skin factor s in Equation (PA.186)). The outcomes of these calculations were divided into three cases:

1. Mobile brine only (i.e., $k_{rg} = 0$ in Equation (PA.187))

2. Brine-dominated flow (i.e., $k_{rb} > k_{rg}$)

3. Gas-dominated flow (i.e., $k_{rg} > k_{rb}$)

Regression procedures were then used to fit algebraic models that can be used to estimate $p(0)$. These regression models were then used to determine $p(0)$, and hence, p_{wf}. The resulting three regression models (or curve fit equations) for flowing bottomhole pressure (p_{wf}) are as

follows. During DBR simulations, these regression models are used in place of the explicit iterative solution of Equations (PA.194) through (PA.197) to compute the flowing bottomhole pressure, p_{wf}, as a function of repository pressure and flow parameters.

1. For a system with only mobile brine (k_{rg} = 0):

$$p_{wf} = a + bx + cy + dx^2 + ey^2 + fxy + gx^3 + hy^3 + ixy^2 + jx^2y \qquad \text{(PA.206)}$$

where $x = \log(J_b)$ and $y = p_w$ (= repository pressure), the coefficients in Equation (PA.206) were determined to be:

$a = 3.2279346 \times 10^{11}$

$b = 9.4816648 \times 10^{10}$

$c = -6.2002715 \times 10^{3}$

$d = 9.2450601 \times 10^{9}$

$e = 4.1464475 \times 10^{-6}$

$f = -1.2886068 \times 10^{3}$

$g = 2.9905582 \times 10^{8}$

$h = 1.0857041 \times 10^{-14}$

$i = 4.7119798 \times 10^{-7}$

$j = -6.690712 \times 10^{-1}$

with a resulting coefficient of determination $R^2 = 0.974$.

2. For brine-dominated flow ($k_{rb} > k_{rg}$):

$$p_{wf} = \frac{a + bx + cx^2 + dy}{1 + ex + fx^2 + gx^3 + hy} \qquad \text{(PA.207)}$$

where $x = \log\left(\frac{k_{rg}}{k_{rb}}\right)$ and $y = p_w$ (= repository pressure), the coefficients in Equation (PA.207) were determined to be:

$a = 1.6065077 \times 10^{6}$

$b = 2.6243397 \times 10^{6}$

$c = 2.4768899 \times 10^{6}$

$d = -5.3635476 \times 10^{-2}$

$e = 7.0815693 \times 10^{-1}$

$f = 3.8012696 \times 10^{-1}$

$g = 4.1916956 \times 10^{-3}$

$h = -2.4887085 \times 10^{-8}$

with a resulting coefficient of determination = 0.997.

3. For gas-dominated flow ($k_{rg} > k_{rb}$):

$$p_{wf} = a + b\frac{1}{x} + cy + d\frac{1}{x^2} + ey^2 + f\frac{x}{y} + g\frac{1}{x^3} + hy^3 + i\frac{y^2}{x} + j\frac{y}{x^2} \qquad \text{(PA.208)}$$

where $x = \log(J_g)$ and $y = p_w$ (= repository pressure), the coefficients in Equation (PA.208) were determined to be:

$a = -1.0098405 \times 10^{9}$

$b = -2.3044622 \times 10^{10}$

$c = 9.8039146$

$d = -1.7426466 \times 10^{11}$

$e = 1.8309137 \times 10^{-7}$

$f = 1.7497064 \times 10^{2}$

$g = -4.3698224 \times 10^{11}$

$h = -1.4891198 \times 10^{-16}$

$i = 1.3006196 \times 10^{-6}$

$j = 7.5744833 \times 10^{2}$

with a resulting coefficient of determination $R^2 = 0.949$.

PA-4.8.7 Boundary Value Pressure p_{wE1}

Some DBR calculations address drilling intrusions that are preceded by an E1 intrusion (Section PA-6.3.6). The effects of a prior E1 intrusion are incorporated into the solution of Equations (PA.187) through (PA.193), and thus into the DBR calculations, by specifying a pressure boundary condition, p_{wE1}, at the location of the prior E1 intrusion (Table PA-14).

Two cases are considered in defining p_{wE1}, depending on the condition of the prior E1 borehole between the pressurized brine reservoir and the repository. In the first case, the prior E1 intrusion is assumed to remain an open borehole connecting the brine reservoir and the repository. In the second case, the prior E1 intrusion is assumed to be filled with silty-sand–like material between the brine reservoir and the repository. The open-borehole case corresponds to drilling intrusions that occur within 200 years of a prior E1 intrusion that penetrated the pressurized brine reservoir, whereas the filled-borehole case corresponds to drilling intrusions that occur more than 200 years after such an E1 intrusion.

PA-4.8.7.1 Solution for Open Borehole

In this case, p_{wE1} is set equal to the flowing well pressure p_{wfBI} of an open borehole between the brine reservoir and the repository, and is given by:

$$Q = f_1(p_{BP}, p_{wfBP}) \quad \text{(PA.209)}$$

$$Q = f_2(p_{wfBP}, p_{wfBI}) \quad \text{(PA.210)}$$

$$Q = f_3(p_{wfBI}, p_{wfBO}) \quad \text{(PA.211)}$$

where

p_{BP} = far-field pressure (Pa) in the brine reservoir

p_{wfBP} = flowing well pressure (Pa) at outlet from brine reservoir

p_{wfBI} = flowing well pressure (Pa) at inlet to repository from brine reservoir

p_{wfBO} = flowing well pressure (Pa) at outlet from repository due to current borehole (Note: The boreholes associated with p_{wfBI} and p_{wfBO} arise from different drilling intrusions and hence are at different locations; see Figure PA-33)

Q = brine flow rate (m^3/s) from brine reservoir to repository, through repository, and then to surface

and f_1, f_2, and f_3 are linear functions of their arguments. The quantities p_{BP} and p_{wfBO} are assumed to be known, with the result that Equation (PA.209), Equation (PA.210), and Equation (PA.211) constitute a system of three linear equations in three unknowns (i.e., p_{wfBP}, p_{wfBI},

and Q) that can be solved to obtain p_{wfBI}. In the determination of p_{wfBI} for use in a particular solution of Equations (PA.187) through (PA.193), p_{BP} is the pressure in the brine reservoir at the time of the intrusion obtained from the solution of Equations (PA.18) through (PA.24) with BRAGFLO, and p_{wfBO} is the flowing well pressure obtained from conditions at the time of the intrusion (from the solution of Equations (PA.18) through (PA.24)) and the solutions of the Poettmann-Carpenter model embodied in Equation (PA.206), Equation (PA.207), and Equation (PA.208) (i.e., given pressure, k_{rg} and k_{rb} at the time of the intrusion, and J_p, p_{wfBO} is determined from the regression models indicated in Equation (PA.206), Equation (PA.207), and Equation (PA.208)).

The definitions of Equation (PA.209), Equation (PA.210), and Equation (PA.211) are now discussed. Equation (PA.209) characterizes flow out of the brine reservoir into an open borehole and has the form (Williamson and Chappelear 1981; Chappelear and Williamson 1981):

$$Q = \left(\frac{2\pi k_{BP} h_{BP}}{\mu \left[\ln\left(r_{eBP} / r_w \right) - 0.5 \right]} \right) \left(p_{BP} - p_{wfBP} \right) \qquad \text{(PA.212)}$$

where

k_{BP} = brine reservoir permeability (m^2)

h_{BP} = effective brine reservoir height (m)

r_{eBP} = effective brine reservoir radius (m)

r_w = wellbore radius (m)

μ = brine viscosity (Pa s)

In the present analysis, k_{BP} is an uncertain analysis input (parameter BH_OPEN:PRMX_LOG in Feng and Kicker (2025a), Table 6). BH_OPEN corresponds to open-borehole conditions; silty-sand–filled boreholes are treated separately (see Section PA-4.8.7.2); h_{BP} = 125.83 m; r_{eBP} = 114 m (Stoelzel and O'Brien 1996), which corresponds to the largest brine reservoir that can be accommodated beneath a single waste panel; r_w = (8.921 in.)/2 = 0.1133 m, which is the inside radius of a 9-5/8 in. outside diameter casing (Gatlin 1960, Table 14.7); $\mu = 1.8 \times 10^{-3}$ Pa s; and p_{BP} is determined from the solution of Equations (PA.18) through (PA.24), as previously indicated.

Equation (PA.210) characterizes flow up an open borehole from the brine reservoir to the repository and is based on Poiseuille's Law (Prasuhn 1980, Eqs. 7-21, 7-22). Specifically, Equation (PA.210) has the form:

$$Q = \left[\frac{\pi D^4}{128\mu\left(y_{BP} - y_{rep}\right)}\right]\left[\left(p_{wfBP} - p_{wfBI}\right) + g\rho\left(y_{rep} - y_{BP}\right)\right] \quad \text{(PA.213)}$$

where

D = wellbore diameter (m)

y_{rep} = elevation of repository (m) measured from surface

y_{BP} = elevation of brine reservoir (m) measured from surface

g = acceleration due to gravity (9.8 m/s^2)

ρ = density of brine (kg/m^3)

and the remaining symbols have already been defined.

In the present analysis, $D = 2r_w$ = 0.2266 m, ρ = 1,230 kg/m^3, and $y_{BP} - y_{rep}$ = 247 m. With the preceding values:

$$128\mu\left(y_{BP} - y_{rep}\right)\Big/\pi D^4 = 6.87\times10^3 \text{ Pa s / } m^3 \quad \text{(PA.214)}$$

$$g\rho\left(y_{rep} - y_{BP}\right) = 2.98\times10^6 \text{ Pa} \quad \text{(PA.215)}$$

Thus:

$$p_{wfBI} = p_{wfBP} - 2.98 \times 10^6 \text{ Pa} \quad \text{(PA.216)}$$

when Q is small ($\leq$ 0.1 m^3/s). When appropriate, this approximation can be used to simplify the construction of solutions to Equation (PA.209), Equation (PA.210), and Equation (PA.211).

Equation (PA.211) characterizes flow through the repository from the lower borehole to the bottom of the borehole associated with the drilling intrusion under consideration and has the same form as Equation (PA.212). Specifically:

$$Q = \left(\frac{2\pi k_{rep} h_{rep}}{\mu\left[\ln\left(r_{e,rep} / r_w\right) - 0.5\right]}\right)\left(p_{wfBI} - p_{wfBO}\right) \quad \text{(PA.217)}$$

where

k_{rep} = repository permeability (m^2)

h_{rep} = repository height (m)

$r_{e,rep}$ = effective repository radius (m)

and the remaining symbols have already been defined. In the present analysis, k_{rep} = 2.4 × 10^{-13} m^2; h_{rep} at the time of the drilling intrusion under consideration is obtained from the solution of Equations (PA.18) through (PA.24) (see Equation (PA.176)); and $r_{e,rep}$ is the same as the radius r_e defined in Equation (PA.183). As previously indicated, p_{wfBO} is obtained from the solutions to the Poettmann-Carpenter model summarized in Equation (PA.206), Equation (PA.207), and Equation (PA.208).

Three equations (i.e., Equation (PA.212), Equation (PA.213), and Equation (PA.217)) with three unknowns (i.e., p_{wfBP}, p_{wfBI} and Q) have now been developed. The solution for p_{wfBI} defines the initial value p_{wE1} in Table PA-14. When the simplification in Equation (PA.216) is used, the resultant solution for p_{wfBI} is:

$$p_{wfBI} = \frac{p_{wfBO} + \left(p_{BP} - 2.98\times10^{6}\right)K_1}{1+K_1} \tag{PA.218}$$

where

$$K_1 = \frac{k_{BP}h_{BP}\left[\ln\left(\frac{r_{e,rep}}{r_w}\right)-\frac{1}{2}\right]}{k_{rep}h_{rep}\left[\ln\left(\frac{r_{eBP}}{r_w}\right)-\frac{1}{2}\right]} \tag{PA.219}$$

and -2.98×10^6 comes from Equation (PA.215). The expression in Equation (PA.219) defines p_{wE1} in the CRA-2026 PA for the determination of DBRs resulting from a drilling intrusion that occurred within 200 years of a preceding E1 intrusion (see Table PA-8).

PA-4.8.7.2 Solution for Sand-Filled or Creep-Closed Borehole

For a borehole filled with silty-sand-like material or closed by creep and connecting the brine reservoir to the repository, the determination of p_{wfBI} is the same as for an open borehole, except that Equation (PA.209) and Equation (PA.210) are replaced by a single equation based on Darcy's Law. Specifically, flow from the brine reservoir to the repository is represented by:

$$Q = \frac{K_{BH}A_{BH}\left[\left(p_{BP} - p_{wfBI}\right) + g\rho\left(y_{rep} - y_{BP}\right)\right]}{\mu\left(y_{BP} - y_{rep}\right)} \tag{PA.220}$$

where

k_{BH} = borehole permeability (m^2)

A_{BH} = borehole cross-sectional area (m^2)

and the remaining symbols have been previously defined. In the present analysis, k_{BH} is an uncertain input for a sand-filled borehole (see parameters BH_SAND:PRMX_LOG and BH_CREEP: PRMX_LOG in Feng and Kicker (2025a), Tables 7 and 8) and A_{BH} is defined by the assumption that the borehole diameter is the same as the drill bit diameter (i.e., 12.25 in. = 0.31115 m). For a sand-filled borehole, the properties from the BH_SAND material are used, while for a creep-closed borehole, the properties from the BH_CREEP material are used.

The representation for flow from the outlet of the borehole for the prior E1 intrusion through the repository to the inlet point associated with the drilling intrusion under consideration remains as defined in Equation (PA.217). Thus, two equations (i.e., Equation (PA.217) and Equation (PA.220)) and two unknowns (i.e., p_{wfBI} and Q) are under consideration. Solution for p_{wfBI} yields:

$$p_{wfBI} = \frac{p_{wfBO} + K_2 p_{BP} - 2.98\times10^6 K_2}{1 + K_2} \tag{PA.221}$$

where

$$K_2 = \frac{\pi k_{BH} r_w^2 \left[\ln\left(\frac{r_{eBP}}{r_w} \right) - \frac{1}{2} \right]}{2\pi h_{rep} k_{rep} \left(y_{BP} - y_{rep} \right)} \tag{PA.222}$$

and -2.98×10^6 comes from Equation PA.215). The expression in Equation (PA.222) was used to define p_{wfBI} in the determination of DBRs for a drilling intrusion that occurred more than 200 years after a preceding E1 intrusion (see Table PA-8).

PA-4.8.8 End of DBR

The CRA-2026 PA includes 31,200 cases that potentially require solution of Equations (PA.187) through (PA.193) to obtain the DBR volume (see Section PA-6.3.6). However, the DBR volume is set to zero without solution of Equations (PA.187) through (PA.193) when there is no possibility of a release (i.e., at the time of the intrusion, the intruded waste panel has either a pressure less than 8 MPa or a brine saturation below the residual brine saturation, S_{br}).

When the pressure and saturation conditions permit a DBR event, gas flow through the borehole may result in temporary loss of well control. In such cases, either (1) the gas flow naturally declines to a manageable level, allowing conventional well-control procedures to be implemented, or (2) aggressive measures are taken to kill the well before the flow declines to a manageable level. Experience at the South Culebra Bluff Unit #1, which blew out in January

1978, suggests that several days may be required to assemble the equipment and personnel needed to regain control of a well under such circumstances; however, this event represents an extreme and atypical case.

Kirkes (2007) reevaluated current drilling practices based on historic information and interviews with drilling personnel active in the WIPP area and concluded that:

1. The South Culebra Bluff #1 is not a suitable analog for a hypothetical WIPP blowout.

2. Basing the WIPP maximum DBR parameter on the single most catastrophic blowout event in the region's history does not reasonably represent "current drilling practice" as directed by regulations.

3. Well-known drilling procedures are sufficient to stop or *kill* a WIPP blowout under the most extreme anticipated pressures in hours, not days.

4. Using 4.5 days for a maximum DBR duration is still quite conservative, in that it assumes flow into the wellbore continues throughout the kill procedure and casing/cementing procedures, even though this assumption is not consistent with current practice.

Therefore, for the CRA-2026 PA, a value of 4.5 days was used for the maximum value used for t_e.

Given the preceding, t_e is defined in PA by:

$$t_e = \begin{cases} \max\left\{3\text{ d}, t_f\right\} & \text{if } t_f \le 4.5\text{ d} \\ 4.5\text{ d} & \text{if } t_f > 4.5\text{ d} \end{cases} \quad \text{(PA.223)}$$

where t_f is the time at which the gas flow out of the well drops below 1×10^5 standard cubic feet per day (SCF/d) and t_e is constrained to be no less than three days. The minimum value of three days reflects the estimated time required to drill from the repository through the Castile and cement the intermediate casing assuming well control is maintained, and no blowout occurs. Gas flow out of the repository in the intruding borehole, and hence t_f and t_e, is determined as part of the solution to Equations (PA.187) through (PA.193).

PA-4.8.9 Numerical Solution

As previously indicated, the BRAGFLO code is used to solve Equations (PA.187) through (PA.193) with the computational grid shown in Figure PA-33, the initial conditions described in Section PA-4.8.2, the boundary conditions listed in Table PA-14, and parameter values appropriate for modeling DBRs. The numerical procedures in use for Equations (PA.187) through (PA.193) are the same as those described in Section PA-4.2.12 for the solution of Equations (PA.18) through (PA.24).

In this implementation, the boundary conditions associated with drilling intrusions (i.e., p_{wf} and p_{wE1} in Table PA-14) are incorporated through fluid withdrawal terms, q_g and q_b (Equations (PA.18) through (PA.24)), rather than as predetermined boundary values. With this approach, the gas and brine conservation equations (Equation (PA.187) and Equation (PA.188)) are expressed as:

$$\nabla \bullet \left[\frac{\alpha \rho_g K_g k_{rg}}{\mu_g} \left(\nabla p_g + \rho_g g \nabla h \right) \right] + \alpha q_g = \alpha \frac{\partial (\phi \rho_g S_g)}{\partial t} \tag{PA.224}$$

$$\nabla \bullet \left[\frac{\alpha \rho_b K_b k_{bg}}{\mu_b} \left(\nabla p_b + \rho_b g \nabla h \right) \right] + \alpha q_b = \alpha \frac{\partial (\phi \rho_b S_b)}{\partial t} \tag{PA.225}$$

The constraints in Equations (PA.187) through (PA.193) remain unchanged.

The source terms q_g and q_b are formally independent of the computational grid (Figure PA-33), but their numerical implementation requires grid-specific definitions. This is because the spatial scale of a borehole is much smaller than the typical grid cell size. Therefore, q_g and q_b are defined using a productivity index (Equation (PA.182)) that accounts for the actual grid cell size in which the borehole is located.

For gas flow out of the repository:

$$q_g(x,y,t) = \frac{k k_{rg}(x,y,t)[\, p_g(x,y,t) - p_{wf}\,]}{\mu_g [\ln(r_e / r_w) + s + c]} \tag{PA.226}$$

Here (x, y) is at the center of the grid cell containing the drilling intrusion. The terms k, k_{rg}, μ_g, r_e, r_w, s, and c are defined in conjunction with Equation (PA.182), p_g is gas pressure, and p_{wf} is the flowing well pressure at the outlet borehole (Table PA-14). The repository's crushed height, h (Equations (PA.182) through PA.205), defines the factor α in Equation (PA.224) and Equation (PA.225). Numerically, $q_g(x, y, t)$ defines the source term $q_{g_{i,j}}^{n+1}$ in Equation (PA.61) and is nonzero only for the grid cells containing the borehole through which gas outflow occurs (down-dip, middle, and up-dip, and other area wells in Figure PA-33).

For brine flow, brine outflow from the repository through a drilling intrusion:

$$q_b(x,y,t) = \frac{k k_{rb}(x,y,t)[\, p_b(x,y,t) - p_{wf}\,]}{\mu_b [\ln(r_e / r_w) + s + c]} \tag{PA.227}$$

along with brine inflow from a pressurized brine reservoir at a prior E1 drilling intrusion:

$$q_b(x,y,t) = \frac{k k_{rb}(x,y,t)[\, p_{wE1} - p_b(x,y,t)]}{\mu_b [\ln(r_e / r_w) + c]} \tag{PA.228}$$

Elsewhere, $q_b(x, y, t) = 0$. In the numerical solution, $q_b(x,y,t)$ defines the source term in the discretized Equation (PA.225), analogous to the discretization in Equation (PA.61). Nonzero values occur only in the grid cells corresponding to:

1. Boreholes with brine outflow (Equation PA.227), and
2. Prior E1 intrusions where brine inflow occurs (Equation PA.228).

PA-4.8.10 Additional Information

Additional details on the DBR analysis are provided in the DBR analysis report (Zeitler 2025). Information on the application of BRAGFLO for DBR calculations is available in the BRAGFLO User's Manual (WIPP Performance Assessment 2025).

PA-4.9 Groundwater Flow in the Culebra Dolomite

The Culebra is the most transmissive saturated unit above the Salado (Beauheim and Holt 1990; Holt 1997). High transmissivity can increase the potential for actinide transport through the Culebra to the LWB subsurface limit, via long-term lateral groundwater flow, following an inadvertent drilling intrusion into the repository.

Groundwater flow in the Culebra is modeled as a steady-state process. The T-fields are initially constructed to be consistent with WIPP site geologic data, measured head and transmissivity, and transient pumping tests. Each T-field is subsequently modified to incorporate impacts of uncertain future processes associated with potash mining and climate change (Section PA-2.4.4.4, Section PA-4.9.4, and Section PA-4.9.5).

PA-4.9.1 Mathematical Description

Groundwater flow in the Culebra is represented by the PDE (Bear 1979):

$$S\left(\frac{\partial h}{\partial t}\right) = \nabla \bullet \left(b\mathbf{K}\nabla h\right) - Q \qquad \text{(PA.229)}$$

where

S = medium storativity (dimensionless),

h = hydraulic head (m),

t = time (s),

b = aquifer thickness (m),

$\mathbf{K}$ = hydraulic conductivity tensor (m/s),

Q = source/sink term expressed as the volumetric flux per unit area ($(m^3/m^2)/s = m/s$).

Further, the Culebra is represented as two-dimensional with the anisotropic hydraulic conductivity tensor:

$$\mathbf{K}(x,y) = k(x,y)\begin{bmatrix} 1 & 0 \\ 0 & A(x,y) \end{bmatrix} \quad \text{(PA.230)}$$

where $k(x,y)$ is the hydraulic conductivity (m/s) at the point (x, y), and A is the anisotropy ratio. The following simplifying assumptions are also made: fluid flow in the Culebra is at steady state (i.e., $\partial h/\partial t = 0$), and source and sink effects arising from borehole intrusions and infiltration are negligible (i.e., Q = 0). Given these assumptions, Equation (PA.229) simplifies to:

$$\nabla \cdot (b\mathbf{K}\nabla h) = 0 \quad \text{(PA.231)}$$

which is solved to obtain $h = h(x,y)$, the hydraulic head in the Culebra. In PA, b = 7.75 m, and $k(x, y)$ in Equation (PA.230) is accounts for an imprecisely known T-field, as discussed in Section PA-4.9.3.

PA-4.9.2 Computational Grid and Boundary Conditions

Equation (PA.231) is evaluated on a 28.4 km east-west by 30.7 km north-south modeling domain (Figure PA-36). The modeling domain is discretized into 87,188 100 × 100 m grid cells. The northern model boundary extends slightly beyond the northern end of Nash Draw, 12 km (7.4 miles) north of the northern WIPP site boundary, and about 1 km (0.62 miles) north of Intrepid Potash's east tailings pile. The eastern boundary lies in a low-transmissivity region that contributes little flow to the modeling domain. The southern boundary lies 12.2 km south of the southern WIPP site boundary, far enough from the WIPP site to have little effect on the transport of radionuclides through the Culebra. The far western boundary of the model passes through the Mosaic (formerly International Minerals and Chemicals) tailings pond (Laguna Uno; see Hunter 1985), which is located within Nash Draw due west of the WIPP site.

Flow domain boundaries used in the CRA-2026 PA are the same as those used in CRA-2019 (Figure PA-36). Powers (2006) examined Culebra confinement and recharge in the SW portion of the flow domain. Findings from that study informed transmissivity field calibrations (Section PA-4.9.3) in the CRA-2009 PABC resulting in the inclusion of a line of recharge cells, oriented NW to SE (Hart et al. 2009). The groundwater flow code has been updated from MODFLOW 2000 to MODFLOW6 (Section PA-4.9.7 and Section PA-6.3.7).

Two types of boundary conditions are specified: constant-head and no-flow (Figure PA-36). Constant-head conditions along the far eastern boundary of the model domain and in the gray area are specified based on the land surface elevation. Constant-head values along the northern, southern, and western boundaries (gray segments of the model domain border) were

assigned from an extrapolated potentiometric surface fit to observed head using a multivariate equation (Bowman et al. 2023). A no-flow boundary is specified in the northwestern corner of the modeling domain, reflecting, the concept that groundwater flows down the axis of Nash Draw, forming a groundwater divide. Grid cells west of the no-flow boundary are specified as inactive in the MODFLOW6 domain, and the constant head cells in the eastern portion are essentially inactive, since their heads are specified, not computed.

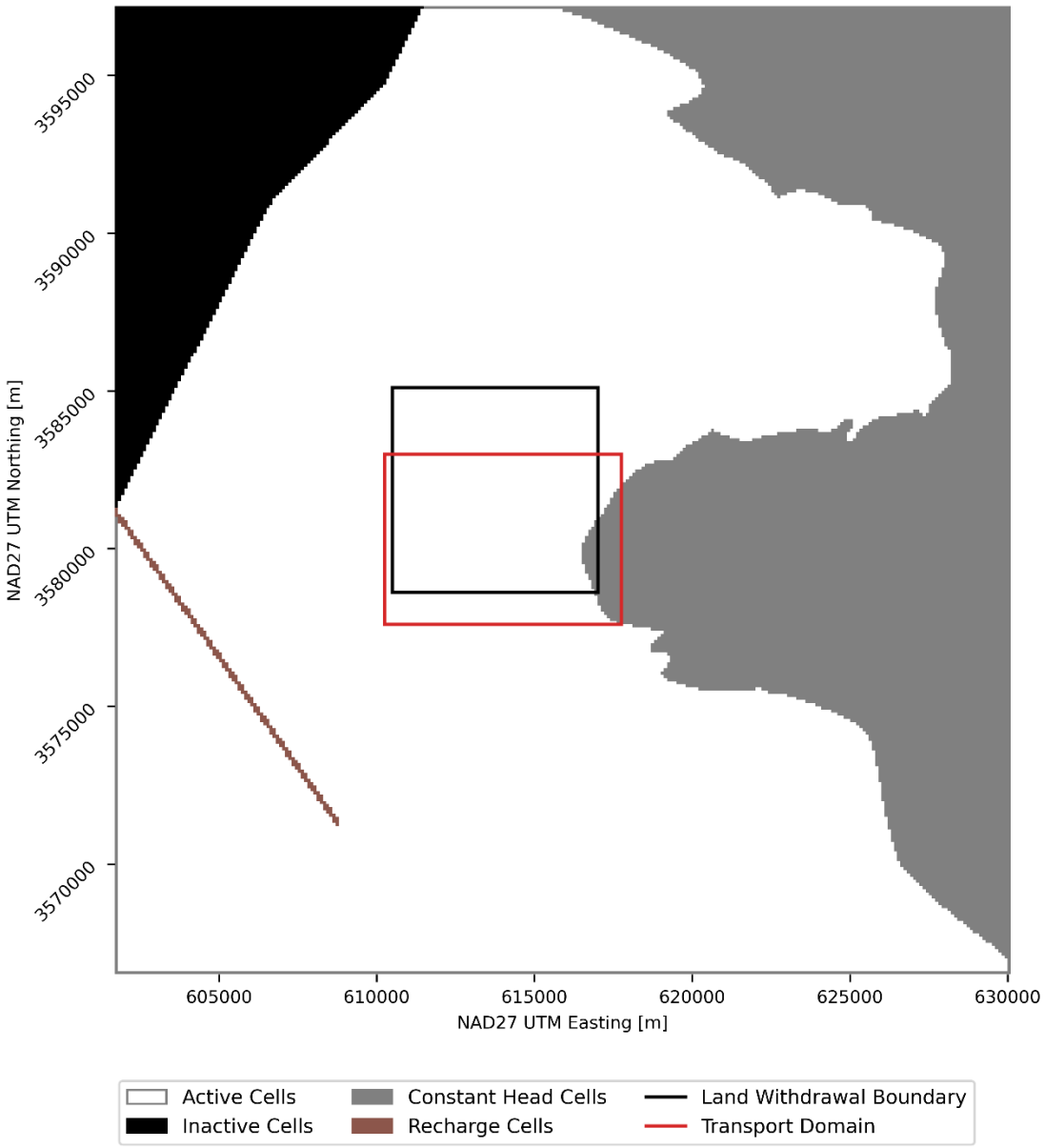


Figure PA-36. Modeling Domains for Groundwater Flow (MODFLOW6) and Radionuclide Transport (SECOTP2D) in the Culebra.

PA-4.9.3 Generation of T-fields

T-field generation begins with construction of 1,000 base geostatistical realizations of Culebra hydraulic transmissivity (T), horizontal T anisotropy, storativity, and recharge fields (collectively referred to as "T-fields") (Hart et al. 2008). The base T-fields are then calibrated to observed head (steady-state) and pumping drawdowns (transient) and the final set of the 100 best fit realizations is selected (Bowman et al. 2023). The domain discretization described in Section PA-4.9.2 was used both to generate stochastic realizations of the base T-field and to implement the groundwater flow model used for T-field calibration.

The T-fields are based on several types of information, including a regression model developed on WIPP site geologic data, measured head levels in the Culebra, and multi-well drawdown pumping tests. Geologic data, including (1) depth to the top of the Culebra, (2) reduction in thickness of the upper Salado by dissolution, (3) presence of gypsum cements in the Culebra, (4) interpretation of high-diffusivity connections between wells from multi-well pumping tests, and (5) the spatial distribution of halite in the Rustler below and above the Culebra, were used to define a geologic regression model that relates transmissivity at any location to a set of hydrogeologic parameters (Appendix TFIELD-2026, Section 5.0).

For the CRA-2026 PA, the 1,000 base T-fields are calibrated to a steady-state snapshot of water-level data in 47 wells, 10 transient pumping test responses at 67 observation locations, and responses to the Mills Ranch pumping event (Bowman et al. 2023). Calibration is automated using the parameter estimation program PEST++IES (White et al. 2020), which iteratively changes parameters for each of the T-fields and forward models flow with MODFLOW6 (Appendix TFIELD-2026, Section 5.1 and 5.2). Realization selection is guided by a scaled objective function that seeks to minimize the residuals between the observations and the modeled output (Appendix TFIELD-2026, Section 5.3).

The T-fields produced during the calibration process are screened against acceptance criteria to form the final set of the 100 best-fit realizations (Appendix TFIELD-2026, Section 5.3.2). Calibrated T-fields that meet the acceptance criteria are then modified to create T-fields that represent the effects of partial and full potash mining (Section PA-4.9.4). This modification increases transmissivity by a random factor between 1 and 1000 in areas containing potash reserves. Steady-state flow simulations are then run with MODFLOW6 using the mining-modified T-fields. Undisturbed and mining-modified flow simulations are characterized with advective particle tracking (Wilgus and Bethune 2025, Section 4.3, 5.2, and 8.2). Particle tracking output enables visualization and quantification of the flow characteristics.

A large number of plausible T-fields $T(x,y)$ (m^2/s) were generated to characterize the uncertainty of Culebra flow properties. The hydraulic conductivity $k(x,y)$ in Equation (PA.230) is defined in terms of the T-field $T(x,y)$ by:

$$k(x,y) = T(x,y)/b \qquad \text{(PA.232)}$$

where *b* is the Culebra thickness – a constant 7.75 m. Bowman et al. (2023) detail the procedure for generating T-fields. During the T-field calibration process, Culebra flow is simulated without mining.

PA-4.9.4 Mining Area and Modification

Potash mining in the McNutt Potash Zone of the Salado is currently ongoing in the Delaware Basin outside the LWB and may continue in the future. Long-term releases within the Culebra could be influenced by future mining activities that remove known potash reserves in the vicinity of the LWB and cause the transmissivity within the overlying Culebra to change. Potential changes in transmissivity can alter flow patterns and impact long-term releases from the Culebra. Therefore, a potash mining scenario is addressed in PA (Section PA-2.2.2.2.2). Two mining scenarios are considered: (1) full mining, in which mining is assumed in all economically feasible potash reserves throughout (inside and outside) the domain, and (2) partial mining, in which mining is assumed to occur only outside the LWB.

Potash mining in the vicinity of the WIPP involves resource extraction below the Culebra in the McNutt Potash zone, a subsection of the Salado Formation above the repository horizon but below the Rustler Formation. The extent of mineable potash ore is periodically assessed by the Bureau of Land Management (Cranston 2009). The most recent available version is used for CRA-2026, which is the same as the dataset used in CRA-2019 (Figure PA-37).

Since the potash-mining horizon is below the Culebra, the areas in the Culebra that are disturbed by mining activities in the Salado are larger than the mined areas due to angle-of-draw effects, in which the subsidence effects are assumed to propagate up and out at 45° angles from horizontal. To accommodate the angle of draw, the mining zone boundaries, as overlaid on the current model grid, extend outward by three cells (300 m) in the x- and y-directions, and by two cells (283 m) in the diagonal directions. Figure PA-38 illustrates the selection of model cells impacted (blue cells labeled A) by mining-related subsidence (red cell labeled M).

The detailed process to convert the dataset shown in Figure PA-37 to a grid of integers corresponding to Culebra MODFLOW6 model cells (indicating whether a model cell was impacted by mining or not) is documented in Appendix MININGMOD of Bethune (2023).

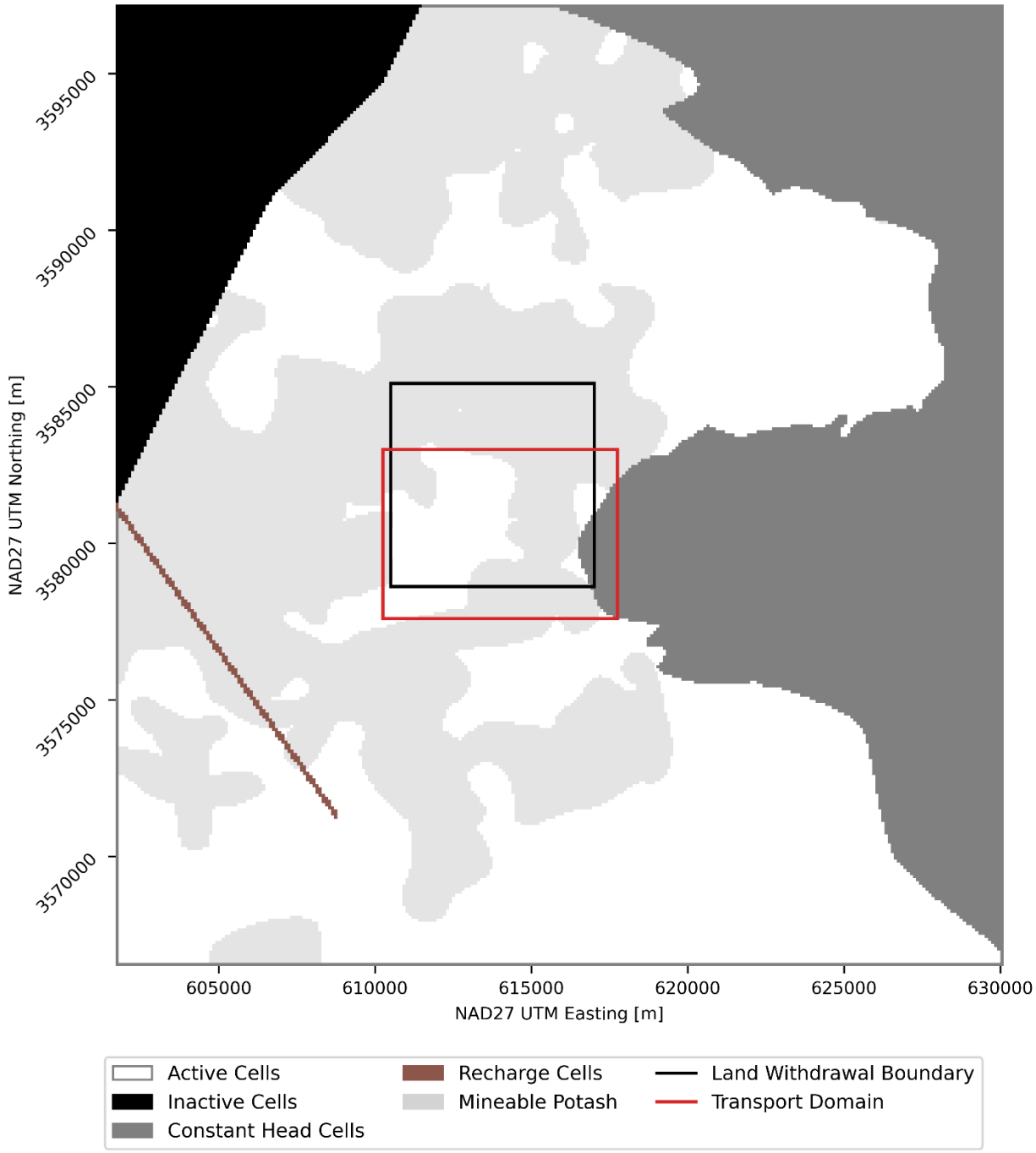


Figure PA-37. Extent of Mineable Potash within Model Domain

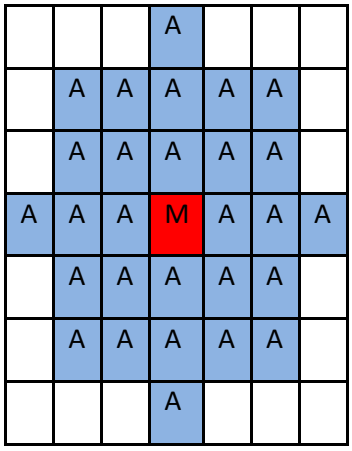


Figure PA-38. Illustration of Model Cells Affected by Mining-Related Subsidence

Figure PA-39 shows the current application definitions for full and partial mining-impacted areas used in CRA-2026. As specified by guidance in 40 CFR 194 and described in Section PA-3.3, economic potash reserves outside the LWB are assumed to have been fully mined by the end of the 100 years of AICs. After the period of AICs, the occurrence of potash mining within the LWB follows a Poisson process with a rate of $\lambda_m = 1 \times 10^{-4}$ yr^{-1}. For any future, this rate is used to determine the time at which full mining has occurred. Radionuclide transport through the Culebra (Section PA-4.10) uses the partial-mining flow fields prior to the time at which full mining has occurred and the full-mining flow fields after that time.

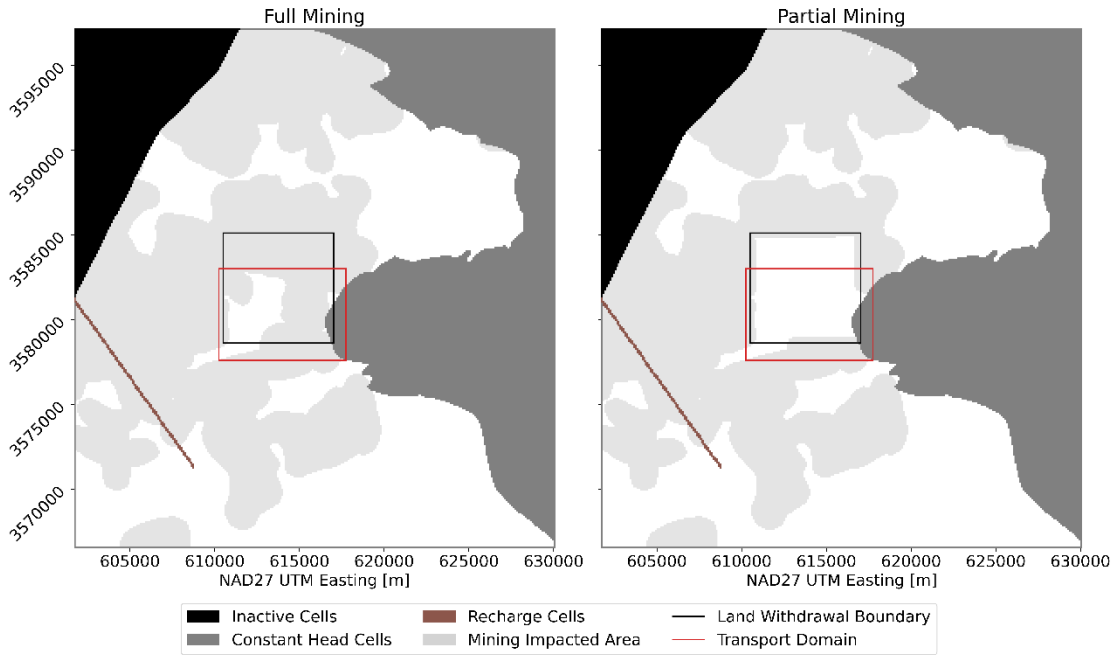


Figure PA-39. Mining Impacted Areas for Full and Partial Mining Scenarios

PA-4.9.5 Flow in the Culebra

Fluid flow ($b\mathbf{K}\Delta h$) is determined using MODFLOW6 to solve Equation (PA.231). Culebra flow is simulated with the mining-modified transmissivity fields for the full and partial mining cases (Figure PA-39). As specified by guidance in 40 CFR Part 194 (p. 5229, U.S. EPA 1996), potash mining increases the Culebra's transmissivity in the vicinity of such mining by an uncertain factor, MF, with a value sampled from a uniform distribution between 1 and 1000 (see parameter CULEBRA:MINP_FAC in Feng and Kicker (2025a), Table 3). In the partial mining case, hydraulic conductivity $k_{PM}(x,y) = k(x,y) = T(x,y)/b$ (Equation (PA.232)) inside the WIPP boundary and $k_{PM}(x,y) = k(x,y) \times MF$ outside the WIPP boundary, where MF is determined by the parameter CULEBRA:MINP_FAC. In the full mining case, hydraulic conductivity $k_{FM}(x,y) = k(x,y) \times MF$ in all areas of the modeling domain.

In turn, $k_{PM}(x,y)$ and $k_{FM}(x,y)$ result in the following definition for the hydraulic conductivity tensor $\mathbf{K}$:

$$\mathbf{K}_i(x,y) = k_i(x,y)\begin{bmatrix} 1 & 0 \\ 0 & A(x,y) \end{bmatrix},\ i = PM, FM \qquad \text{(PA.233)}$$

In the analysis, Equation (PA.231) is solved with each of the preceding definitions of $\boldsymbol{K}_i$ to obtain characterizations of fluid flow in the Culebra for partially and fully mined conditions.

The potential effects of climate change on fluid flow are incorporated into the analysis by an uncertain scale factor (Corbet and Swift 1996a and 1996b). Specifically, the Darcy fluid velocity $\mathbf{v}_i(x,y)$ used in the radionuclide transport calculations is given by:

$$\mathbf{v}_i(x,y) = \left[u_i(x,y), v_i(x,y)\right] = SFC\left[\mathbf{K}_i(x,y)\nabla h_i(x,y)\right]^T,\ i = PM, FM \qquad \text{(PA.234)}$$

where $u_i(x,y)$ and $v_i(x,y)$ represent Darcy fluid velocities (m/s) at the point (x,y) in the *x* and *y* directions, respectively; $\nabla h_i(x,y)$ is obtained from Equation (PA.231) with $\mathbf{K} = \mathbf{K}_{ii}$; and SFC is a scale factor used to incorporate the uncertainty that results from possible climate changes (see parameter GLOBAL:CLIMTIDX in Feng and Kicker (2025a), Table 3).

PA-4.9.6 Numerical Solution

The flow model in Equation (PA.231) is evaluated on the computational grid described in Section PA-4.9.2 using MODFLOW6 (Section PA-6.3.7). MODFLOW6 discretizes the flow equation with a second-order difference procedure (McDonald and Harbaugh 1988, p. 126). Specifically, the discretized form of Equation (PA.231) is:

$$0 = CR_{i,j-1/2}\left(h_{i,j-1} - h_{i,j}\right) + CR_{i,j+1/2}\left(h_{i,j+1} - h_{i,j}\right)$$

$$+CC_{i-1/2,j}\left(h_{i-1,j}-h_{i,j}\right)+CC_{i+1/2,j}\left(h_{i+1,j}-h_{i,j}\right) \quad \text{(PA.235)}$$

where CR and CC are the row and column hydraulic conductances at the cell interface between node *i*, *j*, and a neighboring node (m^2/s). Since the grid is uniform, the hydraulic conductance is simply the harmonic mean of the hydraulic conductivity in the two neighboring cells multiplied by the aquifer thickness. For example, the hydraulic conductance between cells (*i*, *j*) and (*i*, $j-1$) is given by $CR_{i,j-1/2}$, and the hydraulic conductance between cells (*i*, *j*) and (*i* + 1, *j*) is given by $CC_{i+1/2,\,j}$:

$$CR_{i,j-1/2}=\frac{2k_{i,j}k_{i,j-1}}{k_{i,j}+k_{i,j-1}}\times b \text{ and } CC_{i+1/2,j}=\frac{2k_{i,j}k_{i+1,j}}{k_{i,j}+k_{i+1,j}}\times b \quad \text{(PA.236)}$$

where $k_{i,\,j}$ is the hydraulic conductivity in cell *i*, *j* (m/s) and *b* is the aquifer thickness (m).

Figure PA-40 illustrates the cell numbering convention used in the finite-difference grid for MODFLOW6. The determination of *h* is then completed by the solution of the linear system of equations in Equation (PA.235) for the unknown heads $h_{i,j}$. Fluxes at cell interfaces are calculated from the values for $h_{i,j}$ internally in MODFLOW6.

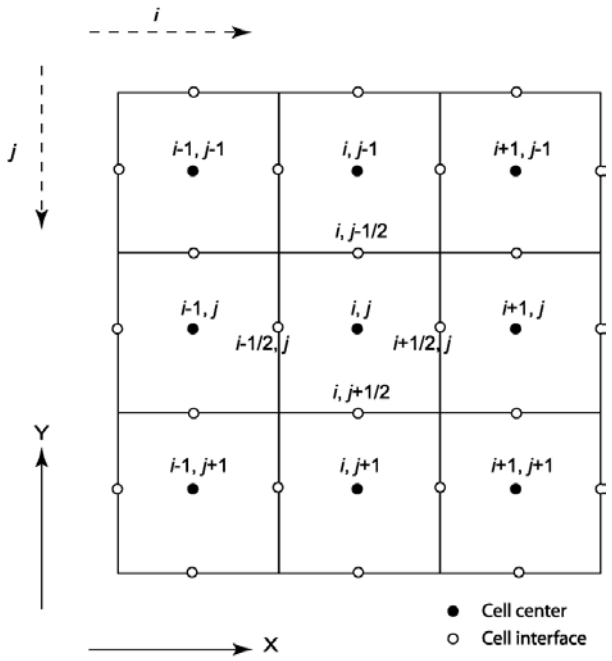


Figure PA-40. Finite-Difference Grid Showing Cell Index Numbering Convention Used by MODFLOW6.

PA-4.9.7 Additional Information

MODFLOW6 is the sixth core release of the groundwater flow software developed by the U.S. Geological Survey. Further description of MODFLOW6 input and output is available in Langevin

et al. (2017). Additional information on the calculation of the T-fields is found in Appendix TFIELD-2026. Flow fields used in the CRA-2026 PA (full and partial mining) are presented in Wilgus and Bethune (2025). Simulations without mining are not directly considered in PA calculations but are also presented in Wilgus and Bethune (2025).

PA-4.10 Radionuclide Transport in the Culebra Dolomite

Radionuclide transport in the Culebra is computed using the SECOTP2D computer code (WIPP Performance Assessment 2022f). The mathematical equations solved by SECOTP2D and the numerical methods used in the code are described in the following sections.

PA-4.10.1 Mathematical Description

Radionuclide transport in the Culebra is described by a parallel-plate, dual-porosity model (Meigs and McCord 1996). The parallel-plate, dual-porosity conceptualization assumes that the numerous fractures within the formation are aligned in parallel and treats the fractured porous media as two overlapping continua: one representing the fractures and the other the surrounding porous rock matrix (see Figure PA-41). In this model, one system of PDEs is used to represent advective transport in fractures within the Culebra, and another PDE system is used to represent diffusive transport and sorption in the matrix that surrounds the fractures.

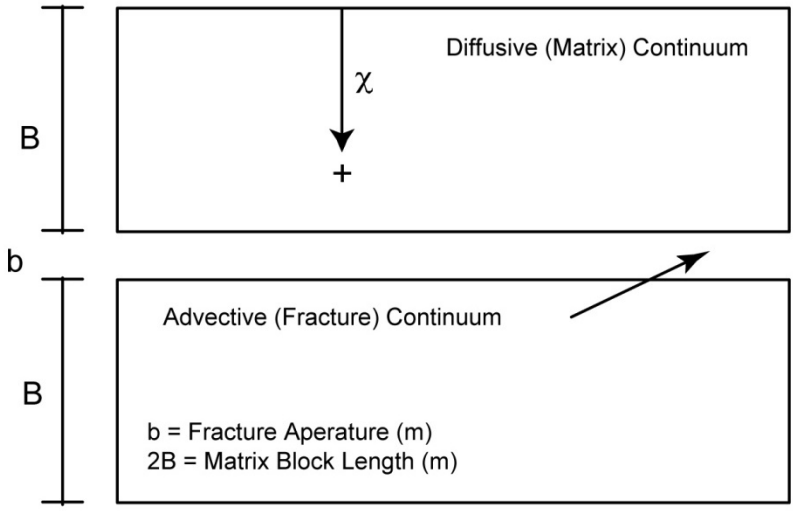


Figure PA-41. Parallel-Plate, Dual-Porosity Conceptualization

PA-4.10.1.1 Advective Transport in Fractures

The PDE system used to represent advective transport in fractures is given by (Bear and Bachmat 1990):

$$\nabla \cdot \left[\phi \mathbf{D}_k \nabla C_k - \mathbf{v} C_k\right] = \phi R_k \left(\frac{\partial C_k}{\partial t}\right) + \phi R_k \lambda_k C_k - \phi R_{k-1} \lambda_{k-1} C_{k-1} - Q_k - \Gamma_k \qquad \text{(PA.237)}$$

for k = 1, 2, …, *nR*, where

nR = number of radionuclides under consideration

C_k = concentration of radionuclide *k* in brine (kg/m^3)

$\mathbf{D}_k$ = hydrodynamic dispersion tensor (m^2/s)

$\mathbf{v}$ = Darcy velocity (i.e., specific discharge) of brine (m/s = (m^3/m^2)/s)

ϕ = advective (i.e., fracture) porosity (dimensionless)

R_k = advective retardation coefficient (dimensionless)

λ_k = decay constant for radionuclide k (s^{-1})

Q_k = injection rate of radionuclide *k* per unit bulk volume of formation ((kg/s)/m^3) (Note: $Q_k > 0$ corresponds to injection into the fractures)

Γ_k = mass transfer rate of radionuclide *k* per unit bulk volume of formation due to diffusion between fractures and surrounding matrix ((kg/s)/m^3) (Note: $\Gamma_k > 0$ corresponds to diffusion into fractures)

The Darcy velocity **v** is obtained from the solution of Equation (PA.231); specifically, **v** is defined by the relationship in Equation (PA.234). The advective porosity ϕ, defined as the ratio of the interconnected fracture pore volume to the total volume, is determined by an uncertain parameter (see parameter CULEBRA:APOROS in Feng and Kicker (2025a), Table 3).

The hydrodynamic dispersion tensor is defined by (Bear 1972; WIPP Performance Assessment 2022f):

$$\mathbf{D}_k = \frac{1}{\|\mathbf{v}\|\phi}\begin{bmatrix} u & -v \\ v & u \end{bmatrix}\begin{bmatrix} \alpha_L & 0 \\ 0 & \alpha_T \end{bmatrix}\begin{bmatrix} u & v \\ -v & u \end{bmatrix} + \tau D_k^* \begin{bmatrix} 1 & 0 \\ 0 & 1 \end{bmatrix} \quad \text{(PA.238)}$$

where α_L and α_T are the longitudinal and transverse dispersivities (m), respectively; *u* and *v* are the *x* and *y* components of $\mathbf{v}$ (i.e., $\mathbf{v} = [u, v]$); D_k^* is the free water molecular diffusion coefficient (m^2 s^{-1}) for radionuclide *k*; and τ is the advective tortuosity. The CRA-2026 PA uses $\alpha_L = \alpha_T = 0$ m and $\tau = 1$. Thus, the definition of $\mathbf{D}_k$ used in PA reduces to:

$$\mathbf{D}_k = D_k^* \begin{bmatrix} 1 & 0 \\ 0 & 1 \end{bmatrix} \quad \text{(PA.239)}$$

The molecular diffusion coefficients D_k^* for the radionuclides under consideration are determined by oxidation state as shown in Table PA-15 (see parameters AM+3:MD0,

PU+3:MD0, PU+4:MD0, TH+4:MD0, U+4:MD0 and U+6:MD0 in Feng and Kicker 2025a, Table 26). Diffusion coefficients vary by oxidation state because the ionic radius, charge, and hydration shell of a radionuclide ion in solution are functions of its oxidation state, all of which govern the resistance the ion encounters as it moves through the fluid. The oxidation state of Pu (i.e., as Pu(III) or Pu(IV)) and U (i.e., as U(IV) or U(VI)) is determined by an uncertain parameter (see parameter GLOBAL:OXSTAT in Feng and Kicker (2025a), Table 3).

Table PA-15. Diffusion Coefficients by Oxidation State

Oxidation State	III	IV	VI
Diffusion Coefficient (m^2/s)	3.00×10^{-10}	1.53×10^{-10}	4.26×10^{-10}

The advective retardation coefficient R_k is defined by (Bear and Bachmat 1990):

$$R_k = 1 + (1 - \phi)\rho_A K_{Ak}/\phi \quad \text{(PA.240)}$$

where

ρ_A = surface area density of fractures in Culebra ($m^2/m^3 = m^{-1}$) (i.e., surface area of fractures (m^2) divided by volume of fractures (m^3))

K_{Ak} = surface area distribution coefficient ($(kg/m^2)/(kg/m^3) = m$) (i.e., concentration of radionuclide *k* sorbed on fracture surfaces (kg/m^2) divided by concentration of radionuclide *k* dissolved in brine within fractures (kg/m^3))

In the CRA-2026 PA, K_{Ak} = 0 and thus R_k = 1.

In concept, the term Q_k in Equation (PA.237) provides the link between the releases to the Culebra calculated with NUTS and PANEL (Sections PA-4.4 and PA-4.5) and transport within the Culebra. In the computational implementation of PA, radionuclide transport calculations in the Culebra are performed for unit radionuclide releases to the Culebra, and the outcomes of these calculations are used to construct the release to the accessible environment associated with time-dependent releases into the Culebra derived from NUTS and PANEL calculations (Section PA-6.4.3). The definition of Q_k is discussed in more detail in Section PA-4.10.1.4.

The initial condition for Equation (PA.237) is:

$$C_k(x, y, 0) = 0 \text{ kg/m}^3 \quad \text{(PA.241)}$$

Furthermore, the boundary conditions for Equation (PA.237) are defined on the boundary of the grid in Figure PA-36. At boundaries brine is assumed to be free of radionuclides, thus the following Dirichlet (Type I) boundary condition is applied:

$$C_k(x, y, t) = 0 \text{ kg/m}^3 \quad \text{(PA.242)}$$

PA-4.10.1.2 Diffusive Transport in the Matrix

The system of PDEs used to represent diffusive transport in the matrix surrounding the fractures is given by (WIPP Performance Assessment 2022f):

$$\frac{\partial}{\partial \chi}\left(\phi'_k D'_k \frac{\partial C'_k}{\partial \chi}\right) = \phi' R'_k \left(\frac{\partial C'_k}{\partial t}\right) + \phi' R'_k \lambda_k C'_k - \phi' R'_{k-1} \lambda_{k-1} C'_{k-1} \quad \text{(PA.243)}$$

where χ is the spatial coordinate in Figure PA-41, D'_k is the matrix diffusion coefficient (m^2/s) for radionuclide *k* defined by $D'_k = D^*_k \tau'$, and τ' is the matrix tortuosity. The remaining terms have the same meaning as those in Equation (PA.237), except that the prime denotes properties of the matrix surrounding the fractures. A constant value ($\tau' = 0.11$) for the matrix (i.e., diffusive) tortuosity is used in PA (Meigs 1996). The matrix (i.e., diffusive) porosity ϕ' is an uncertain input to the analysis (see parameter CULEBRA:DPOROS in Feng and Kicker (2025a), Table 3). The matrix retardation R'_k is defined by:

$$R'_k = 1 + (1 - \phi')\rho_S K_{dk}/\phi' \quad \text{(PA.244)}$$

where ρ_S is the particle density (kg/m^3) of the matrix and K_{dk} is the distribution coefficient ((Ci/kg)/(Ci/m^3) = m^3/kg) for radionuclide *k* in the matrix. The density ρ_S is assigned a value of 2.82×10^3 kg/m^3 (Martell 1996b). The distribution coefficients K_{dk} are uncertain inputs to the analysis and dependent on the uncertain oxidation state of the relevant element (see parameters AM+3:MKD_AM, PU+3:MKD_PU, PU+4:MKD_PU, U+4:MKD_U and U+6:MKD_U in Feng and Kicker (2025a), Table 3).

The initial and boundary value conditions used in the formulation of Equation (PA.243) are:

$$C'_k(x, y, \chi, 0) = 0 \text{ kg/m}^3 \quad \text{(PA.245)}$$

$$\partial C'_k(x, y, 0, t)/\partial z = 0 \text{ (kg/m}^3\text{)/m} \quad \text{(PA.246)}$$

$$C'_k(x, y, B, t) = C_k(x, y, t) \quad \text{(PA.247)}$$

where (x, y) corresponds to a point in the domain on which Equation (PA.237) is solved and B is the matrix half-block length (m) in Figure PA-41 (i.e., $2B$ is the thickness of the matrix between two fractures). The initial condition in Equation (PA.245) means that no radionuclide is present in the matrix at the beginning of the calculation. The boundary value condition in Equation (PA.246) implies that no radionuclide movement can take place across the centerline of a matrix block separating two fractures. The boundary value condition in Equation (PA.247) ensures that the dissolved radionuclide concentration in the matrix at the boundary with the fracture is the same as the dissolved radionuclide concentration within the fracture. The matrix half-block length B is an uncertain input to the analysis (see parameter CULEBRA:HMBLKLT in Feng and Kicker (2025a), Table 3).

PA-4.10.1.3 Coupling Between Fracture and Matrix Equations

The coupling between fracture and matrix equations describes the exchange between low-permeability rock matrices and high-permeability fracture networks. The linkage between Equation (PA.237) and Equation (PA.243) is accomplished through the term Γ_k, defining the rate at which radionuclide *k* diffuses across the boundary between a fracture and the adjacent matrix (see Figure PA-41). Specifically (Bear and Bachmat 1990):

$$\Gamma_k = -\frac{2\phi}{w} D_k^{'} \left. \frac{\partial C_k^{'}}{\partial \chi} \right|_{\chi=B} \tag{PA.248}$$

where *w* is the fracture aperture (m) defined by:

$$w = \phi B \,/(1-\phi) \tag{PA.249}$$

χ is the local coordinate within the matrix block and B is the matrix half-block length (m).

PA-4.10.1.4 Computational Grid and Discretization

Radionuclide transport calculations in the Culebra are performed using a uniform 50 × 50 m grid, and flow in the Culebra is solved on a 100 × 100-meter grid (Section PA-4.9.2; Figure PA-36). Darcy fluid velocities and material properties are mapped onto a 50 × 50-meter grid by subdividing each of the 100-meter model grid cells into four equal-sized cells and copying properties of the larger cells into each of the smaller cells (Bethune 2023, Appendix A). Copied properties include the boundary condition heads for the top and bottom elevation arrays, the starting head array, the T-fields input anisotropy, mining modified conductivity (Section PA-4.9.3), recharge, and storage. The Dirichlet boundary condition head values are smoothed along the exterior two rows and columns of the domain. The zero-gradient Neumann condition at outflow boundaries is resolution-independent and requires no analogous treatment.

PA-4.10.1.5 Source Term

Equation (PA.237) and Equation (PA.243) are solved for unit radionuclide releases to the Culebra. Specifically, a release of 1 kg of each of the four lumped radionuclides (^{241}Am, ^{234}U, ^{230}Th, and ^{239}Pu) is assumed to take place over a time interval from 0 to 50 years. For the CRA-2026 PA IS repository configuration, release into the Culebra occurs at two locations (Wilgus and Bethune 2025): the centroid of panels 1 through 10 (CRP 1) and the centroid of panels 11 and 12 (CRP 2). Each release occurs in a 50 m × 50 m computational grid cell. The volume of this cell is given by:

$$V = 50\ \text{m} \times 50\ \text{m} \times 4\ \text{m} = 10^4\ \text{m}^3 \tag{PA.250}$$

where 4 m is the effective thickness of the Culebra Dolomite (Meigs and McCord 1996). As a result, $Q_k(x, y, t)$ has the form:

$$Q_k(x,y,t) = \frac{1\ kg}{\left(1\times10^4\ m^3\right)\left(50\ yr\right)\left(3.16\times10^7\ s/yr\right)} = 6.33\times10^{-14}\ kg/m^3/s \quad \text{(PA.251)}$$

for $0 \leq t \leq 50$ yr and (x, y) in each release point cell, and $Q_k(x, y, t)$ = 0 (kg/m^3/s) otherwise.

PA-4.10.1.6 Cumulative Releases

If B denotes an arbitrary boundary (e.g., the LWB) in the domain of Equation (PA.237) (i.e., Figure PA-36), then the cumulative transport of $C_k(t, B)$ of radionuclide *k* from time 0 to time *t* across B is given by:

$$C_k(t,B) = \int_0^t \left[\int_B \left\{ \mathbf{v}(x,y) C_k(x,y,\tau) - \phi \mathbf{D}_k(x,y,t) \nabla C_k(x,y,\tau) \right\} b \cdot \mathbf{n}(x,y)\, ds \right] d\tau \quad \text{(PA.252)}$$

where *b* is the thickness of the Culebra (4 m), ϕ is the advective porosity in Equation (PA.237), $\mathbf{n}(x, y)$ is an outward pointing unit normal vector, and $\int_B ds$ denotes a line integral over B.

PA-4.10.2 Numerical Solution

The numerical solution to the coupled PDE system represented by Equation (PA.237) and Equation (PA.243) is computed using SECOTP2D, an implicit finite-volume code for the simulation of multispecies reactive transport. A high-level description of the numerical procedures implemented in SECOTP2D follows; more detail is available in the WIPP Performance Assessment (2022f).

PA-4.10.2.1 Discretization of Fracture Domain

The fracture domain is discretized in space using the block-centered finite-difference method indicated in Figure PA-42. In this formulation, cell concentrations are defined at grid block centers while the velocity components [*u*, *v*] are defined on grid cell faces. A uniform mesh with 50 m × 50 m cells is used for the spatial discretization. Ghost cells are placed outside the problem domain to implement boundary conditions. The temporal discretization is performed using variable time step.

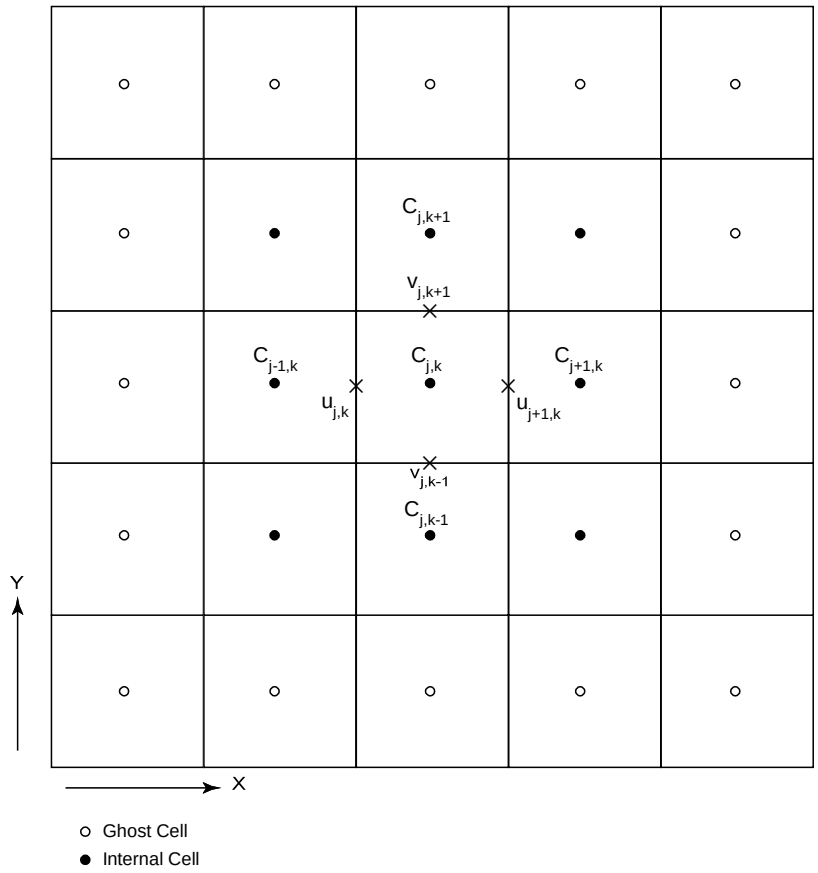


Figure PA-42. Schematic of Finite-Volume Staggered Mesh Showing Internal and Ghost Cells

The dispersive term, $\nabla \cdot (\phi D_k \nabla C_k)$, in Equation (PA.237) is approximated using a second-order central difference formula (Fletcher 1988).

The advective term, $\nabla \cdot \mathbf{v} C_k$, is approximated using the Total Variation Diminishing (TVD) method (Sweby 1984). The TVD method provides a way of accurately resolving advection-dominated transport problems without the occurrence of nonphysical oscillations commonly present in second-order solutions. This method invokes a weighted upstream differencing scheme that locally adjusts the weighting to prevent oscillatory behavior and maximize solution accuracy. The weighting parameters are known as the TVD flux limiters $\Phi(x, y, r)$, where *r* is a function of the concentration gradient and direction of flow. PA uses the van Leer TVD limiter (Sweby 1984, p. 1005), which is defined as:

$$\Phi(x, y, r) = \max\left\{0, \min\left\{2r, \frac{r + |r|}{1 + |r|}\right\}\right\} \quad \text{(PA.253)}$$

At locations where u (i.e., the Darcy velocity in the x direction) is positive, *r* is defined at the *j*–1/2, *k* interface by:

$$r_{j-1/2,k} = \frac{\partial C/\partial x\big|_{j-3/2,k}}{\partial C/\partial x\big|_{j-1/2,k}} \quad \text{(PA.254)}$$

and at locations where u is negative, *r* is defined by:

$$r_{j-1/2,k} = \frac{\partial C/\partial x\big|_{j+1/2,k}}{\partial C/\partial x\big|_{j-1/2,k}} \quad \text{(PA.255)}$$

Similar definitions are made for *r* at the *j*, *k*−1/2 interface in the y-direction with v (i.e., the Darcy velocity in the *y* direction) used instead of u.

Because Φ_k is a function of C_k, the discretized set of equations is nonlinear. This nonlinearity is addressed by treating the flux limiters explicitly (i.e., time lagged). Explicit treatment of the limiter functions, however, can lead to oscillatory and sometimes unstable solutions when the Courant number exceeds unity (*Cr* > 1), where *Cr* is defined by:

$$Cr = max\{Cr_x, Cr_y\}, Cr_x = |u|\,\Delta t/\phi\Delta x\,, Cr_y = |v|\,\Delta t/\phi\Delta y \quad \text{(PA.256)}$$

To avoid this behavior, the application of the TVD method is restricted to regions in which the Courant numbers are less than one. In regions where *Cr* > 1, a first-order full upwind scheme is used, which is unconditionally stable and nonoscillatory.

The discretized form of Equation (PA.237) can be expressed in a delta formulation as:

$$\left(\mathbf{I} + \mathbf{L}_{xx} + \mathbf{L}_{yy} + \mathbf{S}\right)\Delta\mathbf{C}^{n+1} = \mathbf{RHS}^{n} \quad \text{(PA.257)}$$

Where $\mathbf{I}$ is the identity matrix, $\mathbf{L}_{xx}$ and $\mathbf{L}_{yy}$ are finite-difference operators in the x and y directions, $\mathbf{S}$ is an implicit source term that accounts for decay and mass transfer between the matrix and the fracture, $\mathbf{RHS}$ consists of the right-hand-side known values at time level *n*, and $\Delta\mathbf{C}^{n+1} = \mathbf{C}^{n+1} - \mathbf{C}^{n}$. Direct inversion of Equation (PA.257) for a typical Culebra transport problem is very computationally intensive, requiring large amounts of memory and time. To reduce these requirements, the operator in Equation (PA.257) is factored as follows:

$$\left(\mathbf{I} + \mathbf{L}_{xx} + \alpha_x\mathbf{S}\right)\left(\mathbf{I} + \mathbf{L}_{yy} + \alpha_y\mathbf{S}\right)\Delta\mathbf{C}^{n+1} = \mathbf{RHS}^{n} \quad \text{(PA.258)}$$

where α_x and α_y are constants that must sum to one (i.e., $\alpha_x + \alpha_y = 1$). The left-hand sides in Equation (PA.257) and Equation (PA.258) are not equivalent, with the result that the factorization of Equation (PA.257) and Equation (PA.258) is referred to as an approximate factorization (Fletcher 1988). The advantage of approximately factoring Equation (PA.257) is that the resulting equation consists of the product of two finite-difference operators that are easily inverted independently using a tridiagonal solver. Hence, the solution to the original problem is obtained by solving a sequence of problems in the following order:

$$\left(\mathbf{I}+\mathbf{L}_{xx}+\alpha_x\mathbf{S}\right)\Delta\overline{\mathbf{C}}=\mathbf{RHS}^n \tag{PA.259}$$

$$\left(\mathbf{I}+\mathbf{L}_{yy}+\alpha_y\mathbf{S}\right)\Delta\mathbf{C}^{n+1}=\Delta\overline{\mathbf{C}} \tag{PA.260}$$

$$\mathbf{C}^{n+1}=\mathbf{C}^n+\Delta\mathbf{C}^{n+1} \tag{PA.261}$$

PA-4.10.2.2 Discretization of Matrix Equation

The nonuniform mesh used to discretize the matrix equation is shown in Figure PA-43. The mesh is intentionally refined near the origin, where larger solution gradients are expected, and becomes progressively coarser with distance from the origin. The nonuniform physical spacing is transformed into a uniform computational spacing in ξ-space for numerical discretization. The straightforward application of standard finite-difference or finite-volume discretization on nonuniform meshes results in truncation error terms that are proportional to the mesh spacing variation (Hirsch 1988). For nonuniform meshes, the discretization can be performed after a transformation from the Cartesian physical space (χ) to a stretched Cartesian computational space (ξ). The transformation is chosen so that the nonuniform grid spacing in physical space is transformed to a uniform spacing of unit length in computational space. The computational equations contain metric coefficients (i.e., derivatives relating the physical and computational coordinates, such as $\partial\chi/\partial\xi$) that account for local grid stretching and introduce the mesh-size influence into the difference formulas. . Standard unweighted differencing schemes can then be applied to the governing equations in the computational space.

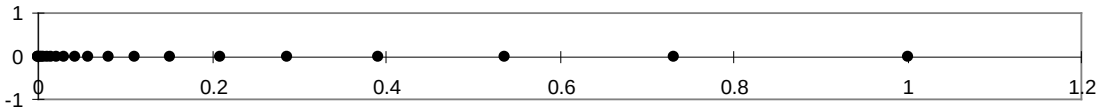


Figure PA-43. Illustration of Stretched Grid Used for Matrix Domain Discretization

The SECOTP2D code applies such a coordinate transformation to the nonuniform diffusion domain mesh, solving the transformed system of equations in the uniform computational space. The transformed matrix equation is written as:

$$\phi' R'_k \frac{\partial \hat{C}'_k}{\partial t} - \frac{\partial \hat{F}'_v}{\partial \xi'} = -\phi' R'_k \lambda_k \hat{C}'_k + \phi' R'_{k-1} \lambda_{k-1} \hat{C}'_{k-1} \tag{PA.262}$$

where

$$\hat{C}'_k = \frac{C'_k}{J} \tag{PA.263}$$

$$\hat{F}'_v = D' \xi'_x \frac{\partial C'_k}{\partial \xi'} \tag{PA.264}$$

In the uniform computational space, a first-order backward difference formula is used to approximate the temporal derivative, while a second-order accurate central difference is used to approximate spatial derivatives.

PA-4.10.2.3 Fracture-Matrix Coupling

The equations for the fracture and the matrix are coupled through the mass transfer term, Γ_k. In the numerical solution, these equations are coupled in a fully implicit manner and solved simultaneously. Because the exchange term depends on concentrations in both domains, the governing equations form a coupled system that must be solved simultaneously to preserve numerical stability and mass conservation. A procedure outlined in Huyakorn et al. (1983) was adapted and redeveloped for an approximate factorization algorithm with the delta formulation and a finite-volume grid. The coupling procedure consists of three steps:

Step 1. Write the mass transfer term G_k in a delta (Δ) form.

Step 2. Evaluate Δ terms that are added to the implicit part of the fracture equation. This is accomplished using the inversion process (LU factorization) in the solution of the matrix equation. After the construction of the lower tridiagonal matrix $\mathbf{L}$ and the intermediate solution, there is enough information to evaluate the D terms. This new information is fed into the fracture equation that is subsequently solved for concentrations in the fracture at the new time level (*n*+1).

Step 3. Construct the boundary condition for the matrix equation at the fracture-matrix interface using fracture concentrations at the (*n*+1) time level. Matrix concentrations are then obtained using the upper tridiagonal matrix $\mathbf{U}$ by back substitution.

A detailed description of this technique and its implementation is given in the SECOTP2D design document (WIPP Performance Assessment 2022f).

PA-4.10.2.4 Cumulative Releases

The cumulative transport $C_k(t, B)$ of individual radionuclides across specified boundaries indicated in Equation (PA.252) is also accumulated during the numerical solution of Equation (PA.237) and Equation (PA.243).

PA-4.10.3 Additional Information

Additional information on the use of SECOTP2D to determine radionuclide transport in the Culebra can be found in the SECOTP2D user's manual (WIPP Performance Assessment 2022f).

PA-5.0 Probabilistic Characterization of Subjective Uncertainty

This section summarizes the treatment of parameter uncertainty in the CRA-2026 PA. This epistemic uncertainty is represented through probability distributions assigned to uncertain input parameters and gives rise to the distribution of CCDFs defined in Section PA-2.5.3.

PA-5.1 Probability Space

The probability space that characterizes epistemic uncertainty can be represented as (S_{su}, $\mathbb{S}_{su}$, p_{su}). The subscript *su* indicates that epistemic (i.e., subjective) uncertainty is being considered. The individual elements of S_{su} are vectors $\mathbf{v}_{su}$ of the form:

$$\mathbf{v}_{su} = [v_1, v_2, \cdots, v_{nv}] \tag{PA.265}$$

where each v_i is an imprecisely known input to the analysis, and *nv* is the number of such inputs.

The uncertainty in the v_i, and hence in $\mathbf{v}_{su}$, is characterized by developing a probability distribution for each v_i:

$$D_i, i = 1,2, \cdots, nv \tag{PA.266}$$

It is the distributions in Equation (PA.266) and any associated correlations between the v_i that define p_{su}. The probability distribution for each parameter is based on all available knowledge about the parameter, including measurements, and describes a degree of belief as to the appropriate range of the parameter value. This degree of belief depends on the numerical, spatial, and temporal resolution of the models selected for use in PA (Section PA-4.0). Correlations and other dependencies between imprecisely known variables are also possible. These relationships represent observed or logical dependencies between the possible parameter values.

The uncertain parameters incorporated into the CRA-2026 PA are identified in Section PA-5.2, and the distributions assigned to these variables are described in Feng and Kicker (2025a), Table 3. Sampling for uncertain parameters is described in PA-6.1 where correlations and conditional relationships are defined.

PA-5.2 Variables Included for Subjective Uncertainty

The CRA-2026 PA identified 64 imprecisely known variables for inclusion in the analysis (see Feng and Kicker 2025a, Table 3). All the uncertain variables in the CRA-2026 PA were also treated as uncertain in the CRA-2019 PA. Table PA-16 lists the uncertain parameters for which the distribution of values has changed between the CRA-2019 PA and the CRA-2026 PA.

Table PA-16. Sampled Parameters with Updated Distributions Since the CRA-2019 PA

Material	Property	Description
BH_SAND	PRMX_LOG	Logarithm of intrinsic permeability (m^2) of the silty-sand-filled borehole (Table PA-8). Used in regions Upper Borehole and Lower Borehole in Figure PA-12.
GLOBAL	PBRINE	Probability that a drilling intrusion penetrates pressurized brine in the Castile. Defines pB_1; see Section PA-3.2.3.
PCS_T2	POR2PERM	Distribution used to calculate permeability from sampled porosity values for panel closures between 100 and 200 yr.
SOLMOD3	SOLVAR	Solubility multiplier (dimensionless) for III oxidation states. Defines $VSOL(III)$ in Equation (PA.66).
SOLMOD4	SOLVAR	Solubility multiplier (dimensionless) for IV oxidation states. Defines $VSOL(IV)$ in Equation (PA.66).
WAS_AREA	BRUCITEC	MgO hydration rate in inundated conditions with ERDA-6 brine. Defines R_{hi} in Appendix GEOCHEM-2026, Equation GEOCHEM.18.
WAS_AREA	BRUCITES	MgO hydration rate in inundated conditions with GWB. Defines R_{hi} in Appendix GEOCHEM-2026, Equation GEOCHEM.18.

Each uncertain variable is assigned a distribution that characterizes the subjective uncertainty in that variable. Distributions for each of the 64 parameters sampled by the LHS code during the PA are described in Feng and Kicker (2025a), Table 3. The subjectively uncertain variables are listed in Table PA-17. The code STEPWISE, used for sensitivity analysis, uses short names for input parameters rather than material:property designations used in other codes. The short names used in STEPWISE are listed in Table PA-17 under the "Variable Name" column and are taken from Table 1 of King and Zeitler (2025).

Table PA-17. Variables Representing Epistemic Uncertainty in the CRA-2026 PA

Material	Property	Variable Name	Description
AM+3	MKD_AM	CMKDAM3	Matrix distribution coefficient (m^3/kg) for Am in the III oxidation state. Defines K_{dk} in Equation (PA.245) for Am.
BH_SAND	PRMX_LOG	BHPRM	Logarithm of intrinsic permeability (m^2) of the silty-sand-filled borehole (Table PA-8). Used in regions Upper Borehole and Lower Borehole in Figure PA-12.
BOREHOLE	DOMEGA	DOMEGA	Drill string angular velocity (rad/s). Defines $\Delta\Omega$ in Equation (PA.99).

Material	Property	Variable Name	Description
BOREHOLE	TAUFAIL	WTAUFAIL	Shear strength of waste (Pa). Defines $\tau\,(R, 1)$ in Equation (PA.97).
CASTILER	COMP_RCK	BPCOMP	Bulk compressibility (Pa^{-1}) of Castile brine reservoir. Defines c_b in Equation (PA.60) for Castile brine reservoir in Figure PA-12.
CASTILER	PRESSURE	BPINTPRS	Initial brine pore pressure in the Castile brine reservoir (Figure PA-12).
CASTILER	PRMX_LOG	BPPRM	Logarithm of intrinsic permeability (m^2) of the Castile brine reservoir. Used in Castile brine reservoir in Figure PA-12.
CONC_PLG	PRMX_LOG	PLGPRM	Logarithm of intrinsic permeability (m^2) of the concrete borehole plugs (Table PA-8). Used in region Borehole Plugs in Figure PA-12.
CULEBRA	APOROS	CFRACPOR	Culebra fracture (i.e., advective) porosity (dimensionless). Defines ϕ in Equation (PA.237).
CULEBRA	DPOROS	CMTRXPOR	Culebra matrix (i.e., diffusive) porosity (dimensionless). Defines ϕ' in Equation (PA.244).
CULEBRA	HMBLKLT	CFRACSP	Culebra fracture spacing (m). Equal to half the distance between fractures (i.e., the Culebra half-matrix-block length). Defines B in Equation (PA.248).
CULEBRA	MINP_FAC	CTRANSFM	Multiplier (dimensionless) applied to transmissivity of the Culebra within the LWB after mining of potash reserves. Defines MF in Section PA-4.9.5.
DRZ_1	PRMX_LOG	DRZPRM	Logarithm of intrinsic permeability (m^2) of the DRZ. Used in regions Upper DRZ and Lower DRZ in Figure PA-12.
DRZ_PCS	PRMX_LOG	DRZPCPRM	Logarithm of intrinsic permeability (m^2) of the DRZ immediately above and below the panel closure (Section PA-4.2.9). Used in region DRZ_PCS in Figure PA-12.
GLOBAL	CLIMTIDX	CCLIMSF	Climate scale factor (dimensionless) for Culebra flow field. Defines SFC in Equation (PA.234).
GLOBAL	GDEPFAC	GDEPFAC	Energy deposition probability for wetted solid radionuclides. Defines P_{dep} in Appendix GEOCHEM-2026, Equation GEOCHEM-23.
GLOBAL	OXSTAT	WOXSTAT	Scalar for selecting elemental oxidation states (dimensionless). See Appendix SOTERM-2026, Section SOTERM-6.3.
GLOBAL	PBRINE	PBRINE	Probability that a drilling intrusion penetrates pressurized brine in the Castile. Defines pB_1; see Section PA-3.2.3.
GLOBAL	TRANSIDX	CTRAN	Index variable for selecting T-field. See Section PA-4.9.3.
PCS_T1	PORE_DIS	T1PDIS	Brooks-Corey pore distribution parameter for panel closures during early times. Defines λ in Equations (PA.30) through (PA.32). See Table PA-5.
PCS_T1	POROSITY	T1POROS	Porosity for panel closures between 0 and 100 yr. See Table PA-5.

Material	Property	Variable Name	Description
PCS_T1	PRMX_LOG	T1PRMX	Log of intrinsic permeability, *x*-direction for panel closures between 0 and 100 yr. See Table PA-5.
PCS_T1	SAT_RBRN	T1SRBRN	Residual brine saturation for panel closures between 0 and 100 yr. See Table PA-5.
PCS_T1	SAT_RGAS	T1SRGAS	Residual gas saturation for panel closures between 0 and 100 yr. See Table PA-5.
PCS_T2	POR2PERM	T2P2PERM	Used to calculate permeability from sampled porosity values for panel closures after 100 yr.
PCS_T2	POROSITY	T2POROS	Effective porosity for panel closures between 100 and 200 yr. See Table PA-5.
PCS_T3	POROSITY	T3POROS	Effective porosity for panel closures after 200 yr. See Table PA-5.
PU+3	MKD_PU	CMKDPU3	Matrix distribution coefficient (m^3/kg) for Pu in III oxidation state. Defines K_{dk} in Equation (PA.245) for Pu(III).
PU+4	MKD_PU	CMKDPU4	Matrix distribution coefficient (m^3/kg) for Pu in IV oxidation state. Defines K_{dk} in Equation (PA.245) for Pu(IV).
S_HALITE	COMP_RCK	HALCROCK	Bulk compressibility of halite (Pa^{-1}). Defines c_r in Equation (PA.44) for Salado region of Figure PA-12.
S_HALITE	POROSITY	HALPOR	Halite porosity (dimensionless). Defines ϕ_0 in Equation (PA.43) for Salado region in Figure PA-12.
S_HALITE	PRESSURE	SALPRES	Initial brine pore pressure (Pa) in the Salado halite, applied at an elevation consistent with the intersection of MB 139. Defines $P_{b,ref}$ for Equation (PA.48) for Salado region in Figure PA-12.
S_HALITE	PRMX_LOG	HALPRM	Logarithm of intrinsic halite permeability (m^2). Used in region Salado in Figure PA-12. See Table PA-5.
S_MB139	PORE_DIS	ANHBCEXP	Brooks-Corey pore distribution parameter for anhydrite (dimensionless). Defines λ in Equations (PA.30) through (PA.32) for regions MB 138, Anhydrite AB, and MB 139 of Figure PA-12 for use with Brooks-Corey model; defines λ in $m = \lambda/(1 + \lambda)$ for Equation (PA.37), Equation (PA.38), and Equation (PA.39) for use with van Genuchten-Parker model in the same regions.
S_MB139	PRMX_LOG	ANHPRM	Logarithm of intrinsic anhydrite permeability (m^2). Used in regions MB 138, Anhydrite AB, and MB 139 in Figure PA-12.
S_MB139	RELP_MOD	ANHBCVGP	Index for relative permeability model (dimensionless) for regions MB 138, Anhydrite AB, and MB 139 in Figure PA-12. See Table PA-6.
S_MB139	SAT_RBRN	ANRBRSAT	Residual brine saturation in anhydrite (dimensionless). Defines S_{br} in Equations (PA.34) and (PA.35) for regions MB 138, Anhydrite AB, and MB 139 in Figure PA-12.

Material	Property	Variable Name	Description
SHFTL_T1	PRMX_LOG	SHLPRM2	Logarithm of intrinsic permeability (m^2) of lower shaft-seal materials for the first 200 years after closure. Used in Lower Shaft region in Figure PA-12.
SHFTL_T2	PRMX_LOG	SHLPRM3	Logarithm of intrinsic permeability (m^2) of lower shaft-seal materials from 200 years to 10,000 years after closure. Used in Lower Shaft region in Figure PA-12.
SHFTU	PRMX_LOG	SHUPRM	Logarithm of intrinsic permeability (m^2) of upper shaft-seal materials. Used in Upper Shaft region in Figure PA-12.
SHFTU	SAT_RBRN	SHURBRN	Residual brine saturation in upper shaft-seal materials (dimensionless). Defines S_{br} in Equations (PA.34) and (PA.35) for Upper Shaft region in Figure PA-12.
SHFTU	SAT_RGAS	SHURGAS	Residual gas saturation in upper shaft-seal materials (dimensionless). Defines S_{gr} in Equation (PA.35) for Upper Shaft region in Figure PA-12.
SOLMOD3	SOLVAR	WSOLVAR3	Solubility multiplier (dimensionless) for III oxidation states. Defines $VSOL(III)$ in Equation (PA.66).
SOLMOD4	SOLVAR	WSOLVAR4	Solubility multiplier (dimensionless) for IV oxidation states. Defines $VSOL(IV)$ in Equation (PA.66).
SPALLMOD	PARTDIAM	SPPDIAM	Particle diameter of waste (m) after tensile failure. Defines d_p in Equation (PA.152).
SPALLMOD	REPIPERM	REPIPERM	Waste permeability of gas (m^2) local to intrusion borehole. Defines *k* in Equation (PA.134).
SPALLMOD	REPIPOR	SPLRPOR	Waste porosity (dimensionless) at time of drilling intrusion. Defines ϕ in Equation (PA.133).
SPALLMOD	TENSLSTR	TENSLSTR	Tensile strength (Pa) of waste. Defines $\bar{\sigma}_r$ in Section PA-4.7.2.3.4.
STEEL	CORRMCO2	WGRCOR	Rate of anoxic steel corrosion (m/s) under brine-inundated conditions. Defines R_{ci} in Appendix GEOCHEM-2026, Equation GEOCHEM.12.
STEEL	HUMCORR	HUMCORR	Rate of steel corrosion under humid conditions. Defines R_{ch} in Appendix GEOCHEM-2026, Equation GEOCHEM-12.
TH+4	MKD_TH	CMKDTH4	Matrix distribution coefficient (m^3/kg) for Th in IV oxidation state. Defines K_{dk} in Equation (PA.244) for Th(IV).
U+4	MKD_U	CMKDU4	Matrix distribution coefficient (m^3/kg) for U in IV oxidation state. Defines K_{dk} in Equation (PA.244) for U(IV).
U+6	MKD_U	CMKDU6	Matrix distribution coefficient (m^3/kg) for U in VI oxidation state. Defines K_{dk} in Equation (PA.244) for U(VI).
WAS_AREA	BIOGENFC	WBIOGENF	Probability of obtaining sampled microbial gas generation rates. Defines B_{fc} in Appendix GEOCHEM-2026, Equation GEOCHEM.16.
WAS_AREA	BRUCITEC	WBRUITEC	MgO hydration rate in inundated conditions with ERDA-6 brine. Defines R_{hi} in Appendix GEOCHEM-2026, Equation GEOCHEM.18.

Material	Property	Variable Name	Description
WAS_AREA	BRUCITEH	WBRUITEH	MgO hydration rate in humid conditions. Defines R_{hh} in Appendix GEOCHEM-2026, Equation GEOCHEM.18.
WAS_AREA	BRUCITES	WBRUITES	MgO hydration rate in inundated conditions with GWB. Defines R_{hi} in Appendix GEOCHEM-2026, Equation GEOCHEM.18.
WAS_AREA	GRATMICH	WGRMICH	Rate of CPR biodegradation (mol $C_6H_{10}O_5$ / kg $C_6H_{10}O_5$ /s) under humid conditions. Defines R_{mi} in Appendix GEOCHEM-2026, Equation GEOCHEM.16.
WAS_AREA	GRATMICI	WGRMICI	Rate of CPR biodegradation (mol $C_6H_{10}O_5$ / kg $C_6H_{10}O_5$ /s) under brine-inundated conditions. Defines R_{mh} in Appendix GEOCHEM-2026, Equation GEOCHEM.16.
WAS_AREA	HYMAGCON	WHYMAGC	Rate of conversion of hydromagnesite to magnesite. Defines R_{hc} in Appendix GEOCHEM-2026, Equation GEOCHEM.21.
WAS_AREA	PROBDEG	WMICDFLG	Index for model of CPR material microbial degradation (dimensionless). Defines D_c in Appendix GEOCHEM-2026, Equation GEOCHEM.17. See Appendix GEOCHEM-2026, Section GEOCHEM-2.4.2.
WAS_AREA	SAT_RBRN	WRBRNSAT	Residual brine saturation in waste (dimensionless). Defines S_{br} in Equations (PA.34) and (PA.35).
WAS_AREA	SAT_RGAS	WRGSSAT	Residual gas saturation in waste (dimensionless). Defines S_{gr} in Equation (PA.35).
WAS_AREA	SAT_WICK	WASTWICK	Increase in brine saturation of waste due to capillary forces (dimensionless). Defines S_{wick} in Equation (PA.57).

PA-6.0 Computational Procedures

This section outlines the computational procedures used to execute the CRA-2026 PA. First, the sampling procedures applied to the probability spaces for epistemic and aleatory uncertainty are outlined. The mechanistic calculations used to evaluate a release (i.e., the function $f(\mathbf{x}_{st})$ in Equation (PA.17)) are tabulated, followed by a description of the algorithms used to compute the releases. This section concludes with a discussion of sensitivity analysis techniques used to identify the uncertain parameters that are primary contributors to the uncertainty in the PA results.

PA-6.1 Sampling for Epistemic Uncertainty

LHS is used to sample from the probability space for epistemic uncertainty to generate a distribution of CCDFs (Section PA-2.5.3). The LHS technique was first introduced by McKay et al. (1979). In LHS, the range of each uncertain parameter v_i is divided into $nLHS$ intervals of equal probability and one value is selected at random from each interval. The $nLHS$ values thus obtained for v_1 are paired at random without replacement with the $nLHS$ values obtained for v_2. These $nLHS$ pairs are combined in a random manner without replacement with the *nLHS* values of v_3 to form *nLHS* triples. This process is continued until a set of $nLHS$ nV-tuples are formed. These nV -tuples are of the form:

$$\mathbf{v}_{su,k} = \left[v_{k,1}, v_{k,2}, \cdots, v_{k,nV}\right], k = 1, \cdots, nLHS \quad \text{(PA.267)}$$

The elements $v_{k,i}$ of the vector $\mathbf{v}_{su,k}$ in Equation (PA.267) must be independent for the random matching procedure to work; a method for generating a LHS with correlated variables was developed by Iman and Conover (1982) and is used in WIPP PA.

A vector $\mathbf{v}_{su,k}$ constitutes the sample from the probability space (S_{su}, $\mathbb{S}_{su}$, p_{su}) for epistemic uncertainty. For more information about LHS and a comparison with other sampling techniques, see Helton and Davis (2003).

LHS stratifies the sampling to ensure that the sampled values cover the full range of each element v_i of $\mathbf{v}_{su}$ as required by 10 CFR 194.34(b). LHS provides unbiased estimates for means and distribution functions of each sampled variable (McKay et al. 1979). In particular, uncertainty and sensitivity analysis results obtained with LHS are robust even when relatively small samples (i.e., $nLHS$ = 50 to 200) are used (Iman and Helton 1988 and 1991; Helton et al. 1995).

Each element of an LHS corresponds to one CCDF of releases. 40 CFR 194.34(d) states that:

> The number of CCDFs generated shall be large enough such that, at cumulative releases of 1 and 10, the maximum CCDF generated exceeds the 99th percentile of the population of CCDFs with at least a 0.95 probability.

For an LHS of size $nLHS$, the preceding guidance is equivalent to the inequality:

$$1 - 0.99^{nLHS} > 0.95 \quad \text{(PA.268)}$$

which results in a minimum value of 298 for $nLHS$. PA uses a total sample size of 300 to represent the epistemic uncertainty. As discussed in the Section PA-6.1.2, the 300 samples are divided among 3 replicates of size 100 each to demonstrate convergence of the mean for the population of CCDFs.

PA-6.1.1 Generation of Latin Hypercube Samples

The LHS program (WIPP Performance Assessment 2022b) is used to produce three independently generated Latin hypercube samples of size $nLHS$ = 100 each, for a total of 300 sample elements. For notational convenience, the replicates are designated by R1, R2, and R3. Each individual replicate is a Latin hypercube sample of the form given in Equation (PA.267), with $nLHS$ = 100.

The random number seeds used in the CRA-2026 PA are the same as in the CRA-2019 PA. Use of the CRA-2019 PA random seeds (and parameter ordering as applicable) results in nearly identical samples of uncertain parameters common to both analyses, which is advantageous for comparing results between the two assessments. Correction of an error in the PRELHS code causes negligible differences in the samples for a few parameters (Docherty 2023b).

The restricted pairing technique (Iman and Conover 1982) is used to induce requested correlations and to assure that uncorrelated variables have correlations close to zero. The variable pairs (S_HALITE:PRMX_LOG, S_HALITE:COMP_RCK) and (CASTILER:PRMX_LOG, CASTILER:COMP_RCK) are assigned rank correlations of −0.99 and −0.75, respectively. All other variable pairs are assigned rank correlations of zero. The restricted pairing technique successfully produces these correlations (King and Zeitler 2025, Table 4).

The LHS code enforces two additional relationships between several parameters. The relationships are WAS_AREA:GRATMICH ≤ WAS_AREA:GRATMICI (Clayton 2008; Nemer and Stein 2005) and PCS_T3: POROSITY ≤ PCS_T2: POROSITY ≤ PCS_T1:POROSITY (Camphouse 2013b). For each pair of variables, LHS rescales the sampled value of the parameter to the left of the ≤ symbol to the new "controlled" value using the equation:

$$v_i' = \frac{v_i - U_{V,lower}}{U_{V,upper} - U_{V,lower}} \times \left(\min(x_i, U_{V,upper}) - U_{V,lower} \right) + U_{V,lower} \quad \text{(PA.269)}$$

where v_i' is the conditioned value of the left-hand variable, v_i is the sampled value of that variable, x_i is the sampled value of the right-hand variable, and $U_{V,lower}$ and $U_{V,upper}$ are the bounds of the distribution assigned to the left-hand variable. This method preserves the probability associated with the value of the left-hand variable.

PA-6.1.2 Statistical Confidence on Mean CCDF

40 CFR 194.34(f) states that

> Any compliance assessment shall provide information which demonstrates that there is at least a 95% level of statistical confidence that the mean of the population of CCDFs meets the containment requirements of § 191.13 of this chapter.

Given that LHS is used, the confidence intervals required by 40 CFR 194.34(f) are obtained with a replicated sampling technique proposed by Iman (1982). In this technique, the sampling in Equation (PA.267) is repeated *nS* times with different random seeds. These samples lead to a sequence $\overline{P}_r(R)$ (r = 1, 2, …, *nS*) of estimated mean exceedance probabilities, where $\overline{P}_r(R)$ defines the mean CCDF obtained for sample r (i.e., $\overline{P}_r(R)$ is the mean probability that a normalized release of size R will be exceeded; see Section PA-2.5.3) and *nS* is the number of independent samples. Then:

$$\overline{P}(R) = \sum_{r=1}^{nS} \overline{P}_r(R) \Big/ nS \tag{PA.270}$$

And:

$$SE(R) = \left\{ \sum_{r=1}^{nS} \left[\overline{P}_r(R) - \overline{P}(R) \right]^2 \Big/ nS(nS-1) \right\}^{1/2} \tag{PA.271}$$

provide an additional estimate of the mean CCDF and an estimate of the standard error (*SE*) associated with the mean exceedance probabilities. The t-distribution with *nS*-1 degrees of freedom can be used to construct confidence intervals for the mean exceedance probability of individual R values (i.e., around $\overline{P}(R)$). Specifically, the 1-α confidence interval is given by $\overline{P}(R) \pm t_{1-\alpha/2} SE(R)$ where $t_{1-\alpha/2}$ is the $1-\alpha/2$ quantile of the t-distribution with *nS*-1 degrees of freedom (e.g., $t_{1-\alpha/2} = 4.303$ for α = 0.05 and *nS* = 3).

PA-6.2 Sampling for Aleatory Uncertainty

Simple random sampling is applied to the probability space for aleatory uncertainty to generate possible futures that are then used to construct a CCDF (Section PA-2.5.2). Specifically, for each vector $\mathbf{v}_{su,k}$ of the LHS sample, individual futures of the form:

$$\mathbf{x}_{st,i,k} = \left[\left(t_{i,1}, e_{i,1}, l_{i,1}, b_{i,1}, p_{i,1}, \mathbf{a}_{i,1}, \right), \cdots, \left(t_{i,n}, e_{i,n}, l_{i,n}, b_{i,n}, p_{i,n}, \mathbf{a}_{i,n}, \right), t_{i,min} \right] \tag{PA.272}$$

are generated for $i = 1, \cdots, nS = 10{,}000$ futures, with n the number of drilling intrusions in the i^{th} future. This sample size (10,000) is sufficient to estimate the 0.999 quantile of the resulting CCDF of releases. The WIPP PA code CCDFGF is used to generate the possible futures.

A possible future, $\mathbf{x}_{st,i,k}$, is comprised of the collection of intrusion and mining events occurring in that future (see Section PA-2.5.1). The subscript *st* denotes that the future is an element of the probability space for aleatory (stochastic) uncertainty (S_{st}, $\mathbb{S}_{st}$, p_{st}), the subscript *i* indicates that the future is one of many possible futures, and the subscript *k* indicates that the probability distributions describing the future depend on a sample element from the probability space for epistemic uncertainty. The possible futures are sampled consistent with the joint probability distribution p_{st} for the elements of S_{st}. In practice, p_{st} is defined by specifying a distribution D_j for each element x_j of $\mathbf{x}_{st,i,k}$. The elements x_j are sampled independently, thus the elements of the sample of futures are independent.

Table PA-18 outlines the algorithm used to generate a single future in PA.

Table PA-18. Algorithm to Generate a Single Future

0.	Initialize the simulation time $t = 0$ yr and the intrusion counter $j = 0$.
1.	Sample the time to the next intrusion Δt with a time-dependent drilling frequency λ_d given in Equation (PA.6) (see Section PA-3.2). Set the intrusion time $t_{i,j} = t + \Delta t$. The index i is the number of the future. If $t_{i,j} > 10{,}000$ yr then proceed to Step 8. Otherwise increment the intrusion counter: $j = j + 1$.
2.	Sample the indicator $e_{i,j}$ for an intrusion into an excavated, waste-filled area with probabilities as given in Equation (PA.8) (see Section PA-3.2.1).
3.	For an intrusion into an excavated, waste-filled area, sample the index $l_{i,j}$ for the penetrated waste panel with probabilities given in Day (2025), Table 2 (see Section PA-3.2.2).
4.	Determine if the intrusion penetrates pressurized brine in the Castile by sampling $b_{i,j}$ with a probability of $p[B_1]$ that the intrusion will penetrate pressurized brine (see Section PA-3.2.3). $p[B_1]$ is subjectively uncertain and is sampled from a cumulative distribution given by parameter GLOBAL:PBRINE (Feng and Kicker (2025a), Table 3).
5.	Determine the plugging pattern by sampling $p_{i,j}$ with probabilities given in Section PA-3.2.4.
6.	Determine the activity level $a_{i,j}$ for cuttings and cavings releases (see Section PA-3.2.5).
	6.1 For penetration of a nonexcavated area (i.e., $e_{i,j} = 0$): $a_{i,j} = 0$.
	6.2 For penetration of an excavated area (i.e., $e_{i,j} = 1$): determine the type of waste encountered (CH-TRU or RH-TRU) by sampling an indicator with probabilities pCH and pRH given by Equations (PA.12) and (PA.13).
	6.3 For penetration of RH-TRU waste: determine the activity $a_{i,j} = [iRH_{i,j}]$ by sampling the index $iRH_{i,j}$ for the RH-TRU waste streams, with probabilities given in King (2026), Table 2.
	6.4 For penetration of CH-TRU waste: determine the activity $a_{i,j} = [iCH_{i,j,1}, iCH_{i,j,2}, iCH_{i,j,3}]$ by sampling three index values for the CH-TRUE waste streams, with probabilities given in King (2026), Table 1.
7.	Repeat Steps 1 – 6 until $t_{i,j} > 10{,}000$ yr.
8.	Sample t_{min} with a time-dependent λ_m given by Equation (PA.14) (see Section PA-3.3).

PA-6.3 Mechanistic Calculations

In the CRA-2026 PA, mechanistic calculations are performed with the models described in Section PA-4.0 for a few selected elements of S_{st} (see Section PA-3.4). The mechanistic calculations are repeated for each LHS element. This section summarizes the calculations performed with each of the models described in Section PA-4.0; Section PA-6.4 outlines the algorithms used to construct releases for the randomly sampled elements $\mathbf{x}_{st,i}$ of S_{st} from the results of the mechanistic calculations. Long (2025) documents the execution of the calculations and the archiving of the calculation results.

PA-6.3.1 BRAGFLO Calculations

The BRAGFLO code (Section PA-4.2) computes two-phase (brine and gas) flow in and around the repository. BRAGFLO results are used in the models for Salado transport (implemented in NUTS and PANEL), spallings (implemented in CUTTINGS_S), and DBR (also calculated by BRAGFLO). Thus, the BRAGFLO scenarios are used to define scenarios for other codes.

The four fundamental scenarios for the CRA-2026 PA (Section PA-3.4) define four categories of calculations to be performed with BRAGFLO (i.e., E0, E1, E2, and E1E2). These four fundamental scenarios were expanded into six specific scenarios by specifying the times of the drilling intrusion. Table PA-19 summarizes the specific scenarios used in the CRA-2026 PA. A total of 6 scenarios $\times$ *nR* $\times$ *nLHS* = 6 $\times$ 3 $\times$ 100 = 1,800 BRAGFLO calculations were conducted.

Table PA-19. BRAGFLO Scenarios in the CRA-2026 PA

Fundamental Scenario (Section PA-3.4)	Specific Scenario	Time of Drilling Intrusion(s)
E0: no drilling intrusions.	S1-BF	N/A
E1: single intrusion through an excavated area of the repository that connects with pressurized brine in the Castile.	S2-BF	350 years
E1	S3-BF	1,000 years
E2: single intrusion through an excavated area of the repository that does not connect with pressurized brine in the Castile.	S4-BF	350 years
E2	S5-BF	1,000 years
E1E2: two intrusions into the same waste panel, the first being an E2 intrusion and the second being an E1 intrusion.	S6-BF	1,000 years for E2 intrusion 2,000 years for E1 intrusion

The BRAGFLO computational grid divides the repository into a lower waste panel (WP), a middle group of four waste panels (SROR), an upper group of five waste panels (NROR), and a group of two waste panels on the west side of the repository (WROR), with the drilling intrusion taking place through the center of the lower panel (Figure PA-12). Thus, the drilling intrusions in Scenarios S2-BF through S5-BF occur at a location in Panel 5, which is the southernmost panel.

In Scenario S6-BF, both intrusions occur at a location in Panel 5, with the effects of flow between the two boreholes implemented through assumptions involving the time-dependent behavior of borehole permeability (Table PA-8).

PA-6.3.2 NUTS Calculations

For Scenarios S1-BF to S5-BF, radionuclide transport through the Salado is computed by the code NUTS (Section PA-4.3) using the flow fields computed by BRAGFLO. Two types of calculations are performed with NUTS. First, a set of screening calculations identifies elements of the sample from S_{su} for which radionuclide transport through the Salado to the LWB or Culebra is possible. Second, radionuclide transport calculations are performed for sample elements that are retained after screening.

Table PA-20 lists the NUTS scenarios for radionuclide transport calculations. Each NUTS scenario uses the flow field computed for the corresponding BRAGFLO scenario. The intrusion times for the NUTS scenarios are accommodated by shifting the BRAGFLO flow fields in time. For example, the NUTS S3 scenario with an intrusion at 3,000 years requires a flow field for the time interval between 3,000 years and 10,000 years; this scenario uses the BRAGFLO S3-BF scenario flow field shifted forward by 2,000 years.

Table PA-20. NUTS Release Calculations in the CRA-2026 PA

NUTS Scenario	Flow field	Intrusion Time (t_1)
S1	BRAGFLO S1-BF scenario	N/A
S2	BRAGFLO S2-BF scenario	E1 intrusion at 100 and 350 years
S3	BRAGFLO S3-BF scenario	E1 intrusion at 1,000, 3,000, 5,000, 7,000, and 9,000 years
S4	BRAGFLO S4-BF scenario	E2 intrusion at 100 and 350 years
S5	BRAGFLO S5-BF scenario	E2 intrusion at 1,000, 3,000, 5,000, 7,000, and 9,000 years

PA-6.3.2.1 Tracer Calculations

All realizations are first evaluated using NUTS in a screening mode to identify those realizations for which a significant release of radionuclides to the LWB cannot occur. The screening simulations consider an infinitely soluble, nondecaying, nondispersive, and nonsorbing species as a tracer element. The tracer is given a unit concentration of 1 kg/m^3 in all waste disposal areas. If the amount of tracer that reaches the selected boundaries (the top of the Salado and the LWB within the Salado) does not exceed a cumulative mass of 10^{-7} kg within 10,000 years, it is assumed that no consequential release to these boundaries is possible. The value of 10^{-7} kg is selected because, regardless of the isotopic composition of the release, it corresponds to a normalized release no greater than 1.04×10^{-6} EPA units, which is effectively equal to the

smallest release displayed in CCDF construction (10^{-6} EPA units) (Stockman et al. 1996). This upper bound corresponds to 10^{-7} kg of ^{241}Am.

PA-6.3.2.2 Transport Calculations

For realizations with greater than 10^{-7} kg of tracer reaching the boundaries, NUTS models the transport of five different radionuclide species (^{241}Am, ^{239}Pu, ^{238}Pu, ^{234}U, and ^{230}Th) as discussed in Section PA-4.3.1.

PA-6.3.3 PANEL Calculations

The code PANEL is used in three ways: to compute radionuclide concentrations in Salado and Castile brine for transport in the Salado (Section PA-4.3.1); to compute radionuclide concentrations in Salado and Castile brine for DBR (Section PA-4.3.4); and to compute radionuclide transport to the Culebra for the E1E2 scenario (BF-S6).

PA-6.3.3.1 Radionuclide Concentration Limits for Salado Transport

The radionuclides considered for transport in the Salado are those 10 radionuclides identified in Section PA-4.3.1. These 10 radionuclides account for over 99.9% of the inventory with potential to comprise a release within 10,000 years. For transport calculations, the 10 radionuclides are lumped into five simplified radionuclides representing three decay chains, as discussed in Section PA-4.3.1. For the E1E2 scenario, the same 10 radionuclides are initially considered individually, and the resulting concentrations are subsequently combined into the five simplified radionuclides (Docherty and Kim 2025, Section 3.1.9).

The total mobile concentration limit for each radionuclide includes both the dissolved solubility and contributions from humic, microbial, mineral fragment, and intrinsic colloids. The dissolved solubility forms the baseline for the colloidal contributions, which are computed as described in Section PA-4.3.2 and Appendix GEOCHEM-2026 (Sections GEOCHEM-4.0 and GEOCHEM-5.0). These limits define the maximum concentration of each radionuclide in brine, but actual concentrations in transport simulations may be further constrained by the available inventory in the waste panel.

PA-6.3.3.2 Radionuclide Concentrations for DBR

Radionuclide concentrations in brine for direct brine releases are calculated using baseline solubilities for five brine volumes (1×, 2×, 3×, 4×, and 5× the minimum brine volume required for a direct brine release; 6,314 m³; Brunell 2025). Concentration calculations are performed separately for Castile and Salado brines and are output at 100, 125, 175, 350, 1,000, 3,000, 5,000, 7,500, and 10,000 years.

PA-6.3.3.3 Radionuclide Transport to the Culebra for E1E2 Scenario

As outlined in Section PA-4.5, the code PANEL is used to estimate releases to the Culebra associated with E1E2 scenarios and to estimate radionuclide concentrations in brine for use in estimating DBRs. An E1E2 scenario assumes two drilling intrusions into the same waste panel: the first an E2 intrusion (Table PA-19) occurring at time t_1, and the second, an E1 intrusion (Table PA-19) occurring at time t_2. PANEL calculations are performed for t_2 = 100, 350, 1,000, 2,000, 4,000, 6,000, and 9,000 years using the flow field produced by the single BRAGFLO calculation for Scenario S6-BF, for a total of $7 \times nR \times nLHS = 7 \times 3 \times 100 = 2{,}100$ PANEL calculations. The BRAGFLO flow field is shifted forward or backward in time as appropriate so that the BRAGFLO solution time corresponding to the second intrusion aligns with t_2 in the PANEL calculation (Docherty and Kim 2025).

PA-6.3.4 DRSPALL Calculations

The code DRSPALL calculates the spallings volume ($S_{w,out}$) produced by an intrusion into a pressurized repository, as given in Equations (PA.113) and (PA.127). Spallings are computed for a set of four pressures for each vector in each replicate, for a total of 4 pressures $\times$ $nR \times nLHS$ = $4 \times 3 \times 100 = 1{,}200$ DRSPALL calculations. Because no changes have been made to the DRSPALL model, assumptions, or inputs since the CRA-2019 PA, rerunning the DRSPALL calculations was not necessary and the CRA-2026 PA therefore uses the same DRSPALL results as were used in the CRA-2019 PA. The CRA-2019 PA used DRSPALL results documented in Kirchner et al. (2015).

PA-6.3.5 CUTTINGS_S Calculations

The code CUTTINGS_S computes the volumes of solids removed from the repository by cuttings and cavings (see Section PA-4.6) and spallings (see Section PA-4.7). The CUTTINGS_S output files also transfer data from the BRAGFLO Salado flow calculation to the BRAGFLO DBR calculation. The same intrusion scenarios and times are used in the calculation of spallings volumes and DBRs. Table PA-21 lists the CUTTINGS_S calculations performed for the CRA-2026 PA, totaling $104 \times nR \times nLHS = 104 \times 3 \times 100 = 31{,}200$ CUTTINGS_S calculations. These scenarios are named with the suffix -DBR to avoid confusion with those used in the BRAGLO Salado flow modeling.

Table PA-21. Scenarios for spallings and DBRs in the CRA-2026 PA

Scenario	Description
S1-DBR	Initially undisturbed repository (E0 conditions). Intrusion at the L, M, U, or O location at 100; 350; 1,000; 3,000; 5,000; or 10,000 years: 24 combinations
S2-DBR	Initial E1 intrusion at 350 years, followed by a second intrusion at the L, M, U, or O location at 550; 750; 2,000; 4,000; or 10,000 years: 20 combinations.
S3-DBR	Initial E1 intrusion at 1,000 years followed by a second intrusion at the L, M, U, or O location at 1,200; 1,400; 3,000; 5,000; or 10,000 years: 20 combinations.
S4-DBR	Initial E2 intrusion at 350 years followed by a second intrusion at the L, M, U, or O location at 550; 750; 2,000; 4,000; or 10,000 years: 20 combinations.

Scenario	Description
S5-DBR	Initial E2 intrusion at 1,000 years followed by a second intrusion at the L, M, U, or O location at 1,200; 1,400; 3,000; 5,000; or 10,000 years: 20 combinations.

The CUTTINGS_S S1-DBR scenario computes volumes of solid material (cuttings, cavings, and spallings) released from an intrusion into an undisturbed repository. For the CUTTINGS_S S1-DBR scenario, releases are computed for four drilling locations: lower, middle, upper, and other, as indicated in Figure PA-33. Initial conditions for each computation are obtained from the BRAGFLO output for the S1-BF scenario at the time of the intrusion according to the mapping shown in Figure PA-34.

The other CUTTINGS_S scenarios (S2-DBR through S5-DBR) compute volumes of solids released by a second or subsequent intrusion. In these calculations, an intrusion into the lower waste panel is taken as representative of the effects on repository conditions of an initial intrusion into any waste panel. Releases are computed for four locations for the second intrusion: lower, middle, upper, and other. These releases are taken as representative of releases from a second intrusion into the same, connected, adjacent, and nonadjacent waste panel, respectively. Initial conditions for Scenarios S2-DBR to S5-DBR are taken from the corresponding BRAGFLO scenario at the time of the second intrusion. For a full CUTTINGS_S run control diagram, see Figure 2 of WIPP Performance Assessment (2021a).

PA-6.3.6 BRAGFLO Calculations of DBR Volumes

Volumes of brine released to the surface during an intrusion are calculated using BRAGFLO, as described in Section PA-4.8. DBR volumes are calculated for the scenarios described in Table PA-21 for an initial intrusion (CUTTINGS_S S1-DBR scenario) and for second or subsequent intrusions (S2-DBR to S5-DBR scenarios). For a full DBR model run control diagram, see Figure 5 of Zeitler (2025).

Initial conditions for the DBR calculations are obtained from the BRAGFLO Salado flow model results from scenarios S1-BF through S5-BF. Salado flow model results from the S1-BF scenario (Section PA-7.1) are used as initial conditions for DBR when modeling a first intrusion into the repository that may have a DBR. Salado flow model results from the S2-BF through S5-BF scenarios (Section PA-8.1) are used as initial conditions for DBR when modeling second or subsequent drilling intrusions that may have a DBR.

PA-6.3.7 MODFLOW6 Calculations

As described in Section PA-4.9, the MODFLOW6 calculations produce flow fields in the Culebra for two categories of conditions: partially mined conditions in the vicinity of the repository and fully mined conditions in the vicinity of the repository (Figure PA-39). As specified in 40 CFR 194.32(b), partially mined conditions are assumed to exist by the end of the administrative control period (i.e., at 100 years after closure). Full mining within the LWB occurs at a random

time after the administrative control period (t_{min}; see Section PA-3.3), after which fully mined conditions are assumed for the remainder of the 10,000-year regulatory period.

The flow fields for partially or fully mined conditions are calculated by MODFLOW6 using the corresponding T-fields (see Section PA-4.9). Thus, a total of $2 \times nR \times nLHS = 2 \times 3 \times 100 = 600$ MODFLOW6 calculations were performed (Table PA-22). The T-fields used in the flow calculation were developed for the CRA-2026 using updated data and a peer-reviewed calibration approach (Appendix TFIELD-2026). The definition of the extent of potash reserves, used to determine the areas to which partial and full mining factors are applied, is unchanged since the CRA-2019 PA (Section PA-4.9.4). For a full flow model run control diagram, see Figure 5 of Wilgus and Bethune (2025).

Table PA-22. MODFLOW6 Scenarios in the CRA-2026 PA

MODFLOW6: 600 Flow-Field Calculations
PM: Partially mined conditions in the vicinity of the repository
FM: Fully mined conditions in the vicinity of the repository
Total calculations = $2 \times nR \times nLHS = 2 \times 3 \times 100 = 600$
Note: Only 100 calibrated T-fields were constructed with PEST++IES and MODFLOW6 for use in the analysis. The T-fields are an input to the calculation of flow fields. In each replicate, the T-field used for a particular flow field was assigned using an index value (CTRAN; see Table PA-17) included in the LHS.

PA-6.3.8 SECOTP2D Calculations

SECOTP2D calculations produce fractional releases to the LWB from a radionuclide source placed in the Culebra as described in Section PA-4.10. The SECOTP2D calculations are performed for the flow fields described in Section PA-6.3.7. The CRA-2026 PA considers radionuclide source placement at two locations in the Culebra (Wilgus and Brunell 2025) for a total of $2 \times nR \times nLHS \times nLocations = 2 \times 3 \times 100 \times 2 = 1{,}200$ SECOTP2D calculations (Table PA-23). For a full Culebra transport run control diagram, see Figure 6 of Wilgus and Bethune (2025).

Table PA-23. SECOTP2D Scenarios in the CRA-2026 PA

SECOTP2D: 1200 Calculations
PM: Partially mined conditions in the vicinity of the repository
FM: Fully mined conditions in the vicinity of the repository
Total calculations = $2 \times nR \times nLHS \times nLocations = 2 \times 3 \times 100 \times 2 = 1{,}200$
Note: Each calculation includes a unit release for each of four radionuclides: ^{241}Am, ^{239}Pu, ^{230}Th, and ^{234}U.

PA-6.4 Computation of Releases

The mechanistic computations outlined in Section PA-6.3 are used to construct releases for each sampled element, $\mathbf{x}_{st,i,}$ of S_{st}. The calculation differs for the undisturbed (UP) scenario described in Section PA-2.2.2.1, and the disturbed (DP) scenarios described in Section PA-2.2.2.2.

PA-6.4.1 Releases from the Undisturbed Repository

Releases for the random future $\mathbf{x}_{st,0}$ in which no drilling intrusions occur (i.e., the UP scenario described in Section PA-2.2.2.1) are computed from the results of the NUTS S1 scenario (Table PA-20). The NUTS code computes the activity of each radionuclide that reaches the accessible environment during the regulatory period via transport through the MBs; these releases are represented as $f_{MB}[\mathbf{x}_{st,0}, f_B(\mathbf{x}_{st,0})]$ in Equation (PA.17). No other viable path to the accessible environment is present in the undisturbed scenario.

PA-6.4.2 Releases from the Disturbed Repository

Releases for a future $\mathbf{x}_{st,i}$ in which drilling and mining events occur are computed by the code CCDFGF (WIPP Performance Assessment 2022a) from the results of the mechanistic calculations summarized in Section PA-6.3. Releases from the disturbed repository (i.e., the DP scenarios described in Section PA-2.2.2.2) can be partitioned into two categories: direct releases to the surface, which occur at the time of a drilling event; and long-term releases, which are due to natural processes acting on the repository system as it is modified by drilling intrusions. Direct releases occur after every intrusion that intersects waste. Long-term releases are primarily due to intrusions that introduce paths for radionuclide transport to the Culebra.

Direct releases for intrusions that intersect CH-TRU waste include cuttings and cavings, spallings, and DBR. Direct releases for intrusions that intersect RH-TRU waste include only cuttings.

The type of intrusion (Section PA-6.4.2.1) determines whether it affects long-term releases. Intrusions that affect long-term releases alter the repository system. Consequently, spallings releases and DBR depend on the type and location of earlier intrusions (Section PA-6.4.2.2 and Section PA-6.4.2.3).

PA-6.4.2.1 Determining Intrusion Type

When an intrusion into waste occurs, the stochastic variables e_i, l_i, b_i and p_i are generated by the algorithm in Table PA-18 and are used in the algorithm shown in Figure PA-44 to determine the type of the intrusion. Brine pocket depletion in Figure PA-44 is never realized in practice, as the threshold for depletion far exceeds the number of intrusions sampled in any realization. Boreholes with a full (solid) plug have no effect on long-term releases. Boreholes that create a connection with a Castile brine reservoir are labeled E1; boreholes that do not connect the repository with a Castile brine reservoir are labeled E2 (Section PA-2.2.2.2.1).

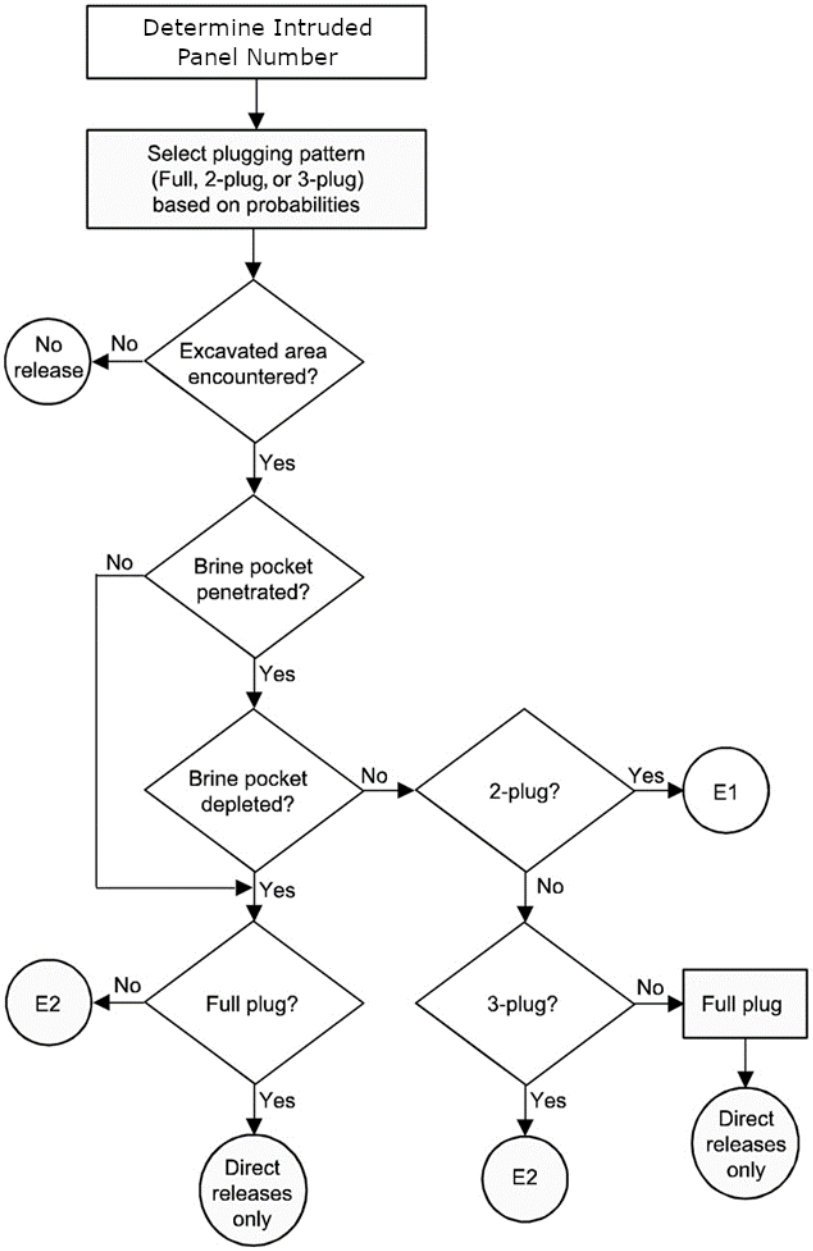


Figure PA-44. Logic Diagram for Determining the Intrusion Type

PA-6.4.2.2 Determining Repository and Panel Conditions

Direct releases by spallings and DBR depend on the conditions in the repository at the time of the intrusion. One of three repository conditions is assigned:

- E0: the repository is undisturbed by drilling,

- E1: the repository has at least one prior E1 intrusion, or
- E2: the repository has one or more prior E2 intrusions, but no prior E1 intrusions.

Each panel is assigned one of four conditions:

- E0: the excavated regions of the panel have not been intruded by drilling,
- E1: the panel has one previous E1 intrusion (intersecting a brine reservoir in the Castile),
- E2: the panel has one or more previous E2 intrusions (none intersect brine reservoirs), or
- E1E2: the panel has at least two previous intrusions, at least one of which is an E1 intrusion.

The repository and panel conditions are used to determine the scenario for spallings and DBR (Section PA-6.4.2.3) and to construct releases to the Culebra (Section PA-6.4.3).

PA-6.4.2.3 Scenario Selection for Spallings and DBR

Scenarios for spallings and DBR are described in Section PA-6.3.4. The S1-DBR scenarios represent an intrusion in a previously undisturbed repository and are enumerated by the waste panel group (lower, middle, upper, or other) where the initial intrusion may occur. The S2-DBR through S5-DBR scenarios are differentiated by the type (E1 or E2) of an earlier intrusion and enumerated by the intrusion location (same, connected, adjacent, and nonadjacent) relative to the earlier intrusion.

The waste panels are divided into four groups:

- Lower, consisting of only Panel 5;
- Middle, consisting of Panels 3, 4, 6, and 9;
- Upper, consisting of Panels 1, 2, 7, 8, and 10; and
- Other, consisting of Panels 11 and 12.

These groupings allow DBR and spallings scenarios to be parameterized using a manageable number of representative initial conditions. These groups correspond to areas in the repository representation in the BRAGFLO model for flow in the Salado (Figure PA-12), which are used to select initial conditions for the scenarios for spallings and DBR (Section PA-4.8).

Spallings and DBR from the initial intrusion are modeled using the conditions in the panel group associated with the intruded panel. Initial conditions for direct releases from subsequent intrusions are modeled by assuming that the initial intrusion occurred in Panel 5 (the lower group), and the subsequent intrusion occurs in one of four relative locations:

- same, i.e., in the lower panel group;
- connected, in the middle panel group;

- adjacent, in the upper panel group; and
- non-adjacent, in the other panel group.

Connected panels have no panel closures between them. Adjacent panels are in the same section (south or west) of the repository but are separated by one or more panel closures. Nonadjacent panels are in different sections of the repository (WIPP Performance Assessment 2022a).

The types of previous intrusions and the relative distances from the current intrusion are used to select the applicable scenario. If the repository condition is E1 (i.e., at least one E1 intrusion has occurred previously), then relative distance is determined by comparing the panel for the current intrusion with the panels with E1 intrusions and selecting the "closest": same is closer than connected, which in turn is closer than adjacent, which is closer than non-adjacent. The applicable scenario is then either S2-DBR or S3-DBR based on the time of the intrusion (WIPP Performance Assessment 2022a). If the repository condition is E2 (i.e., no E1 intrusion has occurred previously), then a similar procedure selects between scenarios S4-DBR and S5-DBR.

PA-6.4.2.4 Construction of Cuttings and Cavings Release

Each drilling intrusion encountering waste is assumed to release a volume of solid material as cuttings, as described in Section PA-4.6.1. The uncompacted volume of waste removed by cuttings (V_{cut}) is computed by Equation (PA.89). Drilling intrusions that encounter CH-TRU waste may also release additional solid material as cavings, as described in Section PA-4.6.2. The combined uncompacted volume of material removed by cuttings and cavings ($V = V_{cut} + V_{cav}$) is computed by Equation (PA.90). For a drilling intrusion that encounters RH-TRU waste, the final eroded diameter D_f in Equation (PA.90) is equal to the bit diameter in Equation (PA.89).

The volume removed may not be entirely waste; rather, the uncompacted volume may include MgO and any void space initially present around the waste containers. The volume of solid waste removed (V_w) is determined by multiplying the uncompacted volume by the fraction of excavated repository volume (*FVW*) occupied by waste, thus:

$$V_W = V \times FVW \qquad \text{(PA.273)}$$

where *FVW* = 0.279 for CH-TRU waste and *FVW* = 1.0 for RH-TRU waste (parameters REFCON:FVW and REFCON:FVRW in Feng and Kicker (2025a), Table 35). The activity in the material released by cuttings and cavings is determined by randomly selecting a subset of waste streams. The vector ($\mathbf{a}_j$) described in Section PA-3.2.5 indicates the type of waste (CH-TRU or RH-TRU) and the selected waste streams. The activity per cubic meter of waste stream volume is computed for each waste stream at a discrete set of times, accounting for radioactive decay and ingrowth using the code EPAUNI. The results of the CRA-2026 PA EPAUNI calculations are presented in Kim and Kicker (2025). Activities at other times are determined by linear interpolation. The cuttings and cavings release for the *j*th intrusion, $R_{cut,j}$, is the product of the average activity per cubic meter $\bar{C}_{r,j}$, of the selected waste streams and the volume of waste released:

$$R_{cut,j} = V_{w,j} \times \bar{C}_{r,j} \quad \text{(PA.274)}$$

The cuttings and cavings release in a random future, $f_C(\mathbf{x}_{st,i})$ in Equation (PA.17), is the sum of $R_{cut,j}$ over all intrusions.

PA-6.4.2.5 Construction of Spallings Releases

Spallings' releases are calculated for intrusions that encounter CH-TRU waste. For the scenarios described in Section PA-6.3.5, spallings volume is calculated with the CUTTINGS_S code. The spallings volume for a random intrusion is constructed by linear interpolation between two spallings volumes from the CUTTINGS_S calculations for the scenario selected as described in Section PA-6.4.2.5.

For each intrusion, the concentration of radionuclides in the spallings volume is computed as the average activity per cubic meter in the CH-TRU waste at the time of intrusion. Activities in each waste stream are computed at a discrete set of times by the code EPAUNI (Kim and Kicker 2025); activities at other times are determined by linear interpolation. Average CH-TRU waste activity is calculated by the code PRECCDFGF using results from the code EPAUNI (WIPP Performance Assessment 2022e).

The spallings release in a random future, $f_{SP}(\mathbf{x}_{st,i})$ in Equation (PA.17), is the sum of spallings release over all intrusions in that future.

PA-6.4.2.6 Construction of DBRs

DBRs are calculated for intrusions that encounter CH-TRU waste. For the scenarios described in Section PA-6.3.5, DBR volume, V_{DBR} in Equation (PA.181), is calculated with the BRAGFLO code (Section PA-4.8.3). The DBR volume for a random intrusion is constructed by linear interpolation on the BRAGFLO output for the scenario selected as described in Section PA-6.4.2.3.

Radionuclide concentrations in brine, C_{bl}, used for DBR calculations are obtained from PANEL simulations (Section PA-4.3.5) for the times listed in Table PA-20 and multiples of 1x, 2x, 3x, 4x, and 5x the minimum brine volume necessary for a DBR (6,314 m^3). Concentrations at other times are computed by linear interpolation on time and brine volume (WIPP Performance Assessment 2022a). The repository conditions (E0, E1, or E2) determine which brine (Salado or Castile) is selected for the concentration calculation. If there has been a previous E1 intrusion, Castile brine is used, otherwise Salado brine is used.

The DBR is computed as the product of the release concentration and the volume, V_{DBR}:

$$\int_{DBR}\left(\mathbf{X}_{st,i}\right) = V_{DBR}\sum_{l} C_{bl} \quad \text{(PA.275)}$$

DBRs in a random future, $f_{DBR}(\mathbf{x}_{st,i})$ in Equation (PA.17), is the sum of DBR over all intrusions in that future.

PA-6.4.3 Radionuclide Transport Through the Culebra

One potential path for radionuclides to leave the repository is through the boreholes to the Culebra, then through the Culebra to the LWB (Docherty and Kim 2025). As described in Section PA-6.3.2 and Section PA-6.3.3, the NUTS and PANEL codes are used to compute radionuclide transport through boreholes to the Culebra $f_{NP}(\mathbf{x}_{st,i})$ for a fixed set of scenarios. Releases to the Culebra for intrusions at other times are determined by an interpolation (WIPP Performance Assessment 2022a).

Each intrusion may create a pathway for releases to the Culebra. The first intrusion (E1 or E2; Section PA-6.4.2.1) in each panel creates a release path, with the radionuclide release taken from the appropriate NUTS scenario. Subsequent E2 intrusions in a panel with only E2 intrusions do not cause additional releases; the WIPP PA assumes that the subsequent E2 intrusion does not introduce a significant source of additional brine and thus does not release additional radionuclides to the Culebra.

An E1E2 intrusion results from the combination of two or more intrusions into the same panel, at least one of which is an E1 intrusion. After a first intrusion, a subsequent E1 intrusion changes the panel's condition to E1E2, as does an E2 borehole into a panel after an earlier E1 intrusion. Once E1E2 conditions exist in a panel, they persist throughout the regulatory period for purposes of scenario selection and long-term release calculations. However, releases from a panel with E1E2 conditions are restarted for each subsequent E1 intrusion into that panel, since additional E1 intrusions may introduce new volumes of brine to the panel.

Releases to the Culebra are summed across all release pathways to the Culebra to obtain the total releases to the Culebra $r_k(t)$ for the k^{th} radionuclide at each time t. Releases to the Culebra include both dissolved radionuclides and radionuclides sorbed to all four types of colloids (Section PA-4.3.3). The release to the Culebra is partitioned into dissolved and colloid species by multiplying $r_k(t)$ by colloid-specific factors (Docherty and Kim (2025), Section 3.3.5). The WIPP PA assumes that dissolved radionuclides are transported in the Culebra and that radionuclides sorbed to humic colloids disassociate and are transported as dissolved radionuclides. It is assumed that other colloid species do not transport in the Culebra (see U.S. DOE (2004), Appendix PA-2004, Attachment MASS, Section MASS-15.2).

Radionuclide transport through the Culebra is computed by the code SECOTP2D (Section PA-4.10) for partially mined and fully mined conditions, as indicated in Table PA-23. These computations assume that a 1 kg source of each radionuclide is placed in the Culebra between 0 and 50 years and calculate the fraction of each source $f_{m,k}(t)$ (m is the mining condition and k is the index for the radionuclide) reaching the LWB at each subsequent time t. For convenience, the time-ordering of the data from SECOTP2D is reversed so that the fraction $f_{m,k}(t)$ associated with year t = 200, for example, represents the release at the boundary at year 10,000 for a release occurring 9,800 years earlier, i.e., between 150 and 200 years.

The total release (kg) through the Culebra of the k^{th} radionuclide, $R_{Cul,k}$, is calculated as:

$$R_{Cul,k} = \sum_{t_i \le t_{\mathrm{m}}} r_k(t_i)\, f_{PM,k}(t_i) + \sum_{t_i > t_{\min}} r_k(t_i) f_{FM,k}(t_i) \quad \text{(PA.276)}$$

where $r_k(t_i)$ is the release of the k^{th} radionuclide to the Culebra (kg) at time t_i, and $f_{PM,k}(t_i)$ and $f_{FM,k}(t_i)$ are the fractions of a 1 kg source placed in the Culebra in the interval (t_{i-1}, t_i) that reach the LWB by the end of the 10,000-year regulatory period for partially mined and fully mined conditions within the LWB, respectively. The sum in Equation (PA.276) is evaluated in two parts, where t_{min} is the time at which mining occurs within the LWB. The total releases through the Culebra $f_{ST}(\mathbf{x}_{st,i})$ are computed by converting the release of each radionuclide $R_{Cul,k}$ from kg to EPA units, then summing over all radionuclides.

PA-6.5 Construction of CCDFs

The sampling of individual futures (Section PA-6.2) and associated CCDF construction is carried out by the CCDFGF program (WIPP Performance Assessment 2022a). The sampled futures $\mathbf{x}_{st,i}$ in Equation (PA.272) are used to construct CCDFs for many different quantities (e.g., cuttings and cavings releases, spallings releases, DBRs, etc.). The construction process is the same for each quantity. For notational convenience, here the function $f(\mathbf{x}_{st,i})$ represents the quantity for which a CCDF is being constructed. The sample $\mathbf{x}_{st,i}$ results in 10,000 values:

$$f\left(\boldsymbol{x}_{st,i}\right), \text{ i = 1, 2, …, 10,000} \quad \text{(PA.277)}$$

which are available for use in CCDF construction. Formally, the resultant CCDF is defined by the expression in Equation (PA.3). In practice, the desired CCDF is obtained after ordering $f(\mathbf{x}_{st,i})$ from smallest to largest or largest to smallest, as described below.

A binning procedure is used in CCDF construction to facilitate the calculation of statistics for a family of CCDFs. Specifically, the range of $f(\mathbf{x}_{st,i})$ is divided into intervals (i.e., bins) by the specified points:

$$f_{\min} = b_0 < b_1 < b_2 < \ldots < b_n = f_{\max} \quad \text{(PA.278)}$$

where f_{min} is the minimum value of $f(\mathbf{x}_{st,i})$ to be plotted (typically 10^{-6} or 10^{-5} for an EPA-normalized release), f_{max} is the maximum value of f to be plotted (typically 100 for an EPA-normalized release), n is the number of bins in use, and the b_i are log-uniformly distributed with 20 values per order of magnitude. A counter nB_j is used for each interval $[b_j\text{–}1, b_j]$. All counters are initially set to zero. Then, as individual values $f(\mathbf{x}_{st,i})$ are generated, the counter nB_j is incremented by 1 when the inequality:

$$b_{j-1} < f\left(\mathbf{x}_{st,i}\right) \le b_j \quad \text{(PA.279)}$$

is satisfied. When necessary, f_{max} is increased in value so that the inequality $f(\mathbf{x}_{st,i}) \le f$max will always be satisfied. Once the 10,000 values for $f(\mathbf{x}_{st,i})$ have been generated, a value of nB_j exists for each interval $[b_j\text{–}1, b_j]$. The quotient:

$$pB_j = nB_j / 10{,}000 \quad \text{(PA.280)}$$

provides an approximation to the probability that $f(\mathbf{x}_{st,i})$ will have a value that falls in the interval $[b_j - 1, b_j]$. The resultant CCDF is then defined by the points:

$$\left(b_j,\ prob\left(value > b_j\right)\right) = \left(b_j,\ \sum_{k=j+1}^{n} pB_k\right) \quad \text{(PA.281)}$$

for $j = 0, 1, 2, \ldots, n-1$, where $prob(value > b_j)$ is the probability that a value greater than b_j will occur. The continuous CCDF is approximated by drawing diagonal lines from the left end of one bin to the left end of the next bin.

When multiple CCDFs appear in a single plot, the bottom of the plot becomes very congested as the individual CCDFs drop to zero on the abscissa. For this reason, each CCDF stops at the largest observed consequence value among the 10,000 values calculated for that CCDF. Stopping at the largest consequence value, rather than the left boundary of the bin that contains this value, permits the CCDF to explicitly show the largest observed consequence. Because a sample size of 10,000 is used in the generation of CCDFs, the probability corresponding to the largest observed consequence is 10^{-4}.

The CCDF construction described in this section is for a single sample element, $v_{su,k}$, of the form indicated in conjunction with Equation (PA.267). Repeated generation of CCDFs for individual sample elements $v_{su,k}$, i.e., for the vectors representing epistemic uncertainty in the model results, leads to the distribution of CCDFs.

PA-6.6 Sensitivity Analysis

Evaluating one or more of the models discussed in Section PA-4.0 and the construction of CCDFs described in Section PA-6.5 creates a mapping:

$$\left\{\mathbf{v}_{su,k},\ \mathbf{y}(\mathbf{v}_{su,k})\right\},\ \text{k = 1, 2, …, nLHS} \quad \text{(PA.282)}$$

from the LHS in Equation (PA.267) (i.e., $\mathbf{v}_{su,k}$) to analysis results (i.e., $y(\mathbf{v}_{su,k})$), where $\mathbf{y}_{su,k}$ denotes the results obtained with the model or models under consideration. A vector notation is used for **y** because, in general, many quantities are predicted in the evaluation. Sensitivity analysis explores the mapping in Equation (PA.282) to determine how the uncertainty in the individual elements of $\mathbf{v}_{su,k}$ affects uncertainty in the elements of $y(\mathbf{v}_{su,k})$. Assessing how input uncertainties affect analysis outputs improves the interpretation of the analysis and informs model enhancements for future PAs. In some cases, sensitivity analysis results are presented using scatterplots in which results from the three replicated LHSs (i.e., R1, R2, and R3; Section PA-6.1.1) are overlaid on a single plot and distinguished by symbol and color to facilitate visual comparison. In these cases, the replicates are not statistically pooled. In other cases, statistical

analyses are performed separately for each replicate, and statistics are compared across the three replicates.

Two principal techniques are used in the sensitivity analysis: scatterplots and stepwise regression analyses. Each technique is briefly discussed. The sensitivity analysis performed for the CRA-2026 PA is described in King et al. (2025).

PA-6.6.1 Scatterplots

Scatterplots, the simplest sensitivity analysis technique, are performed by plotting the points:

$$\left(\mathbf{v}_{su,k}, \mathbf{y}(\mathbf{v}_{su,k})\right),\ \text{k=1,2,...,}nLHS \qquad \text{(PA.283)}$$

for each input variable in the LHS sample, where $\mathbf{v}_{su,j}$ is the *j*-th input variable in the *k*-th LHS realization and $\mathbf{y}(\mathbf{v}_{su,k})$ is the corresponding model result. The resulting plots can reveal relationships between the analysis results and individual input variables, including nonlinear behavior or threshold effects. Examining such plots when LHS is used can be particularly revealing because LHS provides stratified coverage over the full range of each input variable. Iman and Helton (1988) provide an example where scatterplots revealed a complex pattern of variable interactions.

PA-6.6.2 Stepwise Regression Analysis

Stepwise regression analysis provides an alternative to constructing a regression model that includes all sampled input variables simultaneously. With this approach, a sequence of regression models is constructed. The first regression model includes the single input variable that exhibits the strongest relationship with the output variable. The second regression model includes the variable selected in the first step plus the additional input variable that explains the largest fraction of the remaining variability in the output variable. Additional models in the sequence are constructed in the same manner until inclusion of further variables does not meaningfully increase the fraction of variability in the output variable that can be explained. This stepwise regression procedure follows standard regression-analysis methods (Draper and Smith 1981).

Stepwise regression analysis provides insight into the relative importance of individual input variables. First, the order in which variables are selected in the stepwise procedure indicates their relative importance, with more influential variables selected earlier in the sequence. Second, the coefficient of determination (R^2) for each regression model shows how much of the output variability is explained by the variables included up to that step. When input variables are approximately uncorrelated, increases in R^2 between successive steps provide an estimate of the incremental contribution of each added variable.

Rank regression analysis was used to evaluate the sensitivity of the normalized releases to the sampled parameters. The predicted error sum of squares (PRESS) was computed to detect over-fitting of the regression model to the data. Overfitting occurs when the regression methodology causes the fit to favor specific points rather than the general shape of the data curve. In such a case, the minimum value of PRESS may occur earlier than the last step in the regression analysis. No such condition was observed in any of the rank correlation analyses performed in CRA-2026. Details of the sensitivity analysis performed in the CRA-2026 PA can be found in King et al. (2025).

PA-7.0 Results for the Undisturbed Repository

The PA tabulates releases from the repository for undisturbed conditions. Releases from the undisturbed repository to the accessible environment address individual protection requirements outlined in 40 CFR 191.15, and groundwater protection requirements in 40 CFR Part 191 Subpart C. This section shows how the WIPP complies with these two requirements by presenting brine and gas flow (BRAGFLO) and radionuclide transport (NUTS) results from modeling the undisturbed repository.

For the undisturbed repository, only two release pathways exist: radionuclide transport from the repository through the shafts to the Culebra, and lateral transport through the marker beds and the Culebra. The results discussed in Section PA-7.2 show that there are no releases to the accessible environment from the undisturbed repository.

Results of the CRA-2026 PA for the undisturbed repository are summarized in Brunell et al. (2025). The overall structure of the CRA-2026 PA is summarized in Section PA-1.2. Results of the CRA-2026 PA are compared to results from the RPPCR PA (Brunell et al. 2024).

PA-7.1 Flow in the Salado

This section summarizes the results for flow in the Salado for the undisturbed (S1-BF) scenario (see Table PA-19 for an explanation of the BRAGFLO scenarios). The Salado flow model (Section PA-4.2) represents the repository as eight regions in the numerical grid: four waste-filled regions (the WP, SROR, NROR, and WROR as shown in Figure PA-12) and four excavated regions with no waste (the South Operations (SOP) area, Experimental (EXP) area, West Operations (WOP) area, and the West Drifts as shown in Figure PA-12). Three run-of-mine salt panel closures, an abandoned panel closure, and a composite shaft are also modeled. A detailed description of the CRA-2026 PA Salado flow results can be found in Day and King (2025).

Under undisturbed conditions, pressure strongly influences the extent to which contaminated brine may migrate from the repository into the accessible environment. The evolution with time of brine pressures and saturations in repository waste areas is a result of the complex interplay of gas generation, brine production and consumption, the 1-degree (south) Salado dip, and the lack of panel closures between the WP and SROR areas.

Figure PA-45 through Figure PA-48 show minimum, maximum, and mean waste region pressures for scenario S1-BF of the CRA-2026 PA, with comparisons made to the RPPCR PA results.[3] Minimum, maximum, and mean pressure curves shown for the RPPCR PA and the CRA-2026 PA are obtained from the 100 vectors of Replicate 1. Replicate 2 and Replicate 3 show

[3] Non-waste area (SOP, EXP, and WOP) pressures and saturations plots are shown in Day and King (2025).

similar behavior to Replicate 1. Over time, repository pressures increase due to several factors: rapid initial creep closure of rooms, initial brine inflow causing gas generation from corrosion and radiolysis, and the availability of CPR material for microbial gas production. Despite the changes incorporated in the CRA-2026 PA, the resulting mean pressures in the waste regions are similar to those observed in the RPPCR. Several changes incorporated into the CRA-2026 PA affect repository pressurization, including modifications to the repository design, updates to the Salado flow and transport computational grid, adjustments in repository dimensions, and revisions to parameters related to brine saturation and permeability. These changes are discussed in Section PA-1.3. However, the individual impacts of these changes on waste-region pressure are generally small over the time scales considered. Consequently, overall pressures in the CRA-2026 PA remain close to those of the RPPCR.

Brine saturations generally increase toward the south in the repository due to the 1-degree Salado dip and the associated gravity-driven flow of brine (Figure PA-49 to Figure PA-52). Brine saturations are generally decreased in all waste areas for the CRA-2026 PA in comparison to the RPPCR PA. The saturation reduction in the waste under S1-BF may be attributed to the substantially increased brine consumption as a result of inventory concentration increases in activity, cellulose, and iron (Day and King 2025).

The repository shaft is modeled in the WIPP PA as being directly between the EXP and WOPS regions of the repository. The shaft materials do not impede lateral brine flow within the repository. Mean brine flows up the shaft in the CRA-2026 PA remain relatively small (Figure PA-53) (Day and King 2025). Similarly, mean brine flows through anhydrite marker beds across the LWB in the CRA-2026 PA remain relatively small (Figure PA-54). Section PA-7.2 shows that the brine that crosses the LWB in the CRA-2026 PA has not been contaminated with radionuclides. Because the minimum brine flows in both cases are below the y-axis limit, they do not appear in Figure PA-53 or Figure PA-54.

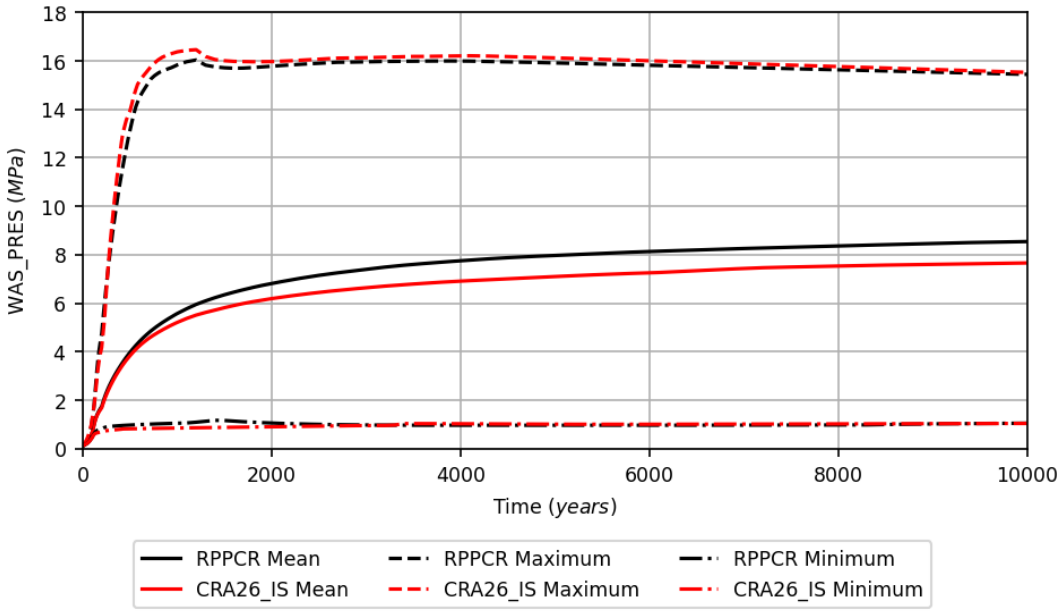


Figure PA-45. Minimum, Maximum, and Mean of WP Pressure, Scenario S1-BF

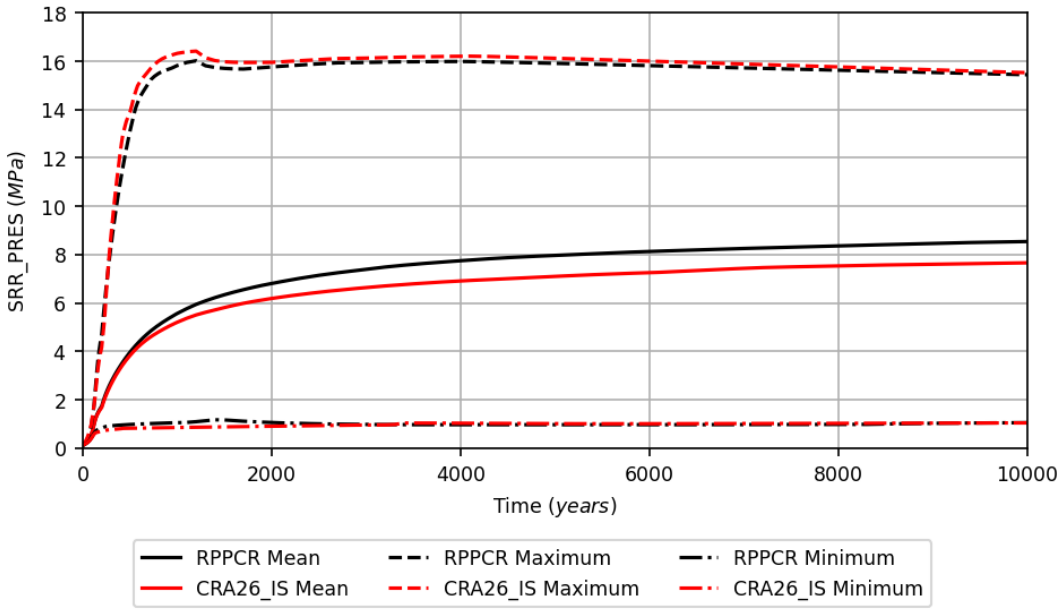


Figure PA-46. Minimum, Maximum, and Mean of SROR Pressure, Scenario S1-BF

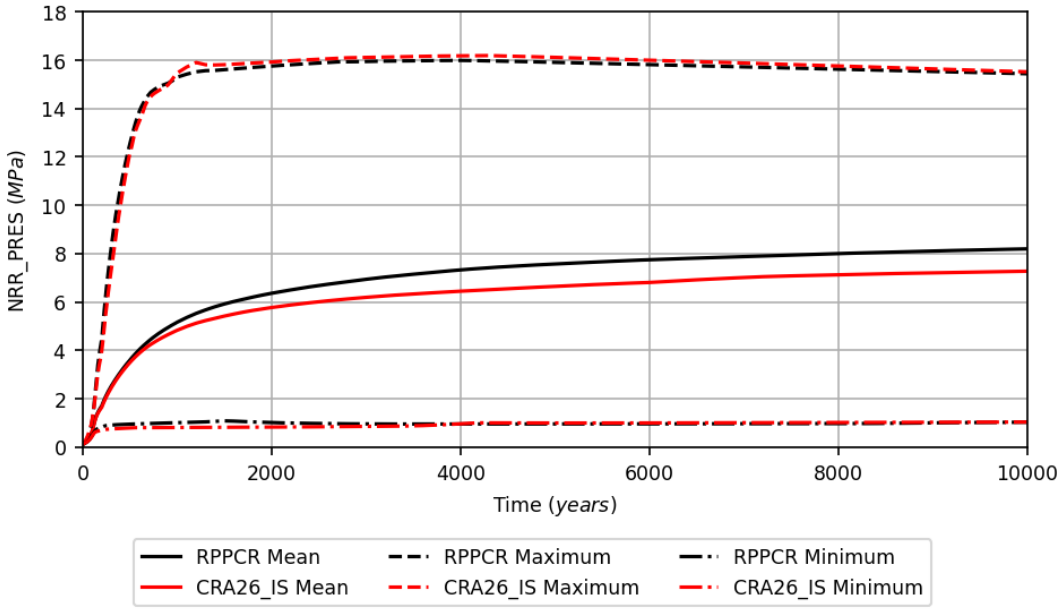


Figure PA-47. Minimum, Maximum, and Mean of NROR Pressure, Scenario S1-BF

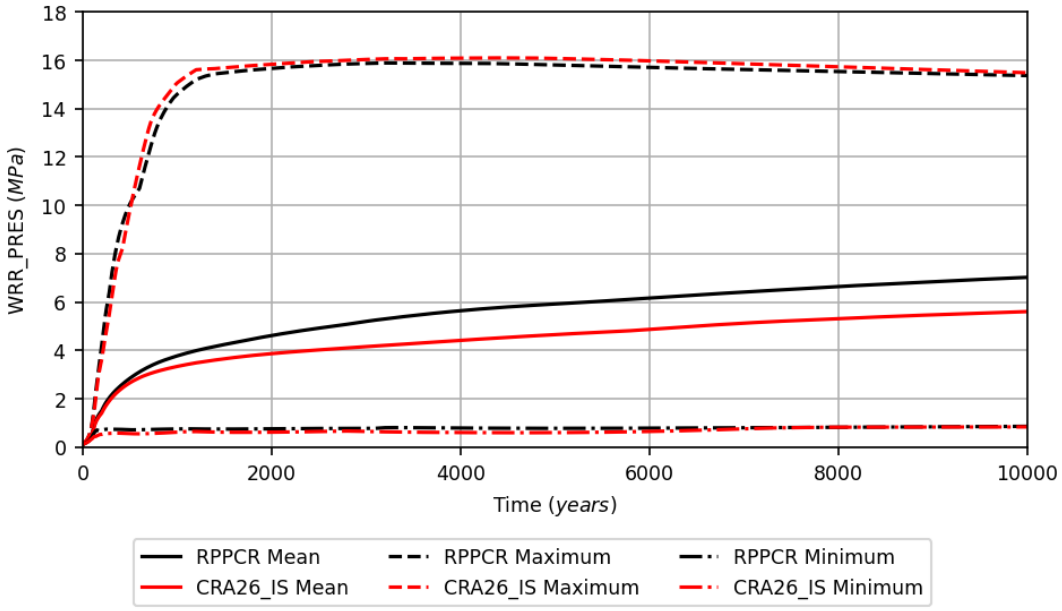


Figure PA-48. Minimum, Maximum, and Mean of WROR Pressure, Scenario S1-BF

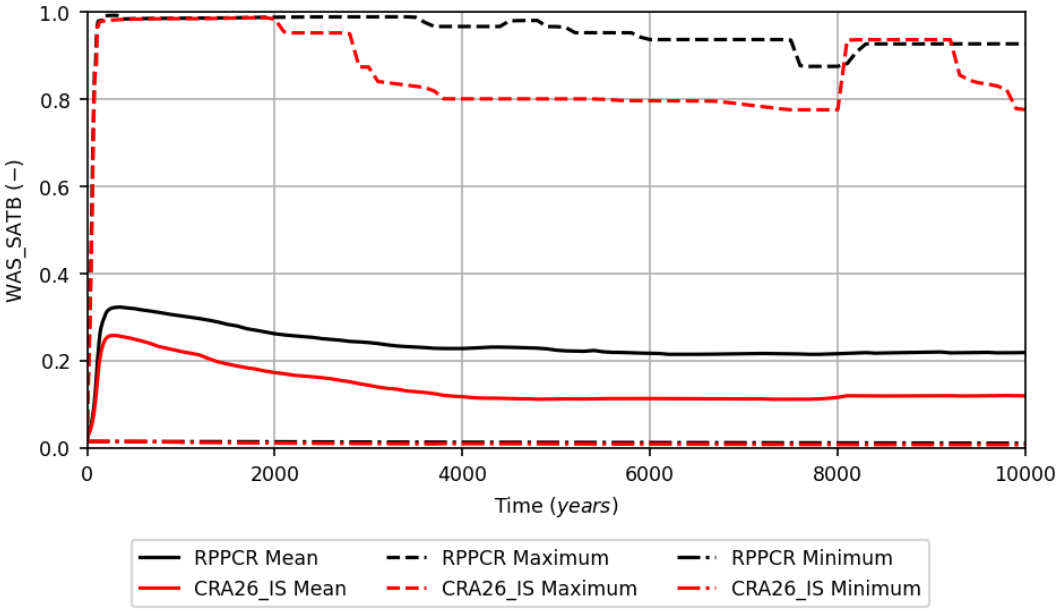


Figure PA-49. Minimum, Maximum, and Mean of WP Brine Saturation, Scenario S1-BF

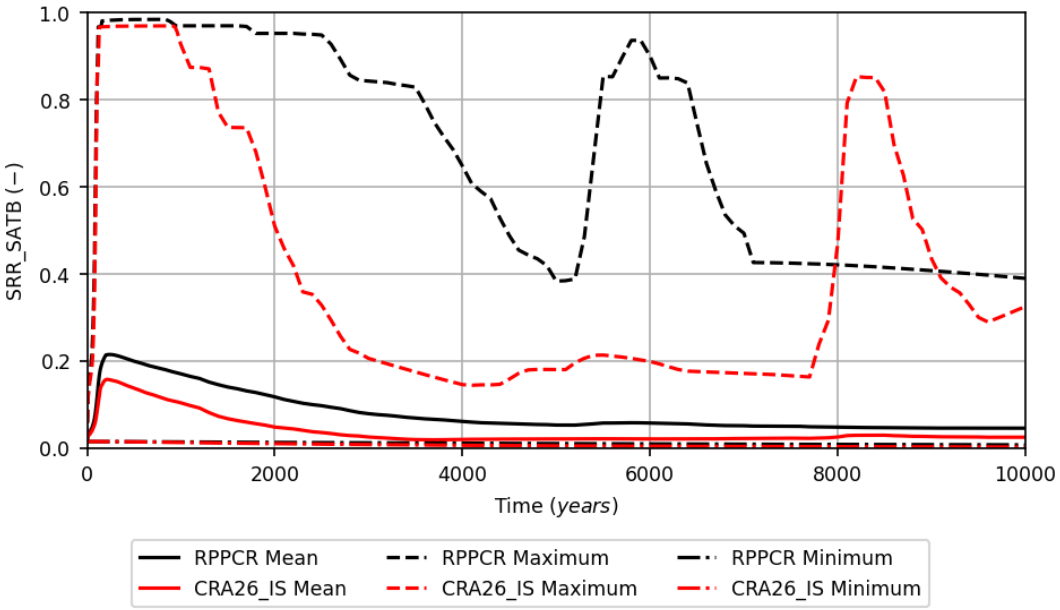


Figure PA-50. Minimum, Maximum, and Mean of SROR Brine Saturation, Scenario S1-BF

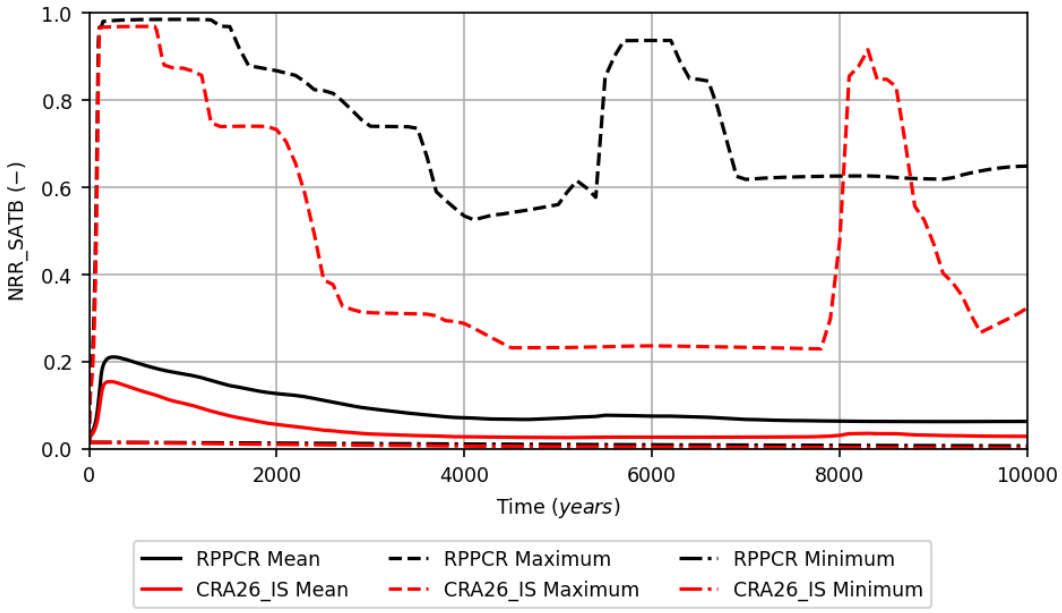


Figure PA-51. Minimum, Maximum, and Mean of NROR Brine Saturation, Scenario S1-BF

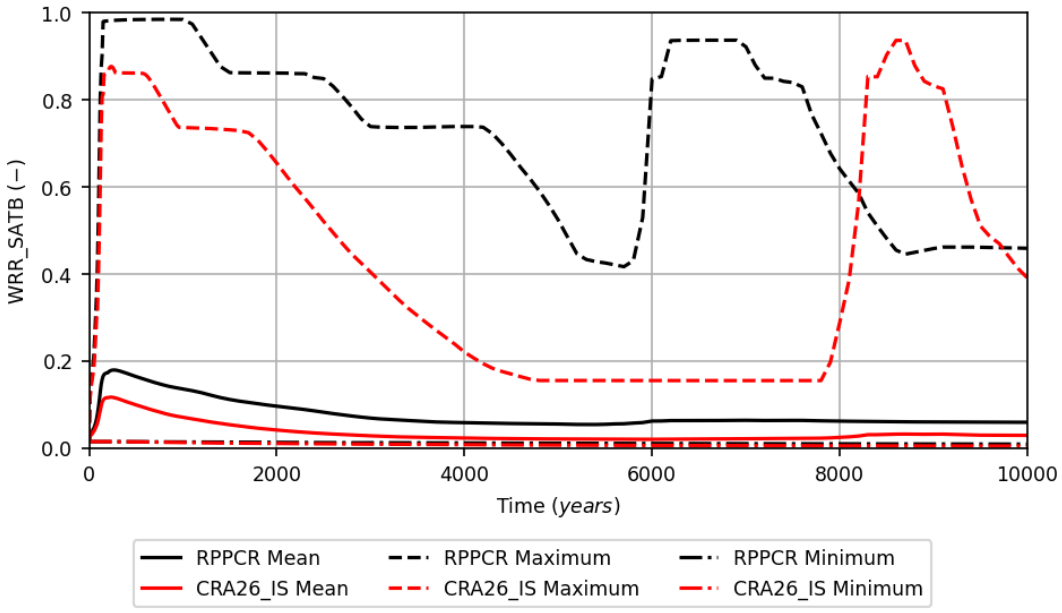


Figure PA-52. Minimum, Maximum, and Mean of WROR Brine Saturation, Scenario S1-BF

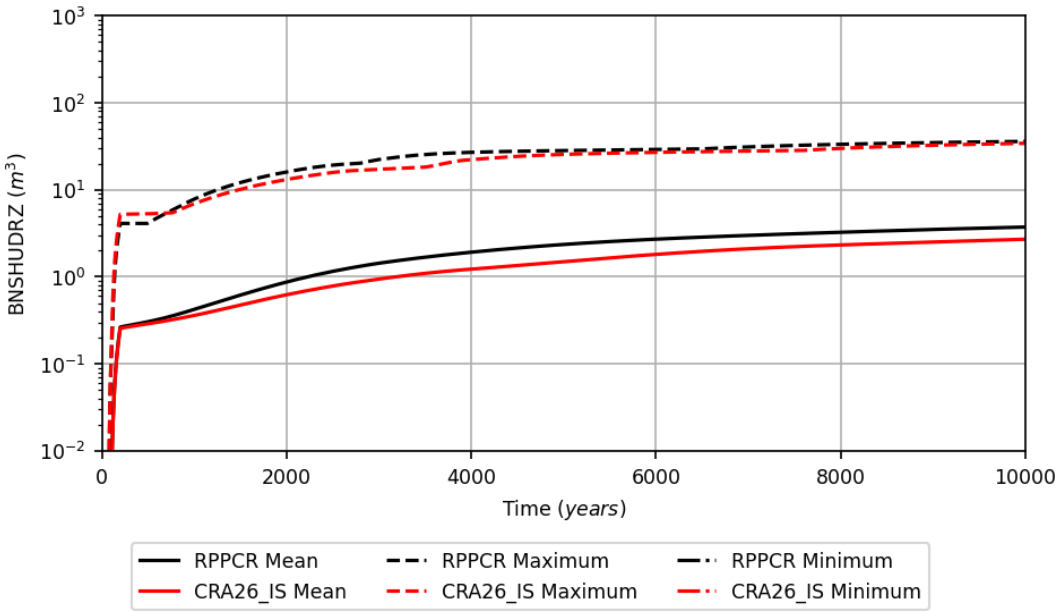


Figure PA-53. Minimum, Maximum, and Mean of Brine Flow up the Shaft, Scenario S1-BF

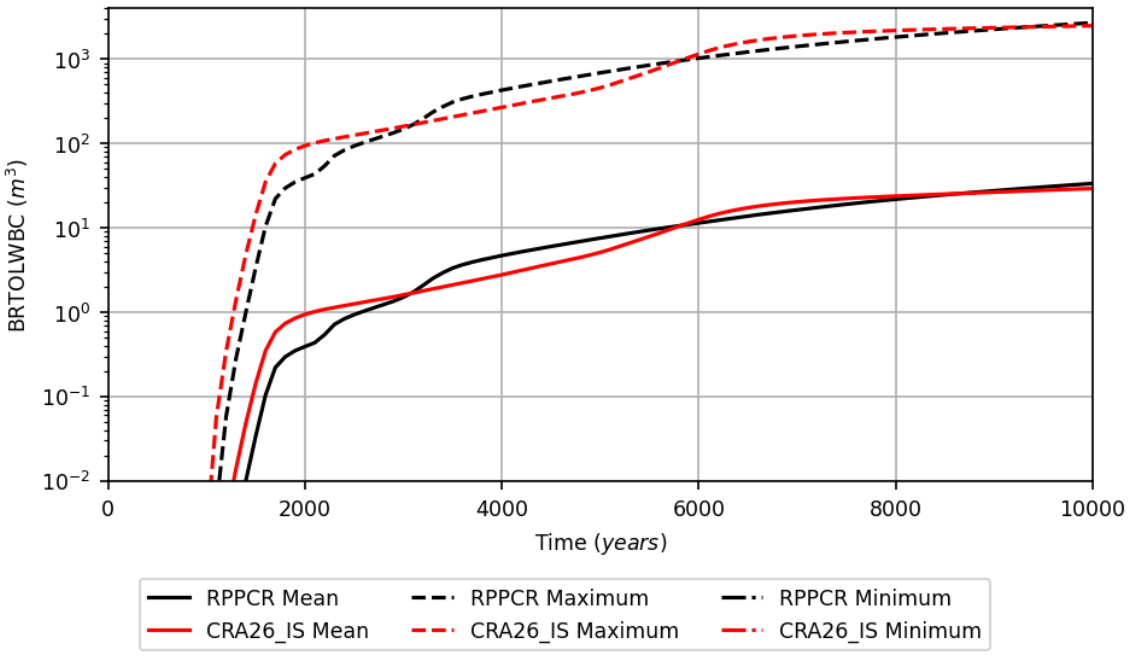


Figure PA-54. Minimum, Maximum, and Mean Brine Flow in Anhydrite Layers Across LWB, Scenario S1-BF.

PA-7.2 Radionuclide Transport

This section summarizes the radionuclide transport results for the undisturbed repository, both up the shaft to the Culebra and through the Salado to the LWB. Radionuclide transport in the Salado (Section PA-4.4) is calculated for the undisturbed scenario using the code NUTS. Docherty and Kim (2025) present a detailed analysis of the NUTS results for the CRA-2026 PA. The NUTS calculations include screening simulations with a non-decaying tracer (Section PA-6.3.2.1). In the undisturbed repository scenario (scenario S1-BF), no vectors had tracer releases exceeding the 10^{-7} kg screening threshold used to identify scenarios with the potential for meaningful radionuclide transport. Consequently, no long-term radionuclide releases up the shaft or through anhydrite marker beds to the LWB are predicted for the undisturbed repository scenario in the CRA-2026 PA.

PA-8.0 Results for a Disturbed Repository

The WIPP repository might be disturbed by exploratory drilling for natural resources during the 10,000-year regulatory period. Drilling could create additional pathways for radionuclide transport through the Salado and could release material directly to the surface. In addition, mining for potash within the LWB might alter flow in the overlying geologic units and locally accelerate transport through the Culebra. The scenarios for disturbed repository performance (Section PA-2.2.2.2) capture the range of consequences resulting from drilling and mining, including changes to the natural environment and the repository system as well as releases from the repository.

Total releases are computed by the code CCDFGF. Total releases comprise transport releases and direct releases. Transport releases generally involve movement of radionuclides up an abandoned borehole into the Culebra, then through the Culebra to the LWB. Transport of radionuclides to the Culebra is computed using the codes NUTS and PANEL (see Section PA-6.3.2 and Section PA-6.3.3) using the brine flows computed by BRAGFLO (see Section PA-6.3.1). Radionuclide transport through the Culebra is computed using the code SECOTP2D (see Section PA-6.3.8) using flow fields calculated by MODFLOW6 (see Section PA-6.3.7).

Direct releases occur at the time of a drilling intrusion and include releases of solids (cuttings, cavings, and spallings) computed using the code CUTTINGS_S (see Section PA-6.3.5) with lookup tables from the code DRSPALL (see Section PA-6.3.4), and DBRs computed using BRAGFLO (see Section PA-6.3.6). Pressure and brine saturation within the waste areas are used as initial conditions for the spallings and DBR direct release models. Results from the undisturbed repository (see Section PA-7.0) are used as the initial conditions for the first intrusion. To calculate initial conditions for subsequent intrusions, and to compute the source of radionuclides for transport in the Culebra, BRAGFLO uses a set of drilling scenarios to calculate conditions within the repository after an intrusion (see Section PA-6.3.1).

This section first summarizes the scenarios used to represent drilling intrusions and the resulting repository conditions calculated by BRAGFLO. Transport releases are presented next, followed by cuttings, cavings, spallings, and DBRs. The CRA-2026 PA results obtained for the disturbed repository are summarized in Brunell et al. (2025). Results of the CRA-2026 PA are compared to results from the RPPCR PA (Brunell et al. 2024).

PA-8.1 Fluid Flow

This section summarizes the results for flow in the Salado and Culebra for the disturbed scenarios. Day and King (2025) provide a detailed presentation of Salado flow results obtained in the CRA-2026 PA. Wilgus and Bethune (2025) provide a detailed set of the CRA-2026 Culebra flow field results.

PA-8.1.1 Salado Flow Results for E1 Intrusion Scenarios

Results are now presented for disturbed scenario S2-BF. Results presented for this scenario are representative of those calculated for E1 intrusion scenarios (scenario S2-BF and scenario S3-BF), with the only difference being the time of intrusion. The trends discussed for scenario S2-BF also apply to scenario S3-BF. Results presented in this section are given for the intruded WP, SROR, NROR, and WROR. In general, the evolution with time of brine pressures and saturations in repository waste areas results from the complex interplay of gas generation, brine production and consumption, the 1-degree (south) Salado dip, and the lack of panel closures between the WP and SROR areas.

Scenario S2-BF represents an E1 intrusion at 350 years. The minimum, maximum, and mean pressures in the WP, SROR, NROR, and WROR are plotted together for the RPPCR PA and the CRA-2026 PA in Figure PA-55, Figure PA-56, Figure PA-57, and Figure PA-58. Pressure is broadly similar in both analyses.

The minimum, maximum, and mean brine saturations are plotted together in Figure PA-59, Figure PA-60, Figure PA-61, and Figure PA-62. Relative to the RPPCR PA, in the CRA-2026 PA, changes to repository dimensions and inventory parameters have impacts on Salado flow results. Brine consumption is increased by higher concentrations of iron, CPR, and decay heat in the waste areas. An increased rate of MgO hydration for the CRA-2026 PA also contributes to increased brine consumption in comparison to the RPPCR PA. As a result, brine saturations are observed to be significantly decreased over all reported waste areas and scenarios in the CRA-2026 PA. For example, mean brine saturation in the WP is lower in the CRA-2026 PA, as shown in Figure PA-59.

Cumulative brine flow up the intrusion borehole potentially transports contaminants to the ground surface, or to the Culebra where they may be transported laterally through the Culebra to the LWB. Maximum and mean brine flows up the intrusion borehole to the Culebra obtained in the RPPCR PA and the CRA-2026 PA are plotted together in Figure PA-63. The decreased brine saturation in the CRA-2026 PA reduces brine mobility in the waste and borehole regions, resulting in a lower overall mean brine flow up the intrusion borehole compared to the RPPCR PA, despite slightly higher mean waste-panel pressures after intrusion. Because the minimum brine flow is below the y-axis limit, it does not appear in Figure PA-63.

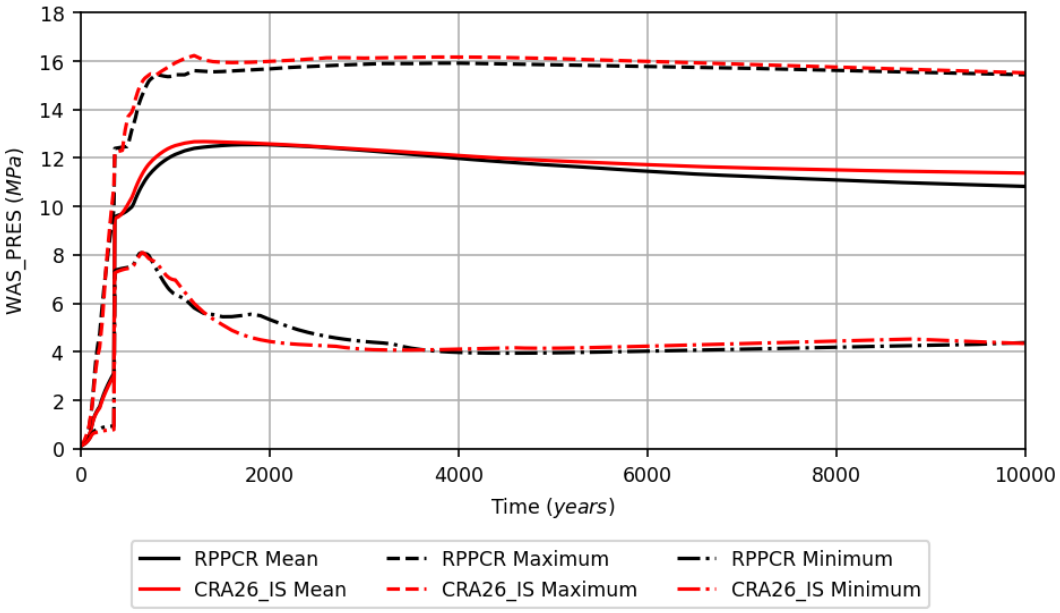


Figure PA-55. Minimum, Maximum, and Mean of WP Pressure, Scenario S2-BF

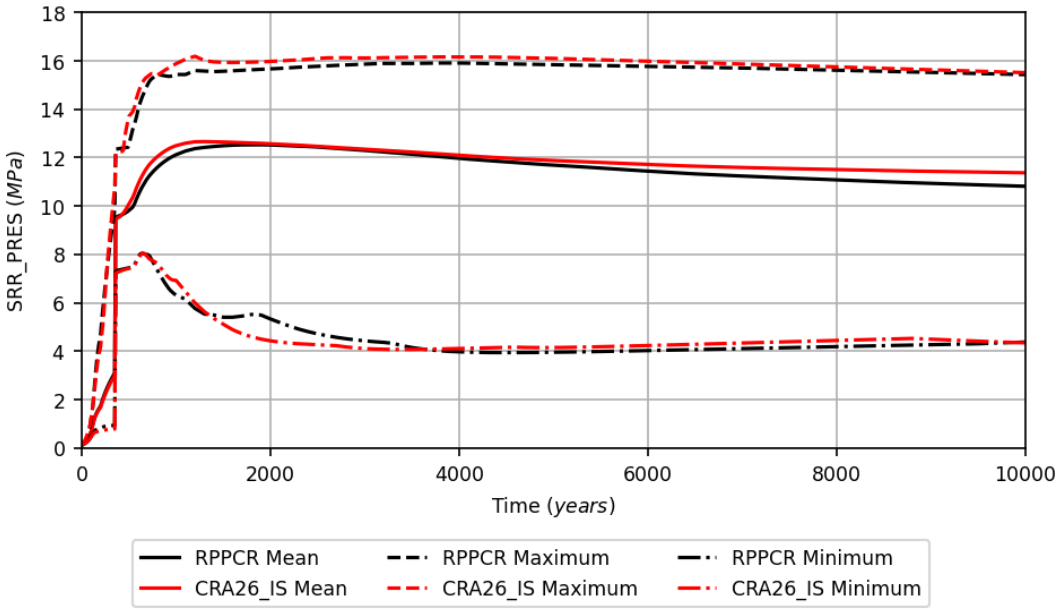


Figure PA-56. Minimum, Maximum, and Mean of SROR Pressure, Scenario S2-BF

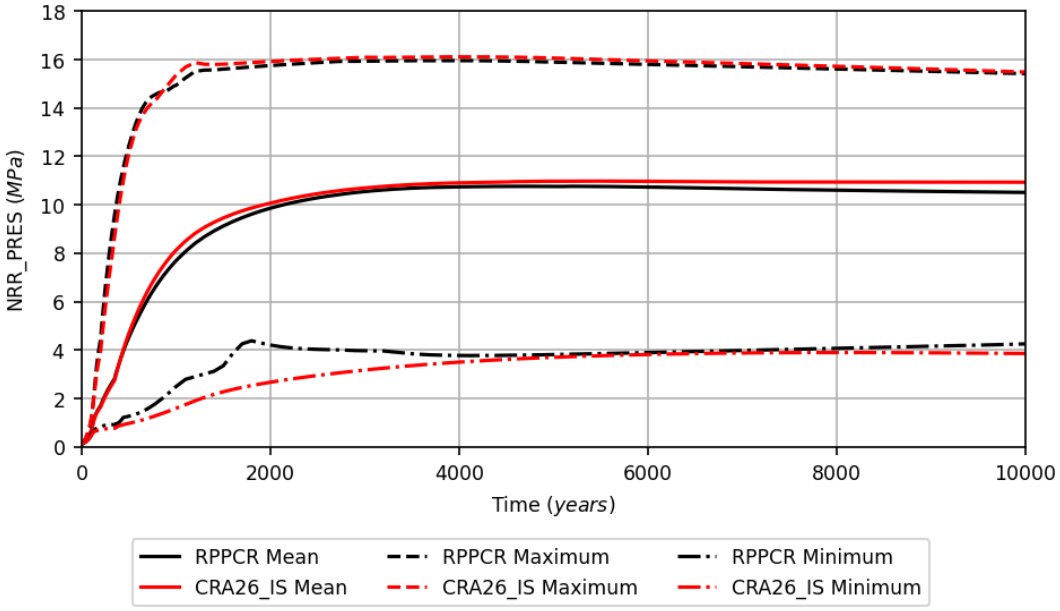


Figure PA-57. Minimum, Maximum, and Mean of NROR Pressure, Scenario S2-BF

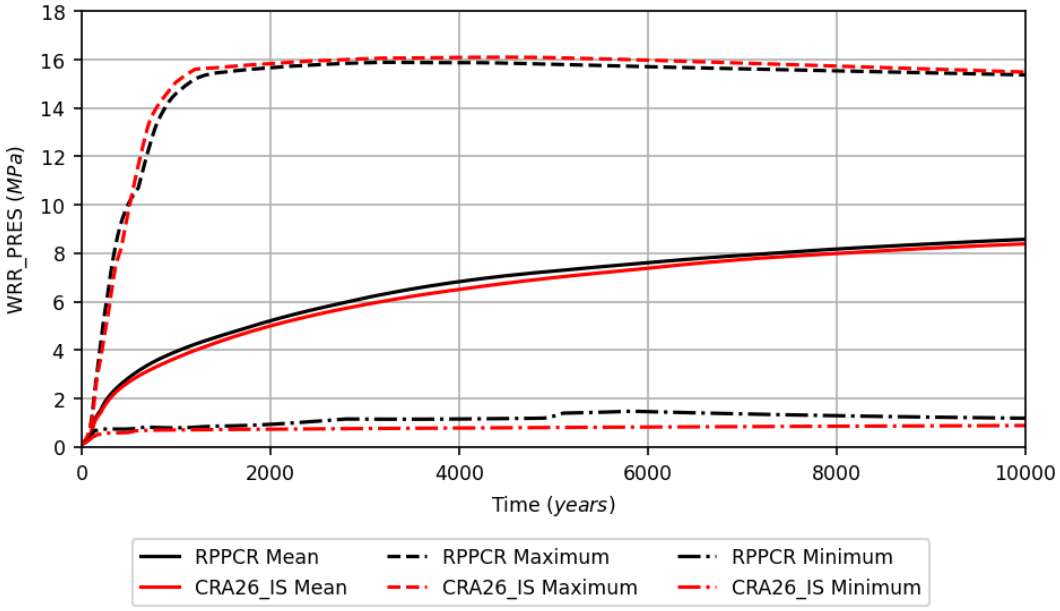


Figure PA-58. Minimum, Maximum, and Mean of WROR Pressure, Scenario S2-BF

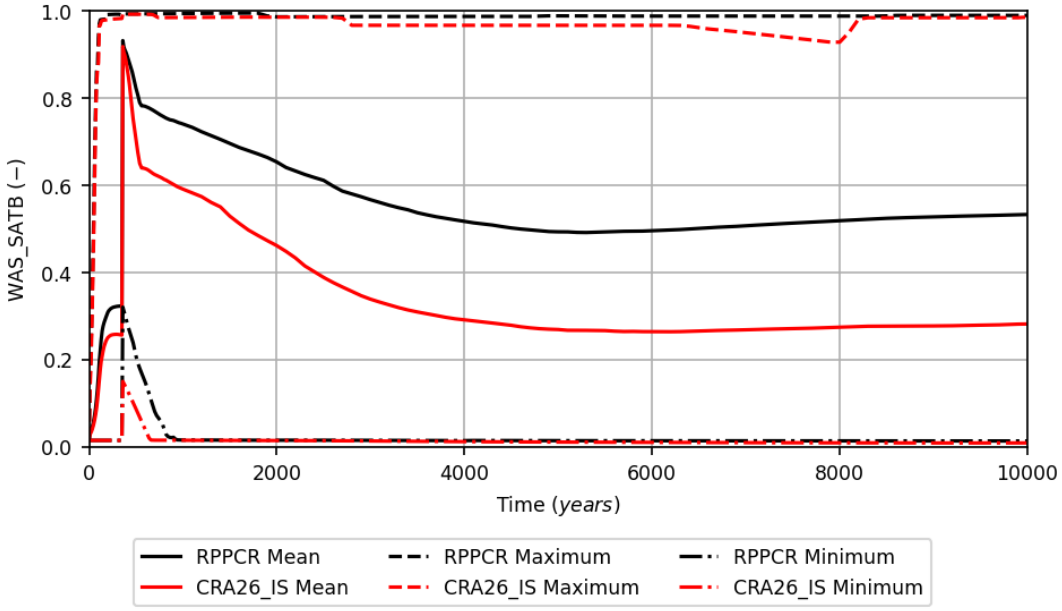


Figure PA-59. Minimum, Maximum, and Mean of WP Brine Saturation, Scenario S2-BF

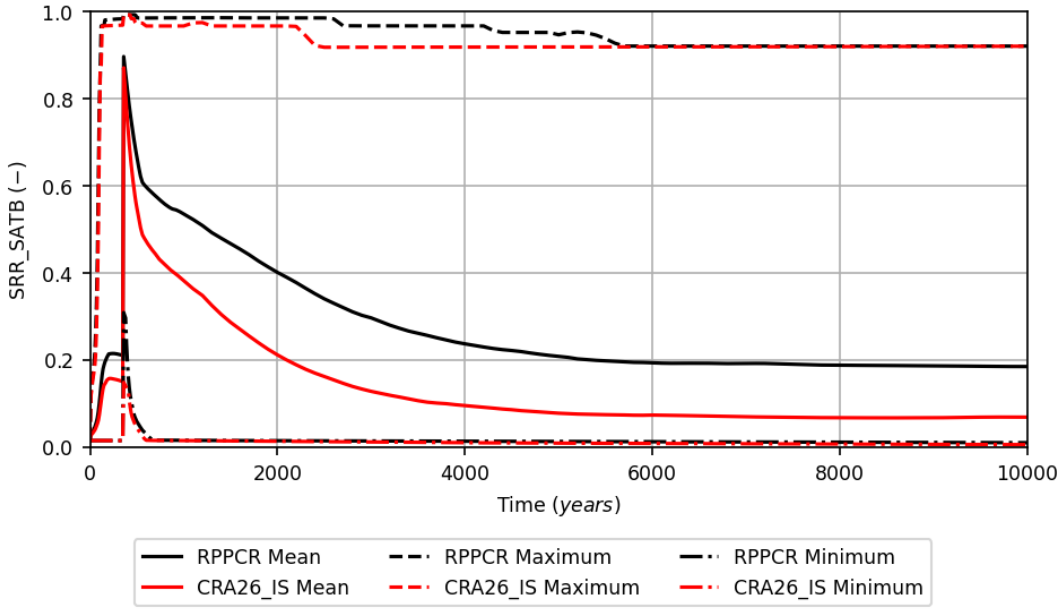


Figure PA-60. Minimum, Maximum, and Mean of SROR Brine Saturation, Scenario S2-BF

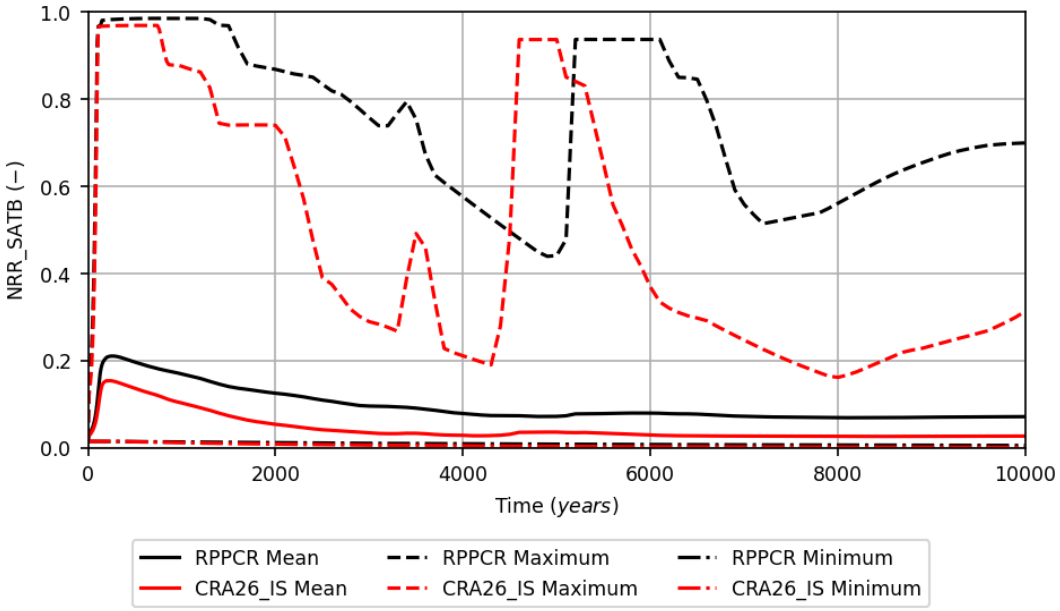


Figure PA-61. Minimum, Maximum, and Mean of NROR Brine Saturation, Scenario S2-BF

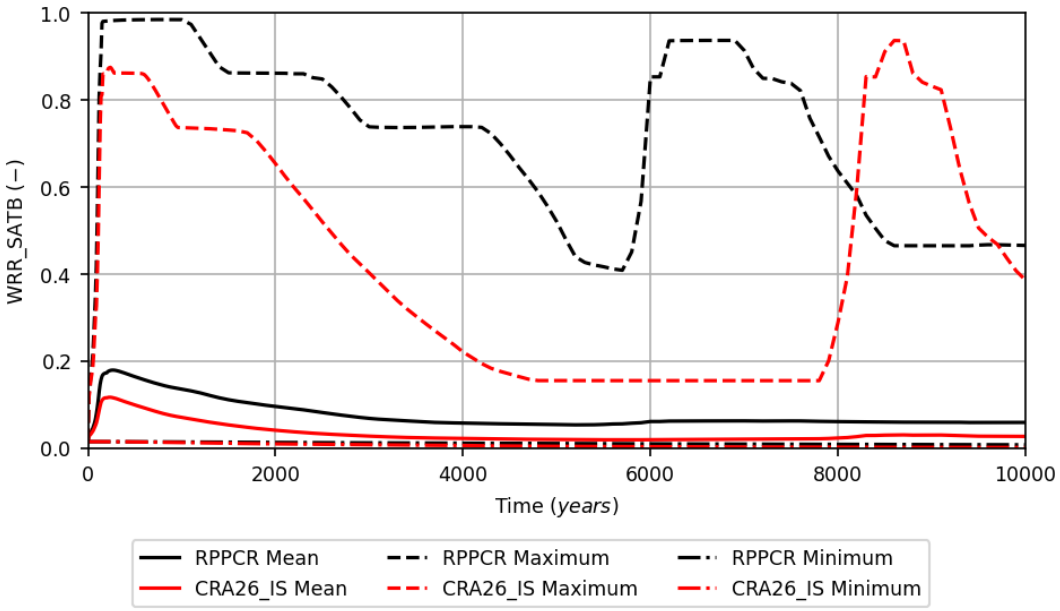


Figure PA-62. Minimum, Maximum, and Mean of WROR Brine Saturation, Scenario S2-BF

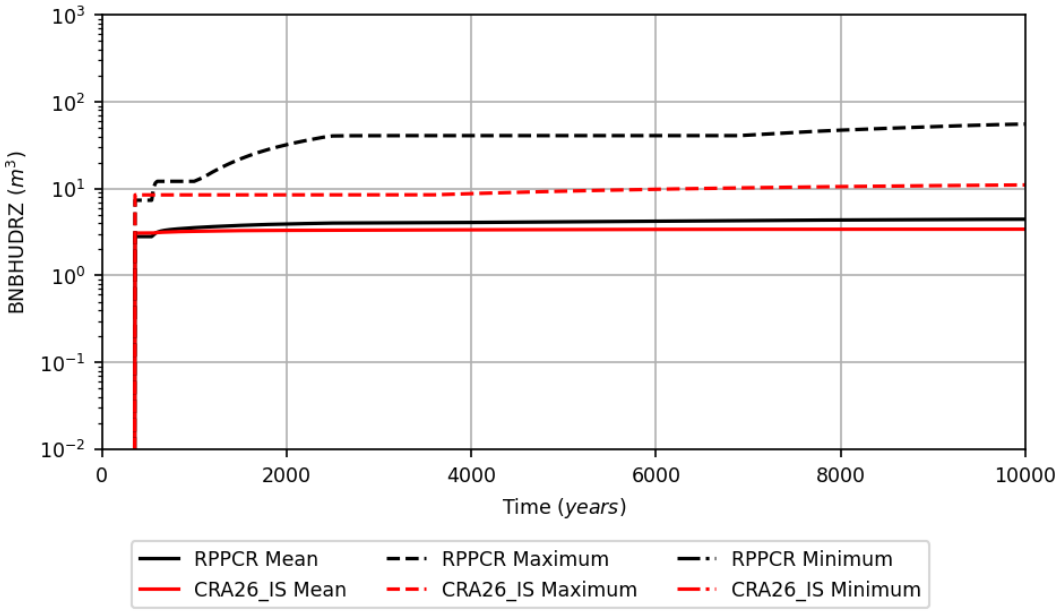


Figure PA-63. Minimum, Maximum, and Mean of Cumulative Brine Flow up the Borehole, Scenario S2-BF

PA-8.1.2 Salado Flow Results for E2 Intrusion Scenarios

Results are presented for disturbed scenario S4-BF, which represents an E2 intrusion at 350 years. These results are representative of those calculated for E2 intrusion scenarios (scenario S4-BF and scenario S5-BF), with the primary difference being the time of intrusion. Trends discussed for scenario S4-BF also apply to scenario S5-BF. Results in this section are provided for the intruded WP, SROR, NROR, and WROR waste areas.

The minimum, maximum, and mean pressures in the WP, SROR, NROR, and WROR are plotted together for the RPPCR PA and the CRA-2026 PA in Figure PA-64, Figure PA-65, Figure PA-66, and Figure PA-67. Mean pressures in the CRA-2026 PA are slightly lower than in the RPPCR PA across all waste areas.

The minimum, maximum, and mean brine saturation curves are plotted together in Figure PA-68, Figure PA-69, Figure PA-70, and Figure PA-71. In the CRA-2026 PA, changes to repository dimensions and inventory parameters significantly influence Salado flow results for E2 intrusion scenarios. Increased inventory concentrations of iron mass, CPR mass, and decay heat lead to increased gas generation and brine consumption on a per waste-area-volume basis. An increased rate of MgO hydration for the CRA-2026 PA also contributes to increased brine consumption in comparison to the RPPCR PA. These changes result in decreased brine saturations across all waste areas and scenarios compared to the RPPCR PA. For example, mean brine saturation in the WP is lower in the CRA-2026 PA, as shown in Figure PA-68.

Cumulative brine flow up the intrusion borehole obtained in scenario S4-BF in the RPPCR PA and the CRA-2026 PA is plotted together in Figure PA-72. The mean brine flow up the intrusion

borehole under S4-BF is reduced in the CRA-2026 PA compared to the RPPCR PA. This reduction is primarily attributed to lower brine pressures and saturations in the WP, which limit the volume of brine available for transport up the borehole. Because the minimum brine flow is below the y-axis limit, it does not appear in Figure PA-72.

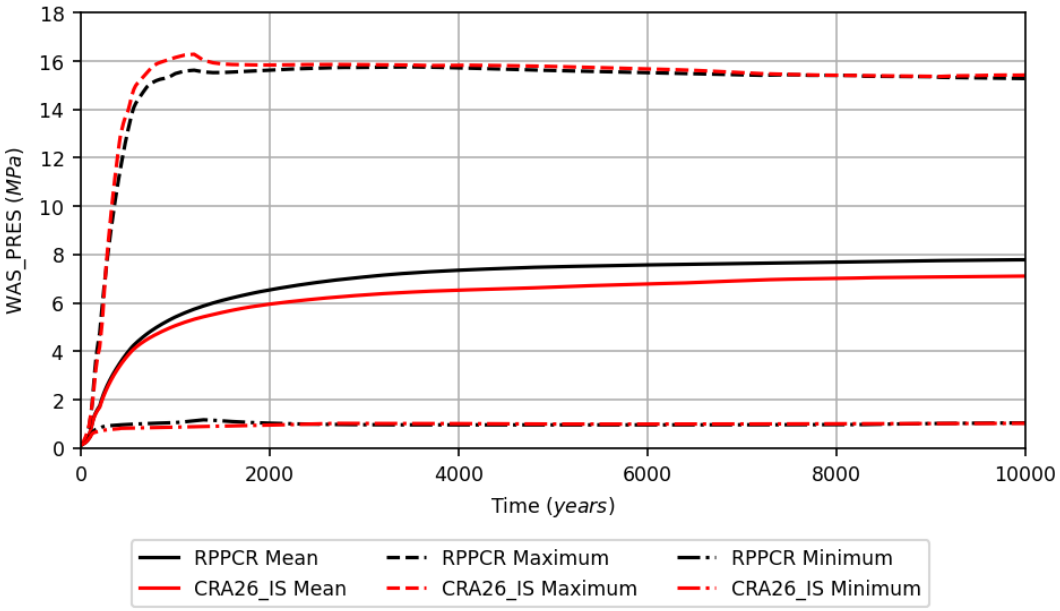


Figure PA-64. Minimum, Maximum, and Mean of WP Pressure, Scenario S4-BF

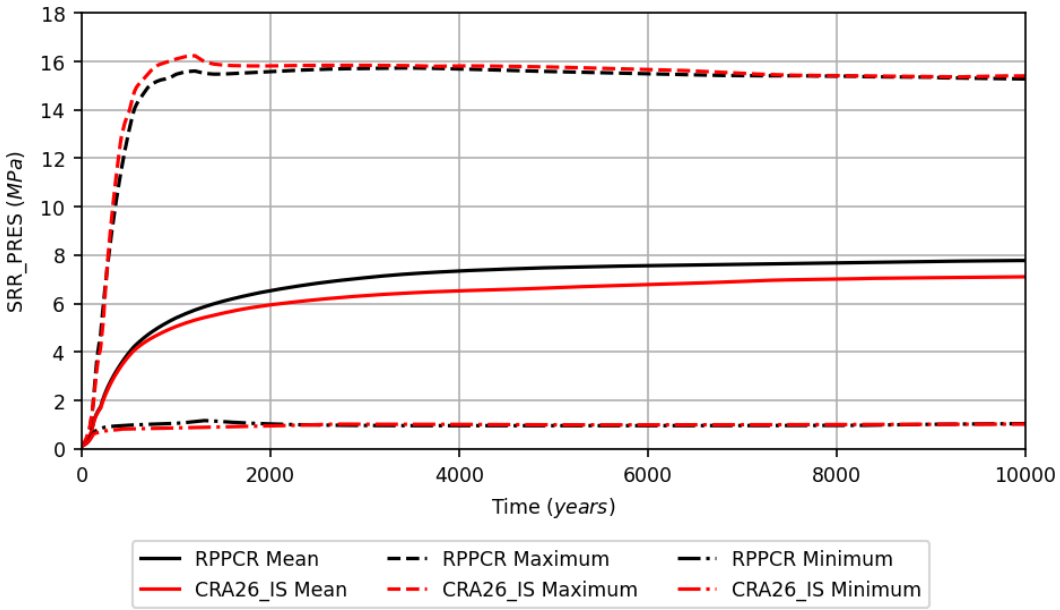


Figure PA-65. Minimum, Maximum, and Mean of SROR Pressure, Scenario S4-BF

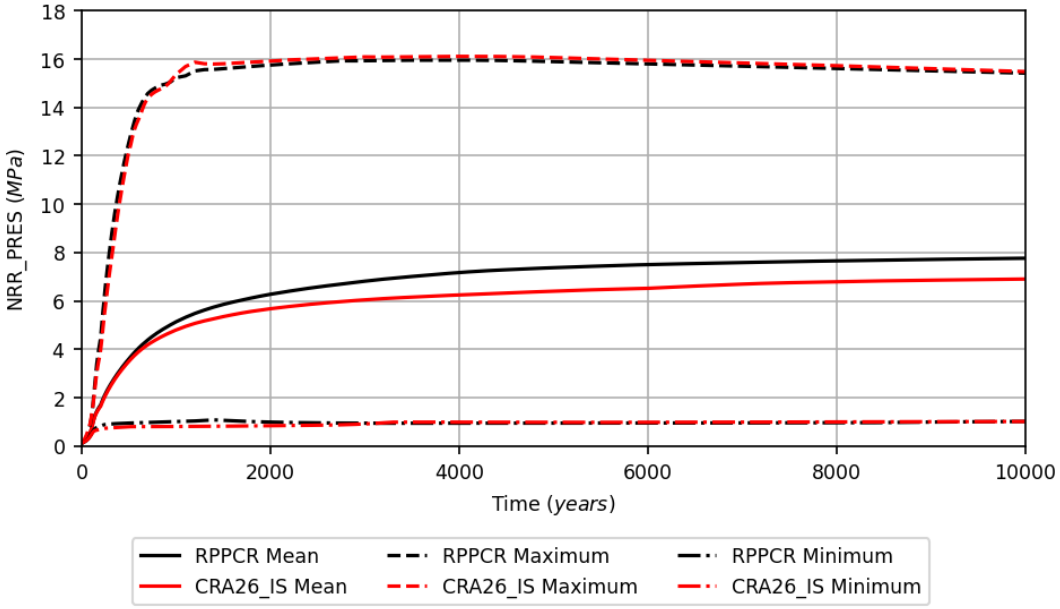


Figure PA-66. Minimum, Maximum, and Mean of NROR Pressure, Scenario S4-BF

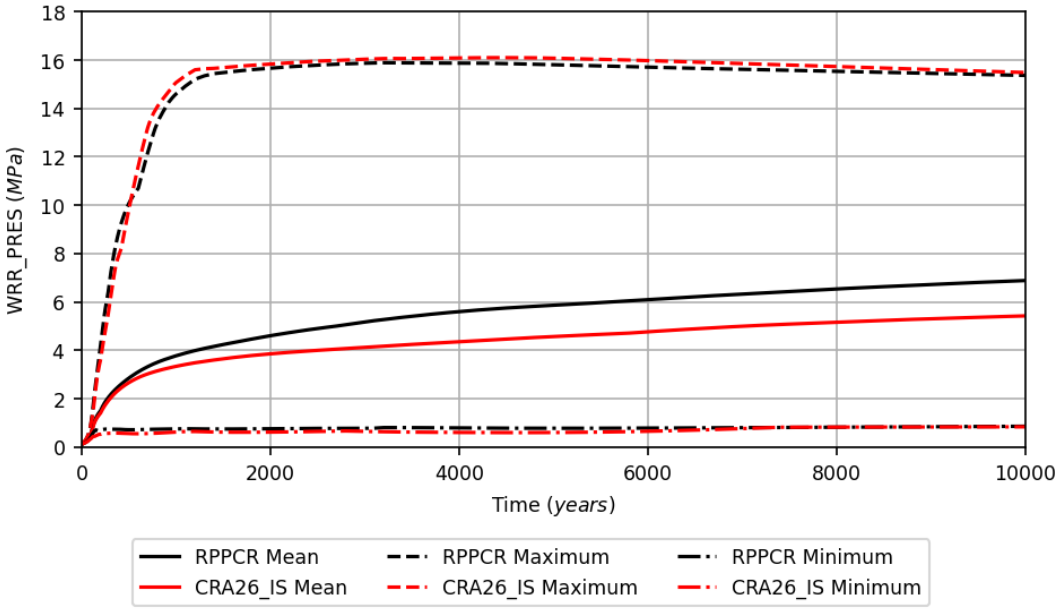


Figure PA-67. Minimum, Maximum, and Mean of WROR Pressure, Scenario S4-BF

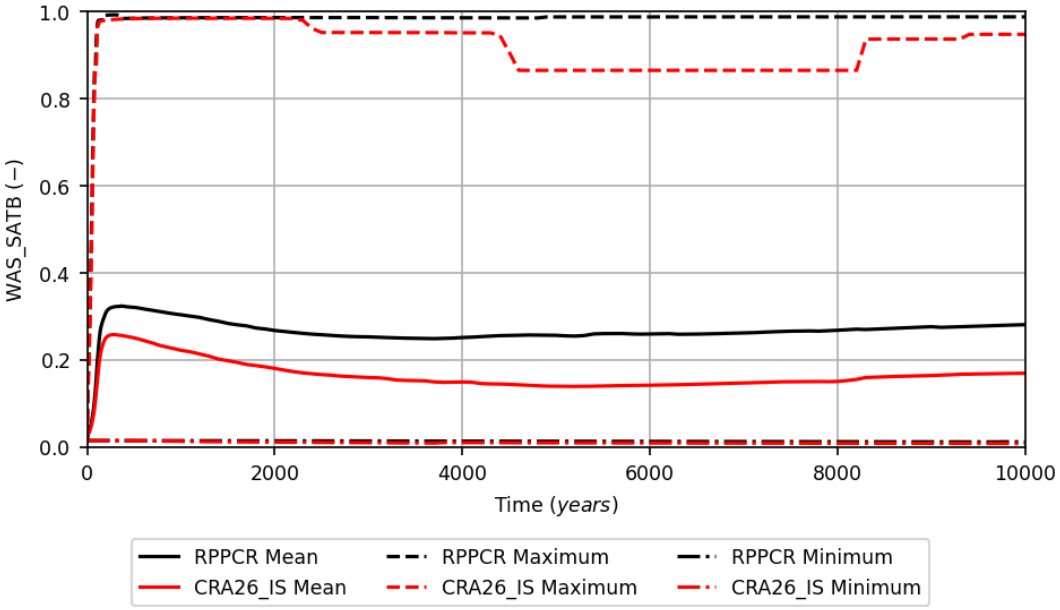


Figure PA-68. Minimum, Maximum, and Mean of WP Brine Saturation, Scenario S4-BF

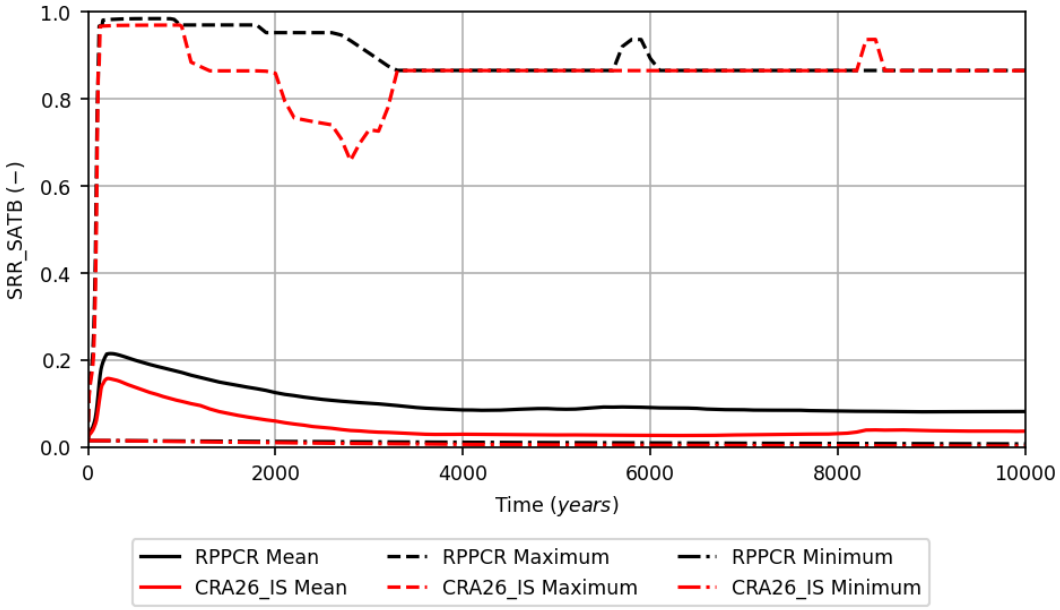


Figure PA-69. Minimum, Maximum, and Mean of SROR Brine Saturation, Scenario S4-BF

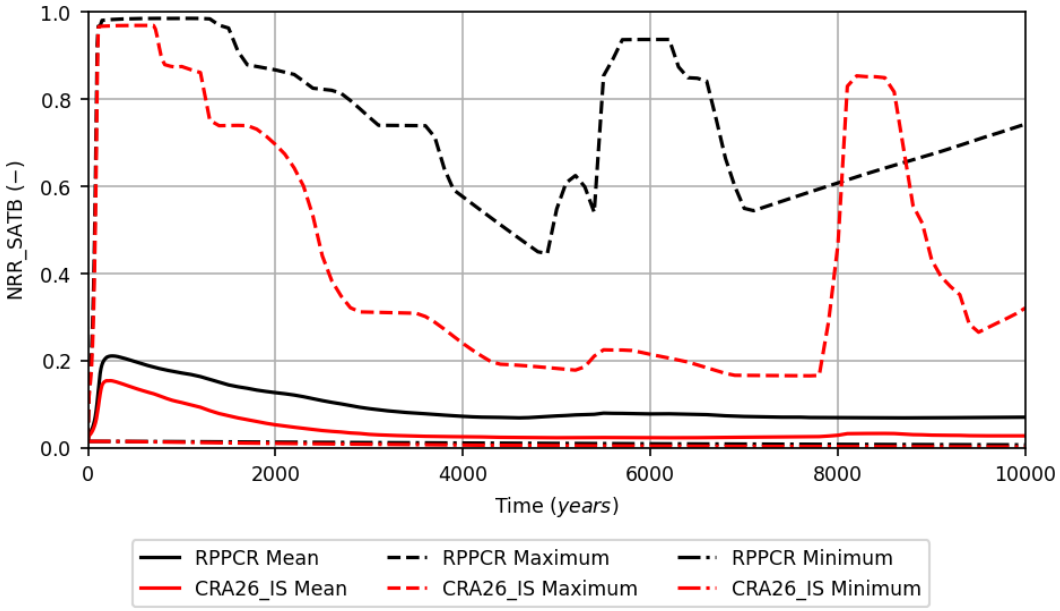


Figure PA-70. Minimum, Maximum, and Mean of NROR Brine Saturation, Scenario S4-BF

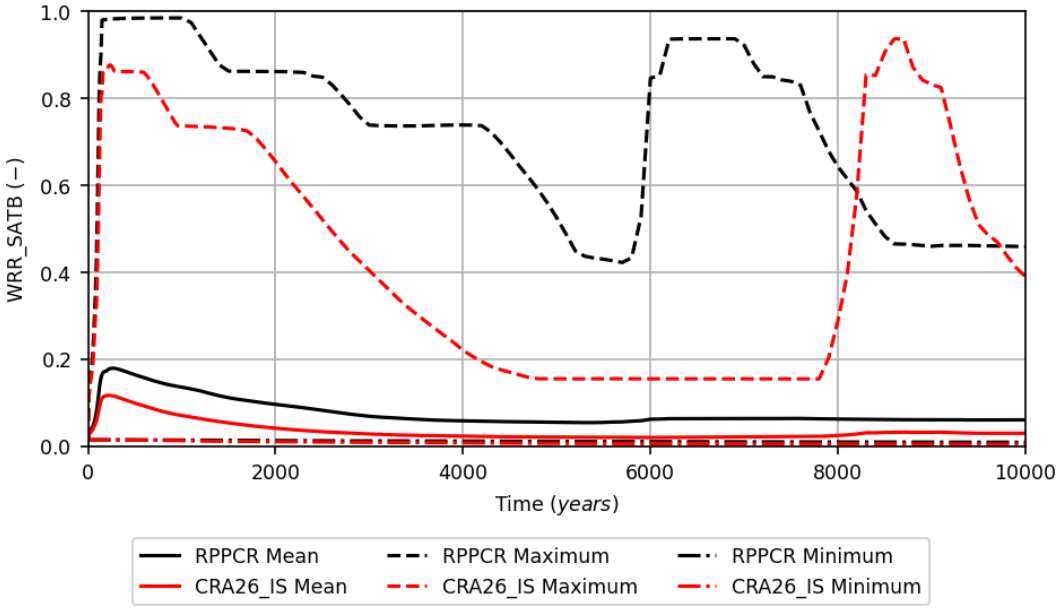


Figure PA-71. Minimum, Maximum, and Mean of WROR Brine Saturation, Scenario S4-BF

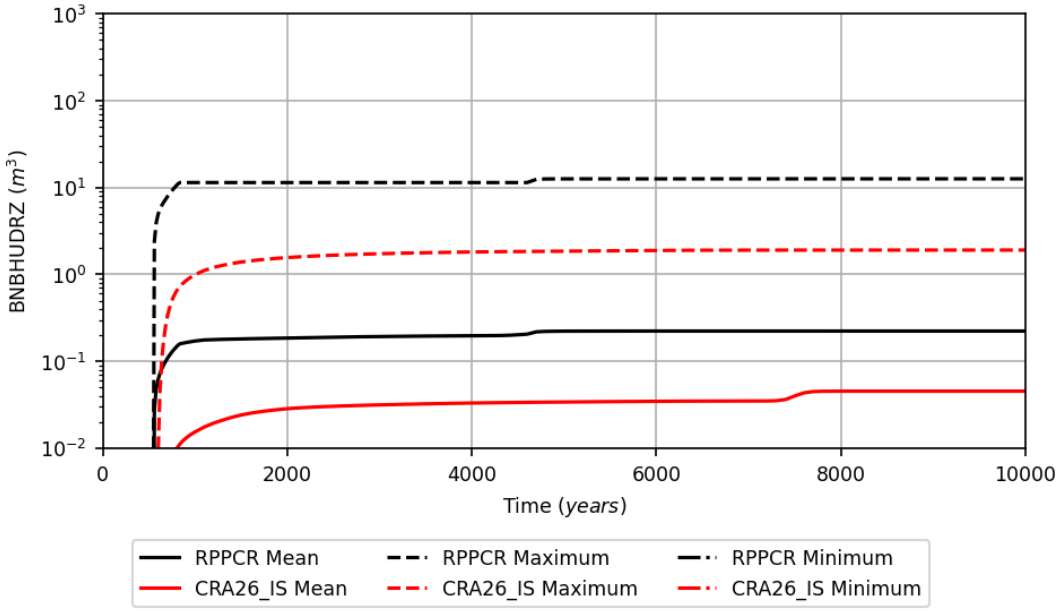


Figure PA-72. Minimum, Maximum, and Mean of Cumulative Brine Flow up the Borehole, Scenario S4-BF

PA-8.1.3 Salado Flow Summarized Results

This section provides summarized results of all Salado flow modeling, including scenarios S1-BF, S2-BF, S4-BF, and S6-BF. Table PA-24 contains summary statistics for pressures, Table PA-25 contains summary statistics for brine saturations, and Table PA-26 contains summary statistics for brine flows. These tables present means and maxima in the EXP, OPS, NROR, SROR, WROR, and WP waste areas over the 10,000-year regulatory period. Brine flow statistics include flows into the repository, up the shaft, and up the intrusion borehole. The summary statistics in Table PA-24 through Table PA-26 confirm the trends observed in Sections PA-8.1.1 and PA-8.1.2, with lower mean pressures, saturations, and brine flows in the CRA-2026 PA relative to the RPPCR PA across all Salado flow scenarios.

Table PA-24. Pressure (MPa) Statistics on Replicate 1 Means

Quantity	Scenario	RPPCR Mean Value[1]	CRA-2026 Mean Value[1]	RPPCR Max Value[2]	CRA-2026 Max Value[2]
Waste Panel Pressure	S1-BF	7.4	6.7	8.5	7.7
Waste Panel Pressure	S2-BF	11.2	11.5	12.6	12.7
Waste Panel Pressure	S4-BF	6.9	6.3	7.8	7.1
Waste Panel Pressure	S6-BF	8.8	8.8	10.3	10.3
SROR Pressure	S1-BF	7.4	6.7	8.5	7.7
SROR Pressure	S2-BF	11.2	11.5	12.5	12.7
SROR Pressure	S4-BF	6.9	6.3	7.8	7.1
SROR Pressure	S6-BF	8.8	8.8	10.3	10.3
NROR Pressure	S1-BF	7.0	6.3	8.2	7.3
NROR Pressure	S2-BF	9.8	10.1	10.8	11.0
NROR Pressure	S4-BF	6.8	6.0	7.8	6.9
NROR Pressure	S6-BF	8.2	8.1	9.4	9.4
South Ops Pressure	S1-BF	4.3	3.2	6.3	4.9
South Ops Pressure	S2-BF	5.6	5.4	8.0	7.9
South Ops Pressure	S4-BF	4.3	3.1	6.1	4.7
South Ops Pressure	S6-BF	4.9	4.3	7.3	6.7
Exp Area Pressure	S1-BF	4.3	3.2	6.3	4.9
Exp Area Pressure	S2-BF	5.6	5.4	8.0	7.8
Exp Area Pressure	S4-BF	4.2	3.1	6.1	4.6
Exp Area Pressure	S6-BF	4.9	4.3	7.2	6.7
West Ops Pressure	S1-BF	4.3	3.2	6.3	4.9
West Ops Pressure	S2-BF	5.6	5.4	8.0	7.8
West Ops Pressure	S4-BF	4.2	3.1	6.1	4.6
West Ops Pressure	S6-BF	4.9	4.3	7.2	6.7
WROR Pressure	S1-BF	5.5	4.5	7.0	5.6
WROR Pressure	S2-BF	6.6	6.4	8.6	8.4
WROR Pressure	S4-BF	5.5	4.4	6.9	5.4
WROR Pressure	S6-BF	6.1	5.5	7.9	7.4

Notes:

[1] Average over the time interval (0-10,000 years) of the Replicate 1 mean.

[2] Maximum over the time interval (0-10,000 years) for the Replicate 1 mean.

Table PA-25. Brine Saturation Statistics on Replicate 1 Means

Quantity	Scenario	RPPCR Mean Value[1]	CRA-2026 Mean Value[1]	RPPCR Max Value[2]	CRA-2026 Max Value[2]
Waste Panel Saturation	S1-BF	0.24	0.14	0.32	0.26
Waste Panel Saturation	S2-BF	0.55	0.34	0.93	0.92
Waste Panel Saturation	S4-BF	0.27	0.16	0.32	0.26
Waste Panel Saturation	S6-BF	0.43	0.27	0.63	0.54
SROR Saturation	S1-BF	0.08	0.04	0.21	0.16
SROR Saturation	S2-BF	0.27	0.14	0.90	0.87
SROR Saturation	S4-BF	0.10	0.05	0.21	0.16
SROR Saturation	S6-BF	0.13	0.07	0.31	0.26
NROR Saturation	S1-BF	0.09	0.04	0.21	0.15
NROR Saturation	S2-BF	0.10	0.04	0.21	0.15
NROR Saturation	S4-BF	0.09	0.04	0.21	0.15
NROR Saturation	S6-BF	0.10	0.04	0.21	0.15
South Ops Saturation	S1-BF	0.65	0.53	0.71	0.58
South Ops Saturation	S2-BF	0.63	0.50	0.68	0.54
South Ops Saturation	S4-BF	0.65	0.53	0.71	0.58
South Ops Saturation	S6-BF	0.64	0.52	0.69	0.56
Exp Area Saturation	S1-BF	0.27	0.15	0.30	0.16
Exp Area Saturation	S2-BF	0.26	0.14	0.29	0.16
Exp Area Saturation	S4-BF	0.27	0.15	0.30	0.16
Exp Area Saturation	S6-BF	0.26	0.14	0.30	0.16
West Ops Saturation	S1-BF	0.03	0.01	0.09	0.09
West Ops Saturation	S2-BF	0.03	0.01	0.09	0.09
West Ops Saturation	S4-BF	0.03	0.01	0.09	0.09
West Ops Saturation	S6-BF	0.03	0.01	0.09	0.09
WROR Saturation	S1-BF	0.08	0.03	0.18	0.12
WROR Saturation	S2-BF	0.08	0.03	0.18	0.12
WROR Saturation	S4-BF	0.08	0.03	0.18	0.12
WROR Saturation	S6-BF	0.08	0.03	0.18	0.12

Notes:

[1] Average over the time interval (0-10,000 years) of the Replicate 1 mean.

[2] Maximum over the time interval (0-10,000 years) for the Replicate 1 mean.

Table PA-26. Brine Flow (m^3) Statistics for Replicate 1

Quantity	Scenario	RPPCR Mean Value[1]	CRA-2026 Mean Value[1]	RPPCR Max Value[2]	CRA-2026 Max Value[2]
Brine Flow into Repository	S1-BF	5.91E+04	4.20E+04	3.09E+05	2.44E+05
Brine Flow into Repository	S2-BF	7.83E+04	6.62E+04	3.09E+05	2.51E+05
Brine Flow into Repository	S4-BF	5.88E+04	4.21E+04	3.11E+05	2.55E+05
Brine Flow into Repository	S6-BF	6.38E+04	4.96E+04	3.03E+05	2.38E+05
Brine Flow up Shaft [3]	S1-BF	3.73E+00	2.71E+00	3.60E+01	3.43E+01
Brine Flow up Shaft [3]	S2-BF	5.11E+00	5.13E+00	3.46E+01	2.96E+01
Brine Flow up Shaft [3]	S4-BF	3.64E+00	2.41E+00	3.42E+01	2.93E+01
Brine Flow up Shaft [3]	S6-BF	4.31E+00	3.89E+00	3.19E+01	2.93E+01
Brine Flow up Borehole [4]	S1-BF[5]	-	-	-	-
Brine Flow up Borehole [4]	S2-BF	4.44E+00	3.41E+00	5.55E+01	1.10E+01
Brine Flow up Borehole [4]	S4-BF	2.23E-01	4.53E-02	1.26E+01	1.91E+00
Brine Flow up Borehole [4]	S6-BF	1.46E+00	5.94E-01	4.70E+01	1.04E+01

Notes:

[1] Replicate 1 mean at 10,000 years.

[2] Maximum over all 100 Replicate 1 vectors at 10,000 years.

[3] As measured at the shaft intersection with Marker Bed 138.

[4] As measured at the borehole intersection with Marker Bed 138.

[5] "-" indicates "not applicable," as there is no borehole in the S1-BF scenario

PA-8.1.4 Culebra Flow

Groundwater flow in the Culebra is characterized by taking the ensemble average flow rate of each replicate set of 100 flow fields for each mining scenario (see Section PA-4.9 and Section PA-6.3.7). Flow fields from simulations without mining (no mining) are not directly considered in PA calculations but serve as input to the mining-modified (full and partial) flow fields.

Figure PA-73 shows the ensemble average of $\log_{10}$ flow rates within the LWB for no mining, as well as Replicate 1 full and partial mining for the CRA-2026 PA. Average flow magnitude is represented with the color scheme and direction of the average flow is given with arrows as unit vectors. Flow field results are identical to the RPPCR (Bethune 2023).

A portion of the boundary formed by the transition from calculated to specified head appears in the SE corner of the LWB (Figure PA-73; Figure PA-36). Observed T in the specified-head region east of the boundary is extremely low (Bowman et al. 2023). Accordingly, simulated flow magnitudes in most specified-head cells are essentially zero (i.e., within $\pm 10^{-10}$ of 0). Values within this tolerance are masked during plotting, so these cells appear as missing/blank in the

plots. However, the full mining scenario impacts flow such that some cells in the specified head region fall outside the tolerance and display small flow values.

Flow values span orders of magnitude within the plotted region. The most prominent feature in the no-mining flow is a pseudo-linear north-south high-transmissivity pathway located in the southern half of the domain, within X cell 130-140 and Y cell 160-180. This feature is documented in the calibrated T fields (Bowman et al. 2023). Without mining, flow is generally oriented toward the south (Wilgus and Bethune 2025, Section 8.2).

Full and partial mining scenario modifications create sharp flow-rate gradients at the edges of the affected areas. The edges lead to more variation in the mining-modified flow fields. In the partial mining case, where mining is assumed to occur only outside the LWB (Figure PA-38), the sharp flow gradients produce a quasi-rectangular shape just inside the periphery of the LWB. In the full mining case the sharp gradients form an irregular-shaped region.

Flow in the mining-modified cases is generally directed toward the south similar to no-mining flow results, except at the mining modification induced sharp flow-rate gradients, as seen in flow direction arrows and documented particle pathway behavior (Wilgus and Bethune 2025, Section 5.2).

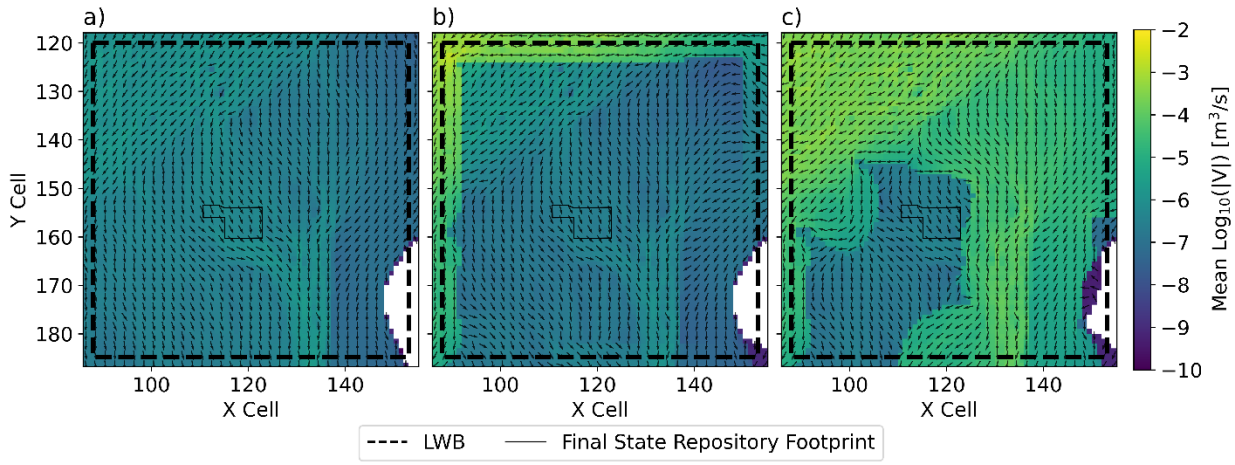


Figure PA-73. Ensemble mean flow for a) no mining, b) partial mining, and c) full mining. Arrows show ensemble mean flow direction as unit vectors.

PA-8.2 Radionuclide Transport

This section summarizes the radionuclide transport results for the disturbed repository scenarios. Day and King (2025) describe the brine and gas flow in the Salado. Detailed analyses of radionuclide transport in the Salado and of mobilized radionuclide concentrations in Salado and Castile brines are described by Docherty and Kim (2025). Appendix TFIELD and Wilgus and Bethune (2025) present analyses of the flow and radionuclide transport within the Culebra.

In the disturbed repository scenarios, radionuclide transport in the Salado is calculated by the code NUTS (see Section PA-6.3.2). Radionuclide transport from the Salado to the Culebra is calculated by NUTS and PANEL (see Section PA-6.3.2 and Section PA-6.3.3.3). Radionuclide transport within the Culebra is calculated by SECOTP2D (see Section PA-6.3.8). For all radionuclide transport calculations, mobilized concentrations of radionuclides in Salado and Castile brines are computed by the code PANEL (see Section PA-6.3.3.1).

PA-8.2.1 Radionuclide Mobilized Concentrations

The PANEL code assumes that the brine volume in the waste panels is constant over time. PANEL calculations account for the effects of decay and ingrowth on radionuclide concentrations. Radionuclides with the greatest mean (across all vectors) mobile concentration in 1x the minimum Castile brine volume are shown in Figure PA-74. The mean total radioactivity concentration in brine (used in the determination of DBRs) is also shown in Figure PA-74, labeled CDBR. Results for Salado brine exhibit the same qualitative temporal behavior and dominant radionuclides as those shown for Castile brine. Concentrations are expressed as EPA units/m^3 to combine the radioactivity of different isotopes. The mean total radioactivity concentration in brine at early times is dominated by ^{241}Am and at later times by ^{239}Pu. The mean total radioactivity concentration in brine increases for the CRA-2026 PA compared to the RPPCR PA, due to increased An(III) solubility and increased radionuclide inventory.

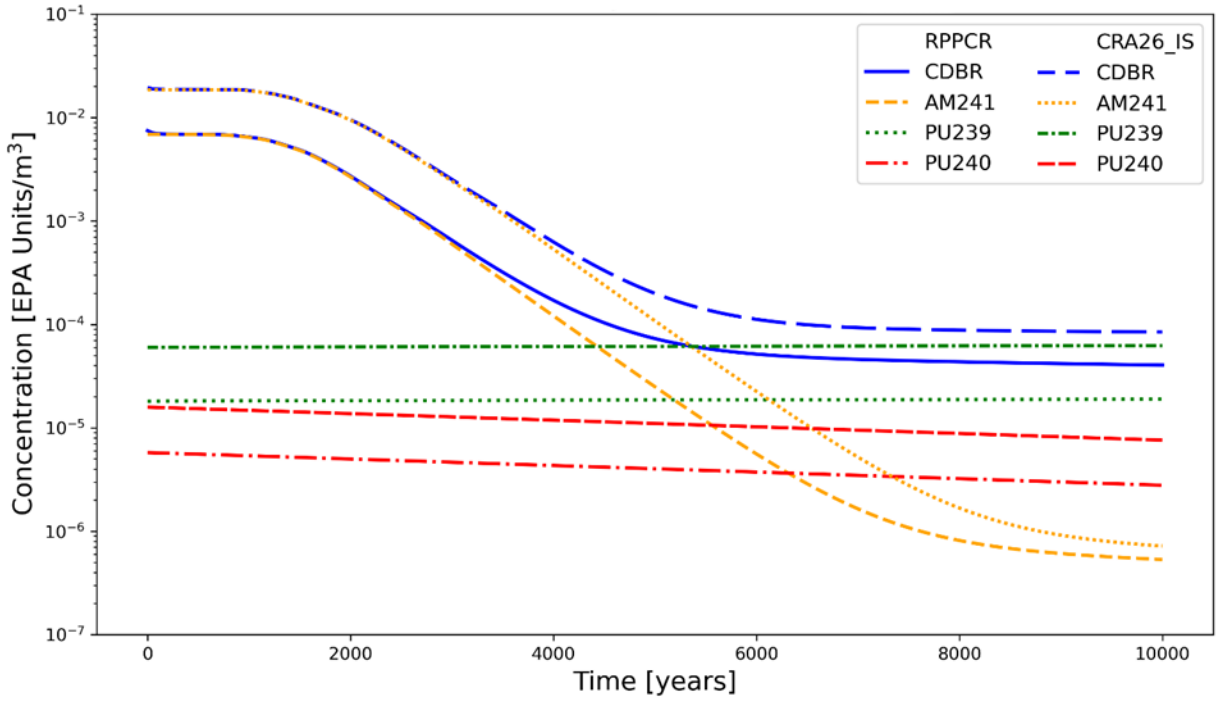


Figure PA-74. Mean Mobilized Radionuclide Concentrations vs. Time, Castile (ERDA-6) Brine

PA-8.2.2 Transport through MBs and Shaft

In the disturbed repository scenarios, none of the 300 realizations of the CRA-2026 PA resulted in releases through the marker beds that exceeded the screening limit (Docherty and Kim 2025). No realization showed transport of radionuclides through the shaft to the Culebra in the CRA-2026 PA.

PA-8.2.3 Transport to the Culebra

Radionuclide transport to the Culebra via a single intrusion borehole (disturbed scenarios S2-BF, S3-BF, S4-BF, and S5-BF) is modeled with the code NUTS (Section PA-4.4). Transport to the Culebra in the multiple-intrusion scenario (S6-BF) is modeled with the code PANEL (Section PA-4.5). A detailed discussion of radionuclide transport to the Culebra can be found in Docherty and Kim (2025).

Figure PA-75 illustrates the cumulative radionuclide discharge through the intrusion borehole for the disturbed repository scenarios S2-BF through S6-BF (there is no borehole for scenario S1-BF). Figure PA-76 illustrates the cumulative brine discharge up the borehole (see Section PA-8.1.3) for these scenarios. Because radionuclide solubilities are not correlated with volume of brine discharges, the results are mixed (i.e., small radionuclide releases may result for cases with higher solubilities or higher brine discharges).

Mean brine discharge is decreased in all intrusion scenarios in the CRA-2026 PA compared to the RPPCR PA. This reduction is attributed to lower brine pressures and saturations in the waste panels.

Overall, the mean radionuclide discharge is reduced in the single intrusion scenarios (S2-BF, S3-BF, S4-BF, and S5-BF). In these scenarios, the mean radionuclide discharge is primarily driven by the largest releases, which see similar decreases in the CRA-2026 PA compared to the RPPCR PA. This reflects the trend seen in the brine discharges. For the multi-intrusion scenario (S6-BF), the mean and maximum radionuclide discharges are slightly increased, though the median discharge is decreased.

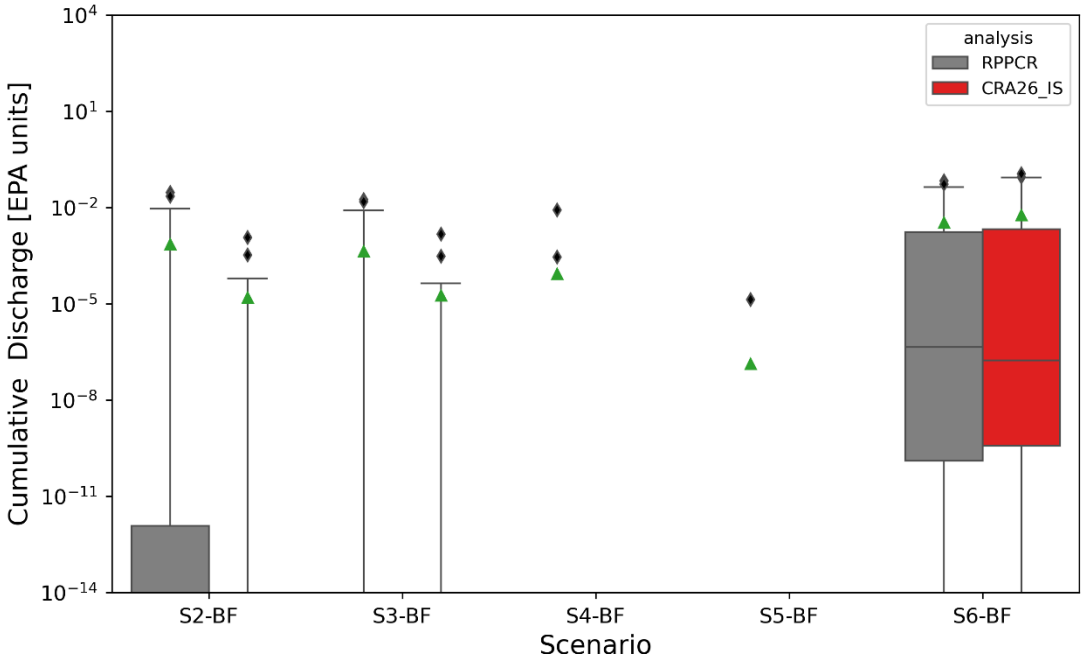


Figure PA-75. Cumulative Radionuclide Discharge to Culebra at 10,000 Years[4]

[4] These boxplots are used to facilitate visualizing and comparing distributions of results. The convention used in this section is that the "box" bottom and top edges indicate the 25th and 75th percentiles, the box interior line indicates the 50th percentile (median), and the triangle marker indicates the mean. The "whiskers" (the extended vertical lines with horizontal bars) indicate the 2nd and 98th percentiles, and the diamond markers exterior to the bars are discrete outliers (i.e., less than the 2nd percentile or greater than the 98th percentile).

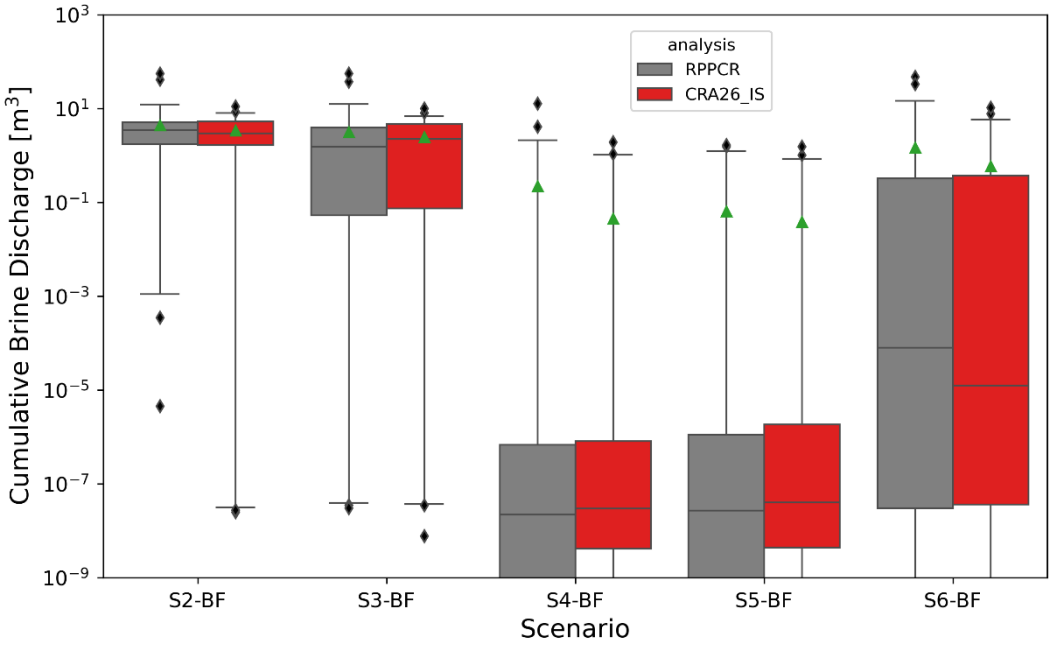


Figure PA-76. Cumulative Brine Discharge Up Borehole at 10,000 Years[4]

Docherty and Kim (2025) describe the cumulative radionuclide discharges for each lumped radionuclide across scenarios S2-BF through S6-BF, including horsetail plots of the full time series of cumulative radionuclide discharges to the Culebra. Notably, the U234L cumulative discharges have decreased in the CRA-2026 PA compared to the RPPCR PA, reflecting the reduced U(VI) baseline solubility, from 1×10^{-3} mol/L to 3×10^{-6} mol/L based on experimental recommendations (Kaplan et al. 2025).

PA-8.2.4 Transport through the Culebra

Radionuclide transport through the Culebra for a fixed source term is calculated with the code SECOTP2D (Section PA-6.3.8). Total release of radionuclides through the Culebra across the LWB for all intrusions in a future is calculated with the code CCDFGF (Section PA-6.5) by convolving the SECOTP2D results with the radionuclide transport to the Culebra calculated by NUTS (Section PA-6.3.2) and PANEL (Section PA-6.3.3.3). This section discusses the SECOTP2D results; total releases through the Culebra are presented in Section PA-9.4.

In each radionuclide transport simulation, 1 kg of each of four radionuclides (^{241}Am, ^{234}U, ^{230}Th, and ^{239}Pu) is released in the Culebra (see Section PA-4.10.1.5). For the CRA-2026 PA, there are two Culebra Release Point (CRP) locations (Wilgus and Brunell 2025). Culebra radionuclide transport calculations were performed for each CRP and both partial-mining and full-mining scenarios using the flow fields computed separately with the code MODFLOW6 (see Section PA-6.3.7). The flow fields are reused for each release point. Radionuclide transport of the ^{230}Th progeny of ^{234}U decay is calculated and tracked as a separate species. In the following

discussion, ^{230}Th refers to the ^{234}U progeny, and ^{23A}Th refers to the initial mass released at the CRP.

The CRA-2026 PA relocates CRP 2 (Section PA-1.3.18), which affects inputs to the SECOTP2D Culebra transport calculations (Section PA-6.3.8) and slightly alters results. The location change of CRP 2 is the only modification made in the CRA-2026 PA since the RPPCR PA that impacts Culebra transport results (Wilgus and Bethune 2025). Accordingly, the CRA-2026 PA results for CRP 1 are unchanged relative to the RPPCR.

Figure PA-77 and Figure PA-78 compare cumulative mass breakthrough beyond the LWB at 10,000 years for Replicate 1 of the CRA-2026 PA and the RPPCR PA. The number of vectors (counts) with cumulative releases greater than 10^{-9} kg is provided in each subplot. Results are shown on logarithmic axes. The gray dashed line is a 1:1 reference. A full set of replicate statistics is provided in Wilgus and Bethune (2025).

Under full and partial mining conditions, in both analyses ^{234}U has the greatest number of vectors that surpass the 10^{-9} kg criterion, while ^{241}Am has the fewest number of vectors. More vectors exceed the criterion in full-mining conditions than in partial-mining conditions, due to the extraction of the potash reserves within the LWB (Section PA-4.9.2).

The CRP 2 results show clustering around, and slightly above, the 1:1 reference line. This pattern indicates that vectors with mass breakthrough > 10^{-9} kg at 10,000 years are systematically biased toward higher mass released in the CRA-2026 PA compared to the RPPCR PA. This increase is attributed to the relocation of CRP 2 to the centroid of Panels 11 and 12 (Wilgus and Brunell 2025), which results in slightly shorter travel times to the LWB for radionuclides released at CRP 2.

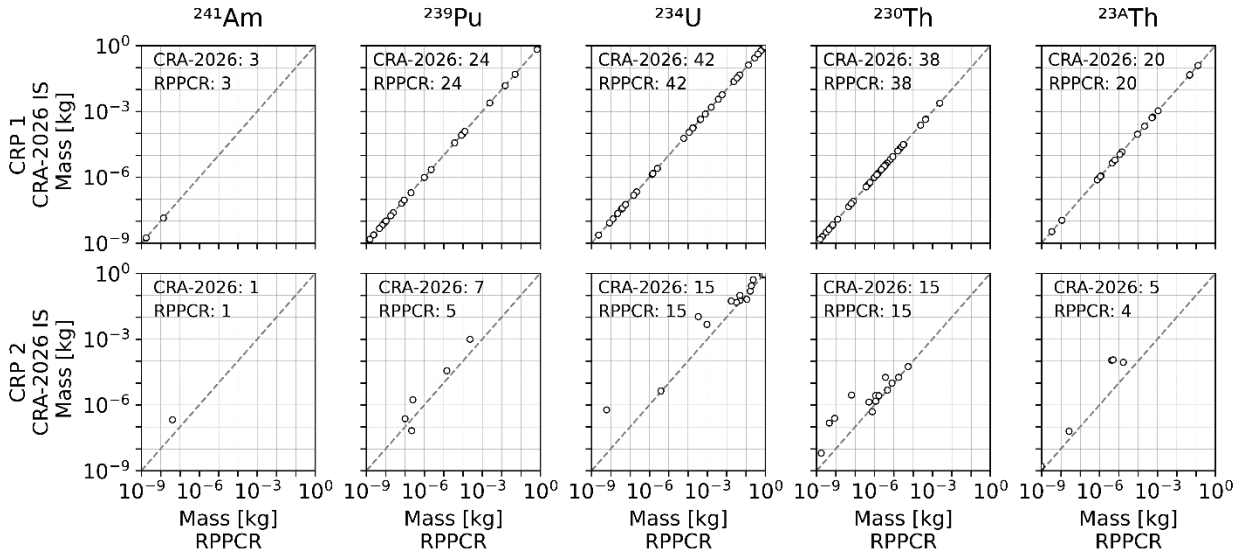


Figure PA-77. Mass Breakthrough by Release Point at 10,000-yr: Full Mining Scenario

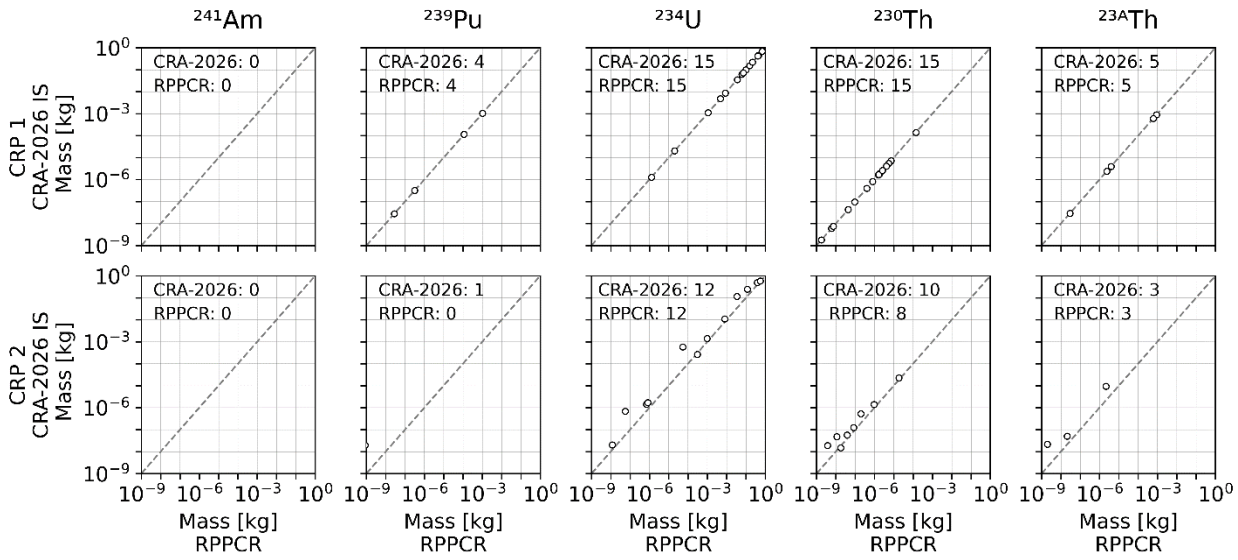


Figure PA-78. Mass Breakthrough by Release Point at 10,000-yr: Partial Mining Scenario

PA-8.3 Direct Releases

Direct releases occur at the time of a drilling intrusion and include cuttings and cavings, spallings, and DBRs. This section presents an analysis of the volume released by each mechanism, while Section PA-9.0 presents the normalized releases by each mechanism.

Brunell and Kicker (2025) provide additional information about the cuttings, cavings, and spallings releases calculated for the CRA-2026 PA. Zeitler (2025) provides a detailed analysis of DBRs in the CRA-2026 PA.

PA-8.3.1 Cuttings and Cavings

Cavings area results are consistent between the CRA-2026 PA and the RPPCR PA, as the input parameters affecting cavings calculations remain unchanged.

Cavings area statistics calculated in the CRA-2026 PA are shown in Table PA-27. The mean cavings area, mean non-zero cavings area, maximum cavings area, and the number of realizations without cavings are identical between the two analyses, reflecting the unchanged input parameters and methodology.

Table PA-27. CRA-2026 PA Cavings Area Statistics

Analysis	Mean Cavings Area (m^2)	Mean Non-Zero Cavings Area (m^2)	Maximum Cavings Area (m^2)	Number of Realizations Without Cavings
CRA-2026	0.011	0.021	0.110	49
RPPCR	0.011	0.021	0.110	49

PA-8.3.2 Spallings

A two-step procedure is used to calculate the volume of solid waste released to the surface due to spallings from a single drilling intrusion. The code DRSPALL computes spallings volumes for discrete repository pressures (10, 12, 14, and 14.8 MPa). These results are then used by CUTTINGS_S, which linearly interpolates between the DRSPALL results based on the repository pressure calculated by BRAGFLO.

The DRSPALL results generated for the CRA-2019 PA were also used in the RPPCR PA and the CRA-2026 PA. These results were produced by running DRSPALL for 100 vectors in each of three replicates at the specified pressure values (see Section PA-4.7.4). No spallings occurred at 10 MPa for any vector.

The uncertainty in spallings volumes arises from four uncertain variables in the DRSPALL calculations: waste permeability, waste porosity, waste tensile strength, and waste particle diameter after tensile failure (Table PA-13). Figure PA-79 indicates that the largest spallings volumes occur when waste permeability is less than 1.0×10^{-13} m^2, but larger permeability values result in a higher frequency of nonzero spallings volumes (Kicker et al. 2015). This observation can be explained as follows: higher permeability values result in lower tensile stresses and less tensile failure, but they also promote fluidization. Lower permeability leads to greater tensile stresses and tensile failure, but the failed material may not fluidize at this low permeability.

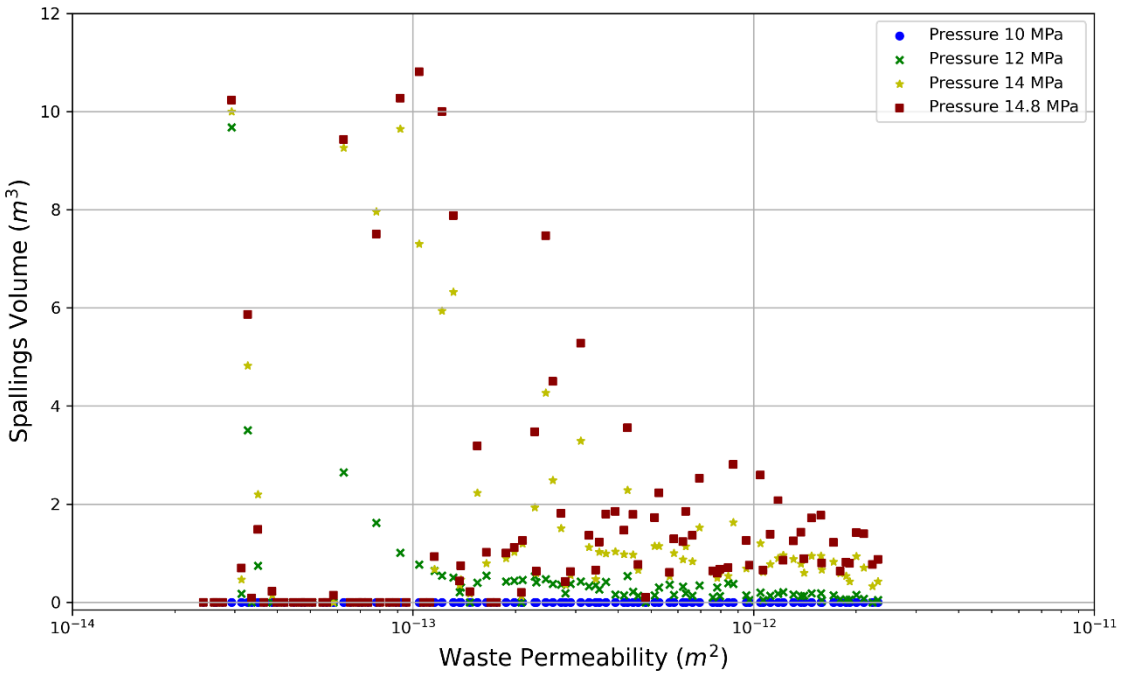


Figure PA-79. Scatterplot of Waste Permeability Versus Spallings Volume for Replicate 1

Smaller particle diameter values (see Figure PA-80) tend to result in larger spallings volumes and a higher frequency of nonzero spallings volumes. The uncertainty in the spallings volumes from a single intrusion is largely determined by the uncertainty in these two parameters. Obvious correlations between spallings volumes and the other two parameters could not be established.

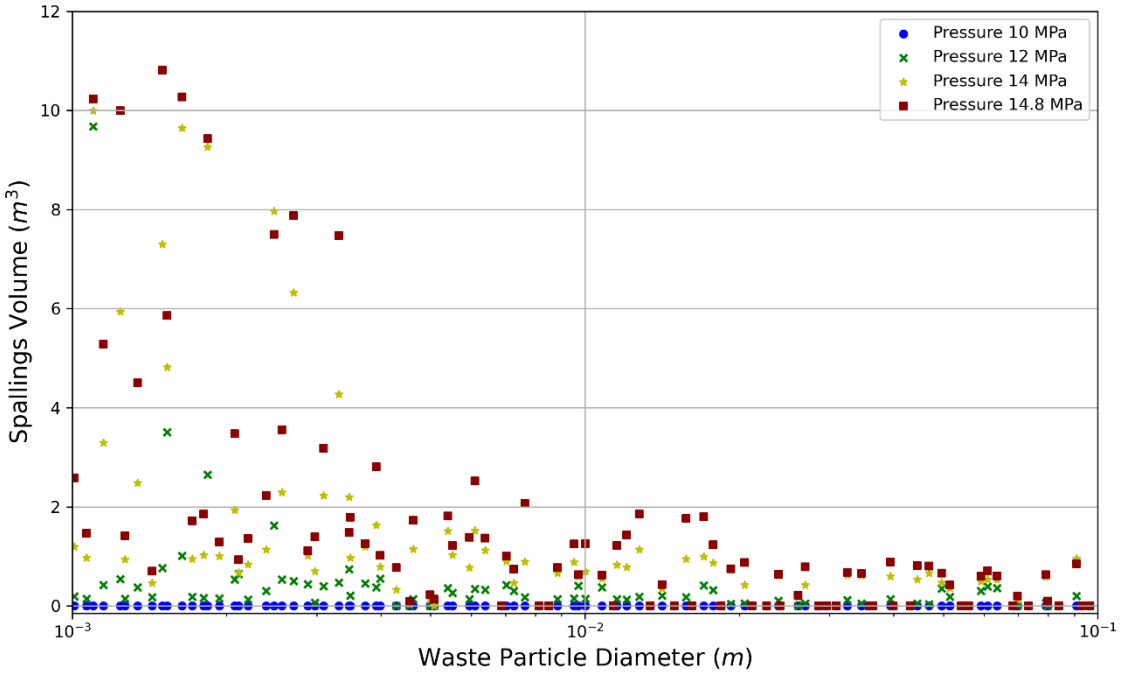


Figure PA-80. Scatterplot of Waste Particle Diameter Versus Spallings Volume for Replicate 1

Table PA-28 summarizes the statistics for spallings volumes in the RPPCR PA and the CRA-2026 PA. Statistics presented in these tables are assessed over all times and vectors by release scenario and drilling location.

The mean nonzero spallings release volume (averaged over all locations) for the CRA-2026 PA has increased for the previously undisturbed scenario (S1-DBR) by 17 percent compared to the RPPCR PA. For scenarios with E1 intrusions (S2-DBR and S3-DBR), the mean non-zero spallings release volumes (averaged over all locations) for the CRA-2026 PA have increased slightly, by 2 percent. For scenarios with E2 intrusions (S4-DBR and S5-DBR), the mean nonzero spallings release volumes (averaged over all locations) for the CRA-2026 PA have increased by 14 percent to 17 percent. Additionally, the percentage of realizations with nonzero spallings volumes (averaged over all locations) has increased for scenarios S2-DBR and S3-DBR but decreased for scenarios S1-DBR, S4-DBR, and S5-DBR.

Mean nonzero spallings volumes have increased slightly for all locations (averaged over all scenarios), with the largest increase observed in the Upper location (North RoR). The number of realizations with nonzero spallings volumes has decreased slightly for all locations and scenarios, with the most notable reduction occurring in the "Other" location (West RoR), where the percentage of realizations with nonzero volumes (averaged over all scenarios) decreased from 12.38% in the RPPCR PA to 9.50% in the CRA-2026 PA.

Table PA-28. Spallings Volume Statistics for Replicate 1

Direct Brine Release Scenario	Lower, Middle, Upper, Other Location	Mean Spallings Volume (m^3) RPPCR	Mean Spallings Volume (m^3) CRA-2026	Fraction of Sim. with Nonzero Releases RPPCR	Fraction of Sim. with Nonzero Releases CRA-2026	Mean of Non-zero Spallings Releases (m^3) RPPCR	Mean of Non-zero Spallings Releases (m^3) CRA-2026
S1-DBR	**All**	**0.24**	**0.24**	**13.83%**	**11.54%**	**1.76**	**2.06**
S1-DBR	L	0.28	0.28	15.67%	13.33%	1.80	2.13
S1-DBR	M	0.28	0.28	15.67%	13.33%	1.80	2.12
S1-DBR	U	0.27	0.27	14.00%	12.83%	1.90	2.09
S1-DBR	O	0.14	0.12	10.00%	6.67%	1.43	1.75
S2-DBR	**All**	**0.39**	**0.41**	**33.75%**	**34.80%**	**1.16**	**1.18**
S2-DBR	L	0.54	0.60	48.60%	50.60%	1.12	1.18
S2-DBR	M	0.54	0.59	48.20%	50.60%	1.12	1.17
S2-DBR	U	0.33	0.33	25.20%	26.60%	1.30	1.26
S2-DBR	O	0.15	0.12	13.00%	11.40%	1.18	1.08
S3-DBR	**All**	**0.36**	**0.38**	**33.25%**	**34.75%**	**1.08**	**1.10**
S3-DBR	L	0.44	0.51	45.20%	49.20%	0.98	1.04
S3-DBR	M	0.44	0.51	44.80%	49.20%	0.98	1.04
S3-DBR	U	0.37	0.36	27.60%	27.60%	1.32	1.29
S3-DBR	O	0.19	0.15	15.40%	13.00%	1.25	1.13
S4-DBR	**All**	**0.20**	**0.20**	**15.20%**	**13.15%**	**1.33**	**1.52**
S4-DBR	L	0.21	0.23	17.20%	15.00%	1.23	1.54
S4-DBR	M	0.21	0.23	17.20%	15.00%	1.22	1.53
S4-DBR	U	0.24	0.23	16.20%	14.80%	1.50	1.57
S4-DBR	O	0.15	0.11	10.20%	7.80%	1.43	1.36
S5-DBR	**All**	**0.28**	**0.28**	**18.85%**	**15.90%**	**1.48**	**1.73**
S5-DBR	L	0.30	0.32	20.80%	18.20%	1.43	1.76
S5-DBR	M	0.30	0.32	20.80%	18.20%	1.42	1.76
S5-DBR	U	0.33	0.32	20.00%	18.00%	1.66	1.76
S5-DBR	O	0.19	0.14	13.80%	9.20%	1.39	1.57
All Scenarios	**All Locations**	**0.29**	**0.30**	**22.63%**	**21.63%**	**1.30**	**1.38**
All	**L**	0.35	0.38	28.96%	28.65%	1.22	1.34
All	**M**	0.35	0.38	28.81%	28.65%	1.22	1.34
All	**U**	0.31	0.30	20.35%	19.69%	1.50	1.53
All	**O**	0.16	0.13	12.38%	9.50%	1.33	1.34

PA-8.3.3 Direct Brine Releases

A DBR to the surface can occur during or shortly after a drilling intrusion. For each vector, the code BRAGFLO calculates the volumes of brine released resulting in a total of 104 combinations of intrusion time, intrusion location, and initial conditions (see Section PA-6.3.6).

Summary statistics of the DBR volumes in the CRA-2026 PA are shown in Table PA-29. Statistics are assessed for Replicate 1 at all times, vectors, and drilling locations. As was also the case in the RPPCR PA, volumes that are less than 1×10^{-7} m^3 are considered inconsequential and are not included in the tally of vectors that result in DBR release volumes in the CRA-2026 .

Because the Salado flow pressures and saturations mapped into the DBR initial conditions differ from those in the RPPCR PA, non-zero DBR volumes occur less often and are smaller on average across scenarios and locations. This results in a lower mean DBR volume. While the frequency of small magnitude releases has decreased, large magnitude releases are more frequent (Figure PA-81), and maximum DBR volumes have increased, as evidenced by the outliers in Figure PA-82. Only 13.76 percent of modeled intrusions produce nonzero DBRs.

Lower intrusions continue to produce the largest average release volumes (Figure PA-83). Decreases in the Middle release volumes (averaged over all scenarios) result in Middle intrusions representing a smaller proportion of the total release volumes (Figure PA-33). Releases from the Upper and Other locations (averaged over all scenarios) have also decreased, both in frequency and magnitude.

The DBR volume analysis also revealed that at low panel saturations, DBR volumes are more sensitive to panel saturation than to panel pressure. Once saturation increases sufficiently to produce a brine-dominated flow regime, DBR volumes become primarily controlled by panel pressure, with panel saturation playing a secondary role.

Table PA-29. RPPCR and CRA-2026 PA DBR Volume Statistics

Statistics / Intrusion Location	Mean Brine Released (m^3)	Mean Brine Released (m^3)	Fraction of Simulations with Non-zero Releases	Fraction of Simulations with Non-zero Releases	Mean Non-zero Brine Release (m^3)	Mean Non-zero Brine Release (m^3)
	RPPCR	CRA-2026	RPPCR	CRA-2026	RPPCR	CRA-2026
S1-DBR	**0.67**	**0.30**	**8.96%**	**5.04%**	**7.48**	**6.05**
L	1.77	0.78	15.17%	9.67%	11.67	8.11
M	0.34	0.20	6.67%	3.67%	5.13	5.53
U	0.42	0.19	8.33%	4.83%	5.02	3.87
O	0.15	0.05	5.67%	2.00%	2.67	2.28
S2-DBR	**2.24**	**1.32**	**37.70%**	**27.75%**	**5.94**	**4.77**
L	5.73	3.66	74.60%	62.40%	7.67	5.87
M	2.45	1.20	55.60%	39.20%	4.41	3.06
U	0.59	0.33	13.80%	6.60%	4.25	5.06
O	0.19	0.10	6.80%	2.80%	2.73	3.57
S3-DBR	**1.40**	**0.69**	**33.30%**	**22.10%**	**4.21**	**3.13**
L	3.73	1.94	68.00%	51.00%	5.48	3.81
M	0.95	0.52	40.00%	27.20%	2.37	1.91
U	0.67	0.25	15.80%	6.80%	4.22	3.68
O	0.26	0.06	9.40%	3.40%	2.80	1.70
S4-DBR	**0.89**	**0.68**	**12.45%**	**7.75%**	**7.18**	**8.79**
L	2.02	1.76	18.40%	15.20%	10.97	11.55
M	0.79	0.52	12.60%	6.80%	6.29	7.65
U	0.58	0.35	12.00%	6.40%	4.86	5.44
O	0.18	0.10	6.80%	2.60%	2.69	3.84
S5-DBR	**1.18**	**0.70**	**14.90%**	**7.90%**	**7.91**	**8.88**
L	2.68	2.07	21.40%	15.20%	12.52	13.61
M	1.00	0.40	14.20%	6.60%	7.04	6.08
U	0.76	0.28	14.60%	6.40%	5.18	4.32
O	0.28	0.06	9.40%	3.40%	2.96	1.79
All Scenarios	-	-	-	-	-	-
L	**3.13**	**1.99**	**38.58%**	**29.88%**	**8.11**	**6.67**
M	**1.08**	**0.55**	**25.08%**	**16.19%**	**4.30**	**3.43**
U	**0.60**	**0.28**	**12.73%**	**6.15%**	**4.67**	**4.48**
O	**0.21**	**0.07**	**7.54%**	**2.81%**	**2.78**	**2.56**
ALL	**1.25**	**0.72**	**20.98%**	**13.76%**	**5.97**	**5.26**

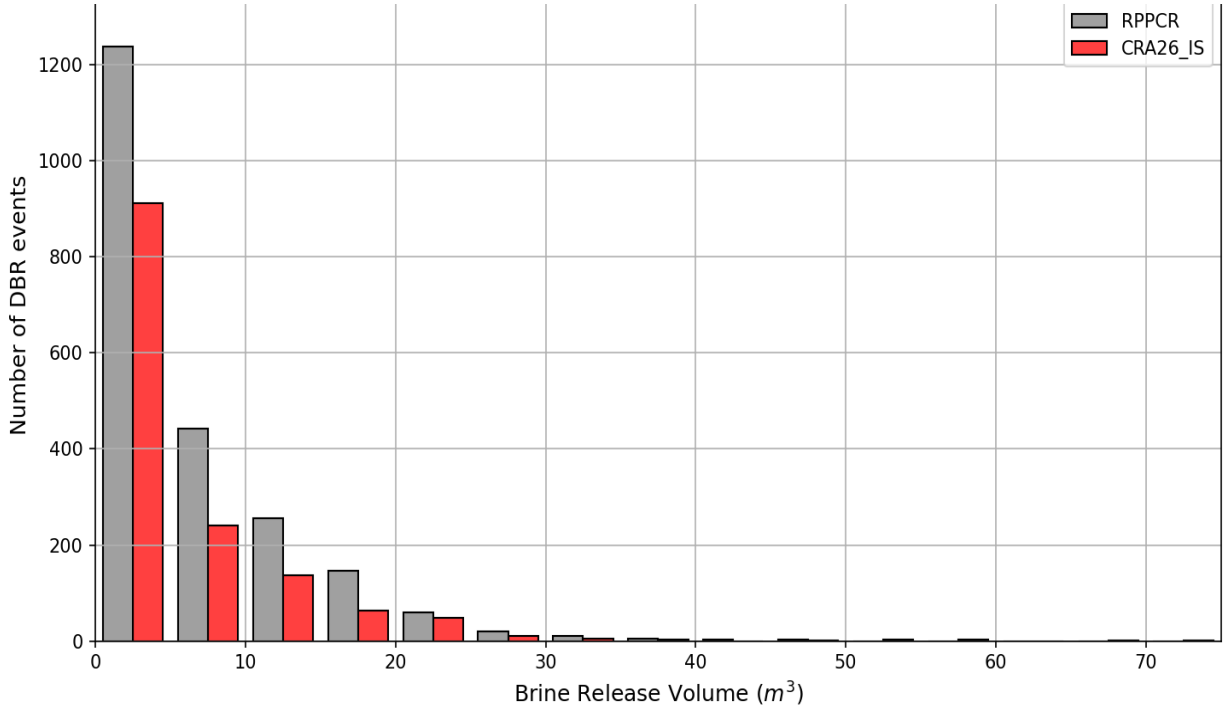


Figure PA-81. Release Volume Frequency, All Intrusions

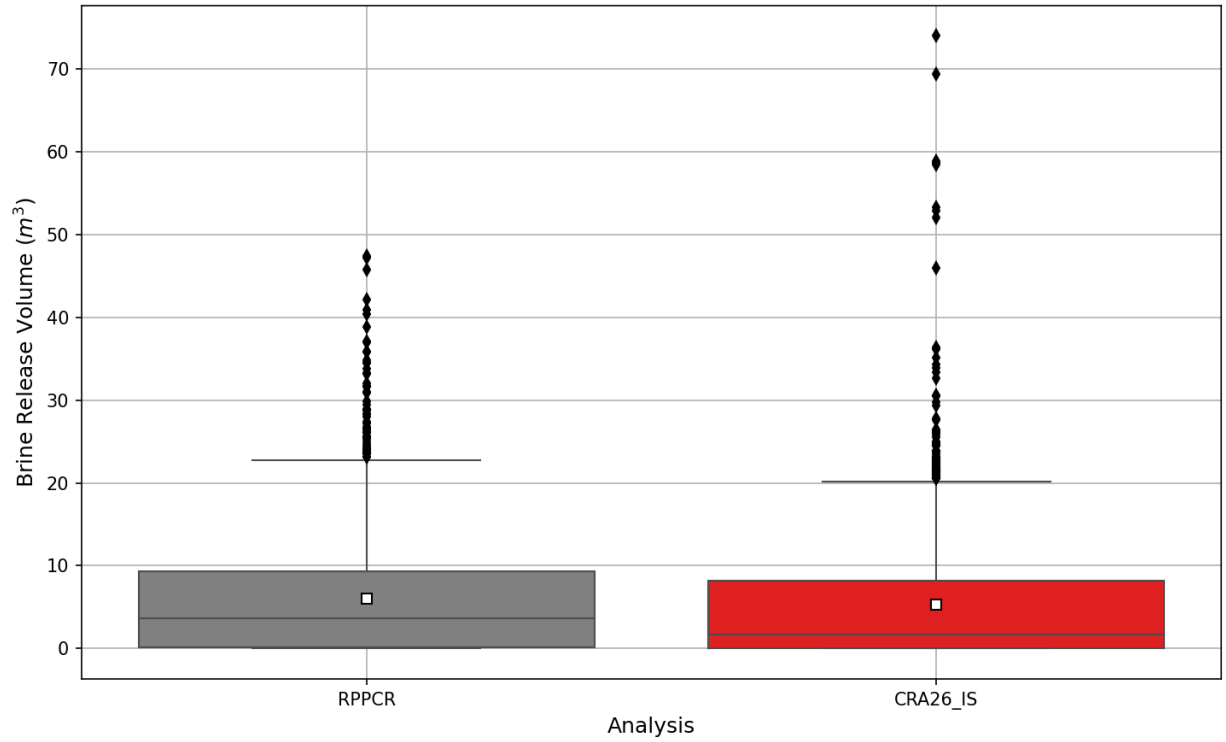


Figure PA-82. Release Volume Boxplots, All Nonzero Events[5]

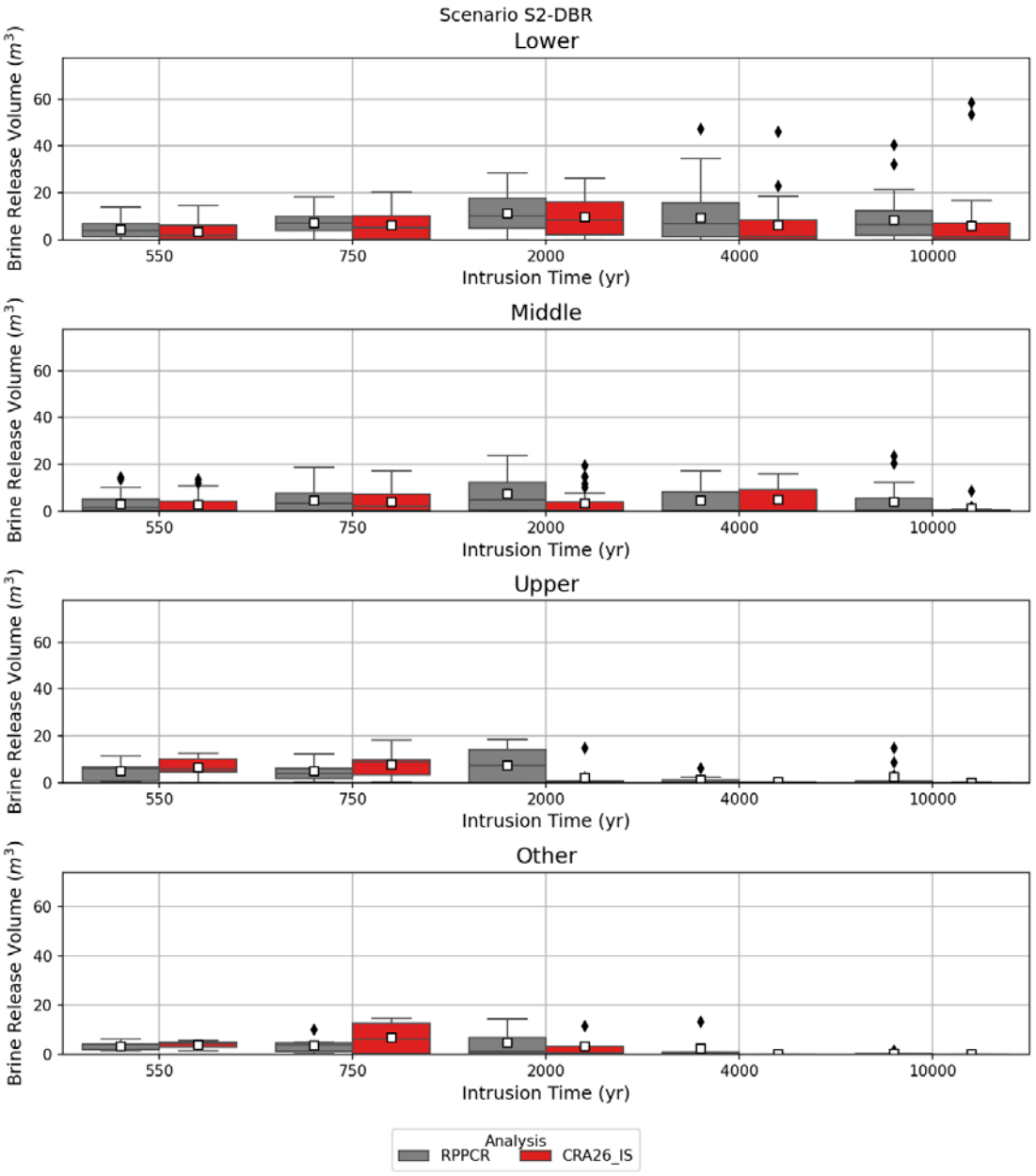


Figure PA-83. S2-DBR Release Volumes, All Intrusions[5]

[5] Boxplots are used to facilitate visualizing and comparing distributions of results. The convention used in this section is that the "box" bottom and top edges indicate the 25th and 75th percentiles, the box interior line indicates the 50th percentile (median), and the triangle marker indicates the mean. The "whiskers" (the extended vertical lines with horizontal bars) indicate 1.5 times the inner-quartile range and the diamond markers exterior to the bars are discrete outliers.

PA-9.0 Normalized Releases

The radioactive waste disposal regulations of 40 CFR Part 191, Subparts B and C, include containment requirements for radionuclides. Specifically, 40 CFR 191.13 requires that cumulative releases from a disposal system to the accessible environment over 10,000 years not exceed the containment limits specified for the probability levels defined in that section. Releases are expressed in EPA units using the radionuclide-specific release limits provided in Appendix A to Part 191, which serve as normalization factors for calculating total releases. As specified in 40 CFR 194.34, the results of performance assessment are presented as CCDFs of total normalized releases.

Releases from the CRA-2026 PA are influenced by the drilling frequency. While the increased drilling frequency leads to more potential intrusions, the smaller repository footprint of the CRA-2026 PA (12 panels) relative to the RPPCR PA (19 panels) reduces the total number of intrusions.

This section discusses each of the four categories of releases that constitute the total release: cuttings and cavings, spallings, DBRs, and transport releases, followed by the total normalized releases for the CRA-2026 PA. Results of the CRA-2026 PA are compared to results from the RPPCR PA (Brunell et al. 2024).

In summary, total mean releases, as well as mean releases by each release mechanism, have slightly increased for the CRA-2026 PA at all but the highest probabilities compared to the RPPCR PA (King et al. 2025). The exceptions to this trend are DBRs and transport releases. Specifically, DBRs decreased significantly at high probabilities and increased slightly at low probabilities for the CRA-2026 PA. Transport releases for the CRA-2026 PA decreased significantly across all probabilities. Total normalized releases for the CRA-2026 PA are therefore dominated by cuttings, cavings, and spallings at high probabilities (and relatively low consequence) and by DBRs and spallings at low probabilities (and relatively high consequence). Despite these shifts, the overall pattern of releases is similar to the RPPCR PA. Cuttings, cavings, spallings, and DBRs (albeit reduced) remain the most significant pathways for release of radioactive material to the land surface at high probabilities, while spallings and DBRs remain the most significant pathways at low probabilities. Contributions to total releases from Culebra transport are negligible in the CRA-2026 PA. The resulting CCDFs of total normalized releases for the CRA-2026 PA are within the regulatory limits defined in 40 CFR 191.13.

PA-9.1 Cuttings and Cavings

The CRA-2026 PA cuttings and cavings releases are presented in this section and compared to results obtained from the RPPCR PA. Cuttings and cavings releases depend on cuttings and cavings volumes and sampled waste stream concentrations. Figure PA-84 shows the 95 percent confidence limits of the overall mean CCDFs for cuttings and cavings for the CRA-2026 PA and the RPPCR PA.

As discussed in Brunell and Kicker (2025), the cuttings and cavings volumes for individual boreholes are unchanged between the CRA-2026 PA and the RPPCR. Total cuttings and cavings releases remain comparable between the CRA-2026 PA and the RPPCR PA due to the higher fraction of repository volume occupied by contact-handled waste (REFCON:FVW) in the CRA-2026 PA, despite the smaller repository footprint. CCDFs for cuttings and cavings releases show slightly higher releases at lower probabilities (P(R)<0.7) in the CRA-2026 PA compared to the RPPCR PA, driven primarily by increased radionuclide activity concentrations in the waste.

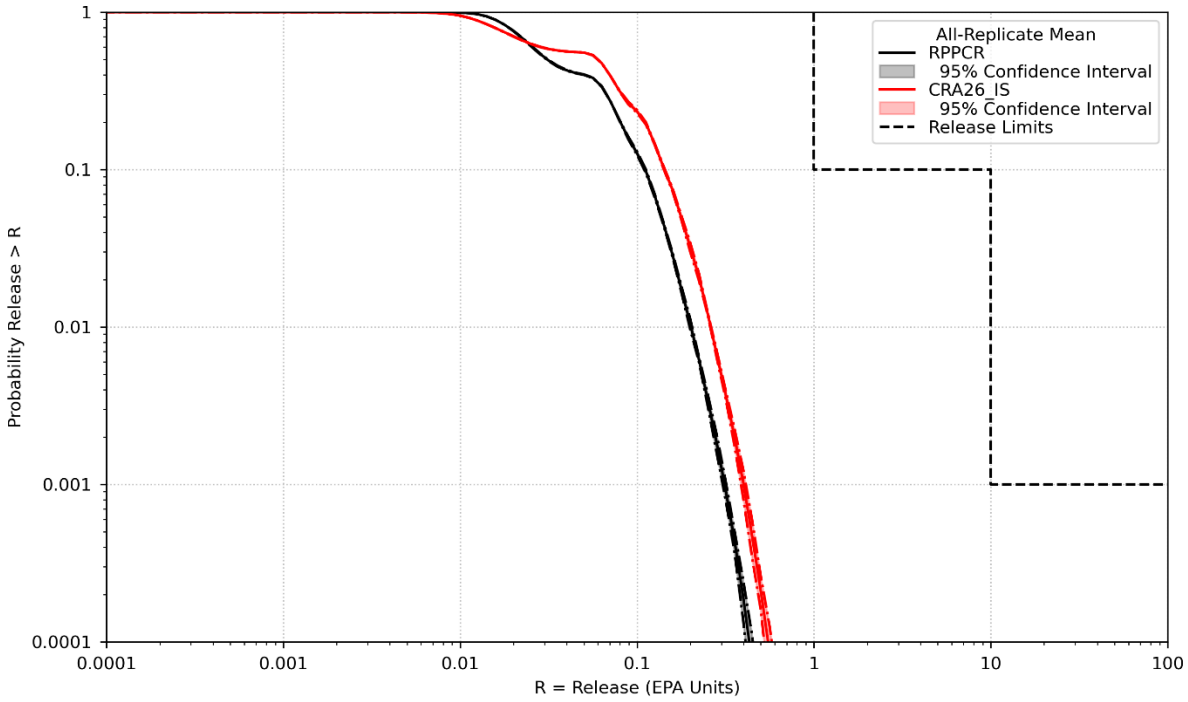


Figure PA-84. Overall Mean CCDFs for Cuttings and Cavings Releases with Confidence Limits

PA-9.2 Spallings

The CRA-2026 PA spallings releases are presented in this section and compared to the results obtained from the RPPCR PA. Figure PA-85 shows the 95 percent confidence limits of the overall mean CCDFs for spallings for the CRA-2026 PA and the RPPCR PA. The DRSPALL methodology used for the CRA-2026 PA is unchanged from the RPPCR PA, with no modifications to the DRSPALL inputs. Therefore, the differences in the spallings results in the plot shown here are not due to changes in the DRSPALL results.

Spallings releases are calculated based on spallings volumes and the average waste activity concentration in CH-TRU waste. Spallings volumes are a function of repository pressure at the time of intrusion, with higher pressures generally resulting in larger spall volumes. Total spallings release volumes in the CRA-2026 PA are comparable to those in RPPCR due to the

higher fraction of repository volume occupied by CH-TRU waste (REFCON:FVW, 0.279 for the CRA-2026 PA vs. 0.197 for the RPPCR PA).

Waste concentration in spallings is calculated as the CH-TRU waste stream volume-averaged concentration. The level of activity (in EPA units) in the CRA-2026 analysis is higher than in the RPPCR analysis due to increased radionuclide activity concentrations in the inventory. The increased radionuclide activity concentrations in the CRA-2026 inventory result in higher spallings releases at both compliance limit probabilities. An in-depth discussion of these changes and their effect on spallings releases is provided in King et al. (2025) and Brunell and Kicker (2025).

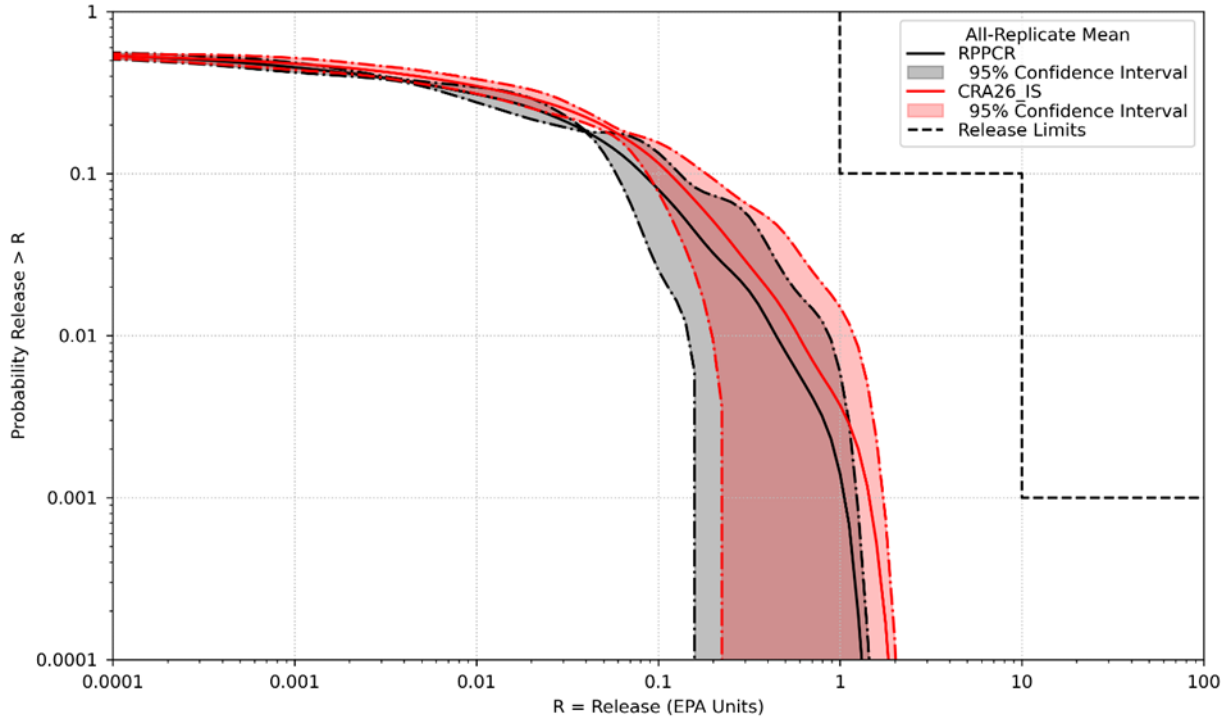


Figure PA-85. Overall Mean CCDFs for Spallings Releases with Confidence Limits

PA-9.3 Direct Brine

The CRA-2026 PA DBRs are presented in this section and compared to results obtained from the RPPCR PA. Figure PA-86 shows the 95 percent confidence limits about the overall mean CCDF for DBRs and compares the CRA-2026 PA results to those from the RPPCR PA. DBRs are calculated from DBR volumes and mobilized actinide concentrations in brine and are influenced by changes in repository conditions at the time of intrusion, as well as by the drilling frequency.

Although the drilling frequency in the CRA-2026 PA is increased from the RPPCR PA, the smaller repository footprint (12 vs. 19 panels) results in fewer intrusions overall. This reduction primarily affects the higher-probability portion of the CCDF, thereby decreasing the likelihood of any DBR. At lower probabilities, however, DBRs are influenced more strongly by the

magnitude of individual releases than by intrusion frequency. In this region of the CCDF, higher waste inventory and increased mobilized actinide concentrations in brine offset the reduction in intrusion frequency, resulting in DBR magnitudes that are comparable to or greater than those in the RPPCR PA.

In the CRA-2026 PA, the average DBR brine volumes decrease at higher probabilities (P(R) > 0.1) compared to the RPPCR and increase at lower probabilities (P(R) > 0.001). As described by Day and King (2025), the CRA-2026 Salado flow results show a decrease in mean brine pressure for scenarios without an E1 intrusion and an increase in mean brine pressure for scenarios with an E1 intrusion (except in the westernmost waste areas). Additionally, there is a substantial decrease in brine saturation across all waste areas and scenarios. These effects lead to mixed impacts on direct brine release volumes: reduced brine saturation decreases the frequency of non-zero DBR volumes, while increased maximum pressures for individual vectors contribute to larger-magnitude release volumes in certain scenarios (Zeitler 2025).

Additional changes from the RPPCR PA further affect direct brine releases in the CRA-2026 PA. The repository footprint is reduced from 19 panels to 12 panels, while radionuclide inventory and waste unit factor (WUF) values are increased. In addition, actinide solubility in the waste area is elevated due to changes in baseline solubility, solubility uncertainty, and colloid enhancement parameters (Docherty and Kim 2025). As shown in Section PA-8.2.1, these changes result in higher mobilized radionuclide concentrations in brine for CRA-2026 PA compared to the RPPCR PA.

Although the smaller repository footprint leads to fewer realized intrusions and a lower probability that any DBR occurs, the increased mobilized radionuclide concentrations result in larger releases when DBRs do occur. This combination of reduced frequency and increased consequence explains the increase in low-probability DBR releases observed in the CRA-2026 PA relative to the RPPCR PA.

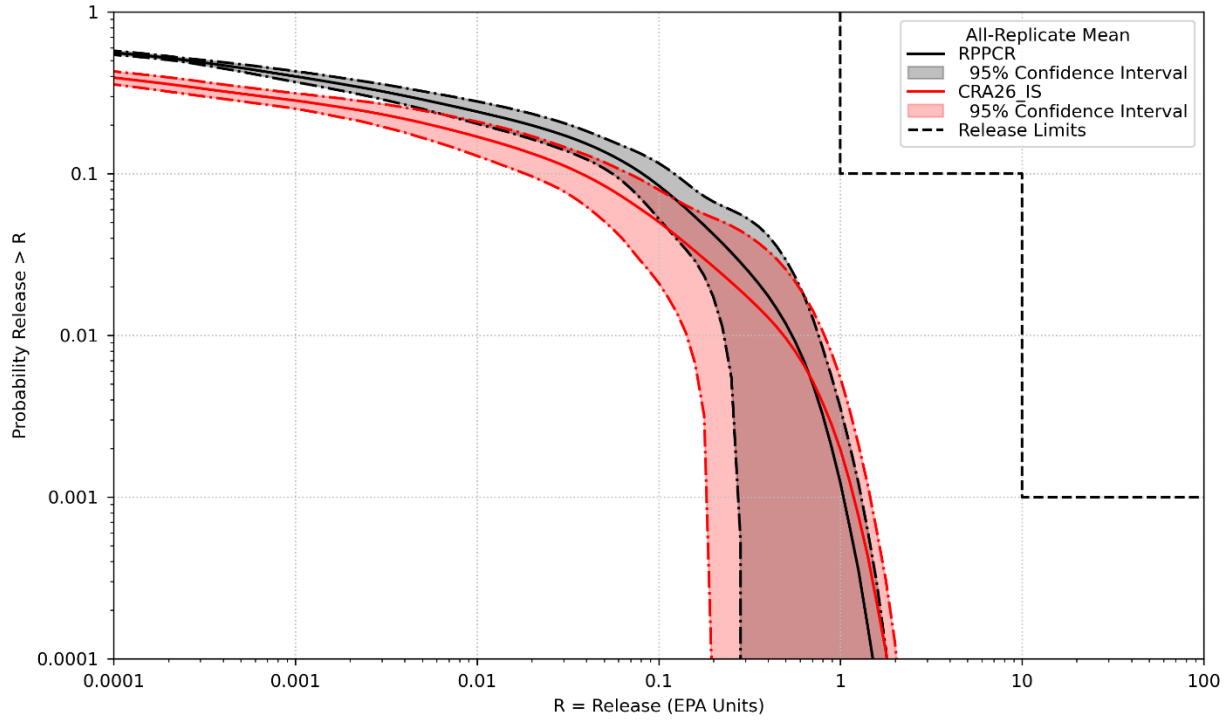


Figure PA-86. Overall Mean CCDFs for DBRs with Confidence Limits

PA-9.4 Groundwater Transport

The CRA-2026 PA normalized transport releases from the Culebra are presented in this section and compared to results obtained from the RPPCR PA. The CRA-2026 PA repository layout uses only the first and second Culebra release points (CRP 1 and CRP 2), as the interim state repository consists of 12 panels. In contrast, the RPPCR included four release points, with CRP 4 showing much higher releases due to westerly flow in the mining-impacted region. The exclusion of CRP 4 from the CRA-2026 PA significantly reduces the potential for radionuclide releases through the Culebra. The slight change in location for CRP 2 has little impact on radionuclide transport in the Culebra (Wilgus and Bethune 2025).

Releases from the Culebra are influenced by drilling frequency, brine flow up the borehole, radionuclide concentrations, and radionuclide transport in the Culebra. The overall mean releases from the Culebra, along with 95 percent confidence limits comparing the RPPCR PA and the CRA-2026 PA, are shown in Figure PA-87. Note that the CRA-2026 PA releases from the Culebra are below the axis limits and therefore do not show up in Figure PA-87.

Overall, the CRA-2026 PA results demonstrate that releases through the Culebra are negligible. Releases from the Culebra remain rare and insignificant compared to the other release mechanisms discussed above.

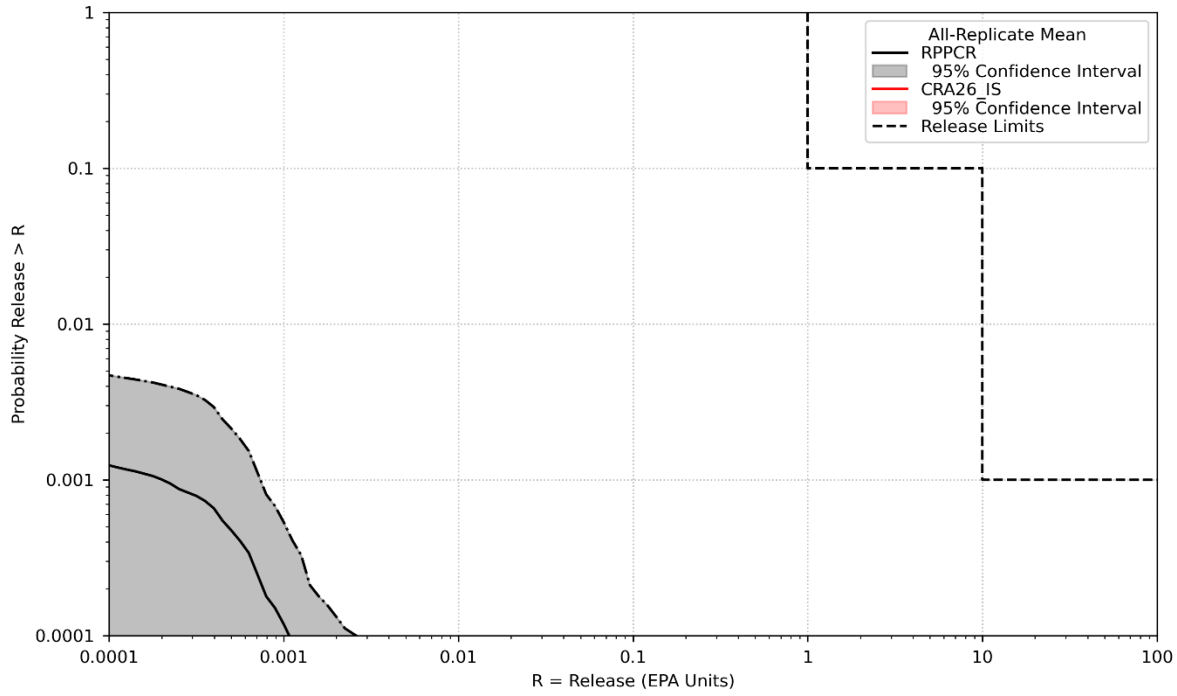


Figure PA-87. Mean CCDFs for Releases from the Culebra with Confidence Limits

PA-9.5 Total Normalized Releases

Total normalized releases are calculated by summing the releases from each intrusion across all intrusions in a future. Releases from an undisturbed repository are insignificant contributions to the total release. CCDFs for total releases obtained in Replicates 1, 2, and 3 of the CRA-2026 PA are plotted in Figure PA-88, Figure PA-89, and Figure PA-90.

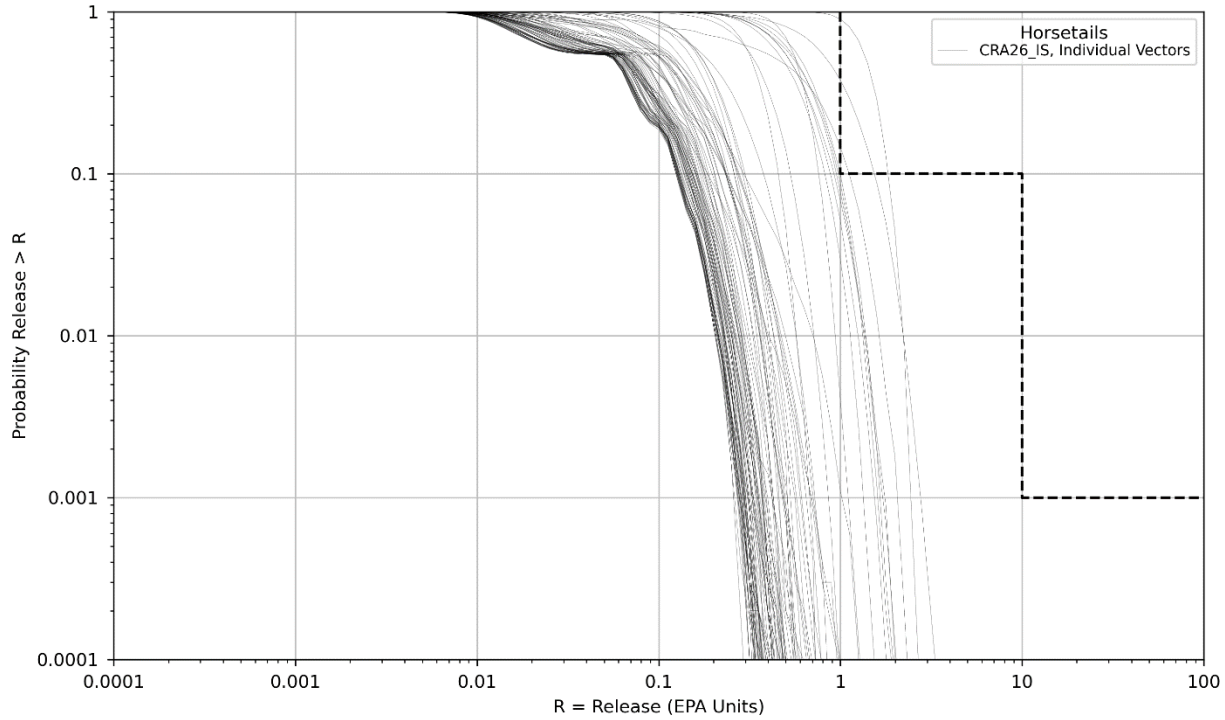


Figure PA-88. Total Normalized Releases, Replicate 1

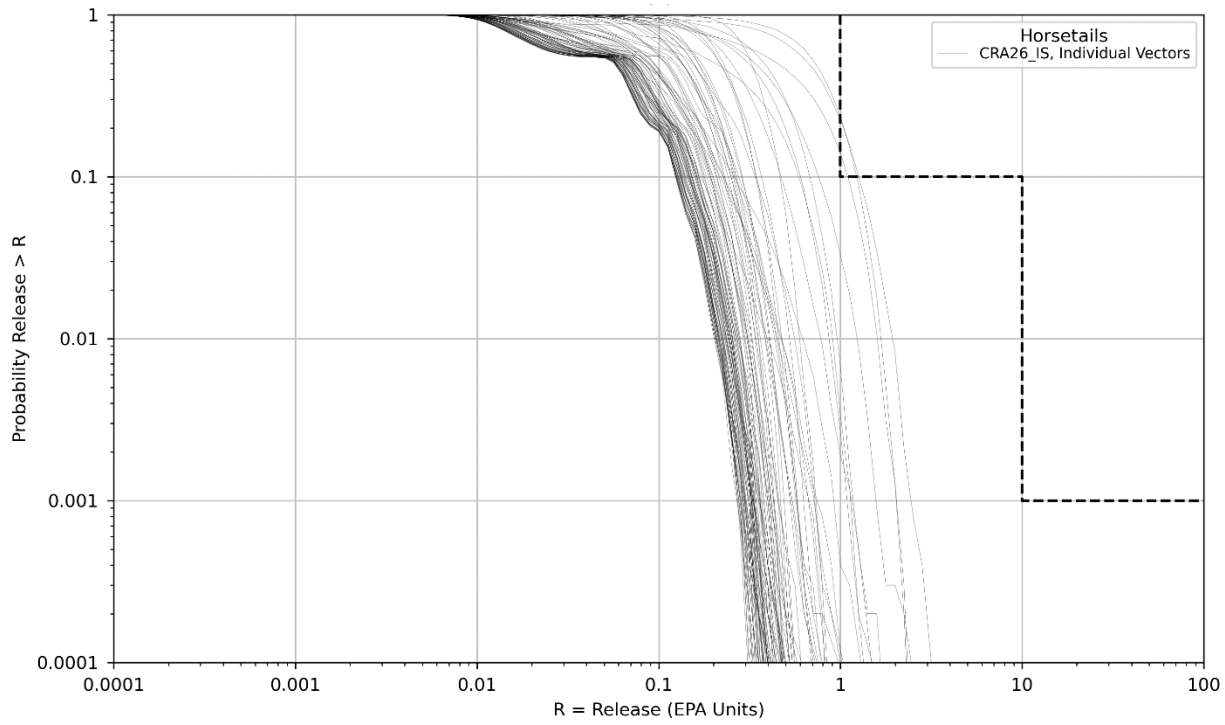


Figure PA-89. Total Normalized Releases, Replicate 2

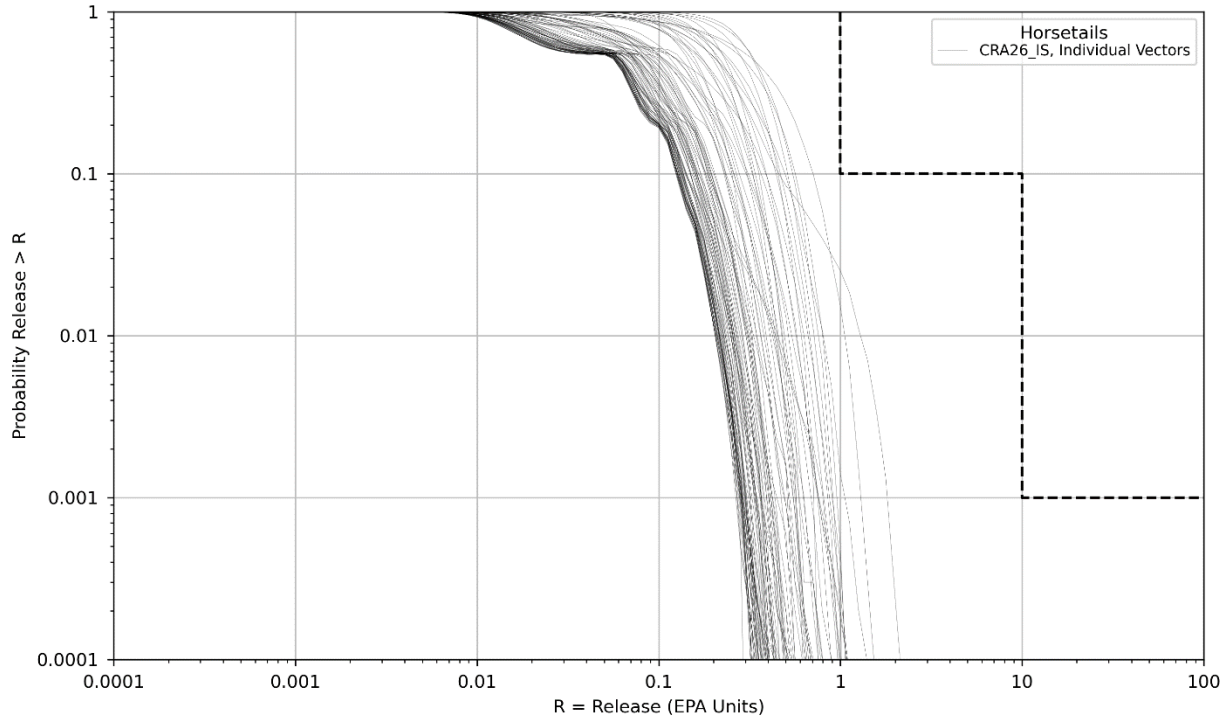


Figure PA-90. Total Normalized Releases, Replicate 3

Mean CCDFs for the release mechanisms that comprise total normalized releases are plotted together in Figure PA-91, along with the overall mean total release. Total normalized releases obtained in the CRA-2026 PA are dominated by cuttings, cavings, and spallings at high probability and by DBRs and spallings at low probability. Compared to the RPPCR PA, DBR contributions are significantly less at high probabilities and slightly more at low probabilities (Figure PA-86). Transport releases through the Culebra remain negligible. Overall, the dominant release mechanisms remain consistent with the RPPCR PA, though the relative contributions of DBRs and spallings have shifted.

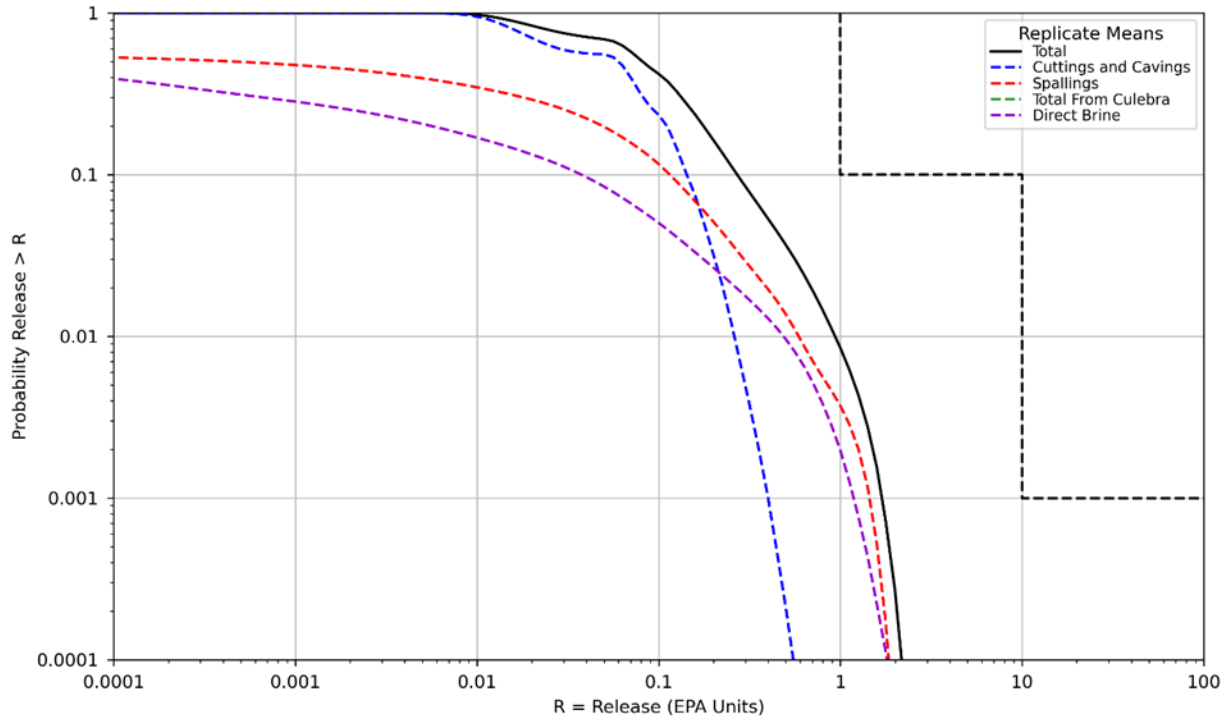


Figure PA-91. Comparison of CRA-2026 Overall Means for Release Components

The overall mean CCDF is computed as the arithmetic mean of the mean CCDFs from each replicate. To quantitatively determine the sufficiency of the sample size, a confidence interval is computed about the overall mean CCDF using the Student's t-distribution and the mean CCDFs from each replicate. Figure PA-92 shows the overall means with 95 percent confidence intervals about the overall means for the RPPCR PA and the CRA-2026 PA. Overall, total normalized releases increase slightly from the RPPCR PA to the CRA-2026 PA, primarily driven by increased contributions from cuttings, cavings, and spallings at the 0.1 probability and increased contributions from spallings and DBRs at the 0.001 probability.

The CCDF and confidence intervals lie below and to the left of the limits specified in 40 CFR 191.13(a). Table PA-30 compares statistics on the overall mean for total normalized releases obtained in the RPPCR PA and the CRA-2026 PA. At probabilities of 0.1 and 0.001, values obtained for the mean total release are slightly higher for the CRA-2026 PA than for the RPPCR PA, but are less than the limits specified in 40 CFR 191.13(a). Thus, the WIPP with the CRA-2026 repository configuration continues to comply with the containment requirements of Part 191.

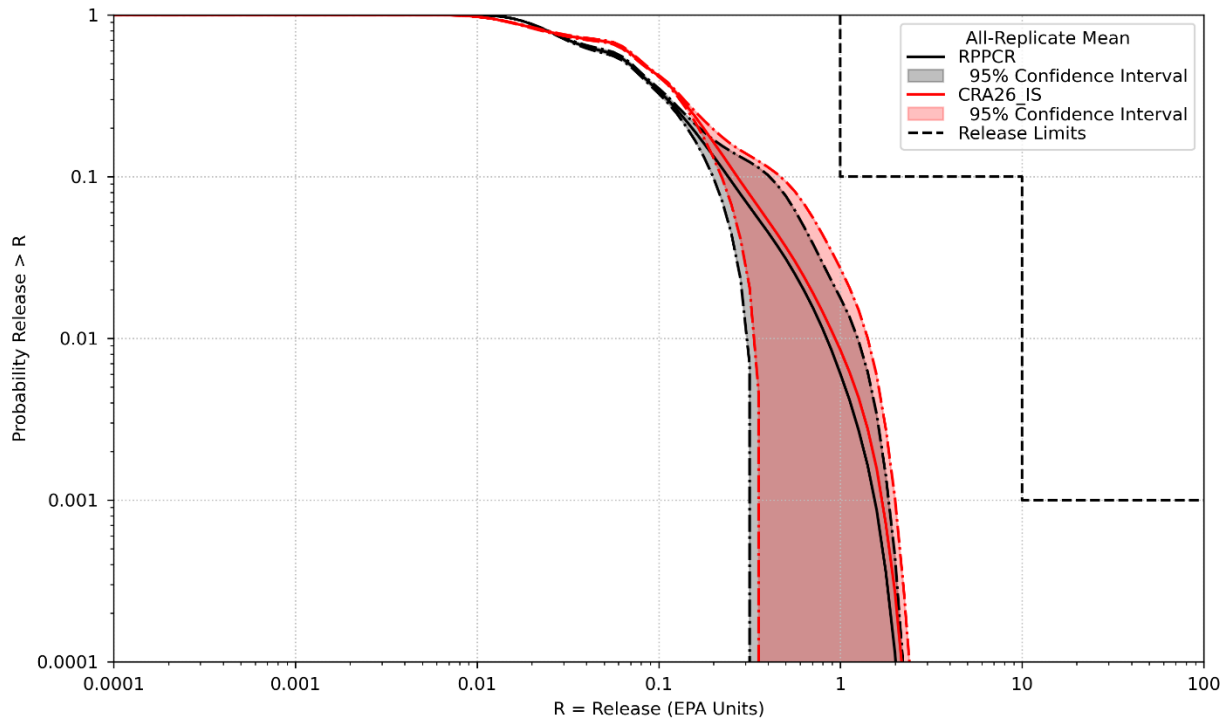


Figure PA-92. Overall Mean CCDFs for Total Normalized Releases with Confidence Limits

Table PA-30. RPPCR and CRA-2026 Statistics on the Overall Mean for Total Normalized Releases in EPA Units at Probabilities of 0.1 and 0.001

Analysis	P(R)>0.1 Lower CI (EPA Units)	P(R)>0.1 Mean (EPA Units)	P(R)>0.1 Upper CI (EPA Units)	P(R)>0.1 Release Limit (EPA Units)	P(R)>0.001 Lower CI (EPA Units)	P(R)>0.001 Mean (EPA Units)	P(R)>0.001 Upper CI (EPA Units)	P(R)>0.001 Release Limit (EPA Units)
RPPCR	0.1990	0.2418	0.4073	1	0.3360	1.5541	1.8716	10
CRA-2026	0.2219	0.2713	0.4679	1	0.3678	1.7121	2.0062	10

PA-9.6 Parameter Sensitivity Analysis

A stepwise linear multiple regression analysis was performed to determine the relative sensitivity of the calculated releases to the sampled parameters for the CRA-2026 PA, with comparisons made to the RPPCR PA (King et al. 2025). The sensitivity analysis is used to determine of which sampled parameters contribute most to the variability (uncertainty) observed in the mean releases by vector. The sensitivity of mean releases of each individual release mechanism, as well as total releases, to sampled parameters was analyzed.

The intact halite porosity (S_HALITE:POROSITY) parameter is the most dominant parameter contributing to variability in total releases across all three replicates. Its importance is driven by its correlation to the DRZ porosity and its role in controlling brine availability and repository pressure, which are critical factors influencing DBRs and spallings releases. The waste shear strength (BOREHOLE:TAUFAIL) parameter is the second-most dominant parameter for total releases, reflecting its impact on cavings releases. The particle diameter for disaggregated waste (SPALLMOD:PARTDIAM) parameter has increased in importance in the CRA-2026 PA due to its influence on spallings releases, which contribute more significantly to total releases compared to the RPPCR PA.

The initial brine pressure in the Castile brine reservoir (CASTILER:PRESSURE) parameter continues to be one of the more important parameters in terms of variability in total releases, due to its impact on DBRs. Among the other parameters, the inundated iron corrosion rate (STEEL:CORRMCO2) parameter remains an important driver of variability in DBRs. STEEL:CORRMCO2 is negatively correlated with DBRs—higher gas generation rates raise repository pressure, which lowers waste area saturations and decreases DBRs. Similarly, the probability of an intrusion hitting a brine reservoir in the Castile (GLOBAL:PBRINE) parameter remains impactful due to its role in determining the likelihood of additional flow of brine to the repository.

In the CRA 2026 PA, the solubility multiplier SOLMOD3:SOLVAR is less influential than before because spallings make up a larger portion of total releases compared to direct brine releases. Spallings releases are independent of actinide solubility, reducing the overall sensitivity of total releases to solubility-related parameters.

PA-9.7 Summary of Comparison with the RPPCR PA

In both the RPPCR PA and the CRA-2026 PA, mean total releases are dominated by direct releases: cuttings and cavings at high intrusion probabilities, and spallings and direct brine releases at lower probabilities. Releases from the Culebra, already small in the RPPCR PA, are further reduced in the CRA-2026 PA to a negligible level. In both PAs, mean total releases remain well below the regulatory limits of 40 CFR Part 191.

Mean total releases in the CRA-2026 PA are slightly higher than in the RPPCR PA. The primary drivers of this increase are higher spallings and direct brine releases. The primary changes from the RPPCR PA that contribute to the increase are inventory, drilling frequency, and repository footprint. The waste inventory incorporated in the CRA-2026 PA has higher activity concentrations and a greater proportion of long-lived radionuclides, which amplify spallings releases. Although the total waste volume is reduced relative to the RPPCR PA, waste density, expressed as waste volume per unit repository volume, has increased. The combined effect of the increased drilling frequency, reduced repository footprint, increased waste density, and inventory changes contributes to the slight increase in mean total releases relative to the RPPCR.

PA-10.0 References

(*Indicates a reference that has not been previously submitted.)

Abdul Khader, M.H., and H.S. Rao. 1974. Flow Through Annulus with Large Radial Clearance. American Society of Civil Engineers, Journal of the Hydraulics Division, vol. 100, no. HY1: 25–39.

Antoun, T., L. Seanman, D.R. Curran, G.I. Kanel, S.V. Razorenor, and A.V. Utkin. 2003. Spall Fracture. New York: Springer-Verlag.

Aronson, D.G. 1986. The Porous Medium Equation. Nonlinear Diffusion Problems. Lecture Notes in Mathematics 1224. New York: Springer-Verlag.

Aziz, K., and A. Settari. 1979. Petroleum Reservoir Simulation. New York: Elsevier.

Barree, R.D., and M.W. Conway. 1995. Experimental and Numerical Modeling of Convective Proppant Transport. Journal of Petroleum Technology, vol. 47 (March): 216–22.

Bateman, H. 1910. The Solution of a System of Differential Equations Occurring in the Theory of Radio-Active Transformations. Proceedings of the Cambridge Philosophical Society, vol. 15: 423–27.

Bean, J.E., M.E. Lord, D.A. McArthur, R.J. MacKinnon, J.D. Miller, and J.D. Schreiber. 1996. Analysis Package for the Salado Flow Calculations (Task 1) of the Performance Assessment Analysis Supporting the Compliance Certification Application (CCA). Albuquerque, NM: Sandia National Laboratories. EPA Air Docket A-93-02, Item II-G-08. ERMS 420238.

Bear, J. 1972. Dynamics of Fluids in Porous Media. New York: Dover.

Bear, J. 1979. Hydraulics of groundwater, McGraw-Hill series in water resources and environmental engineering. McGraw-Hill, New York.

Bear, J. and Bachmat, Y. 1990. Introduction to Modeling of Transport Phenomena in Porous Media. Kluwer Academic Publishers, Dordrecht, Netherlands.

Beauheim, R.L., and Holt, R.M. 1990. Hydrogeology of the WIPP site, in Powers, D.W., Holt, R.M., Beauheim, R.L., and Rempe, N., eds., Geological and Hydrological Studies of Evaporites in the Northern Delaware Basin for the Waste Isolation Pilot Plant (WIPP): Guidebook 14. Geological Society of America (Dallas Geological Society), p. 45-78. ERMS 246378

Belhaj, H.A., K.R. Agha, A.M. Nouri, S.D. Butt, H.F. Vaziri, and M.R. Islam. 2003. Numerical Simulation of Non-Darcy Flow Utilizing the New Forchheimer's Diffusivity Equation. SPE 81499. Paper presented at the SPE 13th Middle East Oil Show & Conference, Bahrain, April, 2003.

Berglund, J.W. 1992. Mechanisms Governing the Direct Removal of Wastes from the Waste Isolation Pilot Plant Repository Caused by Exploratory Drilling. Albuquerque, NM: Sandia National Laboratories. SAND92-7295.

Berglund, J.W. 1996. Analysis Package for the Cuttings and Spallings Calculations (Task 5 and 6) of the Performance Assessment Calculation Supporting the Compliance Certification Application (CCA), AP-015 and AP-016. Albuquerque, NM: Sandia National Laboratories. ERMS 240521.

Bethune, J. 2023. Culebra Flow and Transport Analysis Report for the Replacement Panels Planned Change Request (RPPCR). ERMS 579725. Carlsbad, NM: Sandia National Laboratories. *

Bilgen, E., R. Boulos, and A.C. Akgungor. 1973. Leakage and Frictional Characteristics of Turbulent Helical Flow In Fine Clearance. Journal of Fluids Engineering, Transactions of the ASME, Series I, vol. 95: 493–97.

Bollinger, M. 2024. Letter to Ms. L. Veal. Subject: Planned Change Request for the use of Replacement Panels 11 and 12. March 12, 2024. Carlsbad, NM: U.S. DOE, Carlsbad Field Office. CBFO:ERCD:MG:SV:24-0168. *

Bowman, D., R. Kushnereit, M. Pedrazas, P. Johnson, N. Deeds, and J. Pinkard. 2023. Analysis Report Documenting the Data, Generation, and Calibration of T-fields for CRA-2024. ERMS 579507. Carlsbad, NM: Sandia National Laboratories. *

Brill, J.P., and H.D. Beggs. 1986. Two-Phase Flow in Pipes. 5th ed. Tulsa: University of Tulsa.

Brooks, R.H., and A.T. Corey. 1964. Hydraulic Properties of Porous Media. Hydrology Paper No. 3. Fort Collins, CO: Colorado State University. ERMS 241117.

Brunell, S., J. Bethune, P. Docherty, D. Kicker, S. Kim, J. Long, and T. Zeitler. 2024. Summary Report for the 2023 Replacement Panels Planned Change Request Performance Assessment. Rev. 1. Carlsbad, NM: Sandia National Laboratories. ERMS 581044. *

Brunell, S. 2025. Update to CRA-2026 PA Input Parameters Due to Revised WIPP Repository Dimensions. Carlsbad, NM: Sandia National Laboratories. EIMS-0004799007. *

Brunell, S. and D.C. Kicker. 2025. Analysis Report for Cuttings, Cavings, and Spallings in the 2026 Compliance Recertification Application Performance Assessment: Interim State Repository. Revision 1. Carlsbad, NM: Sandia National Laboratories. *

Brunell, S., B. Day, P. Docherty, D. Kicker, S. Kim, S. King, J. Long, J. Wilgus, and T. Zeitler. 2025. Summary Report for the 2026 Compliance Recertification Application Performance Assessment: Interim State Repository. Rev. 0. Carlsbad, NM: Sandia National Laboratories. EIMS-0005119328. *

Brush, L.H., P.S. Domski and Y. Xiong. 2012. Analysis Plan for WIPP Near-Field Geochemical Process Modeling, Rev. 1. Carlsbad, NM: Sandia National Laboratories. ERMS 556960.

Camphouse, R.C., M. Gross, C. Herrick, D. Kicker, and B. Thompson. 2012. Recommendations and Justifications of Parameter Values for the Run-of-Mine Salt Panel Closure System Design Modeled in the PCS-2012 PA. Memo to WIPP Records Center dated May 3, 2012. Carlsbad, NM: Sandia National Laboratories. ERMS 557396.

Camphouse, R. 2013a. Analysis Package for Salado Flow Modeling Done in the 2014 Compliance Recertification Application Performance Assessment (CRA-2014 PA). Carlsbad, NM: Sandia National Laboratories. ERMS 559980.

Camphouse, R. 2013b. Analysis Plan for the 2014 WIPP Compliance Recertification Application Performance Assessment. Carlsbad, NM: Sandia National Laboratories. ERMS 559198.

Camphouse, R.C., D. Kicker, T. Kirchner, J. Long, B. Malama, and T. Zeitler. 2012a. Summary Report and Run Control for the 2012 WIPP Panel Closure System Performance Assessment. Carlsbad, NM: Sandia National Laboratories. ERMS 558365.

Camphouse, R.C., M. Gross, C. Herrick, D. Kicker, and B. Thompson. 2012b. Memorandum to WIPP Records Center. Subject: Recommendations and Justifications of Parameter Values for the Run-of-Mine Salt Panel Closure System Design Modeled in the PCS-2012 PA. May 3, 2012. Carlsbad, NM: Sandia National Laboratories. ERMS 557396.

Camphouse, R., D. Kicker, S. Kim, T. Kirchner, J. Long, B. Malama, T. Zeitler. 2013. Summary Report for the 2014 WIPP Compliance Recertification Application Performance Assessment. Carlsbad, NM: Sandia National Laboratories. ERMS 560252.

Chambre Syndicale de la Recherche et de la Production du Petrole et du Gaz Naturel. 1982. Drilling Mud and Cement Slurry Rheology Manual. English translation. Houston: Gulf Publishing.

Chappelear, J.E., and A.S. Williamson. 1981. Representing Wells in Numerical Reservoir Simulation: Part 2—Implementation. Society of Petroleum Engineers Journal, vol. 21: 339–44.

Cherimisinoff, N.P., and P.N. Cherimisinoff. 1984. Hydrodynamics of Gas-Solids Fluidization. Houston, TX: Gulf Publishing.

Christian-Frear, T.L. 1996. Salado Halite Permeability from Room Q Analysis. Albuquerque, NM: Sandia National Laboratories. ERMS 414996.

Clayton, D.J. 2008. Analysis Plan for the Performance Assessment for the 2009 Compliance Recertification Application (Revision 1). Carlsbad, NM: Sandia National Laboratories. AP-137. ERMS 547905

Corbet, T., and P. Swift. 1996a. Memorandum to M.S. Tierney. Subject: Distribution for Non-Salado Parameter for SECOFL2D: Climate Index. April 12, 1996. Albuquerque, NM: Sandia National Laboratories. ERMS 237465.

Corbet, T., and P. Swift. 1996b. Parameters Required for SECOFL2D: Climate Index. Record Package. Albuquerque, NM: Sandia National Laboratories. ERMS 417302.

Cranston, C.C. 2009. Minable Potash Ore. Carlsbad, NM: Bureau of Land Management. ERMS 551120.

Cranwell, R.M., R.V. Guzowski, J.E. Campbell, and N.R. Ortiz. 1990. Risk Methodology for Geologic Disposal of Radioactive Waste: Scenario Selection Procedure. Albuquerque, NM: Sandia National Laboratories. NUREG/CR-1667. SAND80-1429. ERMS 226750.

Darley, H.C.H. 1969. A Laboratory Investigation of Borehole Stability. JPT Journal of Petroleum Technology, July: 883–92.

Day, B. 2025. BRAGFLO Grid Development for CRA-2026. Carlsbad, NM: Sandia National Laboratories. EIMS-0004447000. *

Day, B. and S. King. 2025. Analysis Report for Salado Flow in the 2026 Compliance Recertification Application Performance Assessment: Interim State Repository. Carlsbad, NM: Sandia National Laboratories. EIMS-0004944216. *

Docherty, P. 2023a. Analysis Report for Modeling the Castile Pressurized Brine Reservoir. Rev. 0. Carlsbad, NM: Sandia national Laboratories. ERMS 578976. *

Docherty, P. 2023b. Impact Analysis for the Software Problem Report SPR 22-001 for PRELHS Version 2.45. Carlsbad, NM: Sandia National Laboratories. ERMS 578912. *

Docherty, P. and S. Kim. 2025. Analysis Report for Actinide Mobilization and Salado Transport in the 2026 Compliance Recertification Application Performance Assessment: Interim State Repository. Carlsbad, NM: Sandia National Laboratories. EIMS-0005110990. *

Domski, P.S. 2023. Uncertainty Analysis of Actinide Solubilities for the Replacement Panels Planned Change Request (RPPCR) Performance Assessment and the 2024 Compliance Recertification Application (CRA-2024). Carlsbad, NM: Sandia National Laboratories. ERMS 579529. *

Domski, P. 2025a. Prediction of Baseline Actinide Solubilities for the 2026 WIPP Compliance Recertification Application Performance Assessment Interim-State Analysis (CRA-2026 IS). Carlsbad, NM: Sandia National Laboratories. EIMS-0004838025. *

Domski, P. 2025b. Uncertainty Analysis of Actinide Solubilities for the 2026 Compliance Recertification Application (CRA-2026). Sandia National Laboratories. Albuquerque, NM. EIMS-0004446576. *

Domski, P. 2025c. Memo to Seth King. Subject: Th(IV), Np(V), and Am(III) Baseline Solubilities for the 2026 WIPP Compliance Recertification Application Performance Assessment Interim-State Analysis (CRA-2026 IS). June 30, 2025. Carlsbad, NM: Sandia National Laboratories. EIMS-0004833660. *

Draper and Smith, 1981. Applied Regression Analysis, Second Edition, John Wiley & Sons, New York, New York.

Ely, J.F., and M.L. Huber. 1992. NIST Thermophysical Properties of Hydrocarbon Mixtures Database (SUPERTRAPP), Version 1.0, User's Guide. Gaithersburg, MD: U.S. Department of Commerce, National Institute of Standards and Technology, Standard Reference Data Program. ERMS 242589.

Ergun, S. 1952. Fluid Flow Through Packed Columns. Chemical Engineering Progress, vol. 48: 89–94.

Falta, R., M. Hu, E. M. Kwicklis, C. I. Steefel, S. C. Williams-Stroud, and J. A. Thies. 2021. Additional Panels Performance Assessment (APPA) Changed Conceptual Models Peer Review Report. Carlsbad, NM: U.S. Department of Energy, Carlsbad Field Office. *

Feng, M. and D.C. Kicker. 2025a. Input Parameter Report for the 2026 Compliance Recertification Application Performance Assessment: Interim State Repository (CRA-2026 IS) Rev. 0. Carlsbad, NM: Sandia National Laboratories. EIMS- 0005148609. *

Feng, M. and D.C. Kicker. 2025b. Input Parameter Report for the 2026 Compliance Recertification Application Performance Assessment: Final State Repository (CRA-2026 FS) Rev. 2. Carlsbad, NM: Sandia National Laboratories. EIMS-0005148804. *

Fletcher, C.A.J. 1988. Computational Techniques for Fluid Dynamics. 2nd ed. Vols. 1 and 2. New York: Springer-Verlag.

Fox, R.W., and A.T. McDonald. 1985. Introduction to Fluid Mechanics. 3rd ed. New York: Wiley.

Frigaard, I.A., and N.L. Humphries. 1997. High Penetration Rates: Hazards and Well Control—A Case Study. Proceedings, March 1997 Society of Petroleum Engineers/International Association of Drilling Contractors Drilling Conference (SPE paper 37953). Amsterdam: Society of Petroleum Engineers.

Gatlin, C. 1960. Petroleum Engineering: Drilling and Well Completions. Englewood Cliffs, NJ: Prentice-Hall.

Gjerapic, G., J.L. Bean, E.N. Matteo, and M.B. Gross. 2023. Analyses to Bound the Permeability of Degraded Fill Materials in Intrusion Boreholes for WIPP Performance Assessment. Carlsbad, NM: Salado Isolation Mining Contractors, LLC. ERMS 579102. *

Graboski, M.S., and T.E. Daubert. 1979. A Modified Soave Equation of State for Phase Equilibrium Calculations: 3: Systems Containing Hydrogen. Industrial and Engineering Chemistry Process Design and Development, vol. 18: 300–06.

Gross, M. and G. Gjerapic. 2022. Analysis to Bound Brine Reservoir Volumes for WIPP Performance Assessment. Rev. 02. Carlsbad, NM: Nuclear Waste Partnership, LLC. *

Hansen, C. 2021. Review of Conceptual Models for the Additional Panels Performance Assessment. Carlsbad, NM: Sandia National Laboratories. ERMS 575130. *

Hansen, C., S. Brunell, B. Day, S. King, and J. Wilgus. 2025. Analysis Plan for the 2026 WIPP Compliance Recertification Application Performance Assessment. AP-214. Carlsbad, NM: Sandia National Laboratories. *

Hansen, F.D., M.K. Knowles, T.W. Thompson, M. Gross, J.D. McLennan, and J.F. Schatz. 1997. Description and Evaluation of a Mechanistically Based Conceptual Model for Spall. Albuquerque, NM: Sandia National Laboratories. SAND97-1369.

Hansen, F.D., T.W. Pfeifle, and D.L. Lord. 2003. Parameter Justification Report for DRSPALL. Carlsbad, NM: Sandia National Laboratories. ERMS 531057.

Hart, D., R. Holt, and S. McKenna. 2008. Analysis Report for Task 5 of AP-114: Generation of Revised Base Transmissivity Fields. ERMS 552391. Carlsbad, NM: Sandia National laboratories.

Hart, D., R. Beauheim, and S. McKenna. 2009. Analysis Report for Task 7 of AP-114: Calibration of Culebra Transmissivity Fields. ERMS 552391. Carlsbad, NM: Sandia National Laboratories.

Helton, J.C., J.D. Johnson, M.D. McKay, A.W. Shiver, and J.L. Sprung. 1995. Robustness of an Uncertainty and Sensitivity Analysis of Early Exposure Results with the MACCS Reactor Accident Consequence Model. Reliability Engineering and System Safety, vol. 48, no. 2: 129–48.

Helton, J.C., J.E. Bean, J.W. Berglund, F.J. Davis, K. Economy, J.W. Garner, J.D. Johnson, R.J. MacKinnon, J. Miller, D.G. O'Brien, J.L. Ramsey, J.D. Schreiber, A. Shinta, L.N. Smith, D.M. Stoelzel, C. Stockman, and P. Vaughn. 1998. Uncertainty and Sensitivity Analysis Results Obtained in the 1996 Performance Assessment for the Waste Isolation Pilot Plant. Albuquerque, NM: Sandia National Laboratories. SAND98-0365.

Helton, J.C., and F.J. Davis. 2003. Latin Hypercube Sampling and the Propagation of Uncertainty in Analyses of Complex Systems. Reliability Engineering and System Safety. Vol. 81, no. 1: 23–69.

Hirsch, C. 1988. Numerical Computation of Internal and External Flows. Fundamentals of Numerical Discretization. Vol. 1. Chichister, UK: John Wiley & Sons.

Holt, R.M. 1997. Conceptual Model for Transport Processes in the Culebra Dolomite Member of the Rustler Formation. Albuquerque, NM: Sandia National Laboratories. SAND97-0194. *

Howard, B.A. 1996. Memorandum to Sandia National Laboratories. Subject: Performance Assessment Parameter Input. February 23, 1996. Carlsbad, NM: Westinghouse Electric Corporation. ERMS 247595.

Howarth, S.M., and T. Christian-Frear. 1997. Porosity, Single-Phase Permeability, and Capillary Pressure Data from Preliminary Laboratory Experiments on Selected Samples from Marker Bed 139 at the Waste Isolation Pilot Plant. Albuquerque, NM: Sandia National Laboratories. SAND94-0472/1/2/3.

Hunter, R.L. 1985. A Regional Water Balance for the Waste Isolation Pilot Plant (WIPP) Site and Surrounding Area. Albuquerque, NM: Sandia National Laboratories. SAND84-2233.

Huyakorn, P.S., B.H. Lester, and J.W. Mercer. 1983. An Efficient Finite Element Technique for Modelling Transport in Fractured Porous Media: 1. Single Species Transport. Water Resources Research, vol. 19: 841–54.

Iman, R.L. 1982. Statistical Methods for Including Uncertainties Associated with the Geologic Isolation of Radioactive Waste Which Allow for a Comparison with Licensing Criteria. Proceedings of the Symposium on Uncertainties Associated with the Regulation of the Geologic Disposal of High-Level Radioactive Waste, March 9-13, 1981 (pp. 145–57). Ed. D.C.

Iman, R.L. and W.J. Conover. 1982. A Distribution-Free Approach to Inducing Rank Correlation Among Input Variates. Communications in Statistics, B11(3), 311-334. *

Iman, R.L., and J.C. Helton. 1988. An Investigation of Uncertainty and Sensitivity Analysis Techniques for Computer Models. Risk Analysis, vol. 8: 71–90.

Iman, R.L., and J.C. Helton. 1991. The Repeatability of Uncertainty and Sensitivity Analyses for Complex Probabilistic Risk Assessments. Risk Analysis, vol. 11: 591–606.

Jaeger, J.C. and N.G.W. Cook. 1969. Fundamentals of Rock Mechanics, Chapman and Hall Ltd., London, England.

James, S.J., and J. Stein. 2003. Analysis Report for the Development of a Simplified Shaft Seal Model for the WIPP Performance Assessment (Rev 1). Carlsbad, NM: Sandia National Laboratories. ERMS 525203.

Kaplan, U., Swanson, J., and Kutahyali-Aslani, C. 2025. LANL ACRSP Parameter Recommendations for CRA-2026 Performance Assessment. Revision 1. Carlsbad, NM: Los Alamos National Laboratory. LCO-ACP-41. *

Kaufmann, D.W., ed. 1960. Sodium Chloride: The Production and Properties of Salt and Brine. American Chemical Society Monograph 145. New York: Reinhold.

Kicker, D. 2025. Analysis Report for Radionuclide Inventory Screening in the 2026 Compliance Recertification Application Performance Assessment: Interim State Repository. Revision 0. Carlsbad, NM: Sandia National Laboratories. EIMS-0004832100. *

Kicker, D.C., C. Herrick, and T. Zeitler. 2015. Impact of the DRSPALL Modification on Waste Isolation Pilot Plant Performance Assessment Calculations. Carlsbad, NM: Sandia National Laboratories. ERMS 564863.

Kim, S. and D. Kicker. 2025. Analysis Report for Inventory EPA Units in the 2026 Compliance Recertification Application Performance Assessment: Interim State Repository. Revision 1. Carlsbad, NM: Sandia National Laboratories. EIMS-0004940556. *

King, S. 2021a. Methodology for Calculating Initial Waste Area Pressure in the Salado Flow Calculation. Carlsbad, NM: Sandia National Laboratories. ERMS 576464. *

King, S. 2021b. Recalculating of Iron Surface Area for Iron Corrosion in the WIPP PA Calculation. Carlsbad, NM: Sandia National Laboratories. ERMS 576428. *

King, S. 2025a. Area for RH waste disposal for the interim state CRA-2026 PA calculation. Carlsbad, NM: Sandia National Laboratories. EIMS-0004801801. *

King, S. 2025b. Constructed Cumulative Distributions for Approximation of Truncated Normal Distributions. Carlsbad, NM: Sandia National Laboratories. EIMS-0004799476. *

King, S. 2025c. Drilling Rate and Plugging Pattern Probabilities for the CRA-2026 PA Calculations. Carlsbad, NM: Sandia National Laboratories. EIMS-0004437345. *

King, S. 2026. Probabilities of Waste Stream Intersections in the CRA-2026 PA Calculations. Carlsbad, NM: Sandia National Laboratories. *

King, S. and T. Zeitler. 2025. Analysis Report for Parameter Sampling in the 2026 Compliance Recertification Application Performance Assessment. Carlsbad, NM: Sandia National Laboratories. EIMS-0004951492. *

King, S., S. Brunell, and T. Zeitler. 2025. Analysis Report for Normalized Releases in the 2026 Compliance Recertification Application Performance Assessment: Interim State Repository. Carlsbad, NM: Sandia National Laboratories. EIMS-0005040307. *

Kirchner, T., A. Gilkey, and J. Long. 2015. Addendum to the Summary Report on the Migration of the WIPP PA Codes. Carlsbad, NM: Sandia National Laboratories. ERMS 564675.

Kirkes, R. 2007. Evaluation of the Duration of Direct Brine Release in WIPP Performance Assessment (Revision 0). Carlsbad, NM: Sandia National Laboratories. ERMS 545988.

Klinkenberg, L.J. 1941. The Permeability of Porous Media to Liquids and Gases API Drilling and Production Practice. Albuquerque, NM: Sandia National Laboratories. (pp. 200–13). ERMS 208556.

Langevin, C.D., J.D. Hughes, E.R. Banta, R.G. Niswonger, S. Panday, and A.M. Provost. 2017. Documentation for the MODFLOW 6 Groundwater Flow Model. U.S. Geological Survey Techniques and Methods, Book 6, A55. https://doi.org/10.3133/tm6A55

Lee, J. 1982. Well Testing. SPE Textbook Series Vol. 1. New York: Society of Petroleum Engineers of AIME.

Leigh, C., R. Beauheim, and J. Kanney. 2003. SNL WIPP Analysis Plan AP-100, Revision 0, Analysis Plan for Calculation of Culebra Flow and Transport, Compliance Recertification Application. Carlsbad, NM: Sandia National Laboratories. ERMS 530172.

Li, D., R.K. Svec, T.W. Engler, and R.B. Grigg. 2001. Modeling and Simulation of the Wafer Non-Darcy Flow Experiments. Paper presented at the SPE Western Regional Meeting, Bakersfield, CA. March 26–30. SPE 68822

Long, J. 2019. Computational Code Execution and File Management for the 2019 Compliance Recertification Application Performance Assessment (CRA-2019 PA). Carlsbad, NM: Sandia National Laboratories. ERMS 571375.

Long, J., and S. King. 2022. Summary Report on the Migration of the WIPP PA Codes from Solaris to Linux. Carlsbad, NM: Sandia National Laboratories. ERMS 577606. *

Long, J. 2025. Computational Code Execution and File Management for the 2026 Compliance Recertification Application Performance Assessment: Interim State Repository (CRA-2026 IS). Rev. 0. Carlsbad, NM: Sandia National Laboratories. EIM-0004900878. *

Lord, D.L., D.K. Rudeen, and C.W. Hansen. 2003. Analysis Package for DRSPALL: Compliance Recertification Application Part I: Calculation of Spall Volume. Carlsbad, NM: Sandia National Laboratories. ERMS 532766.

Lord, D.L., and D.K. Rudeen. 2003. Sensitivity Analysis Report: Parts I and II: DRSPALL Version 1.00: Report for Conceptual Model Peer Review July 7–11. Carlsbad, NM: Sandia National Laboratories. ERMS 524400.

Lord, D.L., D.K. Rudeen, J.F. Schatz, A.P. Gilkey, and C.W. Hansen 2006. DRSPALL: Spallings Model for the Waste Isolation Pilot Plant 2004 Recertification. Albuquerque, NM: Sandia National Laboratories. SAND2004-0730.

Lorenz, J.C. 2006a. Assessment of the Potential for Karst in the Rustler Formation at the WIPP Site. Albuquerque, NM: Sandia National Laboratories. SAND2005-7303.

Lorenz, J.C. 2006b. Assessment of the Geological Evidence for Karst in the Rustler Formation at the WIPP Site. Caves and Karst of Southeastern New Mexico. L. Land, V.W. (pp. 243–52)

Lucchini, J. and Swanson, J. 2023. LANL ACRSP Parameter Recommendations for CRA-2024 Performance Assessment. Rev. 0. Carlsbad, NM: Los Alamos National Laboratory. LCO-ACP-34. *

Mariner, P. 2025. CRA-2026 IS updates to the WIPP humic colloids models for An(III) and An(IV). Carlsbad, NM: Sandia National Laboratories. EIMS-0004838142. *

Martell, M. 1996a. Memorandum to C. Lattier. Subject: Additional Information for the DRZ [Disturbed Rock Zone] Porosity. November 14, 1996. Albuquerque, NM: Sandia National Laboratories. ERMS 242257.

Martell, M. 1996b. Memorandum to C. Lattier. Subject: Additional Information for the Culebra Transport Parameter Id: 843, idpram: DNSGRAIN, idmtrl: CULEBRA, WIPP Data Entry Form 464 at WPO # 32689. December 10, 1996. Albuquerque, NM: Sandia National Laboratories. ERMS 232689.

Mattax, C.C., and R.L. Dalton. 1990. Reservoir Simulation. SPE Monograph 13. Richardson, TX: Henry L. Doherty Memorial Fund of Society of Petroleum Engineers, Inc.

Matteo, E., and B. Reedlunn. 2020. Increasing the WIPP Shaft Seal Diameter: A Scoping Calculation to Estimate of the Impact on Hydrologic Performance. November 2020. Carlsbad, NM: Sandia National Laboratories. *

McCormick, J., Kirkes R., and Hansen C. 2024. Conceptual Models in WIPP Performance Assessment. Revision 0. October 2024. Carlsbad, NM: Sandia National Laboratories. EIMS-0004385596. *

McDonald, M.G., and A.W. Harbaugh. 1988. A Modular Three-Dimensional Finite-Difference Ground-Water Flow Model. U.S. Geological Survey Techniques of Water-Resources Investigations. Book 6, Chap. A1. U.S. Government Printing Office.

McKay, M.D., R.J. Beckman, and W.J. Conover. 1979. A Comparison of Three Methods for Selecting Values of Input Variables in the Analysis of Output from a Computer Code. Technometrics, vol. 21: 239–45.

McTigue, D.F. 1993. Permeability and Hydraulic Diffusivity of Waste Isolation Pilot Plant Repository Salt Inferred from Small-Scale Brine Inflow Experiments. Albuquerque, NM: Sandia National Laboratories. SAND92-1911.v

Meigs, L. 1996. Memorandum to J. Ramsey. Subject: Non-Salado: Diffusive Tortuosity for the Culebra Dolomite. May 16, 1996. Albuquerque, NM: Sandia National Laboratories. ERMS 238940.

Meigs, L., and J. McCord. 1996. Physical Transport in the Culebra Dolomite. Albuquerque, NM: Sandia National Laboratories. ERMS 239167.

Meigs, L., R.L. Beauheim, and T.L. Jones (eds). 2000. Interpretations of Tracer Tests Performed in the Culebra Dolomite at the Waste Isolation Pilot Plant Site. Albuquerque, NM: Sandia National Laboratories. SAND97-3109.

Mendenhall, F.T., and W. Gerstle. 1995. WIPP Anhydrite Fracture Modeling, Systems Prioritization Method – Iteration 2 Baseline Position Paper: Disposal Room and Cutting Models, Appendix F: Comparison of Two Geomechanical Analysis Codes for WIPP Disposal Room Modeling: SANCHO and SPECTROM-2. Albuquerque, NM: Sandia National Laboratories. ERMS 228733.

Nemer, M.B., and D.J. Clayton. 2008. Analysis Package for Salado Flow Modeling, 2009 Compliance Recertification Application Calculation. Carlsbad, NM: Sandia National Laboratories. ERMS 548607.

Nemer, M.B., and J.S. Stein. 2005. Analysis Package for BRAGFLO, 2004 Compliance Recertification Application Performance Assessment Baseline Calculation (June 28). Carlsbad, NM: Sandia National Laboratories. ERMS 540527.

Nemer, M.B., J.S. Stein, and W. Zelinski. 2005. Analysis Report for BRAGFLO Preliminary Modeling Results With New Gas Generation Rates Based Upon Recent Experimental Results. Carlsbad, NM: Sandia National Laboratories. ERMS 539437.

Nemer, M. 2025. MgO Hydration Rates for the CRA-2026 Under AP-208. Albuquerque, NM: Sandia National Laboratories. EIMS-0004445255. *

Oldroyd, J.G. 1958. Non-Newtonian Effects in Steady Motion of Some Idealized Elastico-Viscous Liquids. Proceedings of the Royal Society of London: Series A: Mathematical and Physical Sciences, vol. 245, no. 1241: 278–97. ERMS 243211.

Özişik, M.N. 1993. Heat Conduction. Second Edition. New York, NY: John Wiley & Sons.

Papenguth, H.W. 1996. Parameter Record Package for Colloid Actinide Retardation Parameters. Sandia WIPP Central Files (SWCF). ERMS 238876.

Podio, A.L., and A.P. Yang. 1986. Well Control Simulator for IBM Personal Computer. IADC/SPE 14737. Paper presented at the International Association of Drilling Engineers/Society of Petroleum Engineers Drilling Conference. Dallas, TX, February 10–12.

Poettmann, F.H., and P.G. Carpenter. 1952. Multiphase Flow of Gas, Oil, and Water Through Vertical Flow Strings with Application to the Design of Gas-lift Installations. Drilling and Production Practice (1952): 257–317.

Popielak, R.S., R.L. Beauheim, S.R. Black, W.E. Coons, C.T. Ellingson, and R.L. Olsen. 1983. Brine Reservoirs in the Castile Formation Waste Isolation Pilot Plant (WIPP) Project Southeastern New Mexico. Carlsbad, NM: Westinghouse Electric Corp. TME-3153. ERMS 242085.v

Powers, D. 2006. Analysis Report Task 1B of AP-114: Identify possible area of recharge to the Culebra west and south of WIPP. Carlsbad, NM: Sandia National Laboratories. ERMS 547094.

Prasuhn, A.L. 1980. Fundamentals of Fluid Mechanics. Englewood Cliffs, NJ: Prentice-Hall.

Prausnitz, J.M. 1969. Molecular Thermodynamics of Fluid—Phase Equilibria. Englewood Cliffs, NJ: Prentice-Hall.

Rechard, R.P., H. Iuzzolino, and J.S. Sandha. 1990. Data Used in Preliminary Performance Assessment of the Waste Isolation Pilot Plant (1990). Albuquerque, NM: Sandia National Laboratories. SAND89-2408.

Roberts, R. 1996. Salado: Brine Compressibility. Records Package. Albuquerque, NM: Sandia National Laboratories. ERMS 412842.

Roberts, R. 1996a. Salado: Brine Density. Records Package. Albuquerque, NM: Sandia National Laboratories. ERMS 412369.

Ruth, D., and H. Ma. 1992. On the Derivation of the Forchheimer Equation by Means of the Averaging Theorem. Transport in Porous Media, vol. 7: 255–64.

Sandia National Laboratories (SNL). 1992. Preliminary Performance Assessment for the Waste Isolation Pilot Plant, December 1992. 5 vols. Albuquerque, NM: Sandia National Laboratories. SAND92-0700/1-5.

Sandia National Laboratories (SNL). 1997. Summary of Uncertainty and Sensitivity Analysis Results for the EPA-Mandated Performance Assessment Verification Test. Albuquerque, NM: Sandia National Laboratories. ERMS 420667.

Savins, J.G., and G.C. Wallick. 1966. Viscosity Profiles, Discharge Rates, Pressures, and Torques for a Rheologically Complex Fluid in a Helical Flow. A.I.Ch.E. Journal, vol. 12: 357–63.

Stein, J.S. 2002. Memorandum to M.K. Knowles. Subject: Methodology behind the TBM BRAGFLO Grid. May 13, 2002. Carlsbad, NM: Sandia National Laboratories. ERMS 522373.

Stein, J.S., and W. Zelinski. 2003. Analysis Report for: Testing of a Proposed BRAGFLO Grid to be used for the Compliance Recertification Application Performance Assessment Calculations. Carlsbad, NM: Sandia National Laboratories. ERMS 526868.

Stockman, C., A. Shinta, and J. Garner. 1996. Analysis Package for the Salado Transport Calculations (Task 2) of the Performance Assessment Analysis Supporting the Compliance Certification Application. Carlsbad, NM: Sandia National Laboratories. ERMS 422314.

Stoelzel, D.M., and D.G. O'Brien. 1996. Analysis Package for the BRAGFLO Direct Release Calculations (Task 4) of the Performance Assessment Calculations Supporting the Compliance Certification Application (CCA), AP-029, Brine Release Calculations. Albuquerque, NM: Sandia National Laboratories. ERMS 417870.

Streeter, V.L. 1958. Fluid Mechanics. 2nd ed. New York: McGraw-Hill.

Sweby, P.K. 1984. High Resolution Schemes Using Flux Limiters for Hyperbolic Conservation Laws. SIAM Journal on Numerical Analysis, vol. 21: 995–1011.

The Earth Technology Corporation. 1987. Final Report for Time Domain Electromagnetic (TDEM) Surveys at the WIPP Site. August. Albuquerque, NM: Sandia National Laboratories. SAND87-7144.

Thomas, J.W. 1995. Numerical Partial Differential Equations: Finite Difference Methods. Texts in Applied Mathematics 22. New York, NY: Springer-Verlag.

Thompson, T.W., W.E. Coons, J.L. Krumhansl, and F.D. Hansen. 1996. Inadvertent Intrusion Borehole Permeability (July). Albuquerque, NM: Sandia National Laboratories. ERMS 241131.

Tierney, M.S. 1990. Constructing Probability Distributions of Uncertain Variables in Models of the Performance of the Waste Isolation Pilot Plant: the 1990 Performance Simulations. Albuquerque, NM: Sandia National Laboratories. SAND 90-2510.

Timoshenko, S.P., and J.N. Goodier. 1970. Theory of Elasticity. 3rd ed. New York: McGraw-Hill.

U.S. Congress. 1992. WIPP Land Withdrawal Act, Public Law 102-579, 106 Stat. 4777, 1992; as amended by Public Law 104-201, 110 Stat. 2422, 1996.

U.S. Congress. 1996. Public Law 102-579. Waste Isolation Pilot Plant Land Withdrawal Act of 1992, as amended by Public Law 104-201, 1996.

U.S. Department of Energy (DOE). 1995. Waste Isolation Plant Sealing System Design Report. Carlsbad, NM: U.S. Department of Energy, Carlsbad Area Office. DOE/WIPP-95-3117.

U.S. DOE. 1997. Supplemental Summary of EPA-Mandated Performance Assessment Verification Test (All Replicates) and Comparison with the Compliance Certification Application Calculations (August 8). Carlsbad, NM: U.S. Department of Energy, Carlsbad Area Office. WPO 46702. ERMS 414879.

U.S. DOE. 2004. Title 40 CFR Part 191 Compliance Recertification Application for the Waste Isolation Pilot Plant. Carlsbad, NM: U.S. Department of Energy, Carlsbad Field Office. DOE/WIPP 2004-3231.

U.S. DOE. 2011. Panel Closure System Design, Planned Change Request to the EPA 40 CFR Part 194 Certification of the Waste Isolation Pilot Plant. U.S. Department of Energy, Carlsbad Field Office. Carlsbad, New Mexico.

U.S. DOE. 2014. Title 40 CFR Part 191 Compliance Recertification Application for the Waste Isolation Pilot Plant. Carlsbad, NM: U.S. Department of Energy, Carlsbad Field Office. DOE/WIPP 2014-3503.

U.S. DOE. 2015. Response to Environmental Protection Agency Letters Dated December 17, 2014 and February 27, 2015 Regarding the 2014 Compliance Recertification Application. U.S. Department of Energy, Waste Isolation Pilot Plant, Carlsbad Field Office. Carlsbad, NM. ERMS 563433.

U.S. DOE. 2016. WIPP UPDATE: October 14, 2016, Plans Call for Controlled Withdrawal from South End of Underground. http://www.wipp.energy.gov/Special/WIPP%20Update%2010_14_16.pdf

U.S. U.S. DOE. 2018. Waste Isolation Pilot Plant Delaware Basin Monitoring Annual Report. Revision 1. Carlsbad, NM: U.S. DOE, Carlsbad Field Office. DOE/WIPP-18-2308.

U.S. DOE. 2019. Title 40 CFR Part 191 Subparts B and C Compliance Recertification Application for the Waste Isolation Pilot Plant, Carlsbad, NM: Carlsbad Field Office. DOE/WIPP 2019-3609. *

U.S. DOE. 2025. Waste Isolation Pilot Plant Delaware Basin Monitoring Annual Report. Revision 0. Carlsbad, NM: U.S. DOE, Carlsbad Field Office. DOE/WIPP-24-2308. *

U.S. Environmental Protection Agency (EPA). 1985. 40 CFR 191: Environmental Standards for the Management and Disposal of Spent Nuclear Fuel, High-Level and Transuranic Radioactive Wastes; Final Rule. Federal Register, (September) vol. 50, 38066–089.

U.S. EPA. 1993. 40 CFR 191: Environmental Radiation Protection Standards for the Management and Disposal of Spent Nuclear Fuel, High-Level and Transuranic Radioactive Wastes; Final Rule. Federal Register, (December) vol. 58, 66398–416.v

U.S. EPA. 1996a. 40 CFR Part 194: Criteria for the Certification and Recertification of the Waste Isolation Pilot Plant's Compliance with the 40 CFR Part 191 Disposal Regulations; Final Rule. Federal Register, (February) vol. 61, 5223–45.

U.S. EPA. 1996b. Background Information Document for 40 CFR Part 194. Washington, DC: Office of Radiation and Indoor Air. (January). EPA 402-R-96-002.

U.S. EPA. 1998a. Response to Comments. Criteria for the Certification and Recertification of the Waste Isolation Pilot Plant's Compliance with 40 CFR Part 191 Disposal Regulations: Certification Decision. Washington, DC: Office of Radiation and Indoor Air. Docket A-93-02, V-C-1.

U.S. EPA. 1998b. Technical Support Document for Section 194.23: Parameter Justification Report (May 18, 1998). Washington, DC: Office of Radiation and Indoor Air. A-93-02-V-B-14.

U.S. Environmental Protection Agency (EPA). 2006a. Technical Support Document for Section 194.14/15: Evaluation of Karst at the WIPP Site (March). Washington, DC: Office of Radiation and Indoor Air.

U.S. EPA. 2006b. Recertification CARD No. 14/15: Content of Certification Application and Compliance Recertification Application(s). Compliance Application Review Documents for the Criteria for the Certification and Recertification of the Waste Isolation Pilot Plant's Compliance with the 40 CFR 191 Disposal Regulations: Final Recertification Decision (March) (pp. 14/15-1 through 14/15-34, pp. 14-A-1 through 14-A-3, and pp. 15-A-1 through 15-A-17). Washington, DC: Office of Radiation and Indoor Air.

U.S. EPA. 2017a. Criteria for the Certification and Recertification of the Waste Isolation Pilot Plant's Compliance with the Disposal Regulations: Recertification Decision. July 19, 2017. 82 FR 137 33106-33122.

U.S. EPA. 2017b. Probability of Encountering Castile Brine Beneath the WIPP Waste Panels Using the TDEM Block Method. June, 2017. Office of Radiation and Indoor Air, Docket EPA-HQ-OAR-2014-0609-0047.

U.S. EPA. 2017c. Technical Support Document for Section 194.24, Evaluation of the Compliance Recertification Actinide Source Term, Gas Generation, Backfill Efficacy, Water Balance and Culebra Dolomite Distribution Coefficient Values. June, 2017. Office of Radiation and Indoor Air, Docket EPA-HQ-OAR-2014-0609-0054.

U.S. EPA. 2017d. Technical Support Document for Section 194.23, EPA Review of Proposed Modification to the Waste Shear Strength Parameter TAUFAIL. July, 2017. Office of Radiation and Indoor Air, Docket EPA-HQ-OAR-2014-0609-0052.

U.S. EPA. 2022. Criteria for the Certification and Recertification of the Waste Isolation Pilot Plant's Compliance with the Disposal Regulations: Recertification Decision. May 3, 2022. 87 FR 26126-26136. *

U.S. U.S. EPA. 2025. Letter from Abigale Tardif to Mark Bollinger, Subject: EPA's Review and Approval of DOE's RPPCR for Waste Panels 11 and 12 at WIPP. July 31, 2025. Washington, DC: U.S. EPA. *

Van Genuchten, R. 1978. Calculating the Unsaturated Hydraulic Conductivity with a New Closed-Form Analytical Model. Report 78-WR-08. Princeton: Princeton University, Department of Civil Engineering, Water Resources Program. ERMS 249486.

Van Soest, G. 2025. Interim State Performance Assessment Inventory Report – 2024. Revision 0. INV-IPA-24. Carlsbad, NM: Los Alamos National Laboratory. *

Vargaftik, N.B. 1975. Tables on the Thermophysical Properties of Liquids and Gases in Normal and Dissociated States. 2nd ed. Washington, DC: Hemisphere.

Vaughn, P. 1996. Memorandum to M. Tierney. Subject: Salado Borehole Diameter. February 23, 1996. Albuquerque, NM: Sandia National Laboratories. ERMS 235329.

Vignes, C., J.E. Bean, and B. Reedlunn. 2023. Improved Modeling of Waste Isolation Pilot Plant Disposal Room Porosity. Carlsbad, NM: Sandia National Laboratories. SAND2023-04826. *

Walas, S.M. 1985. Phase Equilibria in Chemical Engineering. Boston: Butterworth.

Walker, R.E. 1976. Hydraulic Limits are Set by Flow Restrictions. Oil and Gas Journal, vol. 74, no. 40: 86–90.

Walker, R.E., and W.E. Holman. 1971. Computer Program Predicting Drilling-Fluid Performance. Oil and Gas Journal, vol. 69, no. 13: 80–90.

Ward, A. 2025. Letter to Bill McInroy. Subject: Performance Assessment Inventory for Analysis of a 12-Panel Repository Configuration. March 18, 2025. Carlsbad, NM: U.S. DOE, Carlsbad Field Office. CBFO:ERCD:AW:RS:25-0197. *

Weast, R.C., ed. 1969. Handbook of Chemistry and Physics. 50th ed. Cleveland: Chemical Rubber Pub. Co.

Webb, S.W. 1992. Appendix A: Uncertainty Estimates for Two-Phase Characteristic Curves for 1992 40 CFR 191 Calculations, Preliminary Performance Assessment for the Waste Isolation Pilot Plant, December 1992 (pp. A-147 through A-155). Volume 3: Model Parameters. Albuquerque, NM: Sandia National Laboratories. SAND92-0700/3.

Welchon, J.K., A.F. Bertuzzi, and F.H. Poettmann. 1962. Wellbore Hydraulics. Petroleum Production Handbook. Eds. T.C. Frick and R.W. Taylor. Dallas: Society of Petroleum Engineers of AIME. (pp. 31-1 through 31-36).

Whitaker, S. 1996. The Forchheimer Equation: A Theoretical Development. Transport in Porous Media, vol. 25: 27-61.

White, J., R. Hunt, M. Fienen, and J. Doherty. 2020. Approaches to Highly Parameterized Inversion: PEST++ Version 5, a Software Suite for Parameter Estimation, Uncertainty Analysis, Management Optimization and Sensitivity Analysis: U.S. Geological Survey Techniques and Methods 7C26, 52 p. *

Whittaker, A., ed. 1985. Theory and Application of Drilling Fluid Hydraulics. Boston: International Human Resources Development Corporation.

Wilgus, J. and J. Bethune. 2025. Analysis Report for Culebra Flow and Transport in the 2026 Compliance Recertification Application Performance Assessment. Carlsbad, NM: Sandia National Laboratories. EIMS-0005101531. *

Wilgus, J. and S. Brunell. 2025. Re-Calculation of the Location of Culebra Release Point 2 for Use in WIPP PA Rev. 1. Carlsbad, NM: Sandia National Laboratories. EIMS-0004818700. *

Williamson, A.S., and J.E. Chappelear. 1981. Representing Wells in Numerical Reservoir Simulation: Part 1—Theory. Society of Petroleum Engineers Journal, vol. 21: 323–38.

WIPP Performance Assessment. 2021a. Design Document and User's Manual for CUTTINGS_S Version 6.04. Carlsbad, NM: Sandia National Laboratories. ERMS 574596. *

WIPP Performance Assessment. 2021b. Design Document and User's Manual for DRSPALL Version 1.24. Carlsbad, NM: Sandia National Laboratories. ERMS 573906. *

WIPP Performance Assessment. 2021c. Requirements Document, Verification and Validation Plan, And Validation Document for DRSPALL Version 1.24 Carlsbad, NM: Sandia National Laboratories. ERMS 573905. *

WIPP Performance Assessment. 2022a. Design Document and User's Manual for CCDFGF (Version 8.01). Carlsbad, NM: Sandia National Laboratories. ERMS 577625. *

WIPP Performance Assessment. 2022b. Design Document and User's Manual for LHS Version 3.00. Carlsbad, NM: Sandia National Laboratories. ERMS 574194. *

WIPP Performance Assessment. 2022c. Design Document and User's Manual for NUTS Version 2.08. Carlsbad, NM: Sandia National Laboratories. ERMS 573824. *

WIPP Performance Assessment. 2022d. Design Document and User's Manual for PANEL Version 5.02. Carlsbad, NM: Sandia National Laboratories. ERMS 577751. *

WIPP Performance Assessment. 2022e. Design Document and User's Manual for PRECCDFGF Version 3.01. Carlsbad, NM: Sandia National Laboratories. ERMS 577631. *

WIPP Performance Assessment. 2022f. Design Document and User's Manual for SECOTP2D Version 1.44. Carlsbad, NM: Sandia National Laboratories. ERMS 573879. *

WIPP Performance Assessment. 2025. Design Document and User's Manual for BRAGFLO, Version 8.00. Carlsbad, NM: Sandia National Laboratories. EIMS-0004430695. *

Zeitler, T.R., J. Bethune, S. Brunell, B. Day, D. Kicker, J. Long, and R. Sarathi. Summary Report for the 2019 Compliance Recertification Application Performance Assessment (CRA-2019 PA). 2019. Carlsbad, NM: Sandia National Laboratories. ERMS 571376.

Zeitler, T.R. 2023. Consideration of TDEM Data for PBRINE Parameter Including Replacement Panels. Carlsbad, NM: Sandia National Laboratories. ERMS 580108. *

Zeitler, T.R. 2025. Analysis Report for Direct Brine Releases in the 2026 Compliance Recertification Application Performance Assessment: Interim State Repository. Carlsbad, NM: Sandia National Laboratories. EIMS-0004961699. *